

# Linear Friction Welding of AD730™ Ni-Based Superalloy to Additively Manufactured Inconel 718

by

Syedmohammad TABAIE

MANUSCRIPT-BASED THESIS PRESENTED TO ÉCOLE DE  
TECHNOLOGIE SUPÉRIEURE IN PARTIAL FULFILLMENT FOR THE  
DEGREE OF DOCTOR OF PHILOSOPHY  
Ph.D.

MONTREAL, JULY 16<sup>th</sup>, 2021

ÉCOLE DE TECHNOLOGIE SUPÉRIEURE  
UNIVERSITÉ DU QUÉBEC



Syedmohammad Tabaie, 2021



This Creative Commons licence allows readers to download this work and share it with others as long as the author is credited. The content of this work can't be modified in any way or used commercially.

**BOARD OF EXAMINERS**

THIS THESIS HAS BEEN EVALUATED

BY THE FOLLOWING BOARD OF EXAMINERS

Mr. Mohammad Jahazi, Thesis Supervisor  
Department of Mechanical Engineering, École de Technologie Supérieure

Mr. Farhad Rézaï-Aria, Thesis Co-supervisor  
Institut Clément Ader (ICA), Université de Toulouse, CNRS, IMT Mines Albi, France

Mr. Sègla Jean-Luc Kpodjedo, President of the Board of Examiners  
Department of Software Engineering and IT, École de Technologie Supérieure

Mr. Vincent Demers, Member of the jury  
Department of Mechanical Engineering, École de Technologie Supérieure

Mr. Adrian Gerlich, External Evaluator  
Department of Mechanical and Mechatronics Engineering, University of Waterloo

THIS THESIS WAS PRESENTED AND DEFENDED

IN THE PRESENCE OF A BOARD OF EXAMINERS AND PUBLIC

JULY 6<sup>TH</sup>, 2021

AT ÉCOLE DE TECHNOLOGIE SUPÉRIEUR



## ACKNOWLEDGMENT

I would like to convey my earnest gratitude to my supervisor, Professor Mohammad Jahazi. This research work would not have been possible without perspective on various aspects and continual guidance of my supervisor. I am thankful to him for believing in my accomplishments and providing me this opportunity to assimilate. I would also wish to thank Professor Farhad Rézaï-Aria (my co-supervisor) for his kind support, guidance and conveying additive manufacturing process and superalloys expertise during my Ph.D. program. I am really grateful to work under his supervision because he taught me how to be professional and generous in research.

I am very grateful for the opportunity to work with Professor Jonathan Cormier and learn from him. I owe many thanks to him and Dr. Ahad Shafiee for their continuous support with helpful discussion during my thesis. I would like to extend my appreciation to Mr. Adrien Lieurey for his involvement and fabrication of SLM parts. I would like to express appreciation to Aubert & Duval Co. for providing AD730<sup>TM</sup> samples and to TWI Ltd. for welding the samples especially Dr. Alexandre Deveaux and Dr. Bertrand Flipo for their invaluable discussions.

I would like to thank Dr. Mohammad Saadati for helping and training on SEM and EBSD machine and Mr. Radu Romanica, Mr. Morgan Letenneur, and Mr. Majid Heidari for providing facilities at the material laboratory. I would also like to express my gratitude to Professor Mamoun Medraj (at Concordia University), Professor Vladimir Brailovski, Dr. Eslam Fayed and Mr. Salah-eddine Brika for providing heat treatment equipment. I gratefully acknowledge Dr. Ameth Maloum Fall and Mr. Jia Hong Liu for their help and support during dilatometer testing. Gratitude is also expressed for all CM2P members for their cooperation during the entire journey of my Ph.D.

I am gratefully acknowledging the financial support from the Natural Sciences and Engineering Research Council (NSERC) of Canada in the form of a Discovery Grant.

Gratitude is also expressed for all CM2P members (Dr. Yassine Bouissa, Dr. Alireza Aleyari, Dr. Nima Bohlooli, Mr. Muftah Zorgani, and Mr. Ali Vedaei) for their cooperation during the entire journey of my Ph.D.

Finally, I am deeply indebted to my family for all their love and support. Most of all, I would like to thank my supportive, patient, and encouraging my mother whose supports giving me this opportunity to continue my education is so appreciated.

# **Soudage par Friction Linéaire du Superalliage Base Nickel AD730™ à Inconel 718 Fabriqué de Manière Additive**

Seyedmohammad TABAIE

## **RÉSUMÉ**

Le soudage friction linéaire (LFW) est une technologie émergente de soudage à l'état solide pour l'assemblage des pièces métalliques comme par exemple des aubes à des disques (blisks) des turbines à gaz ou la réparation de disques de turbine. Ces dernières années, LFW a été également appliqué à l'assemblage de composants des superalliages à base de nickel (Ni), ainsi que des nombreuses autres applications d'ingénierie, allant de l'automobile à l'agriculture, et permettant de nombreuses autres applications industrielles allant de l'automobile à l'agriculture permettant de nouvelles conceptions, applications ou extension de durée de vie des pièces. Le procédé LFW est bien adapté pour assembler différents alliages puisque le soudage s'effectue à l'état solide évitant la contraction de la soudure ou la fissuration qui très couramment rencontrés dans les techniques de soudage basées sur la fusion de matériaux. D'autre part, la fusion sélective par laser (SLM) de lit de poudres (LPBF), est une technologie avancée économiquement viable pour la fabrication des pièces en superalliages à base de Ni ayant des géométries complexes pour les industries aéronautique, aérospatiale et production d'énergie.

L'objectif de ce travail de thèse était d'étudier l'aptitude du procédé LFW à assembler deux superalliages produits par le forgeage et la fabrication additive, soit Inconel 718 (IN718) -SLM au superalliage à base de Ni AD730™ récemment produit par Auber et Duva. Chaque alliage avait ses propres microstructures initiales et finales qui devaient être étudiés. Ainsi, de nombreux défis et questions techniques et scientifiques devaient être abordés avant l'application industrielle avec la fiabilité accrue de LFW de matériaux différents. Certains de ces défis seront pris en compte dans ce travail de recherche. L'objectif de ces travaux est d'avoir une meilleure compréhension de l'évolution de la microstructure et des propriétés mécaniques du LFWed AD730™ au SLM IN718.

Les essais LFW ont été réalisés à l'aide d'un modèle prédictif de faisabilité de soudage fourni par la littérature. Il est basé sur une simulation thermique 1D qui a été développée pour le soudage dissemblable. Une méthodologie a été envisagée pour déterminer les paramètres LFW afin d'obtenir un joint complet sans défaut (tout au moins acceptable) pour les alliages utilisés. Ce procédé peut également être étendu et appliqué à d'autres alliages métalliques. Il s'agit à estimer les forces de frottement et de forge à l'aide des contraintes d'écoulement du matériau plastique, des données rapportées dans la littérature et de la capacité de la machine de soudage employé. Le temps de frottement a été estimé sur la base d'un modèle thermique analytique pour les deux alliages en tenant compte de leurs propriétés mécaniques à haute température. Il a été déterminé que les échantillons LFWed avec un raccourcissement axial de plus de 2 mm et une valeur optimum à 3.5 mm peuvent être soudés qui sont exempte d'oxydes et de microfissures.

## VIII

La ductilité à chaud du superalliage polycristallin et forgé à base de Ni, AD730<sup>TM</sup>, a été étudiée dans l'intervalle de température de 1050 à 1240 °C. Les températures de résistance nulle (NST) et de ductilité nulle (NDT) ont été déterminées par des essais de traction à chaud en utilisant le simulateur thermomécanique Gleeble<sup>TM</sup> 3800. L'influence de la vitesse de chauffe, représentant le cycle thermique LFW, sur la ductilité à chaud des alliages a également été étudiée. La microstructure et le mode de rupture des échantillons ont été examinés. L'influence de la vitesse de chauffage sur l'étendue de la liquation de la limite des grains et de la formation des cavités a été déterminée. Il a été montré que la perte significative de la ductilité près du point NDT peut être reliée à la réduction de la tension superficielle de l'interface entre les grains et la matrice. De plus, la contribution des mécanismes d'endommagement responsables de la perte de ductilité tels que les précipités durs (par exemple, les carbures MC aux limites des grains), les vides et les cavités a été discutée.

L'influence de la vitesse élevée de chauffage sur l'évolution des phases secondaires précipitées dans la microstructure du SLM IN718 a été étudiée. La caractérisation microstructurale a été faite à l'aide de la microscopie électronique à balayage (MEB) dans et depuis la ligne de soudage (zones affectées thermiquement et mécaniquement) des échantillons soudés. Une combinaison d'analyse thermique par DTA et dilatomètre a été utilisée pour étudier de la précipitation et la dissolution des phases secondaires influençant les caractéristiques microstructurales et propriétés mécaniques. La dissolution des phases  $\gamma''$  et  $\delta$  a été retardée lors que la vitesse de chauffage devient très élevée et décalée vers des températures de plus élevées. La phase de Laves dans les régions inter-dendritiques a été décomposée en zones spécifiques proche de la surface de l'échantillon. Un mécanisme basé sur l'influence de la vitesse de chauffage sur la diffusion de Nb dans les régions inter-dendritiques et aux cœurs des dendrites, a été proposé pour interpréter les changements microstructuraux observés.

Les analyses microscopiques par MEB et l'image XCT-Scan ont montré que des joints soudés sont exempts de micro-porosités, micro-fissures et couches d'oxyde ont été obtenues. Les variations de microstructures ont été également évaluées, notamment en termes de taille de grain, et changements de désorientation ont été déterminés. La recristallisation dynamique (DRX) qui s'est produite dans des deux côtés de la ligne de soudure dissemblable et il a été constaté que DRX discontinu (DDRX) et DRX continu (CDRX) ont eu lieu dans la zone de soudure (ZW) et dans la zone thermomécanique affectée (TMAZ), respectivement. Le changement clair dans la taille et l'orientation des grains sont liés à la sévérité élevée de déformation plastique cumulé cycliquement dans un échantillon soudé qui a subi un traitement thermique d'homogénéisation et à l'effet croissant du mécanisme de renforcement de la solution solide causé par une dissolution partielle des particules de renforcement de deuxième phase dans la matrice.

Les observations au MEB et les cartes EBSD ont montré que la recristallisation dynamique s'est produite dans la zone de soudure pendant le LFW hybride dans l'échantillon soudé des deux alliages soudés. Près de la ligne de soudure, la dissolution des phases  $\gamma'/\gamma''$  et Laves et le raffinement du grain se sont produits, ce qui révèle à la fois les effets de la déformation de compression et de la température élevée sur la recristallisation et le degré élevé de diffusion

des éléments chimiques dans la ZW. Il est montré que la taille, la fraction volumique et la forme des phases secondaires ont augmenté et changé de la ZW au métal de base (BM). La microdureté mesurée, dans la ZW, a indiqué que la résistance de l'alliage AD730<sup>TM</sup> dépend significativement de la taille des grains et éventuellement des précipités ultrafins, tandis que la résistance du SLM IN718 était dominée par la forme (ou la taille) et la présence de phases secondaires.

Un cycle de traitement thermique post-soudage (PWHT) a été réalisé sur des échantillons LFWed dissemblables. La microstructure et la dureté du joint après le PWHT ont été étudiées et comparées à celles des échantillons LFWed. Le mécanisme de durcissement par précipitation de  $\gamma'+\gamma''$  est le principal mécanisme utilisé pour augmenter les propriétés mécaniques de l'alliage SLM IN718. Ces particules ont grossi lors d'un traitement thermique à 980 °C et d'un double vieillissement. L'histoire thermomécanique des joints LFWed peut affecter la microstructure de l'alliage IN718 tel que la morphologie de la phase  $\delta$  après traitement en solution (ST) du type plaque dans la zone de soudure (WZ) au type aiguille dans le matériau de base (BM). Il a été constaté que dans l'AD730<sup>TM</sup>, des particules de taille nanométrique  $\gamma'$  re-précipitaient près de la ligne de soudure pendant un refroidissement rapide après la fin du soudage. Le PWHT développé pourrait homogénéiser la dureté sur les deux alliages et toutes les zones de soudage. La différence de dureté maximale entre chaque zone était de 15 à 20 Vickers pour le WZ et le BM. La différence de dureté maximale entre les deux alliages était de 19 Vickers, ce qui signifie que le PWHT, en deux étapes, pourrait fournir une meilleure homogénéité pour un joint différent que le traitement thermique en une étape qui a été utilisé dans la littérature.

**Mots-clés:** Soudage friction linéaire; Fabrication additive; Fusion sélective laser, superalliage base Ni; AD730<sup>TM</sup>; Inconel 718; Ductilité nulle et températures de résistance nulles; Dissolution des phases, Re-précipitation; Mécanismes de liquidation; La diffusion; Analyse par EBSD; Recristallisation dynamique; Désorientation, Renforcement des mécanismes, Traitement thermique après soudage.



# **Linear Friction Welding of AD730<sup>TM</sup> Ni-Based Superalloy to Additively Manufactured Inconel 718**

Seyedmohammad TABAIE

## **ABSTRACT**

Linear friction welding (LFW) is an emerging solid-state welding technology for joining of blades to disks (blisks) or repairing turbine disks in gas turbines and air engines. In recent years, LFW has also been applied to the assembly of components made of Nickel (Ni)-based superalloys, as well as in many other engineering applications, ranging from automotive to agriculture, and allowing for new designs and applications. The LFW process is well suited for joining dissimilar alloys as they do not suffer from weld shrinkage and cracking which are very common in fusion-based techniques. On the other hand, Selective laser melting (SLM) as a laser powder bed fusion (LPBF) method is being developed as an economically viable technology for fabricating Ni-based superalloys with the complex geometries in aerospace industries and also as an advanced technique for component repair. Gas turbine blades are known for their complex geometries and high time to market delay. The additive layer manufacturing can reduce drastically the time to market.

The focus of this PhD work was to study the suitability of the LFW process to join two superalloys fabricated with two different methods: SLMed Inconel 718 (IN718) superalloy and the newly introduced forged AD730<sup>TM</sup> Ni-based superalloy. Each alloy had individual initial and final microstructures which had to be understood. Thus, many challenges and questions needed to be addressed. Some of these challenges will be considered in this PhD research. The focus of this study is to have a better understanding of the evolution of the microstructure and mechanical properties of LFWed AD730<sup>TM</sup> to SLM IN718.

LFW experiments were carried out using a model from literature based on 1D heat transfer simulation, which was developed and adapted in this work for the dissimilar welding. A methodology was adapted to determine the LFW parameters for achieving an acceptable joint with free defects for the investigated alloys. The method can be extended and applied to other metallic as well. The method consisted in estimation of friction and forge forces by using the plastic flow stresses and data reported in the literature as well as the capability of LFW machine. Friction time was estimated based on an analytical thermal model for both alloys and their mechanical properties at high temperatures. It was determined that the LFWed specimens with axial shortening more than 2 mm and optimum to 3.5 mm were free from oxides and microcracks.

Hot ductility of the forged polycrystalline Ni-based superalloy, AD730<sup>TM</sup> was investigated in the temperature interval 1050–1240 °C. The nil strength (NST) and nil ductility temperatures (NDT) were determined by hot tensile testing using the Gleeble<sup>TM</sup> 3800 known a convenient method for weld thermal simulations. The tests plan and designing the mechanical tests had been done by other CM2P members. The influence of heating rate, representing the LFW thermal cycle, on hot ductility behavior of the alloy was also studied. The microstructure and the fracture mode of samples were examined. The influence of heating rate on the extent of

grain boundary liquation and void formation was determined. It was shown that the significant ductility loss near the NDT point could be related to the reduction of surface tension at interface of the grain boundary and the matrix. In addition, the contribution of hard precipitates (e.g., grain boundary MC carbides), voids, and cavities on damage mechanisms responsible for ductility loss was discussed.

The influence of high heating rates on the evolution of the secondary phases in the microstructure of SLM IN718 was investigated. The microstructural characterizations using Scanning Electron Microscopy (SEM) revealed different regions in the heat-affected zone (HAZ) of the welded additively manufactured specimens. A combination of thermal analysis by DTA and dilatometry was used to show the precipitation and dissolution of the secondary phases and microstructural features. The dissolution of  $\gamma''$  and  $\delta$  phases were delayed under high heating rates and shifted to higher temperatures. The Laves phase at the interdendritic regions was decomposed in specific zones near the surface of the sample. A possible mechanism based on the influence of heating rate on Nb diffusion in the interdendritic regions and core of the dendrites was proposed to interpret the observed changes in the microstructure.

Microscopic analysis and XCT-Scan image showed successful joints free of micro-porosity, micro-cracking, and oxide layers. The microstructures variations were also evaluated, particularly in terms of grain size and misorientation changes. Dynamic recrystallization (DRX) occurred on both sides of the dissimilar weld line, and it was found that Discontinuous DRX (DDRX) and Continuous DRX (CDRX) recrystallization took place in the weld zone (WZ) and in the thermomechanical-affected zone (TMAZ), respectively. A clear change in the size and local grain misorientations levels were related to a greater degree of strain-induced in a homogenized sample and the increasing and the effect of the solid solution strengthening mechanisms caused by a partial dissolution of the second phase strengthening particles in the matrix.

The SEM observations and EBSD maps showed that dynamic recrystallization occurred in the weld zone during hybrid LFW in samples in as-welded condition on both sides. Close to the weld line, the dissolution of  $\gamma'/\gamma''$  and Laves phases and grain refinement occurred which reveals the combined effects of both compressions loading and high temperature on recrystallization on drastic diffusion of chemical elements in the WZ. It is shown that the size, volume fraction, and shape of secondary phases increased and changed from the WZ to the base metal (BM). The measured microhardness, in the WZ, indicated that the strength of AD730<sup>TM</sup> alloy depends significantly on the grain size and also possibly on ultrafine precipitates. The strength in SLM IN718 was dominated by the shape (or size) and the presence of secondary phases.

A post-weld heat treatment (PWHT) cycle was performed on dissimilar LFWed samples. The microstructure and hardness of the joint after the PWHT were studied and compared to those of LFWed samples. The precipitation hardening mechanism of  $\gamma' + \gamma''$  is the main mechanism used to increase the mechanical properties of SLM IN718 alloy. These particles coarsened during heat treatment at 980 °C and double aging. The thermomechanical history of LFWed joints can affect the microstructure of IN718 alloy such as morphology of  $\delta$  phase after solution

treatment (ST) from the plate-like in the weld zone (WZ) to the needle-like in the base material (BM). It was found that in AD730<sup>TM</sup>, nanometric size  $\gamma'$  particles re-precipitated close to the weld line during rapid cooling after welding was completed. The developed PWHT could homogenize the hardness on both alloys and all welding zones. The maximum hardness difference between each zone was 15-20 Vickers for the WZ and the BM. The maximum hardness difference between two alloys was 19 Vickers which means the PWHT, in two steps, could provide a better homogeneity for a dissimilar joint than one-step heat treatment which has been used in literature.

**Keywords:** Linear friction welding; Additive manufacturing; Selective laser melting, Ni-based superalloy; AD730<sup>TM</sup>; Inconel 718; Nil ductility and nil strength temperatures; Dissolution and reprecipitation; Liquation mechanisms; Diffusion; EBSD analysis; Dynamic recrystallization; Misorientation, Strengthening mechanisms, Post-weld heat treatment.



## TABLE OF CONTENTS

	Page
INTRODUCTION .....	1
CHAPTER 1 LITERATURE REVIEW .....	5
1.1 Additive manufacturing .....	5
1.2 Selective Laser Melting .....	5
1.2.1 Selective Laser Melting of Inconel 718 .....	6
1.2.2 Microstructure .....	8
1.2.3 Post-fabrication processing .....	12
1.2.4 Mechanical properties .....	20
1.3 Linear Friction Welding (LFW).....	24
1.3.1 Main LFW parameters .....	27
1.3.2 Microstructure evolution.....	36
1.3.3 Dissimilar LFW of superalloys.....	53
1.3.4 Post-processing heat treatments (PWHT).....	55
1.3.5 Mechanical properties.....	58
1.4 Challenges and objectives.....	63
CHAPTER 2 DETERMINATION OF LFW PROCESS PARAMETERS FOR SLM IN718 TO AD730 <sup>TM</sup> ALLOY.....	65
2.1 Introduction.....	65
2.2 Linear friction welding process .....	65
2.2.1 Friction and forge pressures.....	65
CHAPTER 3 HOT DUCTILITY BEHAVIOR OF AD730 <sup>TM</sup> NICKEL-BASED SUPERALLOY.....	75
3.1 Introduction.....	76
3.2 Materials and Experimental Method.....	78
3.3 Results and Discussion .....	85
3.3.1 Nil strength temperature .....	85
3.3.2 Nil Ductility Temperature.....	92
3.4 Conclusions.....	105
CHAPTER 4 MICROSTRUCTURE EVOLUTION OF SELECTIVE LASER MELTED INCONEL 718: INFLUENCE OF HIGH HEATING RATES.....	107
4.1 Introduction.....	108
4.2 Materials and Methods.....	111
4.2.1 Materials .....	111
4.2.2 Thermal analysis .....	112

4.2.3	Microstructural investigations .....	114
4.3	Results and discussions.....	114
4.3.1	Characterization of the as-SLM sample.....	114
4.3.2	DTA test.....	120
4.3.3	High heating rate tests.....	124
4.3.4	Hardness variations.....	133
4.4	Conclusions.....	134
CHAPTER 5	GRAIN SIZE AND MISORIENTATION EVOLUTION IN LINEAR FRICTION WELDING OF ADDITIVELY MANUFACTURED IN718 TO FORGED SUPERALLOY AD730 <sup>TM</sup> .....	135
5.1	Introduction.....	136
5.2	Experimental Procedures .....	138
5.3	Results and Discussion .....	143
5.3.1	Microstructural evolutions across the weld line .....	143
5.3.2	Grain size evolution .....	145
5.3.3	Misorientation.....	156
5.4	Microhardness.....	160
5.5	Conclusions.....	165
CHAPTER 6	DISSIMILAR LINEAR FRICTION WELDING OF SELECTIVE LASER MELTED INCONEL 718 TO FORGED Ni-BASED SUPERALLOY AD730 <sup>TM</sup> : EVOLUTION OF STRENGTHENING PHASE.....	167
6.1	Introduction.....	168
6.2	Experimental procedure .....	171
6.3	Results and discussion .....	175
6.3.1	Chemical compositional change .....	175
6.3.2	Precipitation distribution analysis.....	177
6.3.3	Effects of thermomechanical compressive strain .....	183
6.3.4	Microhardness.....	190
6.4	Conclusions.....	199
CHAPTER 7	POST-WELD HEAT TREATMENT OF ADDITIVELY MANUFACTURED INCONEL 718 WELDED TO FORGED NI-BASED SUPERALLOY AD730 <sup>TM</sup> BY LINEAR FRICTION WELDING.....	201
7.1	Introduction.....	202
7.2	Experimental procedures .....	205
7.2.1	Post-weld heat treatment.....	205
7.2.2	Microstructural analysis.....	207
7.2.3	Microhardness.....	208
7.3	Results and discussion .....	208
7.3.1	Microstructure evolution.....	208
7.3.2	Microhardness.....	219
7.4	Conclusions.....	227

CONCLUSIONS .....	228
RECOMMENDATIONS.....	233
LIST OF BIBLIOGRAPHICAL REFERENCES.....	235



## LIST OF TABLES

	Page
Table 1.1 Mechanical properties at 20°C for homogeneous and functionally graded IN718 specimen Taken from Popovich et al. (2019, p. 701).....	14
Table 1.2 Maximum heating and cooling rates and peak temperature at different initial locations away from the weld centerline during LFW of Waspaloy Taken from A. Chamanfar et al. (2012b, p. 113).....	49
Table 2.1 Estimation of Linear friction welding parameters to use for SLM IN718 and AD730 <sup>TM</sup> superalloys.....	71
Table 2.2 Linear friction welding parameters determined and used for SLM IN718 and AD730 <sup>TM</sup> superalloys.....	71
Table 2.3 Final LFW parameters used by TWI Co. according to the estimation .....	71
Table 3.1 Chemical composition of AD730 <sup>TM</sup> .....	79
Table 4.1 SLM parameters to fabricate Inconel 718 alloy specimens .....	111
Table 4.2 The average chemical composition of SLM IN718 (wt. %).....	112
Table 4.3 Variation of precipitation (p) and dissolution (d) temperatures of $\gamma'$ , $\gamma''$ , and $\delta$ phases in the SLM-IN718, for different heating rates .....	120
Table 4.4 Chemical composition (wt.%) in sample heated at 100 °C/s.....	127
Table 4.5 Microstructural characteristics of the SLMed IN718 for different heating rates ..	132
Table 5.1 Chemical compositions of AD730 <sup>TM</sup> and SLM IN718 alloys.....	139
Table 5.2 LFW processing parameters in the current study .....	140
Table 5.3 Axial shortening of samples after forging stage in LFW.....	145
Table 6.1 Chemical compositions of bulk of alloys (Wt.%). Chemical potentials for driving the elements by diffusion near the weld line is indicated by positive sign that means element diffusion from AD730 <sup>TM</sup> to SLM IN718 and negative sign in the opposite direction.....	172
Table 6.2 LFW processing parameters in the current study .....	172
Table 7.1 Chemical compositions of bulk of alloys (wt.%) .....	205

Table 7.2 EDS chemical composition analysis of Laves and $\delta$ phases in the PWHTed samples in the TMAZ .....	218
Table 7.3 Comparison of the microhardness values between PWHTed and as-welded samples in different zones.....	221

## LIST OF FIGURES

	Page
Figure 1.1 SLM machine experiment setup.....	6
Figure 1.2 Assessment of weldability diagrams for Ni-based superalloys according to chemical composition of the $\gamma'$ (Al and Ti) and the carbide (Cr and Co) ...	7
Figure 1.3 SEM 3D-composite micrograph showing the columnar structure of the SLM-printed cylinder with respect to the building direction. The black arrows are used to indicate the grain boundary lines.....	9
Figure 1.4 SEM micrographs showing the intermetallic micro-segregation in (a) inside $\gamma$ -phase grains, (b) lower inset shows the $\delta$ needles at stacking faults and carbides at higher magnification, and (c, d) micrograph and the respective chemical compositions of the various precipitates .....	11
Figure 1.5 TTT diagram of Inconel 718 alloy .....	12
Figure 1.6 Variation of the time and temperature of homogenization treatment.....	17
Figure 1.7 (a) SEM micrograph of a homogenized IN718; (b) different precipitates at the grain boundaries; (c, d) shows $\delta$ and MC carbide precipitates .....	18
Figure 1.8 Comparing (a) Yield strength, (b) Ultimate tensile strength and (c) Elastic modulus of selective laser melted IN 718 with conventional manufacturing methods.....	22
Figure 1.9 Comparing (a) the yield and (b) the ultimate strengths of heat treated SLM IN718 .....	23
Figure 1.10 Schematic of the LFW process.....	27
Figure 1.11 Primary $\gamma'$ dissolution temperature of the AD730 <sup>TM</sup> at different heating rates ....	31
Figure 1.12 Microstructure of three regions around weld zone, namely, regions 1 to 3, which correspond to the WZ, the TMAZ, and the HAZ, respectively .....	37
Figure 1.13 SEM micrographs showing a crack-free linear friction joint in IN 738.....	38
Figure 1.14 SEM images of the TMAZ show (a) intergranular and (b) intragranular liquation .....	40
Figure 1.15 EBSD grain map from the WZ to the TMAZ.....	40

Figure 1.16 SEM images from the formation of $\gamma$ - $\gamma'$ eutectic at their interface after constitutional liquation of primary $\gamma'$ particle. Heating rate of 400 °C/s + 3 s holding time at 1200 °C and air cooling.....	46
Figure 1.17 SEM images of from flash (a) and TMAZ (b) at 500 $\mu$ m away from the weld line. There is no indication of liquation or $\gamma/\gamma'$ eutectic products .....	47
Figure 1.18 Dissimilar IFW of Rene 88 to IN718 .....	54
Figure 1.19 Microhardness distributions of joint in IN718. (PR is partial reversion of $\gamma'$ and $\gamma''$ , R is recrystallized zone and W is the WZ) .....	59
Figure 1.20 Microhardness profile across the weld centerline in as-LFWed and PWHTed conditions of Waspaloy.....	60
Figure 1.21 Microhardness profile across the weld of PWHTed IN718 alloy .....	61
Figure 2.1 Calculated temperature variation with time for different LFW process parameters of IN718 superalloy .....	68
Figure 2.2 Calculated temperature variation with time for different LFW process parameters of AD730 <sup>TM</sup> superalloy. Test 1: 133 MPa, Test 2: 150 MPa, Test 3: 187.5 MPa, and Test 4: 285 MPa.....	68
Figure 2.3 Temperature variation with time for different LFW process parameters of IN718 superalloy at a = 3 mm and f = 40 Hz conditions.....	69
Figure 2.4 Temperature variation with time for different LFW process parameters of AD730 <sup>TM</sup> superalloy at a = 3 mm and f = 40 Hz conditions .....	70
Figure 2.5 Linear friction welding cycle for dissimilar SLM IN718 to AD730 <sup>TM</sup> .....	72
Figure 2.6 Variation of temperature as a function of time at the weld interface by applying friction pressure 228 MPa for 7.7 s.....	73
Figure 2.7 Temperature distribution along the x-axis with applied friction pressure 228 MPa after 7.7 s .....	74
Figure 3.1 NDT and NST sample location in the as forged billet .....	79
Figure 3.2 Initial microstructure of AD730 <sup>TM</sup> superalloy .....	80
Figure 3.3 Gleeble <sup>TM</sup> 3800 physical simulator setup and adapted geometry for determining nil strength temperature. Using a special actuator allows maintaining a constant 90 N tensile load on sample throughout experiment. The specimen dimensions are 75 mm long and 6 mm diameter .....	82

- Figure 3.4 Schematic of Gleeble<sup>TM</sup>'s procedure for hot ductility testing, (a) on-heating hot tensile test with constant heating rate, holding time and stroke rate at different temperature. (b) hot ductility curve with respect to testing temperature; note that the NDT is lower than the NST and  $\gamma$  solidus temperature of AD730<sup>TM</sup> .....83
- Figure 3.5 Gleeble<sup>TM</sup> 3800 physical simulator setup and adapted geometry for conducting hot ductility testing. Large load cell is used on the high force jaw system and the lengthwise change is controlled by longitudinal transducer .....84
- Figure 3.6 Variation of the NST point of AD730<sup>TM</sup> with heating rate when compared to the NST of IN718 and Waspaloy.....86
- Figure 3.7 Fracture surface of NST samples at different heating rates. a) 5 °C/s, b) 25 °C/s, c) 50 °C/s, d) 100 °C/s. White arrows indicate the large voids and circled zones indicate small voids coalescence .....88
- Figure 3.8 Voids fraction and size distribution as a function of the heating rate .....89
- Figure 3.9 Distribution of void size fraction between 0 and 10  $\mu\text{m}$  interval as a function of the heating rate.....90
- Figure 3.10 Distribution of void size fraction between 0 and 100  $\mu\text{m}$  as a function of the heating rate.....90
- Figure 3.11 Stress-strain curves of hot tensile tests obtained by Gleeble<sup>TM</sup> 3800.....93
- Figure 3.12 Hot ductility behavior during heating process at different temperatures. The standard deviation on the estimated reduction of area values is less than 2% .....94
- Figure 3.13 Fracture surface after NDT tests of AD730<sup>TM</sup> alloy, a) 1050 °C, b) 1100 °C, c) 1150 °C, d) 1200 °C.....97
- Figure 3.14 Fracture surface after NDT tests of AD730<sup>TM</sup> alloy, e) 1240 °C .....98
- Figure 3.15 SEM images showing void formation and crack growth at grain boundaries in the fracture area obtained from cross-sectioned 1240 °C specimen.....98
- Figure 3.16 SEM images from samples exposed to 1200 and 1240 °C of AD730<sup>TM</sup> showing: a) liquation at the GB, b) GB liquation and joining of the voids, c) carbides at GB and triple junctions, d) liquation at GB and crack growth, e) map analysis of a carbide particle in image (d) .....102

- Figure 3.17 Variations of the liquation thickness from the fracture zone to the parent material in the sample. Obtained from the longitudinal cross section of the NDT test sample 1240 °C. Measurements positions in the fractured sample are indicated by arrows.....103
- Figure 4.1 The time-temperature heating-cooling cycles of SLM IN718 specimens with three heating-up rates to achieve 1000 °C and a dwell time of 10 s and a final identical quenching constant rate of 65 °C/s .....113
- Figure 4.2 Schematic of dilatometer samples and their designated location for microstructural analysis and micro-hardness measurements .....113
- Figure 4.3 OM of as-Fabricated SLM-IN718 along the building direction (Z): (a) measured width and depth of a melt pool; (b) wide columnar grains elongated in the building direction; (c) 3D-reconstruction of cross-sectioned & polished planes of a SLM specimen .....116
- Figure 4.4 Variation of DAS and Laves fraction along the as-SLM IN718 specimen height. The BM to MT area is the middle region between the bottom (B) and the top (T) of the examined samples.....117
- Figure 4.5 Variation of DAS and Laves phase along the height of the as-SLM IN718 samples.....117
- Figure 4.6 FE-SEM micrographs from the microstructure of the as-SLM IN718 sample. (a) Dendritic structure and (b) particles at the interdendritic regions .....118
- Figure 4.7 Variation of the microhardness measured from bottom to the top of as-SLM sample .....119
- Figure 4.8 DTA records obtained on the as-SLM IN718 upon heating at scanning rates of 10, 15, 25, 50, 80, and 100 °C/min up to 1200 °C. The subscripts 'd' and 'p' represent the dissolution and precipitation temperatures of the corresponding phase.....121
- Figure 4.9 Variations of: (a)  $\gamma'$ , (b)  $\gamma''$ , and (c)  $\delta$  phase dissolution temperature (T) with heating rate (Hr) at the top section of the SLM IN718 sample.....123
- Figure 4.10 SEM image showing the microstructure near to the surface area of the sample heated to 1000 °C with 100 °C/s and dwell time 10 s followed by cooling at a constant rate of 65 °C/s .....124
- Figure 4.11 Estimated radial temperature gradients in 4-mm diameter SLM IN718 dilatometer samples for two heating rates. Surface temperature is 1000 °C .....125

Figure 4.12 SEM images showing blocky zones in the sub-surface area at the mid-span of longitudinally cut samples heated to 1000 °C at the rates of (a) 100, (b) 200, (c) 400 °C/s and 10 s holding time, and cooled by constant rate 65 °C/s.....	126
Figure 4.13 Chemical EDS mapping of some principal elements of as-SLM IN718 sample heated to 1000 °C for 200 °C/s.....	131
Figure 4.14 SEM images of the blocky zone show the presence of different precipitates such as semi-spherical $\gamma''$ and $\delta$ particles for sample heated to 1000 °C at a rate of 100 °C/s.....	131
Figure 4.15 Hardness distribution curves of the SLMed IN718, from the surface to the center of the sample for different heating rates in area showed in Figure 4.7. ....	133
Figure 5.1 Schematic presentation of process for LFW of dissimilar welding of forged Ni-based superalloy AD730 <sup>TM</sup> to as-SLM IN718 and H-SLM IN718 superalloys .....	141
Figure 5.2 Linear friction welded samples: (a) SLM IN718 to AD730 <sup>TM</sup> , (b) Homogenized SLMed IN 718 (H-SLM IN718) to AD730 <sup>TM</sup> alloy. The building direction (BD) in the SLM samples is shown with a black arrow. The dashed rectangular area applies to the microstructural analysis.....	142
Figure 5.3 (a) XCT-Scan image from weld area, and (b) OM image of the weld interface rotated counter clockwise relative to (a) shows a crack free weld area. The black particles in the WZ are MC-type carbides .....	144
Figure 5.4 Grain size at various locations from the weld interface in the LFW of SLM and H-SLM IN718 to AD730 <sup>TM</sup> .....	147
Figure 5.5 (a), (b) EBSD grain map and inverse pole figure (IPF) map from the weld line for LFW of SLM IN718 and H-SLM IN718 to AD730 <sup>TM</sup> alloy, respectively. (c) and (d) SEM micrographs from the weld line for LFW of SLM IN718 and H-SLM IN718 to AD730 <sup>TM</sup> alloy, respectively. Laves particles on IN718 side and the GBB on AD730 <sup>TM</sup> side are illustrated by yellow circles .....	148
Figure 5.6 Variation of HAGB, LAGB, and $\Sigma 3$ twin boundaries from the weld interface to the BM on both sides in LFWed samples: (a) as-SLM IN718-AD730 <sup>TM</sup> and (b) H-SLM IN718-AD730 <sup>TM</sup> .....	153

Figure 5.7 EBSD grain map in the as-SLM IN718 after the LFW to AD730 <sup>TM</sup> alloy: (a) in the BM zone, (b) in the BM+TMAZ, (c) in the TMAZ, and (d) in the TMAZ+WZ. IPF map and building direction of as-SLM part are shown .....	155
Figure 5.8 Local misorientation (LM) or average misorientation maps of the analyzed areas from the BM region in the as-SLM IN718 toward the BM region in AD730 <sup>TM</sup> after LFW. (a) and (b) are the BM and the TMAZ on the side of as-SLM IN718, respectively. (c) is the weld line and the WZ on both sides. (d) and (e) are the TMAZ and the BM on the side of AD730 <sup>TM</sup> .....	158
Figure 5.9 Microhardness profiles of two LFWed samples.....	162
Figure 6.1 Schematic presentation of LFW process for dissimilar Ni-based superalloys of AD730 <sup>TM</sup> and as-SLM IN718 and H-SLM IN718 alloys. The building direction (BD) in the SLM sample is shown with black arrow. The dashed rectangular area is EDMed for the microstructural analysis.....	173
Figure 6.2 EBSD grain map from different zones after LFW on both sides. The HAZ on the side of AD730 <sup>TM</sup> was not observed .....	174
Figure 6.3 (a, b) SEM image and EDS map of the analyzed regions in both superalloys across the weld line. (c) Line analysis with length 90 $\mu\text{m}$ corresponding element profiles across the weld line .....	176
Figure 6.4 FE-SEM images of different $\gamma'$ precipitates in LFWed AD730 <sup>TM</sup> and SLM-IN718 (a, b) at the WZ and weld interface .....	177
Figure 6.5 FE-SEM images of different $\gamma'$ precipitates in LFWed AD730 <sup>TM</sup> and SLM-IN718, (c) in the TMAZ or $\sim 0.2$ to 1 mm from the weld interface, and (d) (e) secondary ( $\gamma'_s$ ) and tertiary ( $\gamma'_t$ ) $\gamma'$ in the BM of AD730 <sup>TM</sup> .....	178
Figure 6.6 Variation of (a) volume fraction of $\gamma'$ in AD730 <sup>TM</sup> , and (b) Laves phase and Nb content in the Laves particles in SLM IN718 as a function of the distance from the weld interface.....	181
Figure 6.7 SEM images of microstructural evolution in SLM-IN718 after LFWed to AD730 <sup>TM</sup> alloy: (a, b) the weld line and spherical Laves particles formed in the WZ, (c, d) the TMAZ, (d, e) HAZ with mixed spherical and long-stripped Laves particles, and (f) the BM with long-stripped interdendritic Laves .....	182
Figure 6.8 (a) SEM micrograph from the weld line, (b) variation of Nb in the $\gamma$ matrix obtained from different EDS spot analysis in two superalloys close to the weld line after LFW .....	187

Figure 6.9 Microhardness profiles as a function of distance from the weld line of two LFWed samples .....	191
Figure 6.10 Variation of hardness and the size of secondary phases with distance from the weld line on (a) AD730 <sup>TM</sup> and (b) SLM IN718 sides.....	199
Figure 7.1 Schematic of the PWHT cycle for all LFWed samples.....	207
Figure 7.2 SEM micrograph in the BM zone of IN718 alloy after LFW and PWHT for: (a) W1, (b) W2, (c) W1-DA, (d) W2-DA, and (e) W1-STA .....	209
Figure 7.3 SEM images from sample W1-STA on the side of SLM IN718 alloy in the: (a) BM, (b) intergranular and intragranular $\delta$ phase in the BM, (c) the TMAZ, and (d) the WZ.....	210
Figure 7.4 Size and volume fraction ( $V_f$ ) evolution of the $\delta$ phase from the WZ to the BM, on SLM IN718 side, in different samples after PWHT: (a) volume fraction, (b) length, and (c) width of $\delta$ particles .....	212
Figure 7.5 Precipitation of secondary phases in the weld interface of W1 sample after PWHT: (a) as-welded, (b) W1 direct-aged, (c) on DA-SLM IN718 side in the WZ, and (d) very fine secondary and probably tertiary $\gamma'$ in DA-AD730 <sup>TM</sup> in the WZ .....	214
Figure 7.6 SEM images of $\gamma'$ precipitates in sample W1-STA: (a, c) in the WZ, (b, d) in the BM of AD730 <sup>TM</sup> side.....	215
Figure 7.7 Variation of (a) the volume fraction and (b) the size of primary and secondary (and tertiary) $\gamma'$ on AD730 <sup>TM</sup> side in W1-DA and W1-STA samples from the weld line to the BM.....	216
Figure 7.8 Precipitation of secondary phases in the microstructure of the PWHTed (a-c) W1-DA, (d-f) W1-STA, (g-i) W2-DA on the IN718 (SLM and H-SLM) sides (a, d, g) at the BM, (b, e, h) at the TMAZ, and (c, f, i) at the WZ..	219
Figure 7.9 Microhardness profiles as a function of distance from the weld line of two LFWed samples .....	220
Figure 7.10 Hardness distribution across the weld interface in three other dissimilar joints after PWHT .....	226



## LIST OF ABBREVIATIONS

LFW	Linear Friction Welding
AM	Additive Manufacturing
SLM	Selective Laser Melting
LPBF	Laser Powder Bed Fusion
BD	Building Direction
VED	Volume Energy Density
TMAZ	Thermo Mechanically Affected Zone
PWHT	Post Weld Heat Treatment
HAZ	Heat Affected Zone
PFZ	Precipitate Free Zones
LMP	Larson Miller Parameter
FSW	Friction Stir Welding
IFW	Inertia Friction Welding
WZ	Weld Zone
BM	Base Metal
LFM	Liquid Film Migration
DRV	Dynamic Recovery
DRX	Dynamic Recrystallization
CDRX	Continuous Dynamic Recrystallization
DDRX	Discontinuous Dynamic Recrystallization
OM	Optical Microscopy
SEM	Scanning Electron Microscopy
FE-SEM	SEM Field Emission Gun Scanning Electron Microscopy
EBS	Electron Backscatter Diffraction
BSE	Back Scattered Electron
EBS	Electron Backscatter Diffraction
GB	Grain Boundary
GBB	Grain Boundary Bulging
LAGB	Low Angle Grain Boundary

XXX

HAGB	High Angle Grain Boundary
GROD	Grain Reference Misorientation Deviation
KAM	Kernel Average Misorientation
LM	Local Misorientation
IPF	Inverse Pole Figure
DTA	Differential Thermal Analysis
EDS	Energy Dispersive Spectroscopy
NDT	Nil Ductility Temperature
NST	Nil Strength Temperature
UTS	Ultimate Tensile Stress
DAS	Dendrite Arm Spacing ( $\mu\text{m}$ , nm)
JMA	Johnson Mehl-Avrami
RT	Room Temperature
1D, 2D, 3D	One, Two, Three Dimensional
GTAW	Gas Tungsten Arc Welding
TTT	Time-Temperature-Transformation
RA	Reduction Area
HIP	Hot-Isostatic pressing
HT	Heat Treatment

## LIST OF SYMBOLS

### Latin symbols

$a$	Oscillation amplitude (mm)
$f$	Frequency (Hz), Fraction (%)
$k$	Shear strength (MPa)
$\mu$	Friction coefficient
$L, W, H$	Length, Width and Height of the specimen (mm)
$\sigma_0$	Flow stress (MPa)
$\varepsilon$	Strain
$\dot{\varepsilon}$	Strain rate ( $s^{-1}$ )
$T$	Temperature (K, °C), Thickness ( $\mu\text{m}$ )
$\rho$	Density ( $\text{Kg.m}^{-3}$ )
$\eta$	Thermal efficiency
$C_p, C$	Specific heat ( $\text{J. Kg}^{-1}. \text{K}^{-1}$ )
$\lambda$	Thermal conductivity ( $\text{W.m}^{-1}. \text{K}^{-1}$ )
$\alpha$	Thermal diffusivity ( $\text{m}^2. \text{s}^{-1}$ )
$v$	Rubbing velocity ( $\text{mm.s}^{-1}$ )
$\dot{q}$	Heat generation rate ( $\text{W.m}^{-2}$ )
$x$	Distance from the weld interface
$P_{Fric.}$	Friction pressure (MPa)
$P_{Forge}$	Forge pressure (MPa)
$D$	Diffusion coefficient ( $\text{m}^2. \text{s}^{-1}$ )
$H_r$	Heating rate ( $^{\circ}\text{C}. \text{s}^{-1}$ )
$C_r$	Cooling rate ( $^{\circ}\text{C}. \text{s}^{-1}$ )
$t$	Time (s)
$Q$	Activation energy ( $\text{KJ.mol}^{-1}$ )
$R$	Gas constant ( $\text{J.mol}^{-1}. \text{K}^{-1}$ )
$k$	Boltzmann constant ( $\text{J.K}^{-1}$ )
$\Omega$	Atomic volume

$\gamma_{sl}$	Surface tension (MPa)
$H$	Hatch spacing ( $\mu\text{m}$ )

**Subscripts**

$APB$	Anti-phase boundary
$sl$	Solid-liquid
$r$	Rate
$s$	strain
$m$	melting
$e$	Equivalent
$h$	Holding
$i$	Initial
$f$	Final
$V$	Volume
$A$	Area

## INTRODUCTION

The advantages of using blade integrated to disk or blisk as a single part are: (i) higher aerodynamic efficiency, (ii) reduced engine weight, (iii) waste reduction, and (iv) fewer sites for fatigue failure. However, blisks pose a unique challenge to the aero industry, where substantial damage of blades requires the removal and subsequent discarding of the entire blisk, which can be very costly. Therefore, it is necessary to develop a means to repair blisks.

In today's world of welding industry, friction-based joining processes such as friction welding and friction stir welding is widely used for joining similar and dissimilar metals. These techniques do not involve the melting and solidification of alloys as compared to the conventional fusion welding methods. An emerging technology, LFW, has been developed for manufacturing and repair of aerospace components such as rotating gas turbine components. The LFW for materials is a very stable and fast process, taking as little as a few seconds to create a joint. Surface preparation of the joint does not require an important preparation: any imperfections and impurities such as oxides are removed as flash along with a layer from the surface of the antagonist materials in relative cyclic displacement. It requires no consumables, produces no harmful fumes that require exhausting, and remaining in solid-state during processing. LFW bypasses many of the potential issues associated with solidification, such as segregation or porosity. Due to removing fusion-welding disadvantages and in order to achieve better mechanical properties in aerospace applications, the LFW became as a primary method for fabrication of blisk assemblies for aircraft turbine engines.

On the other hand, the as-cast turbine blades require complex mold construction and complex time-consuming and costly processing for each blade. Additive manufacturing (AM) is transforming all these issues. A laser beam as a source of energy in selective laser melting is directed to fine layer of metallic powders, which are heated and melted. When the laser is removed, the metal rapidly cools. The process is repeated layer by layer until the part from the 3D printer is finished. The time-to-market from the design of a new gas turbine blade to its

production can be reduced from several months and even years to feuy months through in additive manufacturing.

Combining these technologies in order to produce blisks of dissimilar nickel-based superalloys is considered as the major goal of PhD project. The superalloys have been used for many decades in the aerospace industry, due to their good high temperature mechanical properties and corrosion resistance. The Inconel 718 (IN718) superalloy is often used for disks and compressor/turbine blades. Besides, AD730™ is introduced by Auber & Duval Company as a new forged semi-product or raw nickel-based superalloy which can be used as a disk material. The mechanical properties of thus alloy are is comparable to other alloys such as Waspaloy, Ud720, IN718, and IN718 plus. On the basis of aforementioned demands of aerospace industry, the future project objective is to LFW of SLMed polycrystalline IN718 superalloy as a blade to an as-received polycrystalline AD730™ superalloy as forged material candidate for turbine disks and investigation of the microstructural evolution of LFWed component and subsequently achieving the best mechanical properties.

The present thesis is organized, as follows:

1. This thesis begins with a comprehensive literature survey to review the state-of-the-art knowledge regarding slective laser melting and linear friction welding of Ni-based superalloys. The chapter 1 summarizes developments on manufacturing processes of gas turbine discs, and discusses different points of view about microstructural evolution of dissimilar LFWed superalloys. Moreover, an overview on the mechanical properties of LFWed dissimilar materials before and after post-weld heat treatment is presented. Finally, the challenges are identified, and the objectives are defined.
2. Chapter 2 presents details of the materials used during the project and the methodology employed to design and determine LFW process promoters for dissimilar welding according to the literature and industrial limitations.

3. The influence of some LFW process parameters (e.g., high temperature and high heating rate) on hot deformation behavior of Ni-based superalloys specifically AD730<sup>TM</sup> alloy is investigated in chapter 3. Specifically, the experimental procedures and methodology used to determine nil ductility temperature (NDT) and nil-strength temperature (NST) using the Gleeble<sup>TM</sup> 3800 thermomechanical simulator is described. Microstructural characterizations, including fracture surface analysis, void, and porosity quantification are then presented and used to discuss possible governing mechanisms for the obtained NDT and NST results. The results obtained from this chapter are published in the Journal of Materials Science and Engineering: A, September 2019.

Considering that some parts of the work presented in chapter 3 were also carried out by other researchers, their contribution is detailed below:

The NDT & NST experimental process parameters were designed by Jonathan Cormier (ISAE-ENSMA), Alexandre Devaux (Aubert & Duval), Cléa Plouze (internship student at ÉTS) and Davood Shahriari. Thermal and thermomechanical experiments were conducted by Davood Shahriari using Gleeble 3800. Data curation on NST-NDT samples throughout and after thermomechanical testing were completed by Davood Shahriari. Initial fracture surface analysis and voids and porosities quantification using SEM were performed by Cléa Plouze.

4. Chapter 4 focuses on the evolution of second phase particles in the microstructure of SLM IN718 submitted to rapid thermal cycling. In this chapter, a better understanding of the response of an AM microstructure to rapid heating rates is provided which is crucial for predicting the HAZ and HAZ cracking susceptibilities in welded AM parts. The obtained results are presented in a model assisting to design the optimized procedures for welding of additively manufactured components. The results obtained from this chapter are published in the Journal of Metals, April 2020.

5. Chapter 5 discusses the potential of the combination of the LFW and SLM techniques in dissimilar welding of two superalloys with the ultimate goal of evaluating the possibility of manufacturing the new generation of blisks. This chapter specifically focused on the microstructural characterizations of the weldment (e.g., grains and grain misorientation evolutions). Moreover, the effects of these changes on microhardness and strengthening mechanisms after LFW are investigated. The results obtained from this chapter are published in the Journal of Materials Characterization, November 2020.
6. In chapter 6, a detailed microstructural analysis of LFW joints of two dissimilar Ni-based superalloys SLM IN718 and forged AD730<sup>TM</sup> is carried out, with a particular focus on the evolution of the strengthening phases and liquation. Microstructural evolutions, such as changes in volume fraction and size of precipitates in different zones and liquation are correlated with the evolution of microhardness, which could be useful to assess their impacts on strengthening mechanisms and mechanical properties of the joint. The results obtained from this chapter are submitted in the Journal of Materials Science and Technology, November 2020.
7. In chapter 7, the main objective is to provide PWHT cycles for friction welded dissimilar joints in order to achieve homogenized and enhanced microhardness and mechanical properties on both sides in dissimilar weldment. These properties are compared with dissimilar friction welding of IN718 to other alloys. Furthermore, the microstructures of PWHTed samples are characterized for this type of dissimilar joint for the first time. The results obtained from this chapter are submitted in the Journal of Metallurgical and Materials Transactions A, January 2021.

A summary covering all the concluding remarks concerning chapters 3 to 7 is presented in the Conclusions section to link the outcomes of the thesis and present original contributions of the study toward the thesis initial objectives.

## CHAPTER 1

### LITERATURE REVIEW

#### 1.1 Additive manufacturing

Additive manufacturing (AM) as a rapid prototyping technique was introduced to print a 3D part in the 1980s. This technique shapes a part layer-by-layer from a CAD model. In 1986 at the University of Texas Austin, the first AM technique is introduced to the industry by researchers (Wong & Hernandez, 2012; Y. Zhang et al., 2017). These processes have several notable advantages such as versatile geometric functionality, minimal human interplay requirements, and decreased the time of layout cycle (Herderick, 2011). In contrast to standard manufacturing strategies, in which regularly a large amount of material ought to be eliminated at the post-processing stages, the minimal material which is required for generating a part used by AM methods.

In the meantime, there is almost no standardization for AM methods. It is making difficult to have a widespread specification set and absolutely make use of the capacity of the technique in more demanding environments, which includes the aerospace and the nuclear industries (Segerstark, 2017).

#### 1.2 Selective Laser Melting

Selective laser melting (SLM) (Figure 1.1) is a laser-based powder bed fusion or AM technique, which uses a laser as a source of energy in the range of 100-1000 W. It is able to melt powders in the form of successive layers on top of each other to make a part (Petersen-Øverleir, 2015). Laser beam selectively melts step-by-step a layer of metallic powder to fabricate 3D-components with complicated geometries (e.g. gas turbine blades, injection molds, lattices geometry materials, heat exchangers, etc.) which are difficult and costly to acquire through conventional routes with a close to full density (close to 99.7%) and complex structures which designed by CAD model (Deng, Peng, Brodin, & Moverare, 2018; Kruth, Leu, & Nakagawa, 1998; C. Li, White, Fang, Weaver, & Guo, 2017). In this approach,

mechanical properties are comparable to those fabricated by wrought or casting (X. Wang, Gong, & Chou, 2016).

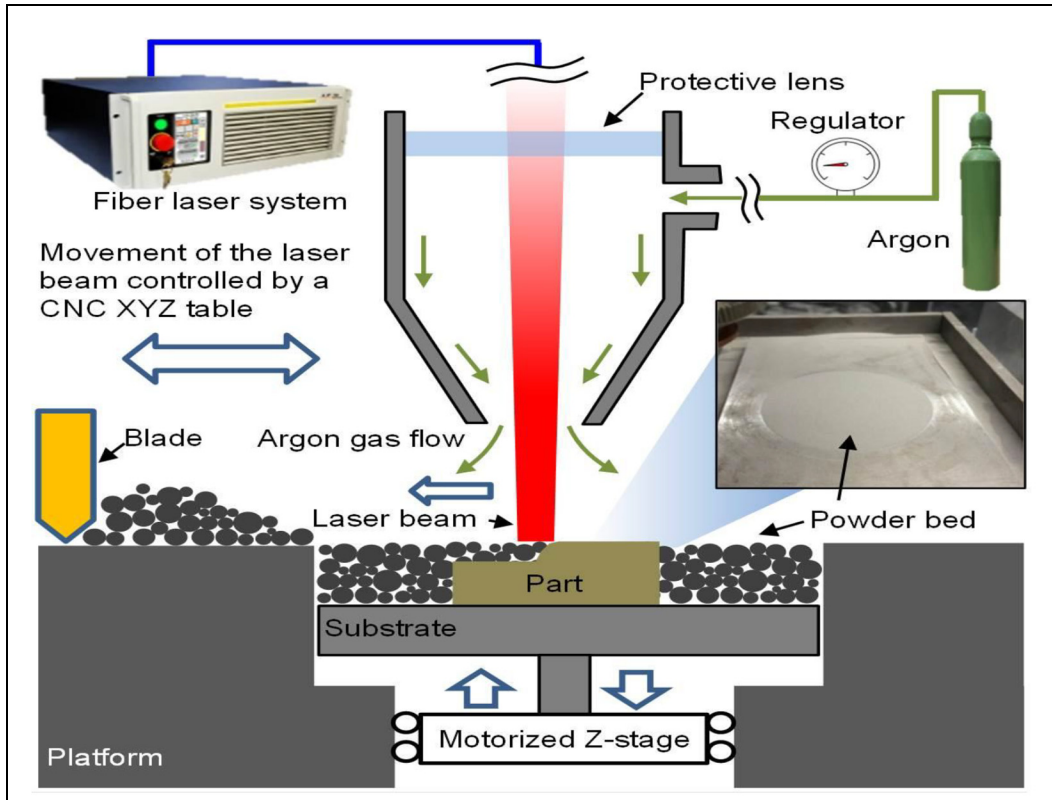


Figure 1.1 SLM machine experiment setup  
Taken from C. Li (2017, p. 20)

### 1.2.1 Selective Laser Melting of Inconel 718

Inconel 718 (IN718) is a solid solution strengthened Ni-based superalloy, which is used in high temperature applications (up to 650 °C) such as turbine blades and disk, pressurized water reactors, and nuclear reactors due to its combination of good weldability, forgeability, high strength, and good corrosion and oxidation resistance (Attallah, Jennings, Wang, & Carter, 2016; deBarbadillo & Mannan, 2012; Seede, Mostafa, Brailovski, Jahazi, & Medraj, 2018). Casting, forging, and extrusion are the mainly conventional fabrication methods to produce IN718 parts. Manufacturing a workpiece from IN718 by conventional machining is difficult

due to the significant level of wear (Moussaoui, Rubio, Mousseigne, Sultan, & Rezai, 2018). The high hardness and low thermal conductivity of IN718 can result in excessive tool wear leading to difficulties in machining finished products made from this alloy (Izquierdo, Plaza, Sánchez, Pombo, & Ortega, 2012; X. Wang, Gong, & Chou, 2015).

Therefore, production of the components closes to the final shape (near net shaping) with the least amount of machining is an issue. In addition, the excellent weldability makes the IN718 particularly interesting in the aerospace fields. IN718 alloy can thus be readily fabricated by AM methods specifically laser powder bed fusion. However, it is necessary to pay attention to the weldability and to eliminate the defects caused by welding and achieve the best microstructure with desired mechanical and/or functional properties. The Ni superalloys with a high  $\gamma'$  fraction have poor weldability (Figure 1.2) due to their important susceptibility to cracking during post-weld heat treatments or reheating known as strain-age cracking (Attallah et al., 2016; Henderson, Arrell, Larsson, Heobel, & Marchant, 2013).

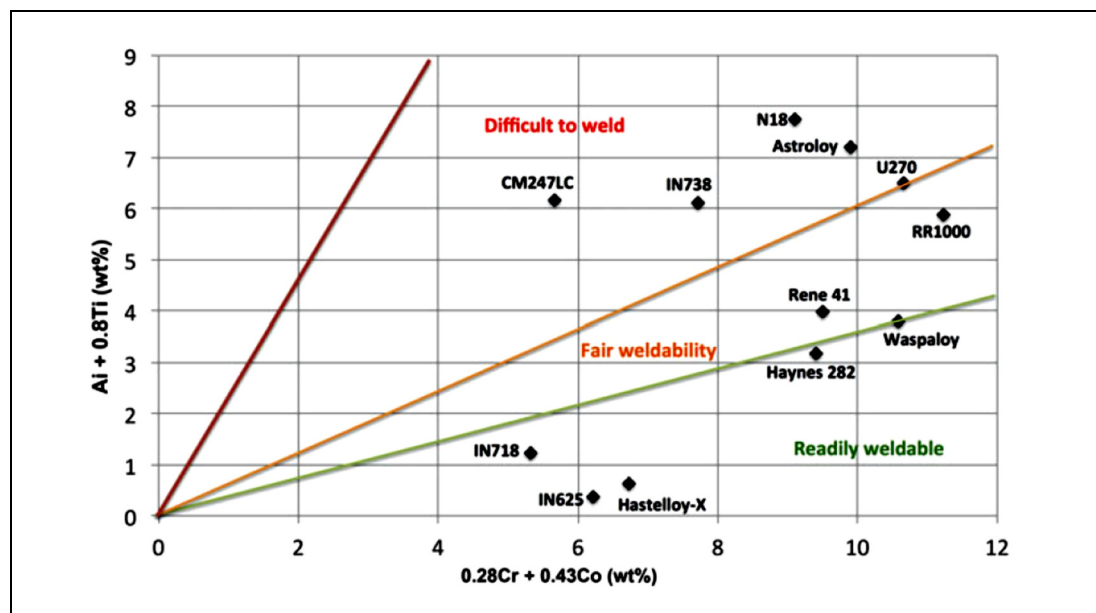


Figure 1.2 Assessment of weldability diagrams for Ni-based superalloys according to chemical composition of the  $\gamma'$  (Al and Ti) and the carbide (Cr and Co)  
Taken from Attallah et al. (2016, p. 758)

Although additive manufacturing (AM) can be described as a multilayer/repeated welding process, and therefore it is still susceptible to the weld cracking. The selective laser melting (SLM) is associated with rapid heating rate and particular rapid cooling rates (about  $10^6$  K/s) (Attallah et al., 2016; Harrison, Todd, & Mumtaz, 2015). Besides, the low aluminum and titanium contents of IN718 improve its weldability, thus making it very suitable for SLM processing (Mostafa et al., 2018; Trosch, Strößner, Völkl, & Glatzel, 2016).

### 1.2.2 Microstructure

As reported in many investigations (Amato et al., 2012; Jia & Gu, 2014; Mostafa, Picazo Rubio, Brailovski, Jahazi, & Medraj, 2017b; Z. Wang et al., 2012), SLM microstructure of IN718 is anisotropic and contains columnar grains grown parallel to the fabrication or building direction (BD) due to the steep thermal gradient generated in the micro-molten pools (Seede et al., 2018). In addition, the combination of rapid melting/solidification and post melting cooling rates in deposited layers causing the non-equilibrium microstructure features in different sections of a SLM part (B. Chen & Mazumder, 2017) (Hu et al., 2016; C. Li et al., 2017). The as-fabricated (as-SLM IN718) reveals the elongated grains with preferential crystallographic orientation and elongated grains with a strong  $\langle 001 \rangle$  direction along building direction (BD) texture (Figure 1.3) (B. Chen & Mazumder, 2017; deBarbadillo & Mannan, 2012; Mostafa et al., 2017b). In general, as-SLMed IN718 parts provide a fine columnar dendrite and cellular interdendritic microstructure (X. Wang et al., 2016). Moussaoui et al. (Moussaoui et al., 2018) reported that the columnar dendrites can be more oriented along the build direction by increasing volume energy density (VED). Zhang et al. (D. Zhang, Niu, Cao, & Liu, 2015) measured primary dendrite arm spacing of  $0.6 \mu\text{m}$  because of the very high cooling rates in SLM. Mostafa et al. (Mostafa et al., 2017b) also measured dendritic arm spacing between  $0.6$  to  $1.25 \mu\text{m}$  in SLMed IN718.

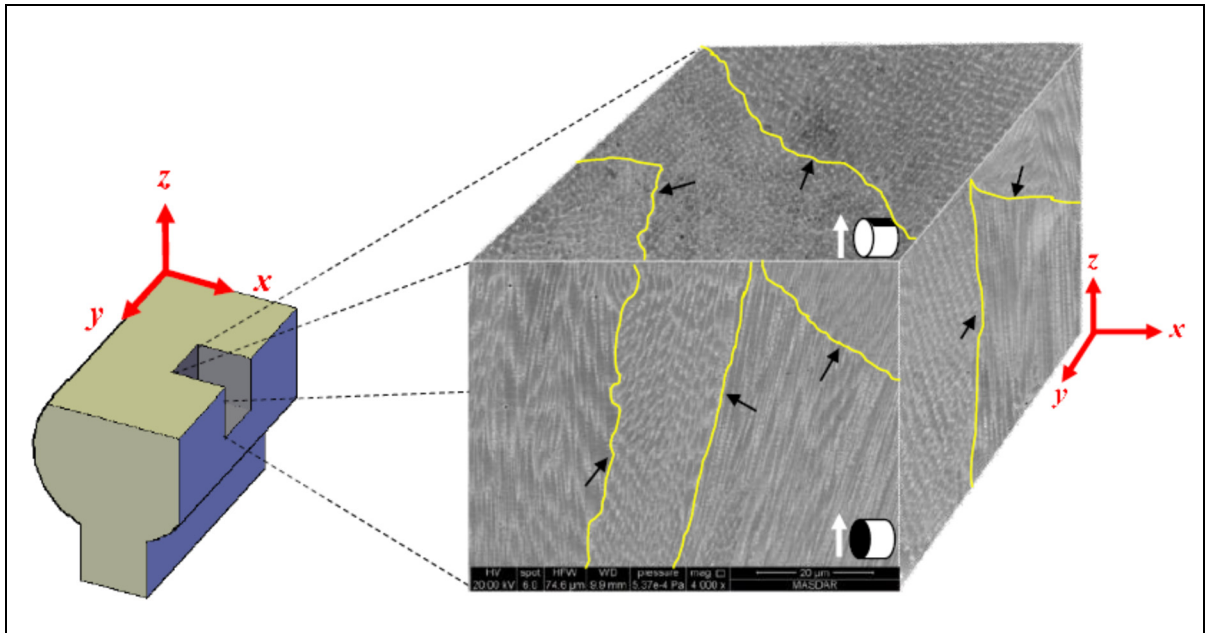


Figure 1.3 SEM 3D-composite micrograph showing the columnar structure of the SLM-printed cylinder with respect to the building direction. The black arrows are used to indicate the grain boundary lines  
 Taken from Mostafa et al. (2017b, p. 196)

The rapid cooling rate induced by high laser energy produces regular fine microstructure in as printed specimen. The oriented structure is determined by the defined building strategy (i.e., the scanning pattern, hatch spacing, and layer thickness). Jia and Gu (Jia & Gu, 2014) reported that applying various laser energy density changes successive such as clustered-coarse and uniformly distributed slender columnar dendritic grains.

Generally, macro-segregation would be completely prevented at high cooling rates, while micro-segregation of the elements of the chemical composition in as-printed IN718 would always occur. At a high cooling rate, the primary dendrite shape changes to a more cell-like form which induced the rapid dendritic/cellular growth of columnar grains (X. Wang et al., 2016). The local temperature fields affects the epitaxial nucleation and growth and grain orientation of grains and their orientations and form at the interface of micro-bath melt pools and the previously already solidified layers (or the plate in the first stage of fabrication) (Wei, Mazumder, & DebRoy, 2015). The grains are elongated several layers and surpassed the melt

pool boundaries, but the grains are elongated perpendicularly close to the surface due to the heat flux direction (Brenne et al., 2016).

As-SLM fabricated specimens generally showed dendritic microstructure, with columnar grains, good metallurgical bonding, and minimal porosity. The degree of orientation of grains decreased from the top to the bottom of the part due to the heat flow direction from the melt pool to the substrate. At the bottom, columnar grains appear narrower due to the higher cooling rate and contain very dense dendrites that grow from the substrate plate. At the bottom of the vertical (v) built parts, there is more reheating locally than the top or the last deposited layers. Thus, the first layer experiences aging which could precipitate  $\gamma'$  and  $\gamma''$  phases due to the local reheating or aging. Laves phase  $(\text{Ni,Cr,Fe})_2(\text{Nb,Mo,Ti})$ , likely  $\delta$ -phase ( $\text{Ni}_3\text{Nb}$ ) precipitates, and carbides particles were also detected in all fabricated specimens (Mostafa et al., 2017b; Parimi, A, Clark, & Attallah, 2014). Prabhakar (Tucho, Cuvillier, Sjolyst-Kverneland, & Hansen, 2017) also showed the possibility of  $\gamma'$  and  $\gamma''$  precipitations reducing the Laves concentration in the lower layers (13% of differences in between top and bottom layers). Hence, the Laves phase fraction within the bottom layers become fewer than the top region of Z built parts (Y. Zhang, Li, Nie, & Wu, 2012).

The SLM microstructure achieved from the rapidly cooled IN718 powder melt, contains Laves phase and  $\gamma''$  particles with different amounts of Nb dispersed in bottom layers of the material (Mostafa et al., 2017b). The region of overlapping interface resulting from hatch spacing between layers and aligned dendritic cells contain more Laves and MC-type carbides. Carbides can precipitate at different temperatures as reported by researchers: 1250 °C (Bouse, 1989), 1250–1255 °C (Mitchell, Schmalz, Schvezov, & Cockroft, 1994), 1257 °C and 1289 °C (Mostafa et al., 2017b). Figure (1.4) shows Laves and  $\delta$  phases within grain boundaries. In general, during SLM,  $\delta$  phase cannot precipitate due to the high cooling rate in the process and the high amount of Nb remains in the matrix and not consumed to form of abundant Laves phase precipitates. Irregular and long striped Laves phases performed worst in terms of strength and ductility. The separation of granular Laves phases and the  $\gamma$  matrix is the main nucleation for the microscopic voids' formation. The fracture of long striped Laves phase is

the main reason for the failure. Long striped Laves phases are easy to break up during the tensile process, while granular Laves phases often fail by interfacial decohesion. The effect of Laves phase on the yield strength is achieved by influencing the volume fraction, the size and the distribution of  $\gamma''$  phase. Compared with long striped Laves phases, granular Laves phases are more beneficial for the plastic deformation of IN718 (Sui, Tan, et al., 2019). However,  $\delta$  phase precipitates from the Laves phase and the matrix following aging at 750–1000 °C for less than 100 hour and maximum precipitation occurs at 900 °C within the grain boundaries (Thomas, El-Wahabi, Cabrera, & Prado, 2006; X. Wang et al., 2016). Proper morphology of disk-shaped  $\delta$  phase at grain boundaries could improve the creep property, while it is generally detrimental for the mechanical properties tensile and/or fatigue) (G. & N., 1991; Mostafa et al., 2017b).

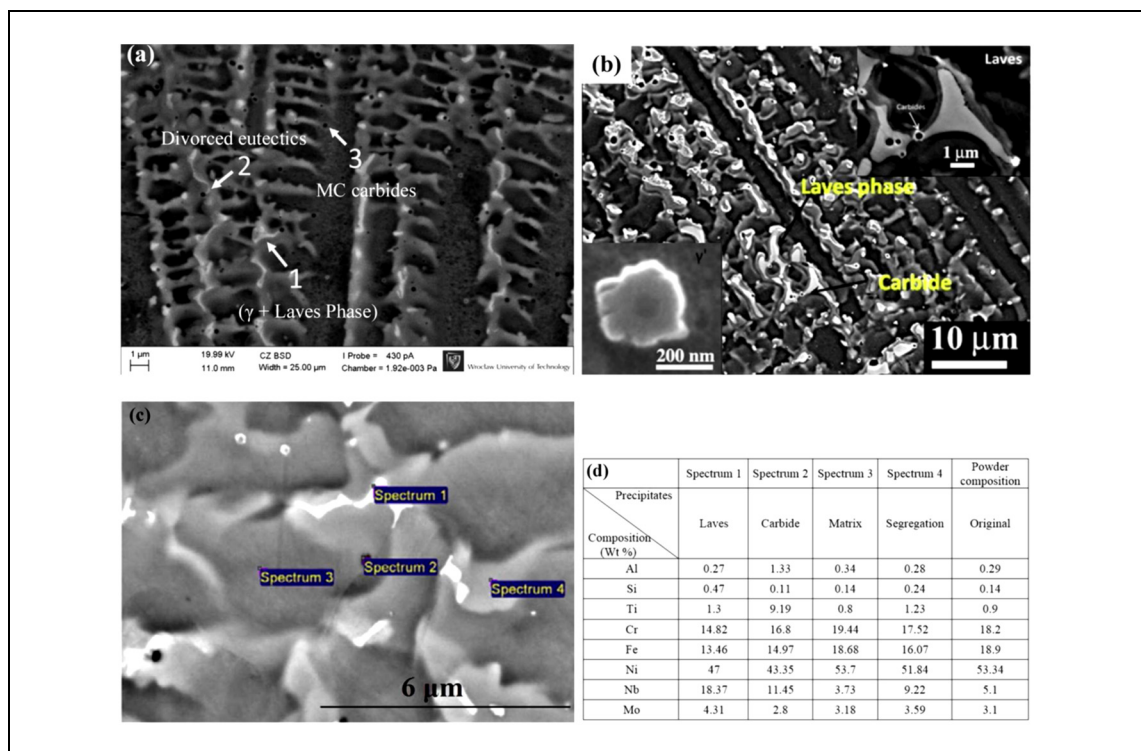


Figure 1.4 SEM micrographs showing the intermetallic micro-segregation in (a) inside  $\gamma$ -phase grains, (b) lower inset shows the  $\delta$  needles at stacking faults and carbides at higher magnification, and (c, d) micrograph and the respective chemical compositions of the various precipitates  
Taken from X. Wang et al. (2016, p. 1890)

As reported in many investigations (X. Wang et al., 2016; X & K., 2015; X & K., 2015) the  $\gamma$  phase as matrix strengthened with coherent and dispersive precipitates of the phases  $\gamma'$  and  $\gamma''$  as IN718 is a desirable microstructure. To achieve  $\gamma'$  and  $\gamma''$  as two strengthening phases, relieve the residual stresses and post-heat treatment are necessary.

### 1.2.3 Post-fabrication processing

For casting and forging, which are studied and quite well-understood processes today, defined specifications for thermal processing are already developed. Wrought IN718 is usually solution heat treated, in order to precipitate  $\delta$  phase and further homogenize the material, before being aged for  $\gamma'$  and  $\gamma''$  precipitation (at 720 °C for 8h, then 620 °C for 8h). The standard thermal processing cycle for forged IN718 is specified in AMS 5662. Phase transformation of IN718 versus time and temperature is shown in Figure 1.5.

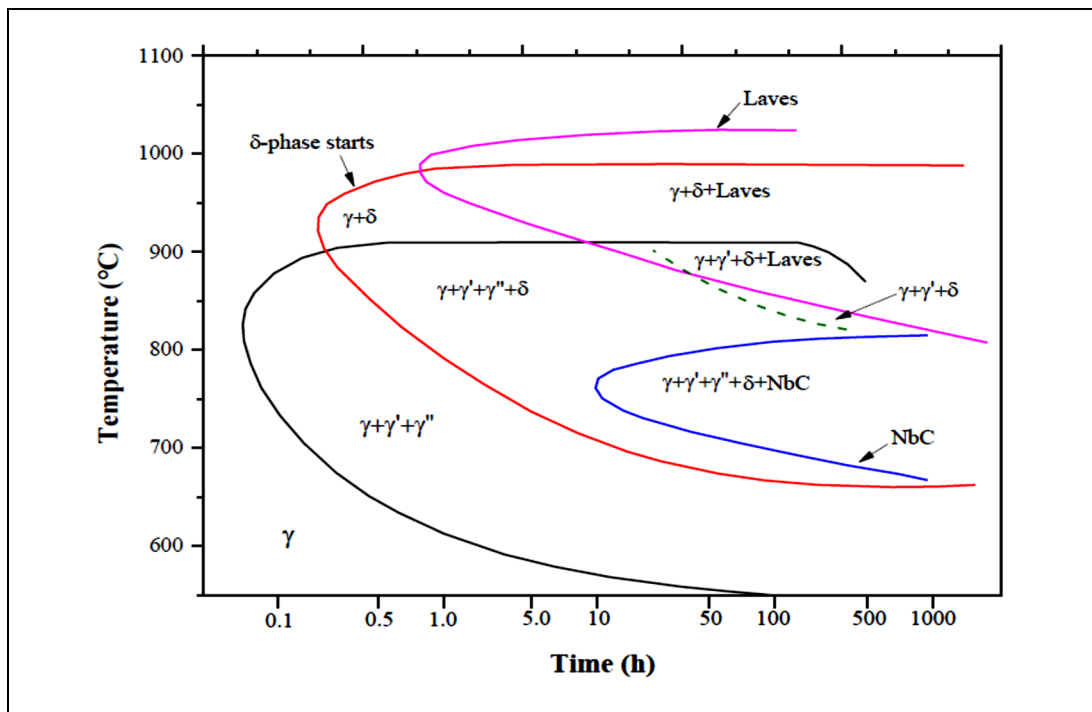


Figure 1.5 TTT diagram of Inconel 718 alloy  
Taken from R.G. Thompson et al. (1986, p. 299)

Cast IN718 alloy, being quite different to wrought, is characterized by coarser grains, interdendritic segregations (presence of Laves phase), and sometimes cast porosities (Deng et al., 2018). The coarse microstructure is proper for high temperature properties such as creep (Donachie & Donachie, 2002). On the other hand, the Laves phase is detrimental for the mechanical properties and it is crucial that this phase is dissolved, and the microstructure is homogenized during heat treatment. Hot isostatic pressing (HIP) can be used for closing cast porosity, and for further homogenizing of the microstructure (Deng et al., 2018). The standard heat treatment algorithm for cast IN718 is defined in Vacuum Melted Homogenization and Solution Heat Treated standard for Nickel alloys (AMS 5383).

As mentioned above, as-fabricated parts contain heterogeneous microstructure, micro-segregation, and defects through which post-heat treatments may alter or eliminate them (SAMES, 2015). In order to reach applications requiring isotropic characteristic, applying post-processing treatments is essential (Seede et al., 2018). The post-heat treatment cycle for alloy IN718 is usually depending on the manufacturing method and the properties that are sought in the final product.

According to Deng et al. (Deng et al., 2018), thermal processing cycles for AM IN718 should be developed specifically depending on the process history (i.e., manufacturing methods such as EBM or SLM), processing parameters, the shape and dimensions of the component, etc. Therefore, recommendations such as ASTM F3055 can be used as a general guideline, and not necessarily as a definite standard for thermal processing. In their comprehensive review on powder-bed laser manufactured IN718, Wang et al. (X. Wang et al., 2016) compared several articles on the subject and proposed an optimal thermal processing cycle for SLM IN718: homogenization (1100 °C for 1.5 h), solution heat treatment (980 °C for 1 h), followed by long two-step aging (720 °C for 8 h + 620 °C for 8h).

Popovich et al. (Popovich, Borisov, Sufiyarov, & Popovich, 2019) applied different heat treatment (HT) on as-fabricated homogeneous SLMed IN718 in accordance with the standard

AMS 5664E for two different laser powers: low level (250 W) and high level (950 W). Their results showed in Table 1.1, with the following states:

- As- fabricated without HT.
- HT<sub>1</sub>: SLM + HT; annealing at 850°C for 2 hours and cooling in air.
- HT<sub>2</sub>: SLM +HIP (at 1180°C/3 hour/150 MPa/ furnace cooling).
- HT<sub>3</sub>: HT<sub>2</sub> + solution annealing at 1050°C /1 hour/ air cooling + aging at 760°C/8-10- hour, furnace cooling at a rate of 55°C/h to 650°C for 8 hours and cooling in air.

Table 1.1 Mechanical properties at 20°C for homogeneous and functionally graded IN718 specimen  
Taken from Popovich et al. (2019, p. 701)

State	$\sigma_{0.2}$ (MPa)	$\sigma_{UTS}$ (MPa)	$\epsilon$ (%)	E (GPa)
Homogeneous specimens without HT				
Cast	488	752	11	200
Forged	916	1055	17	200
SLM (250 W)	668 ± 16	1011 ± 27	22 ± 2	173
SLM (950 W)	531 ± 9	866 ± 33	21 ± 5	113
SLM + HT				
SLM (250 W)	875 ± 11	1153 ± 4	17 ± 2	190
SLM (950 W)	668 ± 7	884 ± 80	7 ± 2	138
SLM + HIP				
SLM (250 W)	645 ± 6	1025 ± 14	38 ± 1	188
SLM (950 W)	481 ± 11	788 ± 12	34 ± 3	183
SLM + HIP + HT				
SLM (250 W)	1145 ± 16	1376 ± 14	19 ± 1	190
SLM (950 W)	1065 ± 20	1272 ± 12	15 ± 4	188
Functionally graded (flat) specimens				
SLM	574 ± 6	873 ± 14	13 ± 2	136
HT	704 ± 8	920 ± 53	4 ± 2	167
HIP	500 ± 6	817 ± 16	21 ± 1	187
HIP + HT	1041 ± 47	1145 ± 68	7 ± 1	196

Table 1.1 shows that the tensile properties of the SLMed alloy are higher than as-cast alloy for both variants (Different laser power) of the laser treatment. However, all these properties are lower than in the forged alloy. An exception is the elongation, which is the highest after the SLM. They noted that the variation of the elongation for the sample built by 950 W seem to be

connected with their localized porosity due to the shrinkage during the solidification. The lower mechanical properties in this sample are result of the larger size of their grains dominantly oriented in direction (001). As a result, the obtained mechanical properties depend primarily on the grain size and on the texture. However, authors expect that the large grains elongated over direction (001) will be useful for the high-temperature properties such as the thermomechanical fatigue and creep. Although IN718 alloy uses at high temperature application, the effects of different heat treatment cycles on general mechanical properties of the alloy are the objective of Table 1.1.

During the homogenization, the columnar grains tend to grow, coarsen and change their orientation to form an equiaxed texture (Mostafa et al., 2017b). As reported by (Amato et al., 2012; D. Zhang et al., 2015), the formation of finer equiaxed grains, after this treatment, could be induced by recrystallization in the specimen. Average grains size decreases due to the disintegration of columnar or elongated large grains by recrystallization homogenizing the microstructure (Mostafa et al., 2017b). The vertical and horizontal cross-sections of the homogenized specimens contain more equiaxed grains than as-fabricated specimens (Seede et al., 2018).

The elimination or dissolving of the Laves phase precipitates is of first concern in homogenization of SLMed IN718 (Manikandan, Sivakumar, Prasad Rao, & Kamaraj, 2015; Radhakrishna & Prasad Rao, 1997). Increasing the temperature beyond 1080°C almost completely dissolves all the Laves phase and homogeneously redistribute the Nb in the matrix, acting as source for precipitating  $\gamma''$  in the following of heat treatment such as solution annealing (SA) and aging or direct aging (DA).

Zhang et al. (F. Zhang et al., 2017) reported that the kinetic of homogenization is based on primary dendrites growth or dendrite arm spacing (DAS). They observed that the dominant columnar grain orientation (Akram, Kalvala, Jindal, & Misra) self-reorganized into equiaxed grains with a dominant orientation (Joel Andersson, Sjöberg, & Chaturvedi). Huang et al. (W. Huang et al., 2019) reported that the alloying elements such as Nb and Mo that aggregated as

the Laves phase at sub-grain boundaries diffuse during the homogenization. The time and temperature are two key parameters in elemental diffusion and solution. They calculated the proper time and temperature of homogenization in accordance with the primary DAS ( $\lambda$ ) and initial solute concentration which is maximum in the interdendritic regions. The minimum concentration is in the center of the dendrites so that it induces a cosine form. They estimated the time and temperature of homogenization according to the following equation:

$$t = \frac{-\ln K \lambda^2}{4\pi^2 D_0} \exp \frac{Q}{RT} \quad (1.1)$$

Where  $t$  and  $T$  are the time and temperature of homogenization, respectively.  $K$  is a constant which approaches zero.  $D_0$  is the diffusion constant and  $Q$  is the diffusion activation energy (specifically for Nb element).

They revealed that homogenization at 1080 °C for 45 min was enough to dissolve the Laves particles and redistribute the Nb in the matrix (Figure 1.6). In some investigations (Seede et al., 2018; Z. Wang et al., 2012) observed that Nb-rich particles in interdendritic regions are replaced by precipitate phases along grain boundary. In addition, as shown in Figure 1.7(b), the needle-like  $\delta$  phase, spherical MC carbides ((Nb<sub>0.78</sub>Ti<sub>0.22</sub>) C), and a white plate-like phase (Figure 1.7(c, d)) that is most likely a Laves phase distributed throughout the specimen. At lower rates of quenching (e.g., furnace cooling) following of homogenization,  $\gamma''$  phase may precipitate and distribute into the matrix (Mostafa et al., 2017b; Seede et al., 2018). Idell et al. (Idell et al., 2016) reported that the  $\gamma''$ -phase partially dissolved in the matrix promoted the formation small (~1000 nm long and ~35 nm thick) needle-like  $\delta$  precipitates.

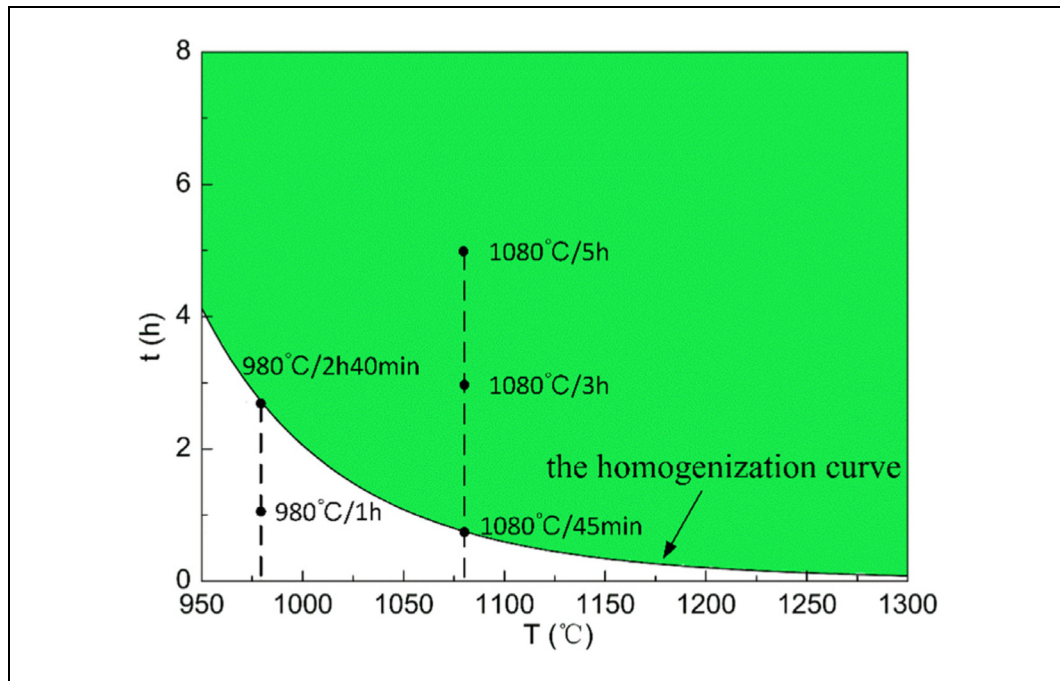


Figure 1.6 Variation of the time and temperature of homogenization treatment  
Taken from W. Huang et al. (2019)

Sui et al. (Sui, Tan, et al., 2019) reported that the total element contents in the IN718 superalloy are assigned to four parts: the matrix without Laves phases,  $\gamma''$  phases and  $\gamma'$  phase,  $\gamma''$  phases,  $\gamma'$  phase and Laves phases. According to their calculation, the presence of Laves phase significantly affects the formation of  $\gamma''$  phase, while has little effect on other precipitation hardening phase ( $\gamma'$ ). The granular and long-stripped Laves phase are potentially nucleation sites for micro-voids formation during tensile test, which can be known as micro-crack directly. They found that the granular Laves phase needs lower critical stress than long-stripped Laves phase to fracture.

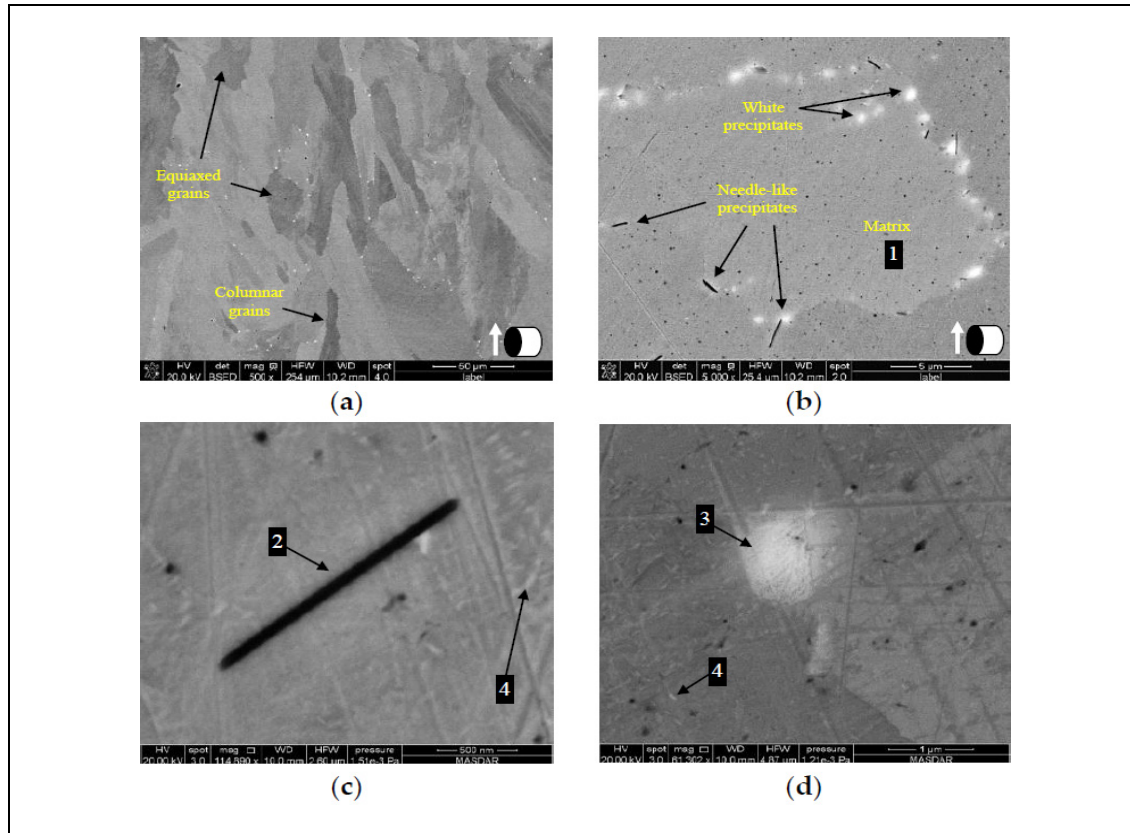


Figure 1.7 (a) SEM micrograph of a homogenized IN718; (b) different precipitates at the grain boundaries; (c, d) shows  $\delta$  and MC carbide precipitates  
 Taken from Mostafa et al. (2017b)

**The solution heat treatment and aging** of the SLMed IN718 alloy produced superior creep strength to the wrought material due to the high fraction of  $\gamma''/\gamma'$  strengthening phases and the nearly completely dissolution of brittle phases ( $\delta$  and Laves) (C. Li et al., 2017).

Mostafa et al. (Mostafa et al., 2018) compared the microstructure and mechanical properties of cast IN718 with SLM IN718, before and after heat treatment. They found that after heat treating the SLM samples, their mechanical properties were superior to those of the cast one, and at about the same level as wrought. In their study, they used two different heat treatment cycles – one with homogenization step and a solution heat treatment step before aging (per AMS 5383), for  $\delta$  precipitation; and the other one with homogenization, but without SHT (no  $\delta$  expected) before ageing. They concluded that when  $\delta$  is present in excessive amounts intragranularly in the sample, it will affect negatively the plasticity of the material. Kuo et al.

(Kuo, Horikawa, & Kakehi, 2017) applied two heat treatment routes. One part of the samples was solution heat treated (980 °C for 1 h) and aged (718 °C for 8 h + 621 °C for 10 h), and another part was directly aged. They concluded that the morphology and the location of  $\delta$  phase particles precipitated after solution treatment affected the ductility of the alloy.

Popovich et al. (V. A. Popovich et al., 2018), used heat treatment AMS 5664E consisting of annealing (850 °C for 2 h) and ageing (720 °C for 8 h + 620 °C for 8 h), in order to specifically tailor the microstructure. They could transform the Laves phase into  $\delta$  phase precipitates and enhance creep properties and fatigue life of the components due to the pinning effect of this phase for grain boundaries. Holland et al. (Holland et al., 2018) applied four-step thermal processing cycle, consisting of stress relief (at 1066 °C for 90 min), HIP (1163 °C at 100 MPa for 4 h), solution treatment (1066 °C for 1 h), ageing (760 °C for 10 h, furnace cool to 650 °C and hold, total aging time 20 h). This treatment resulted in recrystallization and formation of equiaxed grains morphology in the parts. Yoo et al. (Yoo, Book, Sangid, & Kacher, 2018) also used a four-step heat treatment for some of their samples, in order to achieve an equiaxed grain morphology. It was composed of stress relief (1065 °C for 90 minutes), homogenization (1177 °C for 60 min), solution heat treatment (982 °C for 60 min) and aging (718 °C for 8 h + 621 °C for 18 h).

As noted above, the post processing thermal treatment is required to achieve optimum mechanical properties of the components produced by the SLM. According to research conducted, homogenization heat treatment, annealing and hot isostatic pressing (HIP) are carried out on printed parts to remove the segregation and undesirable phases and increase the strength by precipitation hardening phases compared to the as-manufactured condition (Deng et al., 2018).

**As a conclusion**, phase transformation in IN718 begins at 1359 °C with reaction  $L \rightarrow \gamma$ . Then at 1289 °C, liquid transform to  $\gamma + MC$  carbide in an eutectic reaction. In the 1220-1160 °C interval, the Laves phase forms while the liquid phase is gradually disappeared. The  $\delta$  precipitates form as a stable phase based on solid state reaction at  $1145 \pm 5$  °C and till 885 °C

is stable, but it begins to decompose to metastable  $\gamma''$  phase from 1000 °C. From 720 to 600 °C, both  $\gamma''$  and  $\gamma'$  precipitates are observable. The decomposition and phase formation mechanisms controlled by diffusion which depends on time and temperature of process and concentration of solute atoms in the matrix and other precipitates (Lifshitz & Slyozov, 1961). The driving force energy for atomic diffusion in a supersaturated solid solution for transformation  $\delta$ -phase to  $\gamma''$  provided by the post-heat treatment (Jouiad et al., 2016). Moreover, this treatment can act in the opposite way so that Cr and Mo diffuse out from bcc- $\gamma''$  to form orthorhombic- $\delta$  (Wei et al., 2015).

The recommended heating treatment is homogenization followed by the subsequent HIP under a higher temperature and high pressure, then solution treatment and double aging. As a result of this treatment, the IN 718 parts could reach the tensile strength even superior to the wrought ones.

#### **1.2.4 Mechanical properties**

Mechanical properties of as-SLM Ni-based superalloys are improved and comparable to the conventionally fabrication methods (i.e., casting or forging) in terms of tensile strength and hardness, but usually possess low ductility (Amato et al., 2012; C. Li et al., 2017; Z. Wang et al., 2012).

As reported by (Blackwell, 2005; Mostafa et al., 2017b), laser-based AM parts structure have anisotropic mechanical properties due to the columnar grains. Elongated and thinner columnar grains parallel to the building direction (BD) result in higher hardness at the bottom region of the as-printed parts compared to the top (Seede et al., 2018). Popovich et al. (Popovich et al., 2017a) reported that the coarser grains with strong texture  $\langle 001 \rangle$  in the specimens printed by high laser power generates difference mechanical properties. The strength perpendicular to the BD is generally higher than parallel to the BD. While ductility shows the opposite behavior due to the interdendritic  $\delta$ -phase precipitates, which are arrayed perpendicular to the direction of the normal stress in the specimen. Approximately a 10% difference can be observed when comparing the BD in the Horizontal (H) and Vertical (V) orientations. The tensile properties

in the H direction are relatively higher than that of the V direction in order of 50-90 MPa (Y. Zhang et al., 2017).

As described before, the post processing treatments on SLMed IN718 can partially alter the texture and remove the micro-segregation in the as-printed microstructure which leads to enhance the mechanical properties. Wang et al. (X. Wang et al., 2016) reported that the yield strength, ultimate strength, and the hardness of SLMed IN718 increased by 84% (72%–95%), 38% (30%–46%), and 48%, respectively, through applying proper heat treatment cycle. They reported; however, the ductility significantly was reduced due to the interdendritic fine Laves particles.

As shown in Figure 1.8, the tensile strength and elastic modulus of the as-AM parts is comparable or even superior to the casting samples but inferior to wrought ones. Figure 1.9 illustrated that the mechanical properties of the heat treated SLMed IN718 samples are superior to the wrought IN718 (X. Wang et al., 2016).

The highest microhardness value reported (B. Chen & Mazumder, 2017) near the substrate that then gradually decreased towards the top of the vertically built samples. This variation is in accordance with the microstructure and phases distribution. Near the substrate, the microstructure is denser due to the rapid cooling and precipitation of hardening phases by which the microhardness increases. With increasing the height of sample and from bottom to top, the heat conduction becomes increasingly difficult and induces reheating for successive layers. This leads to different secondary dendrite arm spacing ( $\lambda$ ), and different microhardness distribution. Deng et al. (Deng et al., 2018) reported that the sample orientations does not have a significant effect on the hardness values. Popovich et al. (Popovich et al., 2017a) reported in SLM-IN718 by lowering the laser power (i.e. 250 W) input a higher average in hardness (in constant volumetric energy density) can be obtained due to the finer grains.

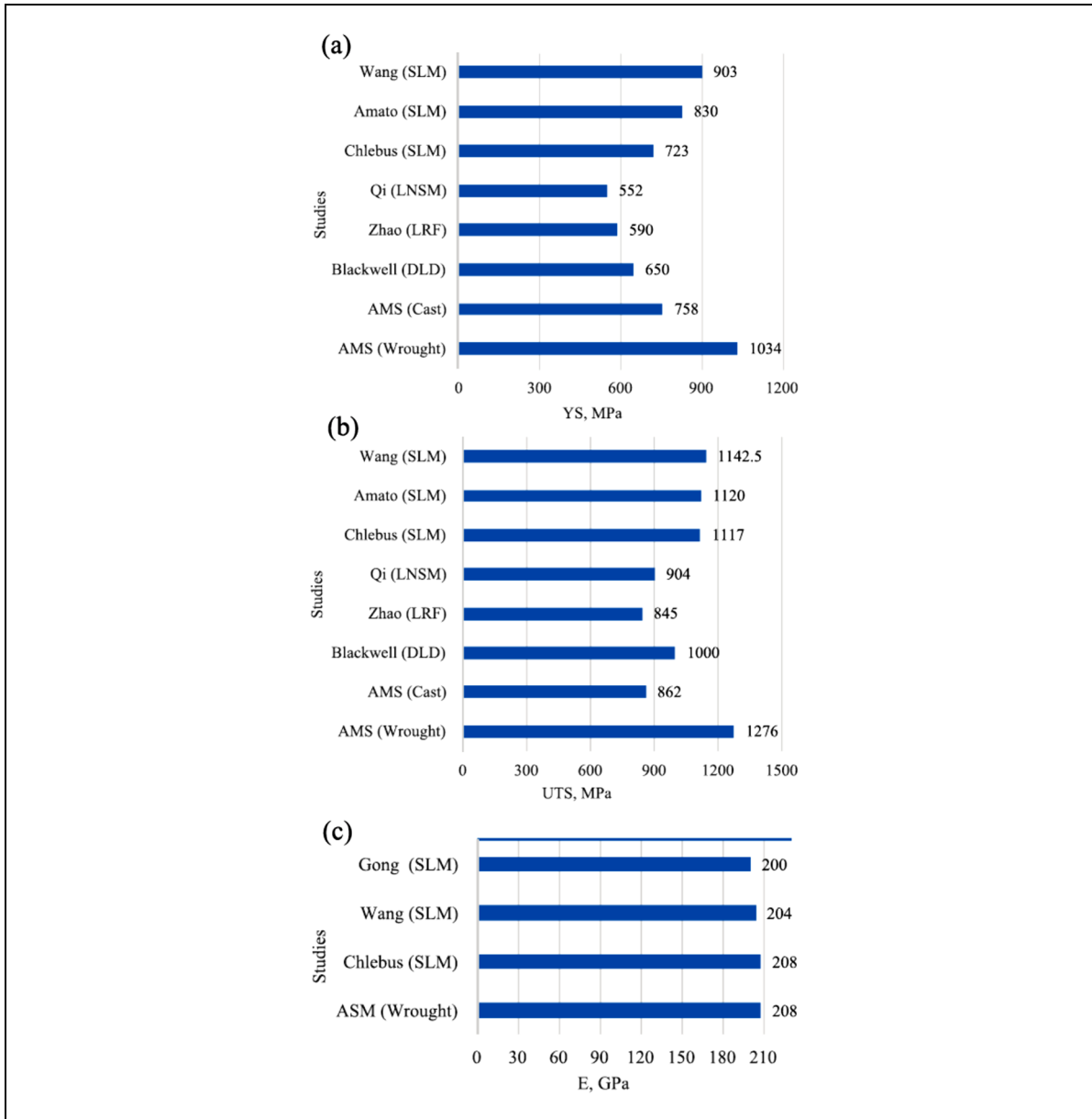


Figure 1.8 Comparing (a) Yield strength, (b) Ultimate tensile strength and (c) Elastic modulus of selective laser melted IN 718 with conventional manufacturing methods  
Taken from X. Wang et al. (2016, p. 1890)

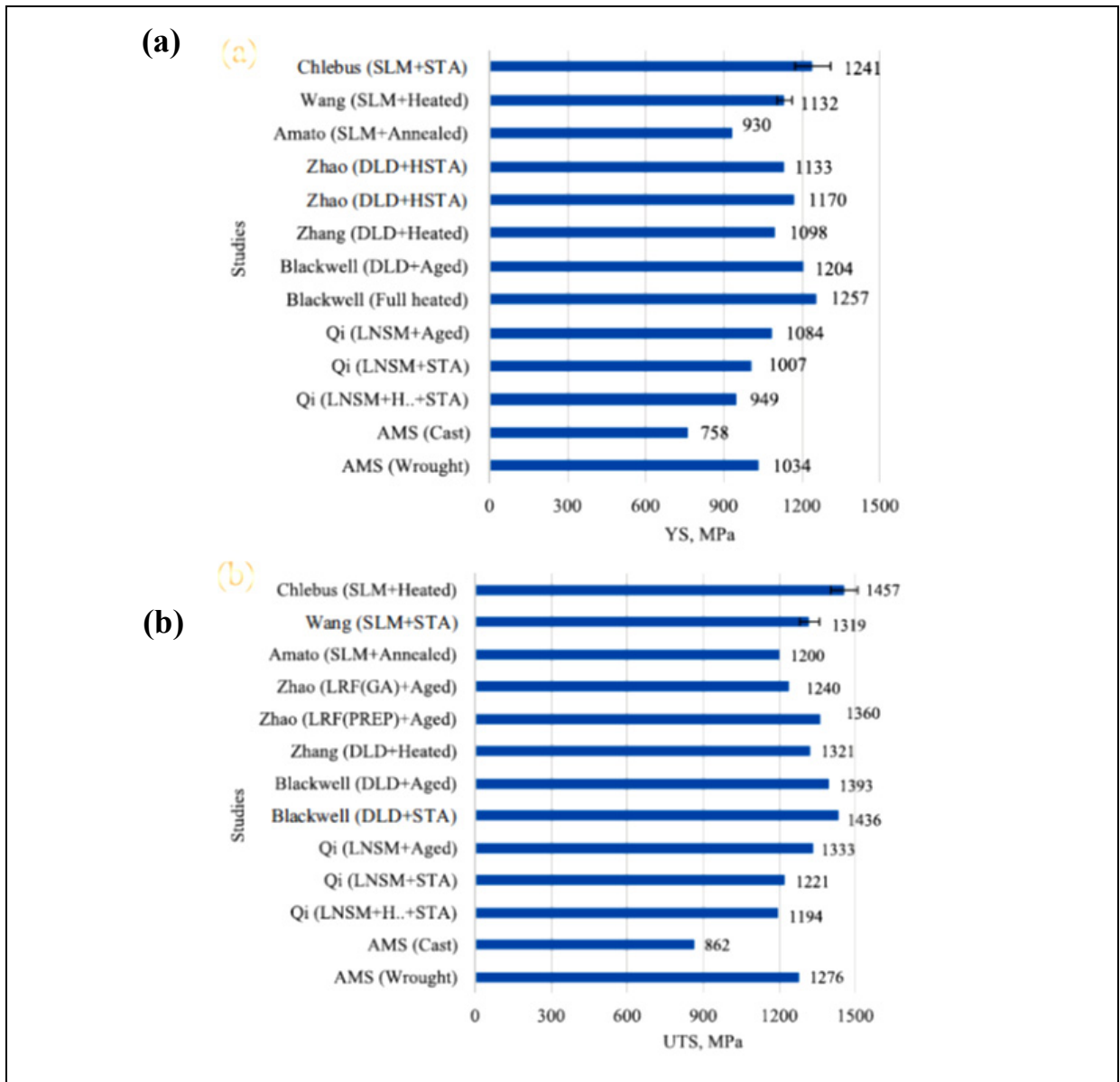


Figure 1.9 Comparing (a) the yield and (b) the ultimate strengths of heat treated SLM IN718 Taken from X. Wang et al. (2016, p. 1890)

Seede et al. (Seede et al., 2018) observed that the hardness of the IN718 alloy increased to 19.3% from 236.9 to 282.6 HV after homogenization due to the dispersion and distribution of  $\gamma''$  precipitates, and the partial recrystallization. Chlebus et al. (Chlebus, Gruber, Kuźnicka, Kurzac, & Kurzynowski, 2015) reported that after homogenization at 1100°C for 1 hour, the microhardness increased from 312 to 463 HV (48%), while HIPing reduced the microhardness of the homogenized samples due to the  $\gamma''$  dissolution and grain coarsening. Solution treatment

and aging allow  $\gamma''$  and  $\gamma'$  phase precipitations along grain boundaries of finer grains (D. Zhang et al., 2015). Li et al. (C. Li et al., 2017) reported that the lower homogeneity in mechanical properties specifically revealed in large standard deviation of hardness. Increasing the annealing temperature increased the grains size and dissolved the  $\delta$  phase into the matrix by which the hardness decreased.

### 1.3 Linear Friction Welding (LFW)

In Russia 1956, Chudikov used rotation friction welding method (RFW) for the first time to generate scientifically high-quality welds between metal rods although the idea of using heat generated at the interface by friction for joining metals and plastics. In 1960, The process was introduced to the US then more focus has been on the analysis of its parameters and thermal aspects. In 1962, the Caterpillar Tractor Company developed a modified version of RFW so-called inertia friction welding (IFW) in which a flywheel is used to store the energy required for welding. In 1959, the reciprocating motion for friction welding and then linear friction welding (LFW) were introduced by Richter in Germany and by Vill in Russia, respectively. Eventually, in 1990 in UK the first dedicated LFW machine established in The Welding Institute (TWI) for solid-state joining metals (Ahmad Chamanfar, Jahazi, & Cormier, 2015).

The purpose of solid-state joining is to remove solidification defects associated with bulk melting (e.g., cracking, solute segregation, and formation of porosities) which often occur in fusion welding methods. In addition, liquation cracking in heat affected zone (HAZ) can be significantly reduced during solid-state joining of Nickel superalloys (Bhamji, Preuss, Threadgill, & Addison, 2013; Ahmad Chamanfar et al., 2015; A. Chamanfar, Jahazi, Gholipour, Wanjara, & Yue, 2012b; Daymond & Bonner, 2003; Ojo, Richards, & Chaturvedi, 2004b).

Friction welding is a solid-state method introduced for welding two parts through the relative movement of one part on another under axial friction and forging pressures and generation of frictional heat between them (Ahmad Chamanfar et al., 2015; W. Y. Li et al., 2008). Due to nature of this process, the molten metal protection is not necessary from oxidation and

contamination. Besides filler metal, flux, protective shielding gas, or vacuum are eliminated from the process (Ahmad Chamanfar et al., 2015; Daymond & Bonner, 2003; Sathiya, Aravindan, & Noorul Haq, 2004).

This technique has been used for welding and repairing of rotating turbine parts. It has many advantages such as improving the life cycle and weight reduction via elimination of over fir tree machining and assembly between blades and disk (blade integrated disk or Blisks). Since fretting crack initiates from the fir tree, the slotted between blade and disk assemblies are susceptible to fatigue damage. In addition, performance improvement is achieved by reducing air leakage from gaps between the platforms of the blades. Typically, weight can be reduced by approximately 20% by adopting the blisk structure. Hence, LFW welding seems to be free from such problems. Therefore, LFW has been proposed as a method of manufacturing blisks and is being put into practical use in applications such as aircraft engines. LFW is a technology for manufacturing blisks by welding blade parts to separately manufactured disks. Shtrikman et al. (Shtrikman, 2010) noted a number of important advantages:

- The dissimilar materials welding materials, specifically the materials that cannot be welded by fusion welding, in particular when their fusion temperatures are very different.
- High accuracy in welded structures.
- The automatic process which can control the process and quality from the beginning to the end of the process for welded coupons.
- No need to use welding tools.

The theory of frictional welding processes is applying the thermomechanical deformation on two parts results in the deforming and welding them on the contact surfaces essentially along with the formation of metallic bonds. The process can occur in 3 or 4 stages in the following sequence (Figure 1.10) (Ahmad Chamanfar et al., 2015; Shtrikman, 2010; Vairis & Frost, 1998):

**Contact phase:** In the first stage, the position of two parts is stabilized on each other and primary pressure applied to fix them (e.g., 3 s). Then, the pressure is released and decreased to

ensure that contact is always made (Ahmad Chamanfar et al., 2015; A. Chamanfar, Jahazi, Gholipour, Wanjara, & Yue, 2012a). No axial shortening, no oscillation, and variation in the temperature of the weld parts occur (Ahmad Chamanfar et al., 2015; A. Chamanfar et al., 2012a; Vairis & Frost, 1998).

**Conditioning phase:** In this stage, one part oscillates relative to the other under a specific frequency, amplitude, and friction pressure for a short period of time which leads to break the surface oxides. Due to the friction pressure and wear in the contact area a heat generated at the interface increases (Ahmad Chamanfar et al., 2015; Vairis & Frost, 1998).

**Burn-off phase:** “Oscillation is continued with the amplitude and frequency of the conditioning phase (Figure 2.15) for a specific period of time or until a specific stroke (or strain rate) from the initial contact position is achieved. As a result of oscillation under applied pressure, frictional heat is generated at the interface leading to the development of a plastic region in the vicinity of the interface” (W. Y. Li et al., 2008). In the plasticized and softened zones, the shearing oscillatory movement between the two parts and the applied pressure, cause the extrusion of the interface material as “flash” (Bhamji, Preuss, Threadgill, & Addison, 2011; W. Y. Li et al., 2008). The shape of flash in superalloys is curvy while for titanium alloys is straight. Consequently, significant axial shortening (e.g. 2 to 4.6 mm for Ni-based superalloys) occurs (Ahmad Chamanfar et al., 2015; A. Chamanfar et al., 2012a). The important parameters in this stage are frequency, amplitude, pressure, axial shortening, and the oscillation time (Nunn, 2005).

**Forge phase:** Oscillation is abruptly stopped and the part is aligned with the stationary one quickly (less than 0.1 s (Karadge, Preuss, Lovell, Withers, & Bray, 2007)) then the forge is loaded and increased to join the two parts (Vairis & Frost, 1998). This leads to an increase in stroke (or strain rate) as a result of the plastic deformation/extrusion which means generation of more flash. In addition, the interface temperature increases due to adiabatic heating from plastic working or compression between the parts (A. Chamanfar et al., 2012a, 2012b). However, The temperature at interface is relatively modest with little or no risk to reach the

alloy to the melting point even when dissimilar alloys with broadly different melting points are welded (Sluetz, Oberle, & Brosheer, 1968). As the high temperature interface material is extruded to the sides (flash), the temperature decreases. Forge pressure and forging time are the key factors in the last phase of the LFW process (Wilhelm, Furlan, & Moloney, 1995).

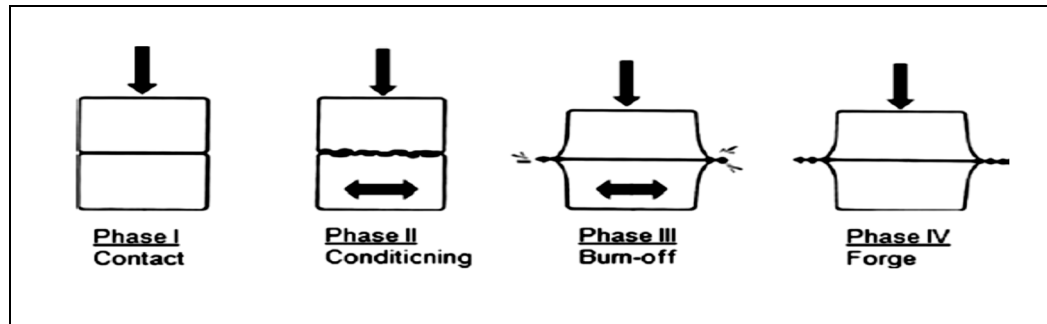


Figure 1.10 Schematic of the LFW process  
Taken from W.Y. Li (2008, p. 293)

### 1.3.1 Main LFW parameters

Various parameters such as friction and forge pressures, amplitude, frequency, and friction and forging time affect the LFW processing. Ma et al. (Ma et al., 2016) reported that these factors also affected microstructural evolutions and mechanical properties of as-welded GH4169 superalloys. Vairis and Frost (Vairis & Frost, 1998, 2000) and Dalgaard (Dalgaard, 2011) introduced a specific power input (SPI) parameter that must be considered for LFW as:

$$SPI \left( \frac{kW}{m^2} \right) = \frac{afF}{2A\pi} \quad (1.2)$$

Where  $a$  is the amplitude (mm) of oscillation;  $f$  the frequency (Hz);  $F$  is axial force (N or  $kg.m/s^2$ ) applied, and  $A$  the weld area ( $mm^2$ ).

The friction and forging are two major stages of LFW that act as thermomechanical phases to deform two coupons under pressure. The friction and forge hot compressive loadings generate

sticking and sliding friction conditions that should be considered for analyzing these two stages. Using the slab analysis approach in plane strain compression conditions, the average pressure due to friction and forge pressures can be estimated by (Hosford, 2014):

$$P_{ave.} = 2K \left(1 + \frac{\mu a}{2h}\right) \quad (1.3)$$

where  $k$  is the shear strength,  $\mu$  is the friction coefficient,  $a$  is width and  $h$  is height of the coupon. Under plane-strain conditions,  $k$  can be expressed as ( $\sigma_0$  is the yield stress):

$$k = \frac{\sigma_0}{\sqrt{3}} \quad (1.4)$$

Hence, the average pressure at the beginning of plastic yielding under LFW:

$$P_{ave.} \geq \frac{2\sigma_0}{\sqrt{3}} \quad (1.5)$$

Therefore, accurate estimation of material flow stress is a necessary condition to determine the pressure that allows the plastic deformation of the material. Generally, the plastic flow of a material is a function of strain ( $\epsilon$ ), strain rate ( $\dot{\epsilon}$ ) and temperature ( $T$ ). A combination of data on hot deformation and LFW of Ni-based superalloys and analytical calculations are used to estimate the proper flow stress and its relation as a function of the above variables which are described in **the following**:

### 1.3.1.1 Strain rate

A wide range of strain rate values (between 0.1 to 2000 s<sup>-1</sup>) has been calculated and proposed for LFW (Ahmad Chamanfar et al., 2015; A. Chamanfar, Jahazi, Gholipour, Wanjara, & Yue, 2013; W. Li, Vairis, Preuss, & Ma, 2016; Ma et al., 2017; Turner, Gebelin, Ward, & Reed, 2011). However, most of the authors have reported strain rates ranging between 0.1 and 20 s<sup>-1</sup>. The strain rate of 2000 s<sup>-1</sup> is also reported (Turner et al., 2011) using numerical simulation

results with no experimental support. Vairis et al. (Vairis & Frost, 2007) reported that the minimum strain rate occurs at the friction stage and reaches its maximum value during the forging stage. Therefore, the friction pressure can be estimated at a strain rate of about 0.1 or 1 s<sup>-1</sup> while in forge phase it can be calculated based on the available data on high strain rate value for certain materials or the same.

Vairis and Frost (Vairis & Frost, 1998) calculated the maximum strain rate ( $\dot{\epsilon}$ ) in the weld area of the LFW process during the oscillation stage as:

$$\dot{\epsilon} = \frac{a.f}{l} \quad (1.6)$$

Where  $a$  is the amplitude,  $f$  is the frequency and  $l$  is the length of the specimen in the direction of oscillation (Masoumi, Shahriari, Jahazi, Cormier, & Flipo, 2017). The strain rate for LFW of superalloys can be obtained in the range of 3 to 18 s<sup>-1</sup>. Mary and Jahazi (C. Mary & Jahazi, 2008) measured the strain rate in the weld area to be 6.2 s<sup>-1</sup> for LFW of IN718 alloy. Masoumi et al. (Masoumi et al., 2017) determined the amount of 3.85 s<sup>-1</sup> for LFW of AD730 alloy.

Chamanfar et al. (A. Chamanfar et al., 2013) proposed a microstructural model to predict the strain rate in the LFWed Waspaloy by measuring the grains size variation induced by recrystallization according to the Zener–Holloman relationship. They measured the strain rate around 13 to 18.5 s<sup>-1</sup> at different peak temperatures based on Vairis’s model and grains size modeled. In addition, they compared the grains size modeled with Turner’s numerical simulation (Turner et al., 2011) which strain rate measured higher than 1000 s<sup>-1</sup>. They (A. Chamanfar et al., 2013) revealed that microstructure changes during cooling of LFW compared to its variation during quenching phase of hot compression tests were negligible due to the higher cooling rate 82 °C/s in LFW, and quenching in 3 to 4 s for samples after the test.

Ma et al. (Ma et al., 2016) revealed that the rapid heating and cooling rates in LFW process restricted the sizes of recrystallized grains and formed the fine grains in the weld zone due to the interaction of significant shear and friction forces and compression stress which broken the

original grains. In the TMAZ, the temperature, shear forces, and compression stresses are lower than the WZ by which the grains size alteration is less with increasing the distance from the WZ.

### 1.3.1.2 Deformation temperature

The temperature must be high enough to plasticize the alloy during the process. The strength of Ni-based superalloys is strongly dependent on the presence of precipitation hardening particles (i.e.,  $\gamma'$  in AD730<sup>TM</sup> and  $\gamma''$ ,  $\gamma'$ , and  $\delta$  in IN718). The minimum temperature to start deformation is the dissolution temperature of those phases. Regarding AD730<sup>TM</sup>, Masoumi et al. (Masoumi, Jahazi, Shahriari, & Cormier, 2016; Masoumi, Shahriari, Jahazi, Cormier, & Devaux, 2016b) reported that since the heating rate varies at different locations from the joint interface, the dissolution kinetics of the  $\gamma'$  particles is expected to change with the distance from the weld interface. Figure 1.11 shows the influence of the heating rate on primary  $\gamma'$  dissolution temperature for the AD730<sup>TM</sup> alloy. The lowest dissolution temperature for  $\gamma'$  is around 1060°C. Thus, the minimum temperature needed to be reached before the application of load for deformation in the initial stage of the LFW process is about 1060 °C. In many investigations (Azadian, Wei, & Warren, 2004; Johansson & Persson, 2014; Ruan, Ueshima, & Oikawa, 2018; Y. Wang, Shao, Zhen, Yang, & Zhang, 2009), a range of temperature is reported for dissolution of  $\gamma''$ ,  $\gamma'$ , and  $\delta$  phases, 885-946°C, 909-936 °C, and 995-1035 °C; respectively, for IN718 alloy.

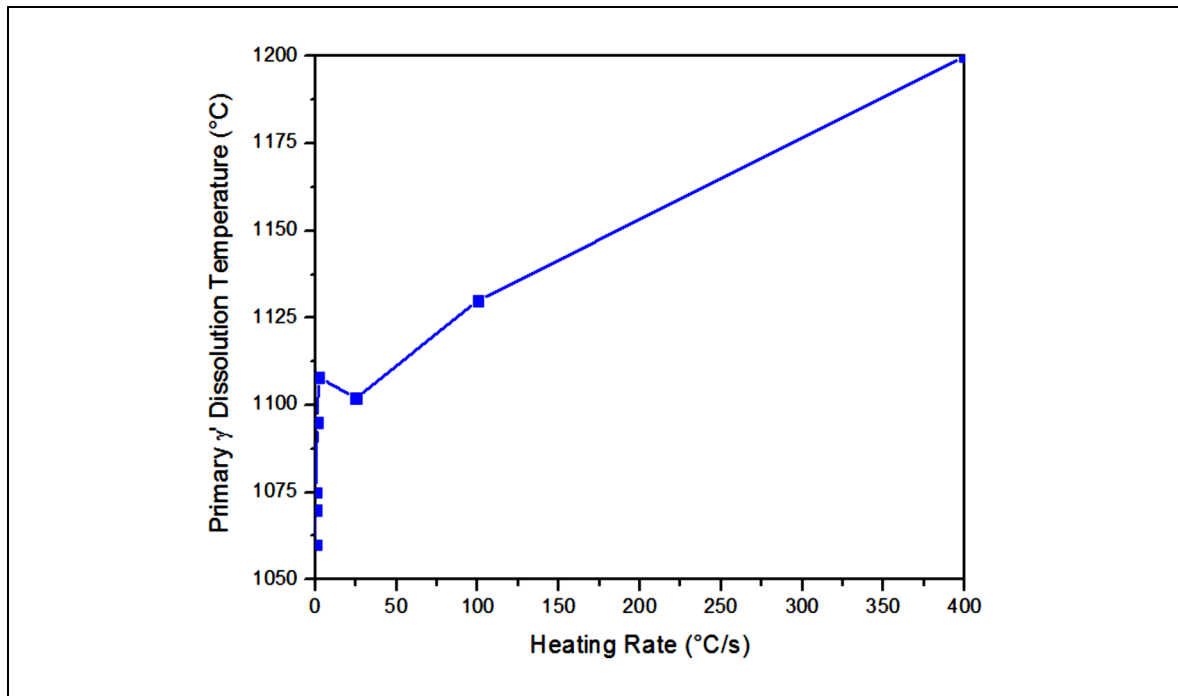


Figure 1.11 Primary  $\gamma'$  dissolution temperature of the AD730<sup>TM</sup> at different heating rates  
Taken from Masoumi et al. (2016b, p. 286)

Yang et al. (X. Yang et al., 2015) reported that measured temperature by using an infrared thermal imaging instrument indicated that the temperature at the joint interface was about 1100°C during friction stage of LFW of a Ni-based superalloy. Masoumi et al. (Masoumi et al., 2017) and Chamanfar et al. (A. Chamanfar et al., 2013) reported that the weld interface temperature in the steady state zone was between 0.75 and 0.95 of the melting temperature ( $T_M$ ). This value for AD730<sup>TM</sup> can be considered is near 0.85  $T_M$  as the upper limit which corresponds to 1150°C (the  $T_M$  for AD730<sup>TM</sup> was taken as 1350 °C based on the literature (A. Devaux, 2012)) which is almost same as IN718 alloy.

### 1.3.1.3 Influence of adiabatic heating

The temperature increases at the interface of two parts due to friction movement and straining induced by compression loading where adiabatic heating needs to be considered. Adiabatic heating is only present during friction stage. Thus, it is only estimated for low strain rates of

0.1 s<sup>-1</sup> and 1 s<sup>-1</sup> corresponding to the beginning and the end of friction stage of the LFW process. The adiabatic heating can be obtained by  $\Delta T = \frac{0.95\eta}{\rho C_P} \int_0^\epsilon \sigma. d\epsilon$ . The  $\eta$  is the thermal efficiency (63.5% for strain rate of 0.1 s<sup>-1</sup> and 95% for strain rate of 1s<sup>-1</sup>),  $\rho$  the density of the alloy (8155.33 Kg.m<sup>-3</sup> at 1150 °C),  $C_P$  the specific heat (792.68 J.Kg<sup>-1</sup>.K<sup>-1</sup> at 1150 °C),  $\epsilon$  the maximum strain (0.8) and  $\sigma$  maximum flow stress (peak stress) during hot deformation (all these data are reported by Masoumi et al. (Masoumi et al., 2017)). They found out the peak stress values for AD730<sup>TM</sup> and some other Ni-based superalloys (like AD730<sup>TM</sup>) at strain rates of 0.1 s<sup>-1</sup> and 1s<sup>-1</sup> is set in the temperature range of 1000-1250 °C. They revealed that the peak stress at 1150 °C is approximately 120 MPa at strain rate of 0.1 s<sup>-1</sup> while it is around 290 MPa at strain rate of 1 s<sup>-1</sup>. According to the above equation,  $\Delta T$  was calculated to be ~10 °C for a strain rate of 0.1 s<sup>-1</sup> and ~30 °C for a strain rate of 1 s<sup>-1</sup>. Therefore, the maximum weld interface temperature or the upper limit of temperature for plastic deformation at the end of friction stage is approximately 1200 °C.

Moreover, the estimated forge pressure based on the available data at the highest strain rate values (10 and 20 s<sup>-1</sup>) for similar Ni-based superalloys were obtained (the superalloys 617B and 740H) (Masoumi et al., 2017). Therefore, the measured peak stresses for these alloys were used for the calculations of forge pressure at strain rates of 10 and 20 s<sup>-1</sup>.

Based on the above analysis, they estimated that the peak stress at strain rate of 0.1s<sup>-1</sup> and at deformation temperature range of 1060 °C to 1150 °C can be used for the friction pressure while the flow stress at strain rate of 20 s<sup>-1</sup> and deformation temperature of 1060 °C to 1200 °C (or even 1250 °C) can be applied for the forge pressure. As a result, the peak stress at about 1060 °C is 260 MPa while it is around 120MPa at 1150 °C. Then, according to Eq. (1.3), friction pressure for AD730<sup>TM</sup> was calculated to be ranging from 133 to 285MPa. According to their calculations, the weld joint temperature interval of 1060-1200°C varies between 530 and 240 MPa, respectively, and the forge pressures during the LFW process of AD730<sup>TM</sup> alloy was obtained to be between 265 and 580 MPa.

The increased temperature at strain rates  $1 \text{ s}^{-1}$  and  $20 \text{ s}^{-1}$  obtained about  $13.5^\circ\text{C}$  and  $25.5^\circ\text{C}$  at  $1200^\circ\text{C}$ , respectively. This indicates that 20 times increase in strain rate arises the temperature about  $12^\circ\text{C}$ . It is generally accepted that as the strain rate increases the temperature increase and reaches almost the steady-state value (Oluwasegun et al., 2014; D. Zhao, 1993).

#### 1.3.1.4 Oscillation Frequency and Amplitude

The frequency and amplitude of oscillation also influence the maximum weld line temperature. The weld interface temperature increases rapidly by increasing these parameters at the early stages of the LFW. Then, the temperature reaches an almost a quasi-stabilized regime. In order to quantify the impact of these parameters, Addison's equation (Addison, 2010) was used:

$$v_r = 4 \cdot a \cdot f \quad (1.7)$$

where  $v_r$  is the rubbing velocity,  $a$  and  $f$  are the oscillation amplitude and frequency, respectively. A sound LFW joint can be formed by increasing the rubbing velocity which may cause a slight increase of the heat input, and consequently, higher temperature and removal rate of oxide layers. Therefore, the rubbing velocity has to be kept as a maximum value. The maximum values were selected for oscillation amplitude and frequency within the operating window of the LFW machine.

#### 1.3.1.5 Heat input

In order to estimate the heat input ( $HI$ ) in the friction phase for the selected LFW process parameters, the following equation was used (W. Li et al., 2016; Vairis & Frost, 1998, 2000):

$$HI = q = \mu \cdot \dot{v}_r \cdot P_{Frict} \quad (1.8)$$

where  $\mu$  is the friction coefficient and  $P_{\text{Fric}}$  is friction pressure. A fixed rubbing velocity is considered based on the capacity of the LFW machine. The friction coefficient can be taken equal to 0.6 or 0.5 for Ni-based superalloys, as reported in the literature (Geng, Qin, Zhou, & Zou, 2019; W.-Y. Li, Ma, & Li, 2010). However, the  $\mu$  can be considered as a variable parameter due to the elevated temperature (from 0.6 to 0.2) during the process.

### 1.3.1.6 LFW process time

To determine the optimum time for LFW, an analytical procedure based on one dimensional (1D) thermal modelling can be used. During the LFW process, heat losses by radiation and convection are usually negligible (Maalekian, 2007). Therefore, the temperature distribution in each solid part can be determined by solving the 1D heat conduction equation (Yilbas & Sahin, 2014). Geng et al. (Geng, Qin, Zhou, et al., 2019) used the 3D modelling based on variation of friction coefficient during the process. Heat equation for three-dimensional without energy generation is given by:

$$\frac{\partial T}{\partial t} = \alpha \left( \frac{\partial^2 T}{\partial x^2} + \frac{\partial^2 T}{\partial y^2} + \frac{\partial^2 T}{\partial z^2} \right) \quad (1.9)$$

where  $T$  is the temperature,  $t$  is the time,  $x$ ,  $y$ ,  $z$  are the heat flow directions, and  $\alpha$  is the thermal diffusivity. The thermal diffusivity is related to thermal conductivity  $\lambda$ , density  $\rho$ , and specific heat  $C_P$  through the following equation (Bergman, Lavine, Incropera, & Dewitt, 2011):

$$\alpha = \frac{\lambda}{\rho C_P} \quad (1.10)$$

The concept of instant heat source in an infinite medium is used to solve the heat conduction in relation to the LFW process. The analytical solution for 1D transient temperature distribution with time, in the case of frictional heat generation at a rate of  $\dot{q}$  ( $W/m^2$ ) diffusing along the  $x$  distance from the weld interface, is given by (Grong, 1997):

$$T(x, t) = T_i + \frac{\dot{q}}{2\lambda} \left[ \sqrt{\frac{4\alpha t}{\pi}} \exp\left(-\frac{x^2}{4\alpha t}\right) - x \operatorname{erfc}\left(\frac{x}{2\sqrt{\alpha t}}\right) \right] \quad (1.11)$$

Where  $T_i$  is the ambient temperature. According to (1.10) for  $x = 0$ , the temperature distribution is given by:

$$T(0, t) = T_i + \frac{\dot{q}}{\lambda} \sqrt{\frac{\alpha t}{\pi}} \quad (1.12)$$

Masoumi et al. (Masoumi et al., 2017) reported that using eq. (1.12), the maximum temperature of the weld interface is 1250 °C at the end of the process. The thermal diffusivity and thermal conductivity of the investigated alloy are  $2.79 \times 10^{-6} \text{ m}^2 \cdot \text{s}^{-1}$  and  $11.15 \text{ W} \cdot \text{m}^{-1} \cdot \text{K}^{-1}$  (Masoumi et al., 2019; Seret, 2019), respectively. For IN718 alloy, these values are  $3.31 \times 10^{-6} \text{ m}^2 \cdot \text{s}^{-1}$  and  $11.098 \text{ W} \cdot \text{m}^{-1} \cdot \text{K}^{-1}$  (Luo & Zhao, 2019). They selected processing time for 10s considered to be sufficient for reaching the maximum temperature of 1250°C at the weld interface which was enough for inducing plastic deformation over the entire weld interface.

### 1.3.1.7 Axial shortening

The shortening length along the loading direction is called the axial shortening where the axial force is applied and also termed as-upset or burn-off of joints and some are expelled as the flash from around the joint. Masoumi et al. (Masoumi et al., 2017) and Chamanfar et al. (A. Chamanfar et al., 2013) reported that it is a reasonable approximation to assume that when the material flow starts at  $0.85 T_M$  which could dissolve a significant volume fraction of the  $\gamma'$  precipitates. At this temperature, the alloy is plasticized and could be deformed easily, which can provoke the axial shortening in both parts.

In order to reach a better microstructure after LFW, the influences of the three most important process parameters (i.e., temperature, friction, and forge pressures) need to be considered and quantified (Masoumi et al., 2017). In general, the change of process parameters of the device

initially causes a change in the axial shortening due to the thermal effects in the piece that changes the microstructure and the area affected by the welding, which ultimately influences the mechanical properties of the weld pieces. According to Chamanfar et al. (A. Chamanfar et al., 2012a), the axial shortenings less than 2 mm weaken the joint integrity after LFWed and PWHTed Waspaloy due to lack of bonding and/or presence of oxides at the weld interface. They revealed that welded samples with 2 mm axial shortening or higher exhibited yield strength and UTS very close to those of the base metal.

The variation of the temperature during LFW of superalloys has been carried out by a few research groups (A. Chamanfar, Jahazi, Gholipour, Wanjara, & Yue, 2010; Caroline Mary & Jahazi, 2006). However, the temperature measurement at the interface during welding is nearly impossible due to, flash formation, axial shortening or the highly dynamic nature of the process. To understand the effect of the temperature on the bulk (or weldment), we need to know and assess microstructural evolution in all regions within the bulk which will be addressed in the next section.

### **1.3.2 Microstructure evolution**

A general microstructure of the weld area reveals three different regions in polycrystalline alloys. These regions characterized as namely, regions 1, 2, and 3 from the interface to parent material or base metal (BM). The first region corresponds to the weld zone (WZ), second is the thermomechanically affected zone (TMAZ), and the third one named the heat affected zone (HAZ), respectively (Figure 1.12). Microstructural evolution occurs across the weld interface as a result of high thermal gradients and applied compressive strain induced by friction and forging pressures (M. M. Smith, 2017a). This description is a general macrostructural evolution for LFW of polycrystalline superalloys inhere can be defined based on IN718, Inconel 738 (IN738), and AD730 Ni-based superalloys. The welded microstructural regions should be considered in four categories: (1) grains size, (2) morphology of the grain boundaries, (3) stored energy or level of misorientation of grains, (4) and microchemistry or phase transformation (e.g., precipitates and liquation).

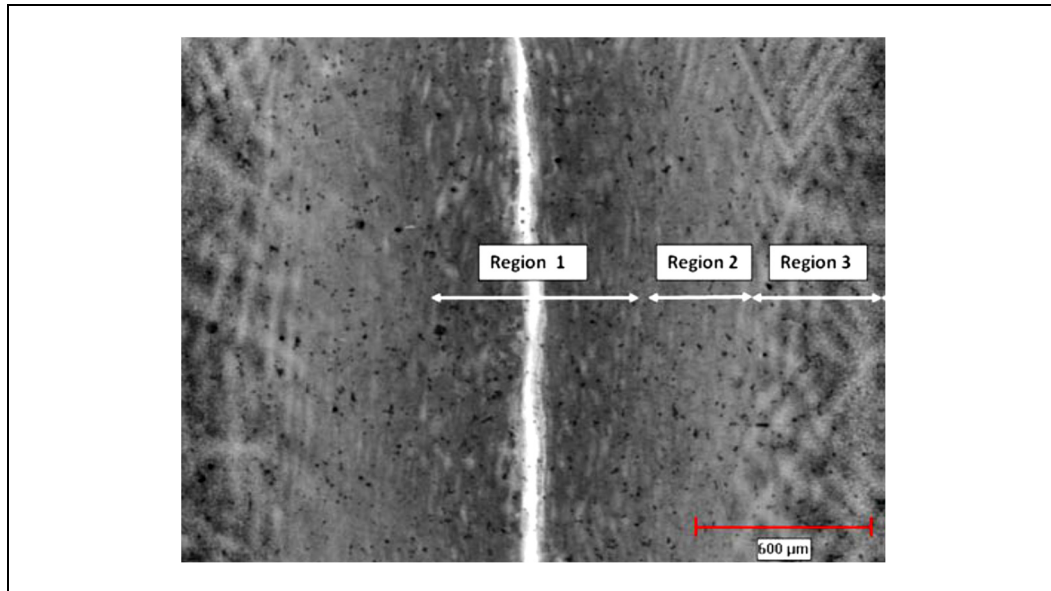


Figure 1.12 Microstructure of three regions around weld zone, namely, regions 1 to 3, which correspond to the WZ, the TMAZ, and the HAZ, respectively  
Taken from M. M. Smith (2017a)

**Weld zone (WZ) (region1):** As shown in Figures 1.12 and 1.13, this area is exposed to the temperatures above the secondary phases' solvus (the highest temperature in the process). The peak temperature can increase up to 0.9 to 0.97 of  $T_M$  (Ola, Ojo, Wanjara, & Chaturvedi, 2011a; Swaminathan et al., 2009). In the case of LFW of IN738, Ola et al. (Ola et al., 2011a) reported that  $\gamma'$  precipitates and  $\gamma$ - $\gamma'$  eutectic completely dissolved, while for some alloys  $\gamma'$  particles have been observed during LFW and MC carbides remained in the weld line.

In wrought superalloys, MC carbides are uniformly distributed in the microstructure in intragranular positions. These particles re-precipitated within the WZ during LFW of Waspaloy (A. Chamanfar et al., 2010, 2012b). However, they don not influence drastically on the mechanical properties due to their relatively low volume fraction ( $\sim 0.25\%$  (Weaver & Semiatin, 2007)) and uniform distribution (Sabol & Stickler, 1969; WhIttenberger, 1992). However, MC carbides make the matrix chemically stable by absorbing some elements such as Ti, Mo, and Nb (WhIttenberger, 1992). Masoumi et al. (Masoumi et al., 2017) reported that

in the WZ of LFWed AD730<sup>TM</sup> alloys, the primary  $\gamma'$  and secondary  $\gamma'$  are completely dissolved at 1220 °C and 1150 °C, respectively.

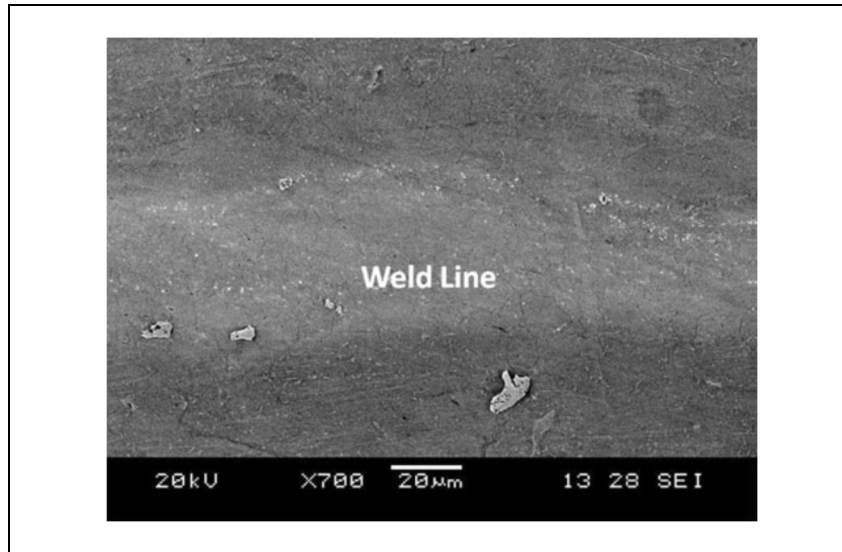


Figure 1.13 SEM micrographs showing a crack-free linear friction joint in IN 738  
Taken from Ola et al. (2011a, p. 921)

In addition, due to the combination of high strain and strain rates at elevated temperatures during LFW the recrystallization occurs dynamically (DRX) (Ola et al., 2011a). The occurrence of recrystallization (RX) has been reported within WZ of LFWed IN738, IN718, Waspalloy, and AD730<sup>TM</sup> (Ahmad Chamanfar et al., 2015; A. Chamanfar et al., 2012a, 2012b; Ma et al., 2016; Masoumi et al., 2017; Ojo et al., 2004b; Ola et al., 2011a; M. M. Smith, 2017a).

Further away from the WZ of LFWed IN738, the microstructure progressively exhibits various features in different regions consisting of deformed or partially recrystallized grains, and beyond 300  $\mu\text{m}$  (Ojo et al., 2004b; Ola et al., 2011a) the recrystallization is localized along prior grain boundaries. In the case of LFW of GH4169 alloy (similar to IN718), Ma et al. (Ma et al., 2016) reported that the WZ is dominated by high angle grain boundaries (HAGB) around 93.1%, which showed that the Dynamic Recrystallization (DRX) which occurred in the WZ was enough.

**The thermomechanically affected zone (TMAZ) (region 2):** The TMAZ has been observed away from the WZ between 180 and 600  $\mu\text{m}$  (Masoumi et al., 2017; Ola et al., 2011a; M. M. Smith, 2017a). Ola et al. (Ola et al., 2011a) in the microstructure of LFWed IN738 also observed a complete dissolution of  $\gamma'$  precipitates and  $\gamma$ - $\gamma'$  eutectic in this zone, while the MC carbides survived. The primary and secondary  $\gamma'$  precipitates that were presented in the pre-weld solution heat treated IN738 were dissolved completely in both zones. However, their observations revealed the presence of re-solidified fine  $\gamma$ - $\gamma'$  eutectic products that formed from the residual liquid during cooling.

The main microstructural difference between region 1 and 2 is attributed to the RX of grains. In region 1, the fully recrystallized grains formed, while RX in the TMAZ is localized to prior grain boundaries (Ola et al., 2011a). Based on the TMAZ, an identification method proposed by Mary and Jahazi (Caroline Mary & Jahazi, 2006), this zone is divided into two parts: the RXed and partial reversion zones (Ma et al., 2016). Furthermore, a significant microstructural change, in the TMAZ, is possibility of grain boundary liquation during LFW. Figure 1.14 (a) shows SEM image of the TMAZ as evidence of occurrence liquation at grain boundary in the weldment. On the contrary, in many research (Ma et al., 2016; Masoumi et al., 2017; M. M. Smith, 2017a) this phenomenon has not been reported.

Smith et al. (M. Smith, Bichler, & Sediako, 2016) reported that in LFW of forged and as-serviced IN718, the morphology of  $\delta$  phase and its volume fraction changed considerably across the weld interface. The initial change in the  $\delta$  phase is detected in the TMAZ. The partial dissolution of this phase has resulted in a  $\delta$  phase with a ribbon-like morphology at this zone. Besides, there was no  $\delta$  phase observed within the DRX area (Figure 1.15) in the middle of the weld interface. Second, nitrides and MC carbides were observed in the WZ. Finally, in this case, no defects were observed (e.g., porosity, cracks, and liquation).

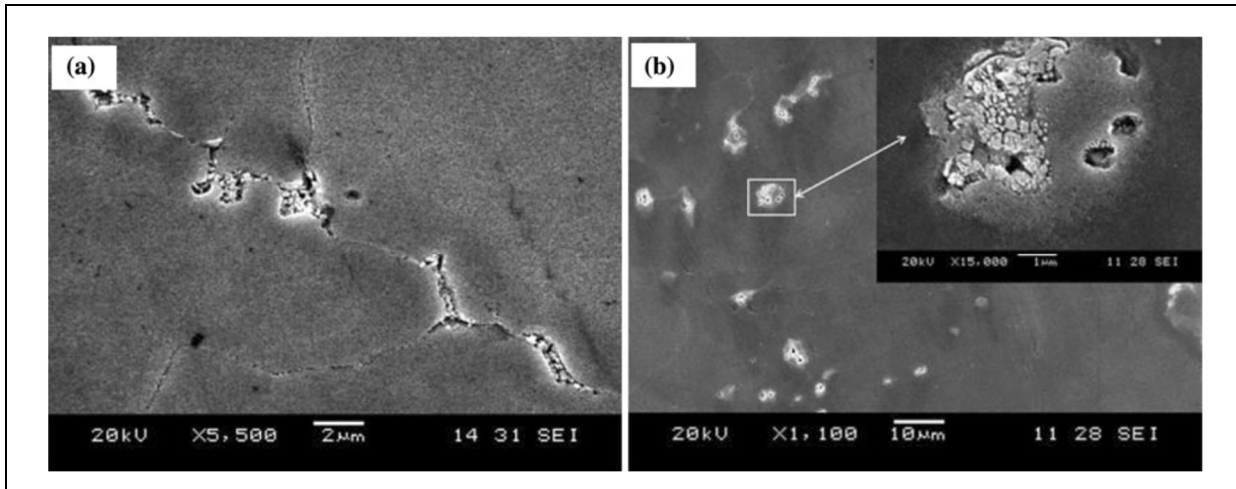


Figure 1.14 SEM images of the TMAZ show (a) intergranular and (b) intragranular liquation  
Taken from Ola et al. (2011a, p. 921)

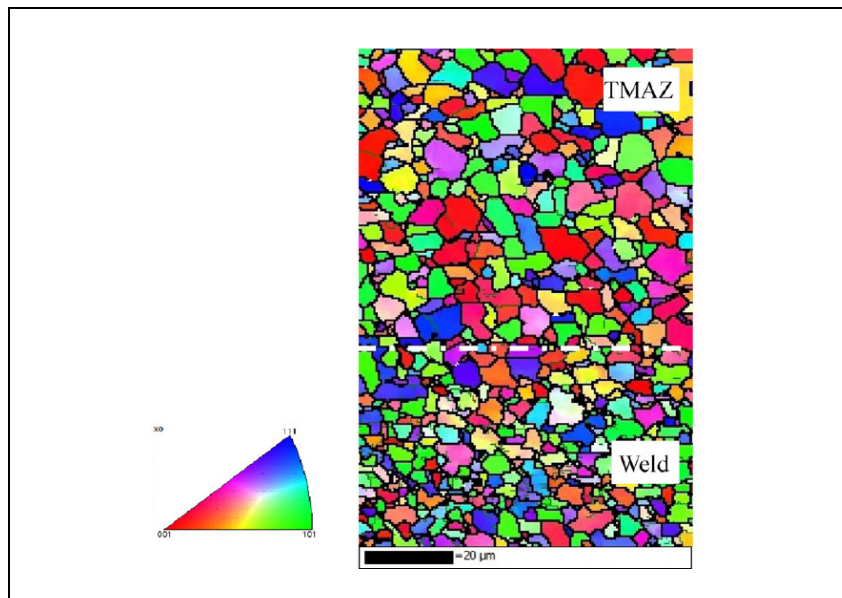


Figure 1.15 EBSD grain map from the WZ to the TMAZ  
Taken from Ma et al. (2016, p. 85)

As reported in many investigations (Ahmad Chamanfar et al., 2015; Ma et al., 2016; Masoumi et al., 2017; Ola et al., 2011a), the temperature decreases with distance away from the weld interface, into the TMAZ and the next region (HAZ), and subsequently into the BM. This gradient across the weld line suggests that indications of liquation should be more evident in the WZ in compare with the thermomechanical affected zone (Ola et al., 2011a). Longer

friction time means more time to input the heat which consequently widens the TMAZ. Moreover, more heating time would offer more time for  $\gamma''$  and  $\gamma'$  reversion. The phase reversion in IN718 happened from the first zone to the TMAZ resulting in the decrease of the amount of the strength hardening phase, which directly weakens thermomechanical properties of the TMAZ (Ma et al., 2016). In addition to the effect of temperature, another variable that was found to play a significant role is compressive stress (or strain) which will discuss in the section 1.3.2.3 and chapters 5 and 6.

**The Heat Affected Zone (HAZ or region 3):** Masoumi et al. (Masoumi et al., 2017) reported notable changes in the microstructure of the similar LFW of AD730 superalloy that occurred in a specific distance (4 to 4.5 mm) on both sides from the weld line to a total width of the TMAZ and the HAZ (8 to 9 mm). Secondary and primary  $\gamma'$  precipitates dissolved partially. Partial dissolution of the coarse primary  $\gamma'$  precipitate was also observed in the research conducted by Ola et al. (Ola et al., 2011a), which is attributed to the temperature gradient that existed across the LFWed joint. No RX was reported in the HAZ by them.

Unlike fusion welding, LFW could be an excellent alternative in order to avoid solidification defects such as cracking, the formation of stray grains, and HAZ cracking (Ahmad Chamanfar et al., 2015). Ni-based superalloys are also susceptible to HAZ cracking induced by liquation of the  $\gamma'$  around the grain boundaries. The liquation of the second phases and consequently microcracking can be suppressed by applying LFW method for these alloys. Liquation has been reported in numerous Ni-based superalloy systems including: IN738 (Ojo, Richards, & Chaturvedi, 2004a; Ola et al., 2011a), IN738 LC (Ojo & Chaturvedi, 2005), CMSX-486 (Ola, Ojo, Wanjara, & Chaturvedi, 2011b), IN718 (X. Huang, Chaturvedi, Richards, & Jackman, 1997; Ma et al., 2017; Radhakrishnan & Thompson, 1991; M. Smith, Bichler, Gholipour, & Wanjara, 2017; M. Smith et al., 2016; M. M. Smith, 2017a; Thompson, Mayo, & Radhakrishnan, 1991; Thompson, Radhakrishnan, & Mayo, 1988). However, liquation is not reported in LFWed AD730 (Masoumi et al., 2017; Masoumi et al., 2018).

Several conditions are necessary for cracking after a phase has liquated. First, a liquid film must wet the grain boundaries. Second, a critical tensile stress at the liquid/matrix interface must be reached in order for a crack to open and propagate (ASM, 1997; Mahesh C. Chaturvedi, 2007). Liquation at the HAZ is known to occur by non-equilibrium phase transformations below the alloy's bulk solidus (sub-solidus liquation) and at equilibrium melting above the alloy's bulk solidus when sufficient time is allowed for precipitates to melt (supersolidus liquation). Subsolidus liquation mechanisms can be grouped into two categories: (i) grain boundary penetration or (ii) grain boundary liquation (M. M. Smith, 2017a). Subsolidus non-equilibrium HAZ liquation is generally considered more detrimental in relation to cracking since it (Mahesh C. Chaturvedi, 2007):

1. Influences the nature of melting at supersolidus temperatures by altering the diffusion kinetics during subsequent heating by establishing non-equilibrium film along the grain boundaries at lower temperatures.
2. Increases the effective melting temperature range of the alloy, thereby increasing the duration where HAZ liquation cracking may occur.

Even if a critical stress is not achieved at the liquid/matrix interface to create a crack, the formation of a liquid may also have a deleterious effect on the alloy's bulk properties, such as the production of a brittle or otherwise mechanically unfavorable re-solidified alloy during cooling (M. M. Smith, 2017a).

Huang et al. (Z. W. Huang et al., 2007) studied on the microstructures of as-weld and PWHTed 720Li alloy to IN718. They reported that different high temperature mechanical properties between two alloys caused IN718 alloy to be ejected (more than U720Li) from the WZ into the flash at a lower temperature than the other alloy. As a result, in the weld line region, the alloy 720Li is exposed to a higher temperature and longer time than IN718.

### 1.3.2.1 Liquation

The LFW is a solid-state welding technique in which melting and solidification cracking are not expected to occur. However, the possible occurrence of liquation micro-cracking during LFW noticeably affect the mechanical properties of product produced due to the formation of a liquid film which is weak with regard to thermal and mechanical stresses.

Theoretically, liquation occurring at non-equilibrium subsolidus temperatures and heating/cooling rates can be classified into: (i) grain boundary penetration and (ii) grain boundary segregation. Both mechanisms may be active in the HAZ during fusion welding (Mahesh C. Chaturvedi, 2007). At high temperatures (more than 0.8 melting point), the formation of intergranular liquid films along the particle-matrix interface through a eutectic-type reaction leads to constitutional liquation of second-phase particles (Ojo et al., 2004b). Ola et al. (Ola et al., 2011a) observed the constitutional liquation of  $\gamma'$  precipitates and re-solidified eutectic micro-constituent in the TMAZ of LFWed IN738. While Chamanfar et al. (A. Chamanfar et al., 2012b) observed no liquation in LFW of Waspaloy. In the following some of the mechanisms by which non-equilibrium subsolidus liquation occurs, as well as parameters that affect an alloy's susceptibility to liquation cracking will be discussed.

**Grain boundary penetration** involves a phenomenon called constitutional liquation of second phase particles, where low melting point particles melt and form a continuous liquid film (Mahesh C. Chaturvedi, 2007). Constitutional liquation has been accepted by many researchers and others within the scientific community to explain non-equilibrium liquation in a variety of alloys.

Under equilibrium conditions, slow heating of an alloy to elevated temperatures enables the alloy's second phase particles to dissolve by diffusion into the matrix before a eutectic type of reaction takes place. However, during constitutional liquation, rapid heating causes the particles to liquate faster than diffusion can occur, resulting in a eutectic reaction between the second phase particles and the matrix (ASM, 1997; Mahesh C. Chaturvedi, 2007). Since HAZ

cracking is an intergranular defect, penetration of the grain boundary by the liquid film is usually a precursor to crack formation (ASM, 1997). The amount of liquid that forms along the particle-matrix ( $\gamma/\gamma'$ ) interface depends on the heating rate, initial particle size, and the dissolution kinetics of the constituent particle at elevated temperatures (ASM, 1997; Mahesh C. Chaturvedi, 2007). To nucleate a crack, a substantially thick liquid must remain at the grain boundaries, while tensile stresses develop in the material during cooling. Once the tensile stresses reach the critical magnitude, the crack initiates and propagates through the intergranular liquid/grain boundary interface (A. Chamanfar et al., 2012b; Ojo & Chaturvedi, 2005; M. M. Smith, 2017a).

Constitutional liquation has been observed in many material processing operations, including welding operations, hot rolling, forging, drawing and extrusion (R. Messler, 2004). It has been observed in many different precipitates hardened alloys, including superalloys (X. Huang et al., 1997; Ojo & Chaturvedi, 2005; Ola et al., 2011a, 2011b; M. M. Smith, 2017a; Soucail & Bienvenu, 1996; Thompson et al., 1991) rapid heating precluded complete dissolution of the precipitates prior to reaching eutectic temperature ( $T_e$ ). Constitutional liquation can occur at any temperature between  $T_e$  and solidus temperature if the heating rate is sufficiently fast to hinder normal diffusion processes (e.g., thermodynamic equilibrium condition) and allow the low melting point phase to exist beyond  $T_e$  where eutectic type reactions can occur with the matrix.

Constitutional liquation can be explained by examining a simple binary alloy with specific composition of phase particle precipitates within the matrix with an initial composition. By increasing the temperature from the single-phase region to the two-phase region and above the eutectic temperature, as the temperature approaching the  $T_e$ , the phase particles continue to shrink and the gradient of phase's atoms in the matrix continues to increase. However, there is a concentration gradient of atoms between the phase and the matrix that, at  $T_e$ , will allow for a liquid to form (M. M. Smith, 2017a). The magnitude of the concentration gradients that result from the dissolution of the phase precipitates are governed by (M. M. Smith, 2017a):

- 1) Heating rates – faster heating rates result in a steeper concentration gradient.

- 2) The mobility of phase's atoms into the matrix – faster diffusion of atoms results in a shallower concentration gradient.

**Grain boundary segregation** involves the diffusion of active elements (like Nb, B and S (X. Huang et al., 1997; Ping, Gu, Cui, & Harada, 2007; M. M. Smith, 2017a)) to the grain boundary during to elevated temperatures exposure where they (i) may form constitutionally liquating compounds or, (ii) may act as a melting point depressant (in Ni alloys) or, (iii) if present in the liquid formed during liquidation of Nb-rich intermetallic, these elements may alter the properties of the liquid film (Mahesh C. Chaturvedi, 2007).

Elements can diffuse to the grain boundary by two diffusion-controlled mechanisms, equilibrium segregation and non-equilibrium segregation (Mahesh C. Chaturvedi, 2007). Equilibrium segregation occurs when a sufficiently high temperature is maintained to allow solute atoms to diffuse from inside of the grain towards the grain boundary, where their absorption reduces the boundary's free energy. However, this mechanism is limited to a few atomic layers from the grain boundary (M. M. Smith, 2017a).

Non-equilibrium segregation occurs during the cooling stage following annealing or hot plastic deformation of the material. This mechanism requires the formation of solute vacancy complexes and presence of concentration gradients between the grain boundary and the grain's interior. A concentration gradient is formed by the annihilation of vacancies at the grain boundaries during cooling. As the vacancies move, they drag solute atoms, resulting in the enrichment of these atoms at the grain boundary (Mahesh C. Chaturvedi, 2007; Harries & Marwick, 1980). It was found that equilibrium segregation increases as temperature decreases, while non-equilibrium segregation increases as temperature increases. Non-equilibrium segregation was also reported (X. Huang et al., 1997) to be affected by the cooling rate, where mid-range cooling rates (e.g., air cooling at 20°C/s) allowed for sufficient time to form solute vacancy complexes, which were not observed at higher cooling rates (e.g., 400°C/s). Therefore, in an effort to control liquation, and liquation cracking, it is necessary to understand

how the microstructure, alloy composition, and the heating/cooling rates influence the onset of liquation or the initiation of a critical tensile stress (Figure 1.16).

Even though liquation of low melting point precipitates in an alloy may occur, it does not necessarily result in cracking. But they can act as crack initiation sites under thermal and/or mechanical loading under industrial conditions. There are a number of contributing factors that have been shown experimentally to influence an alloy's susceptibility to liquation cracking (M. M. Smith, 2017a). These factors are grain size (ASM, 1997; M. M. Smith, 2017a), size of precipitates (ASM, 1997; Soucail & Bienvenu, 1996; Thompson et al., 1991), particles dissolution rate (ASM, 1997; M. M. Smith, 2017a), type of precipitates (ASM, 1997; R. Messler, 2004; M. M. Smith, 2017a), impurities (ASM, 1997; X. Huang et al., 1997; Masoumi et al., 2017; Ojo et al., 2004b; Radhakrishnan & Thompson, 1991; Thompson et al., 1988), temperature (heating and cooling Rates) (Ola et al., 2011a, 2011b; M. M. Smith, 2017a; Soucail & Bienvenu, 1996), and presence of critical tensile stress (Ola et al., 2011a, 2011b).

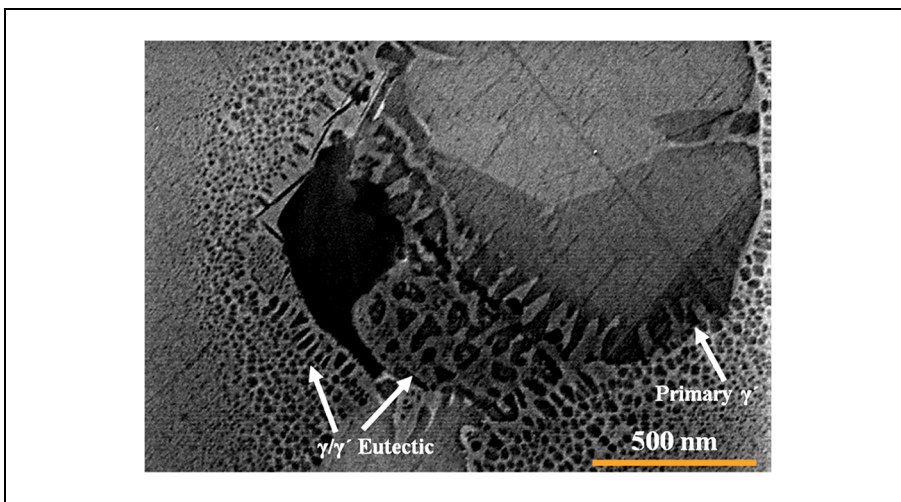


Figure 1.16 SEM images from the formation of  $\gamma$ - $\gamma'$  eutectic at their interface after constitutional liquation of primary  $\gamma'$  particle. Heating rate of 400 °C/s + 3 s holding time at 1200 °C and air cooling  
Taken from Masoumi et al. (2017, p. 2686)

Soucail and Bienvenu (Soucail & Bienvenu, 1996) performed experimental and numerical simulations on the dissolution of the  $\gamma'$  phase under equilibrium and non-equilibrium heating

of a Ni-bases superalloy. They suggested that there is a significant departure from equilibrium dissolution kinetics of the  $\gamma'$  phase during rapid heating, with the temperature for complete solid-state dissolution of the  $\gamma'$  phase increasing as the heating rate increased. Furthermore, the departure is shown to increase as the size of the  $\gamma'$  phase increased.

Masoumi et al. (Masoumi et al., 2017) explained that two assumptions could be made on the possibility of  $\gamma'$  liquation during LFW of AD730<sup>TM</sup> alloy and most probably other Ni-based superalloys:

- 1) Processing conditions (temperature, friction and forge pressures, strain and strain rate) are such that no liquation occurs during LFW, and
- 2) Liquation is produced but disappeared before eutectic re-solidification.

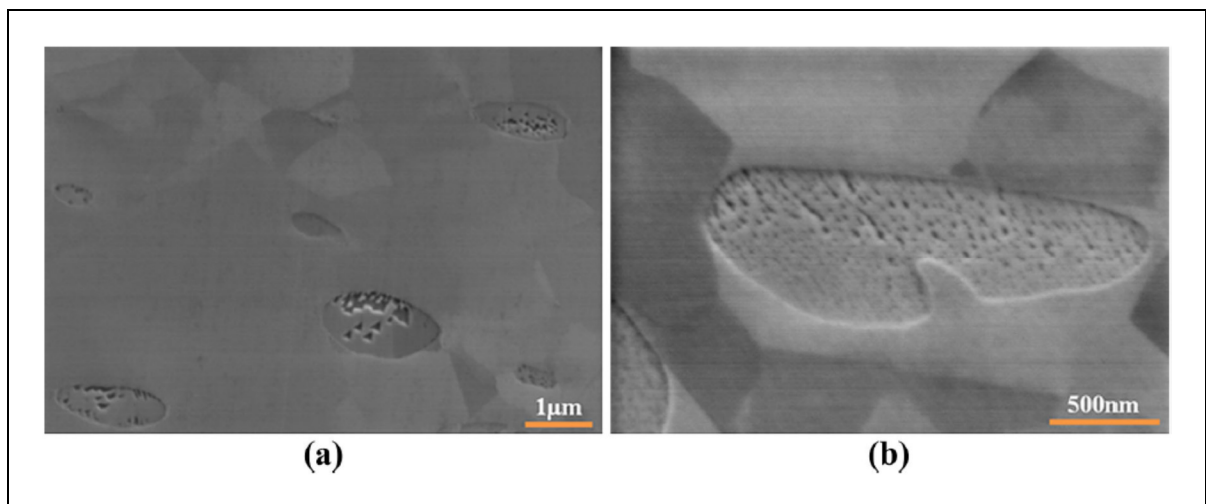


Figure 1.17 SEM images of from flash (a) and TMAZ (b) at 500  $\mu\text{m}$  away from the weld line. There is no indication of liquation or  $\gamma/\gamma'$  eutectic products  
Taken from Masoumi et al. (2017, p. 2686)

They revealed that high heating rates, such as those applied during LFW (350-500  $^{\circ}\text{C}/\text{s}$ ), can induce non-equilibrium liquation of second-phase particles. They suggested that in order to accurately determine the liquation temperature, it is better not to apply pressure during the heating cycle (Masoumi et al., 2017; Masoumi et al., 2018). Based on the literature (Mahesh C. Chaturvedi, 2007), the necessary conditions for constitutional liquation are slow phase dissolution, rapid heating, and microscopic equilibrium at the particle/matrix interface.

Masoumi et al. (Masoumi et al., 2017) concluded that it is reasonable to consider that the liquated phase at the interface can be eliminated by the imposed pressure and that is probably the reason why no trace of liquated phase was observed at the weld interface in the case of LFW of AD730<sup>TM</sup>. However, generally, the combination of high temperature, friction, and forge pressures during LFW can result in liquation and crack-resistant microstructure in LFWed superalloy although they did not observe liquation in their case (Figures 1.16 and 1.17). As reported by Ola et al. (Ola et al., 2011a, 2011b) this could be because of the effects of compression, strain and strain rate.

### **1.3.2.2 Effects of Heating and Cooling Rates**

The measurement of the real temperature generated at the weld line is a restriction to understand the WZ evolution and its microstructure in friction FW methods (Ahmad Chamanfar et al., 2015). To measure the temperature, thermocouples (Masoumi et al., 2017) and infrared camera (IR) (M. M. Smith, 2017a) have been used. Many methods (Soucail & Bienvenu, 1996; Soucail et al., 1992) involve the use of microstructural study to estimate the peak temperature. The use of Gleeble thermomechanical simulator machine at different temperatures and compressive strains with a careful correlation of weld microstructural analysis introduced as a method (Masoumi et al., 2017; Ola et al., 2011a). The temperature at the weld line during the process could arise to 0.9 to 0.97 of melting point (Ola et al., 2011a). Chamanfar et al. (A. Chamanfar et al., 2010) suggested that for FW processes, the temperatures should reach  $\sim 50^{\circ}\text{C}$ –  $60^{\circ}\text{C}$  below the solidus temperature of the alloy to provide sufficient softening or plasticisation of the weld centerline to produce a high-quality weld (Table 1.2).

Table 1.2 Maximum heating and cooling rates and peak temperature at different initial locations away from the weld centerline during LFW of Waspaloy  
Taken from A. Chamanfar et al. (2012b, p. 113)

Initial location from Interface (mm)	Maximum Heating rate (K/s or °C/s)	Peak Temperature (K, (°C))	Average Cooling Rate from Peak Temperature to 773 K (500°C) (K/s or °C/s)
Interface	-	1553 (1280)	82
1.5	643 ± 107	1399 ± 9 (1126 ± 9)	63 ± 16
2.8	459 ± 241	1283 ± 33 (1010 ± 33)	56 ± 12
4.2	165 ± 19	1083 ± 30 (810 ± 30)	40 ± 8
5.5	95 ± 4	913 ± 35 (640 ± 35)	19 ± 2

Masoumi et al. (Masoumi et al., 2017) reported that the solvus temperature of primary  $\gamma'$  precipitates in AD730<sup>TM</sup> superalloy is considered to be 1220 °C. In addition, under equilibrium conditions, solvus temperature for secondary  $\gamma'$  started around 800 °C and 1110 °C for the primary  $\gamma'$  (Masoumi, Jahazi, et al., 2016). In contrast, under non-equilibrium condition at heating rate of 400 °C/s, this temperature went up to 1150 °C for the secondary and 1220 °C for the primary  $\gamma'$ . The LFW conditions can increase internal heating (up to 1250 °C) and enhance the atomic diffusion which at the end could impact the extent of liquation. Thus, the dissolution of the  $\gamma'$  particles severely depends on the thermodynamic equilibrium or non-equilibrium circumstances. Dissolution kinetics of  $\gamma'$  particles in AD730<sup>TM</sup> alloy is significantly altered due to the increasing temperature, accumulated plastic strain, and the initial  $\gamma'$  characteristics (i.e., its size, morphology, and the composition) (J. Cormier, Milhet, Champion, & Mendez, 2008; Giraud et al., 2012; Masoumi, Jahazi, et al., 2016; Soucail & Bienvenu, 1996).

As mentioned before, the peak temperature in the weld line in LFW of AD730<sup>TM</sup> reached 1250 °C. However, no liquation was observed in the WZ or flash (Masoumi et al., 2017). They indicated that the temperature decreases from the WZ to a distance of 0.7 mm from 1250 °C to 1200 °C, respectively. The evolution of the  $\gamma'$  area fraction ( $F_{s\gamma'}$ ) as a function of the processing time (t) for dissolution heat treatment at 1100 °C for AD730<sup>TM</sup> superalloy was determined and is equal to (Masoumi, Jahazi, et al., 2016):

$$F_{s\gamma'} = 2.47 + 34.53 \exp\left(\frac{-t_e}{0.57}\right) \quad (1.13)$$

where  $t_e$  is the holding time at 1100 °C which considered as the effects of heating and cooling rates on  $\gamma'$  evolution which calculated by Soucail and Bienvenu (Soucail & Bienvenu, 1996):

$$t_e = \frac{RT_m^2}{Q} \left( \frac{1}{H_r} + \frac{1}{C_r} \right) + t_m \quad (1.14)$$

where R is the gas constant,  $T_m$  the holding temperature,  $Q$  the activation energy for the dissolution of the  $\gamma'$  phase,  $H_r$  and  $C_r$ ; respectively, the heating and cooling rates, and  $t_m$  is the holding time.

Regarding these equations and the phase transformation in IN718 alloy, considering the effect of thermal behavior on phase transformation at the interface of LFWed AD730™ to SLM IN718 and across from weld line is one of the major objectives of this dissertation.

### 1.3.2.3 Effect of compressive strain

Apart from the effect of temperature, the externally imposed compressive stress is another variable that has a significant role in the microstructure evolution during LFW process (Ola et al., 2011a). Most of the weld parts, during LFW, are macroscopically under compression loading except the flash that is extruded away from the joint area and contained tensile stress. Compressive strain mostly imposed during the forging stage, while tensile stresses are usually observed as residual stresses which occurred during cooling after the forging. Indeed, tensile stresses are generated during the friction stage (Z. W. Huang et al., 2007; Karadge et al., 2006; Kim & Fuji, 2002). Therefore, it is critical to indicate the reason for no crack formation despite the observed occurrence of liquation and the possibility of the presence of tensile stress in some cases (Z. W. Huang et al., 2007; Karadge et al., 2006; Kim & Fuji, 2002).

Normal tensile stresses and grain boundary liquation provide the HAZ liquation intergranular cracking. This kind of stress is essential for the cracking of liquation film formed at high temperatures (Ola et al., 2011a). During the friction and forging stages, imposed compressive load provides some resistance to crack formation. As reported by Ola et al. (Ola et al., 2011a), compressive stress did not only result in crack prevention but also healed the short cracks in Rene 88<sup>DT</sup> (intergranular liquation cracking).

In the case of fusion welding methods, the stability of grain boundary liquid to lower temperatures and solidification causes intergranular liquation cracking. Tensile stresses created during cooling could be sufficient to cause micro-fissuring by decohesion along one of the intergranular solid-liquid interfaces. Any factor that can reduce this stability will improve the resistance of welded material to liquation cracking. The stability of both intergranular and intragranular liquid during welding may be reduced by imposing compressive strain during LFW through the altering the kinetics of the resolidification within grain boundary and particle/matrix interface (Ola et al., 2011a).

Solid-state back-diffusion of solute atoms into the solid matrix away from the liquid phase is a phenomenon by which grain boundary liquid can resolidify (Radhakrishnan & Thompson, 1992). Under compressive strain, diffusion of solute atoms can be enhanced (Barker & Purdy, 1998). Ola et al. (Ola et al., 2011a, 2011b) simulated the LFW of IN738 by Gleeble thermomechanical simulator and reported the effect of stress-induced compressive strain on back-diffusion which control the isothermal re-solidification of intragranular metastable liquid. They observed that imposing compressive strain significantly aided re-solidification of the intragranular liquid where strain-induced increased the diffusivity of solute atoms resulted in enhanced back-diffusion and healing.

Apart from back-diffusion, intergranular liquid film migration (LFM) is another effective mode through which non-equilibrium grain boundary liquid can rapidly solidify at high temperatures. This is characterized by a homogeneously alloyed solidified zone produced by the migration process of liquid films (Ojo et al., 2004a, 2004b). The dominant mechanism in

explaining LFM is the diffusional coherency strain (Hillert, 1983). According to this, a rapid equilibration process is set up by lattice solute back-diffusion which can induce a metastable liquid in the interface of two grains. Coherency strains induced by the lattice mismatch could develop if there is a sufficient size difference between the solute and matrix atoms radius. Ojo et al. (Ojo et al., 2004a) reported diffusional coherency strain in the HAZ due to the atomic size mismatch between  $\gamma'$  constituent elements and matrix atoms in IN738 which can cause intergranular LFM where no externally applied stress is involved. In the contrary, by applying externally compressive stress during LFW, the formation of LFM is controlled by lattice solute back-diffusion and can be aided by strain-enhanced diffusivity (Barker & Purdy, 1998). Rapid solidification by the LFM process is dependent and controlled by rapid solute diffusional transport within the intergranular liquid film. The difference in the liquid composition occurs due to the existence of a differential strain ( $\Delta\varepsilon$ ) between the adjacent grains, which causes the liquid composition at equilibrium with the strained solids to differ.

Generation of similar levels of coherency stress in adjacent grains, owing to symmetrical lattice back-diffusion,  $\Delta\varepsilon$  does exist between the grains due to the difference in the values of the crystallographic orientation-dependent modulus of elasticity in the two grains (Handwerker, Cahn, Yoon, & Blendell, 1985). An increase in differential strain will produce a corresponding increase in concentration difference across the film (or liquid composition or  $\Delta C$ ), which would imply a higher driving force for LFM, and as such, any factor that effectively increases the magnitude of  $\Delta\varepsilon$  can significantly accelerate the LFM process. LFM can thus be explained by the diffusional coherency strain mechanism. The  $\Delta\varepsilon$  is generated mainly by coherency strain produced by a change in the intragranular chemical composition induced by the solute lattice back-diffusion. However, during LFW, in addition to diffusional coherency strain that may be present, an externally induced compressive strain, which is generally several orders of magnitude higher, is involved.

The presence of a relatively large  $\Delta\varepsilon$  is attributed to the externally applied stress which could notably alter the free energy of adjacent grains with regard to that of the liquid phase in between them, to produce a relatively high  $\Delta C$  (different in chemical composition of two adjacent

points). It has been recognized that coherency strain energy is a function of the size of the migrated region (Ola et al., 2011a). Loss of coherency significantly reduces driving force which limits the effectiveness of LFM and could immobilize the grain boundary film. Thus, it is preventing complete elimination of the intergranular liquid. A complete solidification of grain boundary liquid film would occur only under the non-steady state migration process in which the intergranular liquid is not being constantly supplied with extra solute atoms, such as from intragranular liquid (Ola et al., 2011a). Therefore, without applying external stress, LFM is not effective to completely remove the grain boundary liquid during holding at the peak temperature of process, and the residual liquid ahead of the migrated zone transformed to eutectic products by non-equilibrium solidification reaction during cooling stage. In conclusion, compressive stress enhanced the rapid high temperature re-solidification of intergranular liquid via LFM. It is characterized by a combination of enhanced initiation stage, higher migration velocity. The elimination of both intergranular and intragranular liquid films during LFW of IN738 was achieved by a combination of solute back-diffusion and LFM, which were enhanced by imposed compressive strain (Ola et al., 2011a).

The effect of compressive loading and its strain on plastic deformation increased the rapid solidification which aided resistance to crack initiation. Indeed, a material under compression shows higher hot ductility behavior in comparison with the case under tensile loading where intergranular liquation produces zero hot ductility (Ola et al., 2011a).

### **1.3.3 Dissimilar LFW of superalloys**

Linear friction welding of similar alloys experiences a significant variation of microstructure due to thermomechanical process resulting in the full or partial dissolution of  $\gamma'$  and/or  $\gamma''$  near the weld zone because of the temperature reached in the range of forging temperature near the weld interface and WZ. As mentioned before, LFW is characterized by fast heating conditions resulting in a superheating effect which could be different in two dissimilar alloys.

In dissimilar case, one part may be considerably harder than the other and with higher melting point. When the temperature increases, the hard material will penetrate into the softer part and deform it in certain depth and displace this deformed volume and expel it out the contact area as flash before melting (Ahmad Chamanfar et al., 2015; Maalekian, 2007). Therefore, the overall friction and forge pressures and time are the key factors of deformation and the amount of axial shortening that depends on the high temperature strength of the alloys. As a result, the softer alloy generates more flash (Figure 1.18) (Ahmad Chamanfar et al., 2015).

Dissimilar welds reveal a better diffusion of alloying elements across the weld interface due to the gradient in chemical composition between two alloys. The elements diffuse across the weld interface and the chemical composition gradient decreases in the vicinity of the weld line. This phenomenon is somehow similar to the diffusion bonding mechanism, i.e., electron sharing and bond formation between atoms. The width of this transition zone depends on the alloy composition and welding parameters. Similar mechanism is also observed in pin on disc wear testing even at room temperature. The generated heat during LFW reduce the yield stress of both materials making easier the deformation under the contact surface in both alloys.

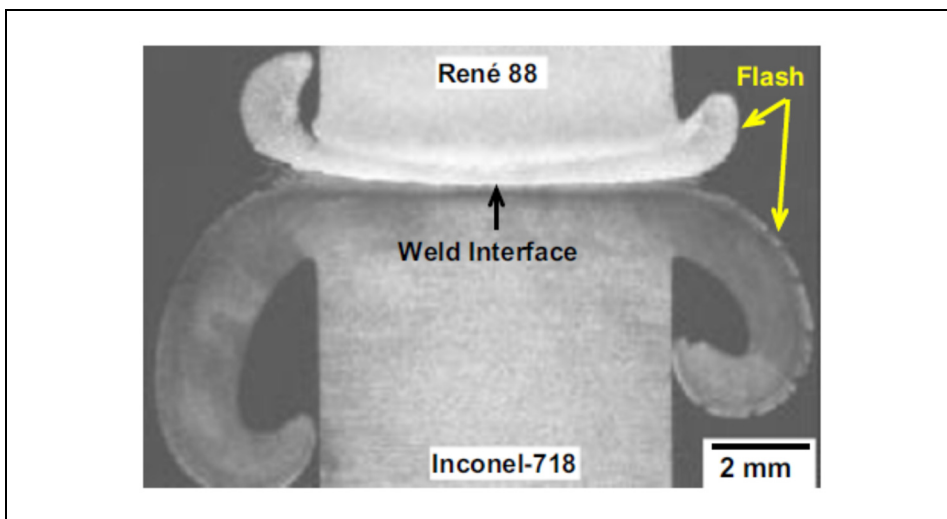


Figure 1.18 Dissimilar IFW of Rene 88 to IN718  
Taken from Roder, Helm, Neft, Albrecht, & Luetjering (2005a, p. 649)

Senkov and Mahaffey (Mahaffey, Senkov, Shivpuri, & Semiatin, 2016; O. N. Senkov, Mahaffey, & Semiatin, 2018; Oleg N. Senkov, Mahaffey, Semiatin, & Woodward, 2014) welded Mar-M247 to LSHR by IFW method and reported 8-23 $\mu$ m as the depth of the composition transition range. This transition resulted in a mechanical intermixing at the mating surface due to high level of plastic deformation and additional grain boundary diffusion across the interface during the process. They reported that the  $\gamma'$  dissolution temperature in LSHR is 1157°C and for Mar-M247 is 1225 °C. At low temperature (750°C), LSHR has higher yield strength, while Mar-M247 has higher yield strength than LSHR at a higher temperature. Therefore, they observed the largest upset in LSHR alloy and more barreling in Mar-M247. They concluded that limited plasticity of Mar-M247 caused lack of bonding at the weld interface which could be controlled or modified by applying high moment of inertia to increase the width of the transition zone on two sides of welded parts.

Huang et al. (Z. W. Huang et al., 2007) IFWed IN718 to U720Li. They realized that the high  $\gamma'$  volume fraction of alloy 720Li exhibits a wider HAZ than the mainly  $\gamma''$  strengthened IN718. In conclusion, dissimilar welding allows tailoring the microstructures and provide the expected mechanical properties. For example, using LFW method to joint a fine grain disk to a blade with coarse grains to optimize the properties.

#### **1.3.4 Post-processing heat treatments (PWHT)**

Post weld heat treatment (PWHT) is a technique for improving the properties of weldment. Ni-based superalloys which are precipitation hardened materials requiring PWHT to relieve the residual stresses during thermomechanical processing. These alloys need to be treated to reprecipitate hardening phases within the microstructure. Damodaram et al. (Damodaram, Raman, & Rao, 2013) studied the room temperature tensile properties of friction welded IN718. They realized that PWHT depends on thermal history conditions due to the dissolution of the strengthening  $\gamma''$  precipitates in the WZ. After a direct aging (DA) treatment a significant improvement in the mechanical properties was revealed.

Ma et al. (Ma et al., 2016) recommended performing PWHT on LFWed GH4169 alloy (similar IN718) due to the weak bonding of the joint. For example, a homogenous microstructure after heat treatment may lead to higher yield strength for bonded samples. A modified cyclic solution heat treatment could decrease microcracks and improve tensile and fatigue properties of laser welded IN718 joints due to second phases precipitation (D. Shi et al., 2012; Steuer, Piegert, Frommherz, Singer, & Scholz, 2011; Steuer & Singer, 2014).

In the case of AD730<sup>TM</sup> alloy, the microstructure of solution and age treated AD730<sup>TM</sup> usually contains about 37%  $\gamma'$  up to 700 °C. Masoumi et al. (Masoumi et al., 2018) reported that applying subsolvus PWHT led to coarsening of re-precipitated  $\gamma'$  particles formed in the WZ after LFW during cooling. The morphology of the coarsened particles was cuboidal, and their average size and volume fraction were determined to be 230 nm and 4%, respectively. The tertiary  $\gamma'$  particles were formed between the cuboidal precipitates during cooling from 1080 °C, and they coarsened during the aging heat treatment (for the AD730<sup>TM</sup> alloy) at 730 °C, as they were 40 nm in size after PWHT. Besides, grains size measurements revealed that the average grain size of the weld interface was about 8  $\mu\text{m}$  in PWHT condition, which is twice of that in the as-LFWed condition.

As reported by Chamanfar et al. (A. Chamanfar et al., 2012a), superalloys with low volume fraction  $\gamma'$  (less than 40%) need to have a proper PWHT for recovering the  $\gamma'$  particles and restore the hardness. The unimodal size distribution, spherical morphology, high density, small size, and short interparticle spacing are the features of the  $\gamma'$  reprecipitation. Thus, it is necessary to do a proper PWHT to achieve desirable microstructure and mechanical properties.

Smith et al. (M. Smith et al., 2017; M. M. Smith, 2017a) reported that PWHT on LFWed IN718 resulted in complete dissolution of  $\delta$  phase in all regions of the sample along with a substantial increase in the grains size away from the weld line on both sides. The treatment could improve the room temperature hardness and tensile properties of the welded samples. This can be attributed to the larger volume fraction of the  $\gamma''$  ( $\text{Ni}_3\text{Nb}$ ) phase due to complete dissolution of  $\delta$  ( $\text{Ni}_3\text{Nb}$ ) phase during solutionizing. The  $\delta$  phase was uniformly re-solutionized even if the

starting materials had a large variation in  $\delta$  phase volume fraction. Therefore, PWHT was compatible for use on LFWed samples. As Smith et al. (M. Smith et al., 2017; M. Smith et al., 2016) also reported that the ST included holding the as-LFW IN718 samples at 1020 °C for 1 hour in an Argon atmosphere, followed by air cooling to room temperature. The DA consisted of holding at 745 °C for 8 hours under the same atmosphere, followed by furnace cooling at a rate of 25 °C/min to 645 °C for 8 hours and air cooling to room temperature.

For AMed parts, different thermal gradients from the WZ to the BM, induce different microstructures and phase transformations along the parts. No pre-heat treated SLMed part obviously has individual microstructure and phase transformation in comparison with the part which has been HIPed and homogenized. In the case of SLMed IN718, Nb segregation in the Laves phase formation can be the notable difference before and after heat treatment. After HIP + homogenization, microstructure could contain equiaxed grains and be Laves phase-free (after water quenching). After LFW process, the microstructure might be the same as for polycrystalline IN718 which was described in general microstructure of the LFW although more investigation is necessary to identify the impact of Nb segregation because microstructure of pre-weld heat treated as-SLMed IN718 is not completely isotropic, and each treatment cycle has a special impact on Nb distribution and other phases.

To obtain the microstructure containing a stable matrix strengthened with coherent and dispersive precipitates such as  $\gamma'$  and  $\gamma''$  phases, post-heat treatment is necessary. The comparison between many studies (Chlebus et al., 2015; Goel et al., 2020; X. Wang & Chou, 2016; X. Wang et al., 2016) suggests that optimization of SLM processing parameters and prolonged PWHT can enhance the part properties by controlling mechanical properties of grain boundaries. This can be through removing the micro-segregation in the as-printed microstructure, elimination of Laves phase, inducing the  $\delta$ -phase at the grain boundaries, and precipitation of secondary phases (such as  $\gamma'$  and  $\gamma''$  in IN718 superalloy). In order to determine a desired heat treatment cycle, the characterization of the initial microstructure is very important, subsequently choosing between solutionizing + aging and direct aging.

Finally, it should be noted that under optimum LFW parameters, LFWed Ni-based superalloys possess proper mechanical properties, with fracture during tensile testing occurring mostly in the BM and the TMAZ and the tensile strength of joints being comparable to that of the parent material. The toughness and fatigue properties of these joints are also comparable to the powder metallurgy (PM) although severe grain refinement can induce low fracture toughness at the weld centerline.

### 1.3.5 Mechanical properties

The microstructure of the welded component determines the mechanical properties (C. Mary & Jahazi, 2008). The LFW process imports substantial microstructural changes in materials. The dissolution and subsequent reprecipitation of particles such as  $\gamma'$  and/or  $\gamma''$ ,  $\delta$  and Laves phases and grain recrystallization control the properties (Masoumi, Jahazi, et al., 2016; Masoumi, Shahriari, Jahazi, Cormier, & Devaux, 2016a). Many investigations (Jonathan Cormier & Cailletaud, 2010; J. Cormier, Milhet, & Mendez, 2007; Damodaram, Ganesh Sundara Raman, & Prasad Rao, 2014; Damodaram et al., 2013; le Graverend et al., 2010) reported that a reduction in the volume fraction of  $\gamma'/\gamma''$  led to a decline in the mechanical properties of the welded parts.

As previously mentioned, in order to predict maximum temperature dissolution, theoretical modelling of  $\gamma'$  precipitation is commonly used for Ni-based superalloys in friction welded materials (Ola et al., 2011a). For alloys (such as Waspaloy) with low volume fraction of  $\gamma'$  ( $\leq 30\%$ ), dissolution of  $\gamma'$  is almost complete in the vicinity of the weld line and  $\gamma'$  reprecipitation does not occur during cooling period. Therefore, applying a proper PWHT is essential to recover the  $\gamma'$  phase and restoring the hardness (Ahmad Chamanfar et al., 2015). On the other hand, alloys containing higher volume fraction of  $\gamma'$  ( $>40\%$ ), dissolution of  $\gamma'$  particles occurs during welding but very fine  $\gamma'$  particles reprecipitates near the weld interface during cooling period due to high levels of  $\gamma'$  composing elements (Ti and Al) which induce a relatively higher hardness values in the TMAZ (Ahmad Chamanfar et al., 2015).

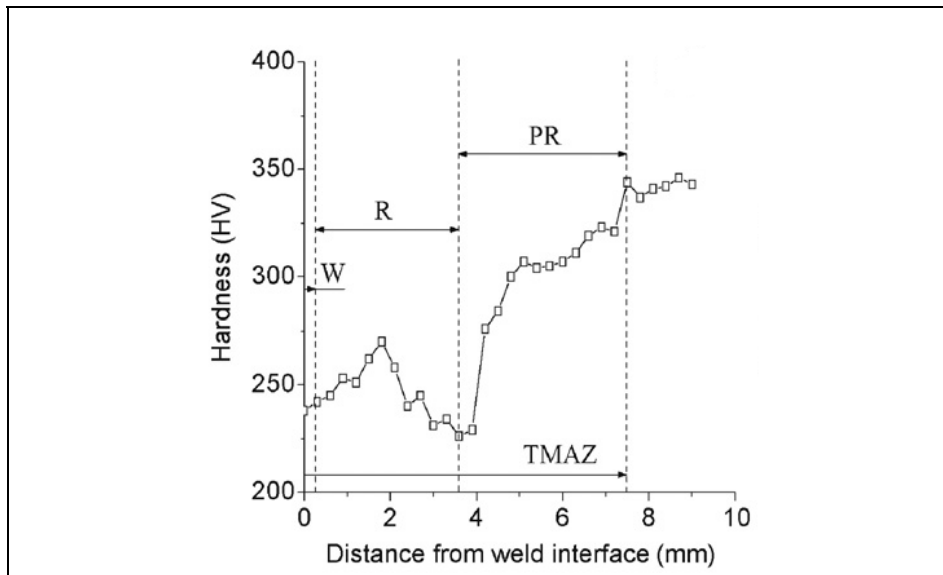


Figure 1.19 Microhardness distributions of joint in IN718. (PR is partial reversion of  $\gamma'$  and  $\gamma''$ , R is recrystallized zone and W is the WZ)  
Taken from Ma et al. (2016, p. 85)

In the case of IN718, Ma et al. (Ma et al., 2016) reported that  $\delta$  phase always accompanies with very fine  $\gamma''$  which reduces the mechanical properties. The metastable  $\gamma''$  phase may precipitate in the range of 550 °C to 900 °C (or till 1000 °C). At first, it might aggregate then coarsens and subsequently turns into  $\delta$  phase at high temperatures (more than 700 °C) and consequently reduces the mechanical properties. They reported that the reversion of  $\gamma''$  and  $\gamma'$  at high temperatures decreased the solid solution strengthening. They observed the white particles aligned along the weld line which were detected as carbides or oxides by energy dispersive X-ray spectroscopy (EDS). The microhardness in all samples declined from the base material to the WZ, but then it restored to a similar value in the WZ (Figure 1.19). This variation could be attributed to the increase of  $\delta$  phase and dynamic recovery and recrystallization. The  $\delta$  precipitates are able to decrease the grain boundaries migration and hinder them, thereby hindering dynamic recovery and recrystallization. It was found out that  $\delta$  precipitates begin to dissolve considerably at 980 °C and totally dissolve up to 1035 °C (Ma et al., 2016).

According to the results which concluded by Chamanfar et al. (A. Chamanfar et al., 2012a) in the case of LFWed Waspaloy, due to the reprecipitation and growth of  $\gamma'$  (secondary and

tertiary) after PWHT, the hardness recovered in the WZ and TMAZ (Figure 1.20). Primary  $\gamma'$  particles at the grain boundaries inhibited the grain growth during the thermomechanical process. In contrast, the presence of the intragranular secondary and tertiary  $\gamma'$  particles increased the strength of the alloy (Z. W. Huang et al., 2007). With increasing particle size, the hardness increases to a maximum, after which it declines. This critical particle diameter referred to as the “strongest size” depends on the volume fraction of the particles (Jackson & Reed, 1999).

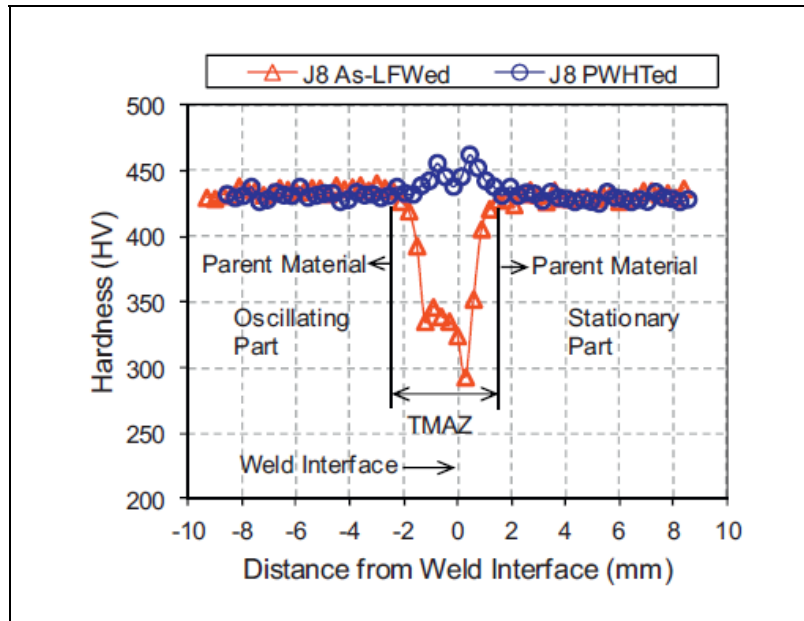


Figure 1.20 Microhardness profile across the weld centerline in as-LFWed and PWHTed conditions of Waspaloy  
Taken from A. Chamanfar et al. (2012a, p. 117)

Chamanfar et al. (A. Chamanfar et al., 2012a) suggested that the  $\gamma$  grain size and  $\gamma'$  characteristics and their evolutions do not contribute to the hardness peak observed in the TMAZ in PWHT condition. Thus, other factors such as  $\gamma'/\gamma$  misfit and/or residual plastic work in the material are probably responsible for the observed peak in the microhardness profile of LFWed Waspaloy.

Damodaram et al. (Damodaram et al., 2013) reported that hardness and tensile strength of friction welded IN718 improved after direct aging (DA). This is attributed to the grain refining due to dynamic recrystallization during LFW and precipitation during DA (Figure 1.21). Besides, welds subjected to DA treatment after friction welding exhibited similar values of hardness/tensile strength irrespective of whether they were welded with prior solution treatment (ST) or solution treatment plus aging (STA) conditions. As they reported, the samples without STA exhibited lower hardness and room temperature tensile strength at the WZ in comparison with the base material in STA condition due to the dissolution of  $\gamma''$  at the WZ when the temperature reached 1118 °C.

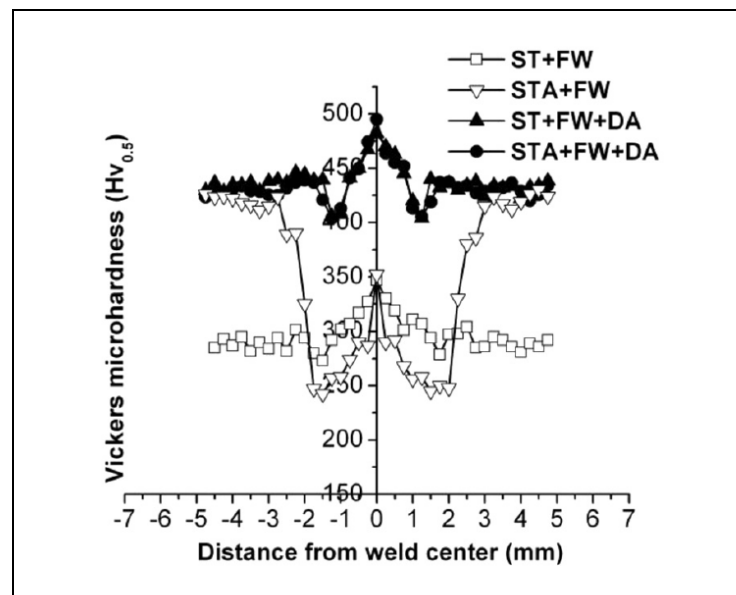


Figure 1.21 Microhardness profile across the weld of PWHTed IN718 alloy  
Taken from Damodaram et al. (2013, p. 781)

Masoumi et al. (Masoumi et al., 2018) observed cavities preferentially initiated within the grain boundaries at the WZ of LFWed AD730™ alloy after creep test due to the nucleation of voids around the primary  $\gamma'$  or carbide precipitates and the decohesion of these particles. Furthermore, voids nucleated at grain boundaries growth, coalesced, and connected to the surface assisting the surface creep crack growth. By their examination, PWHTed parts had higher creep life and strength than as-LFWed parts.

Proper PWHT can reduce the residual stresses induced by LFW (Karadge et al., 2006). For instance, it has been reported (Ahmad Chamanfar et al., 2015) that aging at certain temperature for each dissimilar IFW could be 732°C for IN718, 760°C for U720-Li, and 810°C for RR1000. The level of residual stresses has been relieved to below 400 MPa in all the three weldments cases.

Up to the present time, although detailed microhardness, microstructure, and residual stress analysed for IFWed and LFWed Ni superalloys such as IN718 (Bhamji et al., 2011; Karadge et al., 2007), 720Li (Daymond & Bonner, 2003; Karadge et al., 2007; W.-Y. Li et al., 2010), RR1000 (Karadge et al., 2007; TWI, 2001), IN738 (Ahmad Chamanfar, 2012), Waspaloy (Ahmad Chamanfar, 2012; A. Chamanfar et al., 2012a, 2012b; Qian & Lippold, 2002) and Ni-base single crystals (Priti Wanjara, Dalgaard, Gholipour, & Larose, 2012), little work has been published on their the tensile properties. Li et al. (H. Y. Li, Huang, Bray, Baxter, & Bowen, 2007) studied dissimilar LFW of U720LI to IN718. They indicated that the total elongation and yield strength of weldments were respectively 12% and 110% that of the weaker base metal (i.e. IN718 (Brand, Karhausen, & Kopp, 1996)).

Chamanfar et al. (A. Chamanfar et al., 2012a) showed that LFWed Waspaloy samples with axial shortening higher than 2 mm exhibited yield strength and UTS very close to those of the parent material, which could be related to the size of the TMAZ. They used the rule of mixtures to estimate the contribution of the TMAZ to the overall elongation of the weldment. Ma et al. (Ma et al., 2016) reported that all tensile specimens failed at the TMAZ or the WZ. They explained that tensile strength of the joint was still lower than that of the base metal although DRV and DRX refined the grains at the WZ and TMAZ. This behavior may be caused by:

1. Segregation of the alloying elements in the grain boundary at high temperatures, such as Nb in the form of the Laves and  $\delta$  phases, which could weaken the boundaries.
2. The reversion of  $\gamma''$  and  $\gamma'$  from the WZ to the TMAZ can decrease the amount of the strengthening phases, which directly weakens the TMAZ.
3. The carbides or oxides along the weld interface are detrimental to the tensile strength of the joints.

## 1.4 Challenges and objectives

Linear friction welding process provides significant benefits over the conventional mechanical assembly techniques and fusion welding methods by providing quality and performance improvements or weight reduction and economic benefits.

Nowadays, reducing the processing time and machining are taken into consideration. Accordingly, selective laser melting as a rapid prototyping method is an alternative method to fabricate blades or blisks. Combination of these two processing techniques (SLM and LFW) will reduce the cost, time, and the machining of the final product (BLISK or Blade-Integrated Disk). In addition, the production speed will significantly increase. Thus, the final weight of the aero-engine decreases which will approximately reduce percentage of fuel consumption in the aircraft engines. Additionally, one can control the properties of the blades and discs independently using two different alloys by tailoring their microstructures, which facilitates easy troubleshooting during periods of inspection. Tailoring microstructure in dissimilar joints will not be easy due to the different microstructure and mechanical properties of each alloy.

The present study encompasses a review of the several aspects of producing the process of Ni-based superalloys and joining them together with a new welding method. In the light of the fact that the microstructural changes have the significant influences on mechanical properties of components, the metallurgical and mechanical engineers want to control and tailor the microstructure and improve the mechanical properties of weldment by understanding microstructural evolution. Determination of the best way to weld two dissimilar Ni-based superalloys by LFW is set as the objective of the final project. Regarding LFW's parameters, their determination depends on the mechanical properties and hot deformation behavior of each part which must be known and measured for dissimilar joint and specifically for a AMed part before LFW. It should be noted that the specification of this objective is on the basis of achieving other objectives. These objectives will bring some problems and difficulties with them. For example, characterization of microstructure for both materials before and after LFW, which fabricated by additive manufacturing and forge process, determination of the heat

treatment cycles for both alloys before and/or after welding, phase transformation during LFW and its effects on the microstructure to assess the mechanical properties.

On the basis of the analysis of the state-of-the-art presented above, the main objectives of the present research project have been identified as:

1. Identification of dominant failure mechanisms during high temperature deformation of AD730<sup>TM</sup> and study on hot ductility of the alloy.
2. Effects of high heating and cooling rates on microstructural evolution of SLM IN718 during dissimilar LFW to characterize the heat-affected zone in this alloy.
3. The influence of welding process on microstructural evolution (e.g., dynamic recrystallization mechanisms, grains size, and misorientation) and its effects on microhardness and mechanical properties.
4. Determination of the influence of LFW process on the microstructural evolution on different precipitates in different zones and liquation in correlation with the evolution of microhardness, which could be useful to assess their impacts on strengthening mechanisms and mechanical properties of the joint.
5. Designing a new post-weld heat treatment cycle for a dissimilar joint and investigation on its effects on the microstructure and the mechanical properties.

## CHAPTER 2

### DETERMINATION OF LFW PROCESS PARAMETERS FOR SLM IN718 TO AD730<sup>TM</sup> ALLOY

#### 2.1 Introduction

In the present chapter the process parameters that were assessed and used for feasibility of joining dissimilar alloys from different fabrication methods by LFW.

#### 2.2 Linear friction welding process

The rectangular coupons block  $26 \times 13 \times 37 \text{ mm}^3$  (length  $\times$  width  $\times$  height) of AD730<sup>TM</sup> and SLMed IN718 are machined by wire electro-discharge machining (EDM). Prior welding, the contact surfaces are grounded with 800-grit SiC abrasive paper and cleaned with acetone to remove surface contaminants and oxides. The FW34-E20 LFW machine at TWI, Cambridge, UK is the LFW machine which are used. This process generally consists of four major phases.

##### 2.2.1 Friction and forge pressures

As mentioned in section 1.3.1 and Eqs. 1.3-5, the average friction and forging pressures were chosen based on strain rate and deformation temperature variations during LFW. Therefore, the mechanical properties of both alloys at high temperatures ( $>1150 \text{ }^\circ\text{C}$ ) and medium ( $0.1\text{-}1 \text{ s}^{-1}$  while oscillation) and high strain rates ( $>10 \text{ s}^{-1}$  while forging) were considered. Furthermore, friction coefficient variation could affect our estimation ( $\mu = 0.6\text{-}0.2$ ). The whole estimations have been done based on the parameters that had been applied in the case of similar LFW of AD730<sup>TM</sup> alloy (Masoumi et al., 2019).

The temperature in the bulk of the material increases with increasing the process time. When alloy flow starts at  $0.85 T_M$ , a significant volume fraction of the precipitates is already been dissolved, which could enhance the cyclic plastic deformation of the materials.

As reported by Masoumi et al. (Masoumi et al., 2019) friction and forge pressures of AD730<sup>TM</sup> alloy were in the range of 133-285 MPa (up to 1050 °C) and 265-580 MPa (up to 1250 °C with considering adiabatic temperature), respectively. In the case of IN718 alloy, in many investigations, it is reported that the lowest temperature for  $\gamma'/\gamma''$  and  $\delta$  phases dissolutions is around 1000-1020 °C. Thus, the minimum temperature that needs to be reached before the application of deformation in the initial stage of the LFW process is considered to be 1000 °C. In this study,  $0.85 T_M$  was considered as the upper limit which corresponds to 1150 °C (the melting temperature of AD730<sup>TM</sup> and IN718 alloys was taken as  $\sim 1350$  °C based on the literature). In IN718 alloy, all precipitates (except MC carbides) can be dissolved at 1150 °C. According to the model that has been designed by them and considering a LFW of dissimilar materials, lower and upper limits of temperatures to define the average pressures could be 1050 °C and 1250 °C, respectively.

Mostafa et al. (Mostafa et al., 2018) reported that at  $\dot{\epsilon} = 0.1 \text{ s}^{-1}$  (in the friction stage), the yield stress of SLM IN718 is 240 MPa, 140 MPa, and 90 MPa at 1000 °C, 1050 °C, and 1150 °C, respectively. At high strain rates ( $> 10 \text{ s}^{-1}$ ), there are few data about hot deformation of SLM IN718 (Mostafa et al., 2018; Thomas et al., 2006; Trosch et al., 2016). However, we are able to use similar alloys same as GH690 (Z.-x. Shi, Yan, Duan, & Zhao, 2017) or GH4169 (Geng, Qin, Li, et al., 2019; X. Yang et al., 2015). For instance, at high strain rates (in the forging stage), the yield stress was 350 MPa, 340 MPa, 250 MPa, and 220 MPa at 1000 °C, 1050 °C, 1150 °C, and 1200 °C, respectively. Therefore, the average friction and forge pressures ( $P_{ave.} \geq \frac{2\sigma_0}{\sqrt{3}}$ ) for IN718 alloy should be in the ranges of 104-277 MPa and 254-404 MPa, respectively.

As a result, at the friction stage,  $T_{\min}$  and  $T_{\max}$  for both alloys are 1000 and 1150°C, respectively. The friction pressure ( $F_{Fr}$ ), in dissimilar LFW, was estimated in the range of 133-277 MPa. Furthermore, the forge pressure ( $F_{Fo}$ ) was estimated in the range of 265-404 MPa.

In this study, the oscillation amplitude and frequency were assumed 2.5 mm and 40 Hz within the operating window of the LFW machine to compare our results for IN718 with similar welding of AD730<sup>TM</sup>. According to Eqs. 1.3 – 1.5 and 1.9 – 1.12 for 1D analytical thermal simulation and by using these LFW process parameters, the estimated temperature profiles were calculated for different test conditions and are presented in Figure 2.1. The lowest friction pressure (133 MPa) has the minimum heat input into the interface reaching approximately the estimated maximum weld line temperature after about 9.3 s. In contrast, for the highest pressure in the range (277 MPa), in which frictional heat input is the highest, the estimated maximum weld line temperature (1250 °C **which is considered nil ductility temperature of the alloys during compression explained in Chapter 3**) is obtained after 2.2 s.

As shown in Figure 2.2 (Masoumi et al., 2019), the estimated maximum weld line temperature for LFW of AD730<sup>TM</sup> (1250 °C) were obtained after 5.8 and 2.5 s by applied threshold (187.5 MPa) and optimum (285 MPa) friction pressures, respectively. However, in the case of LFW of IN718, this temperature can be obtained after 4.7 s and 2 s by applying 187.5 MPa and 285 MPa (Yellow line in Figure 2.1), respectively.

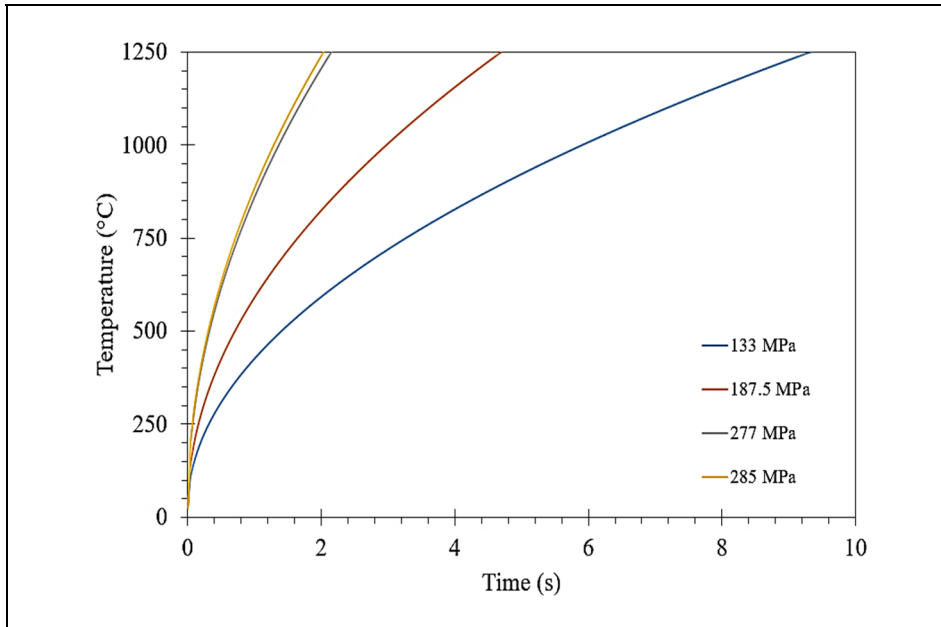


Figure 2.1 Calculated temperature variation with time for different LFW process parameters of IN718 superalloy

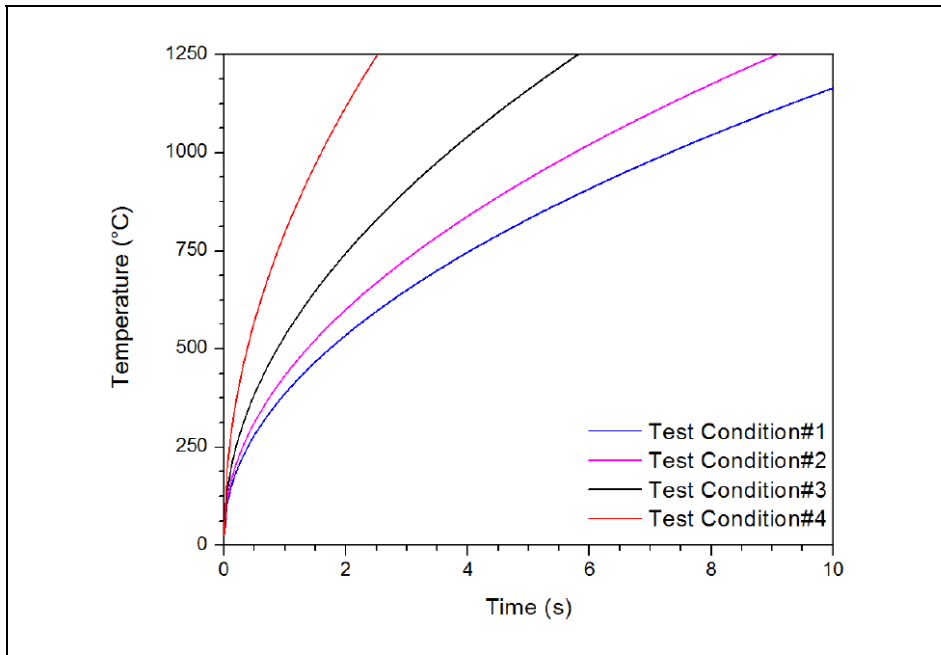


Figure 2.2 Calculated temperature variation with time for different LFW process parameters of AD730™ superalloy. Test 1: 133 MPa, Test 2: 150 MPa, Test 3: 187.5 MPa, and Test 4: 285 MPa  
Taken from Masoumi et al. (2019, p. 108)

As mentioned in chapter 1, the main process parameters are determined. The increasing rubbing velocity which causes a slight increase of the heat input (Eqs. 1.7 and 1.8), temperature, plastic deformation, and removal rate of oxide layers from the contact surface during oscillation and fractioning. Therefore, the rubbing velocity must be kept as a maximum value to form a LFW joint. According to TWI approval, the maximum values were selected for oscillation amplitude ( $a = 3$  mm) and frequency ( $f = 40$  Hz) within the operating window of the LFW machine. Figure 2.3 shows the 1D time-temperature estimation for LFW of IN718 (i.e., as a material with lower strength at high temperatures) at different friction pressures:

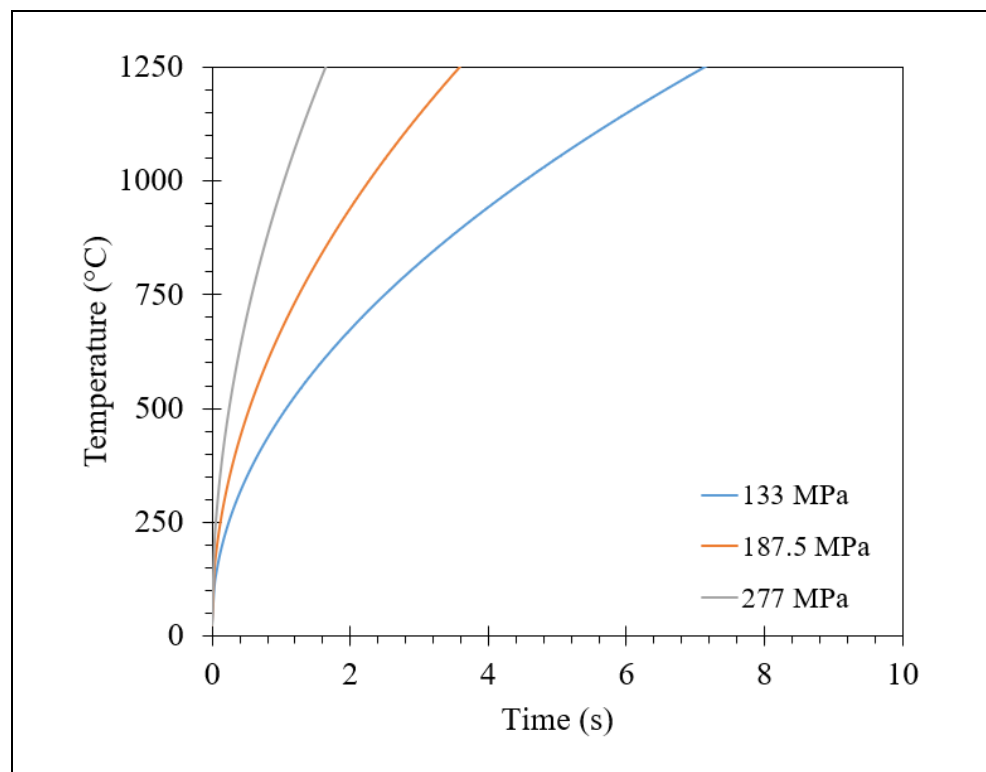


Figure 2.3 Temperature variation with time for different LFW process parameters of IN718 superalloy at  $a = 3$  mm and  $f = 40$  Hz conditions

According to Figure 2.3, during LFW of IN718, the maximum temperature ( $1250$  °C) at the weld interface with applying friction pressures 133 MPa, 187.5 MPa, and 277 MPa can be obtained after 7.1 s, 3.6 s, and 1.7 s, respectively. During LFW of AD730<sup>TM</sup> in these new

conditions, Figure 2.4 illustrates that this temperature is reached after 8.5 s, 4.3 s, and 2 s, respectively.

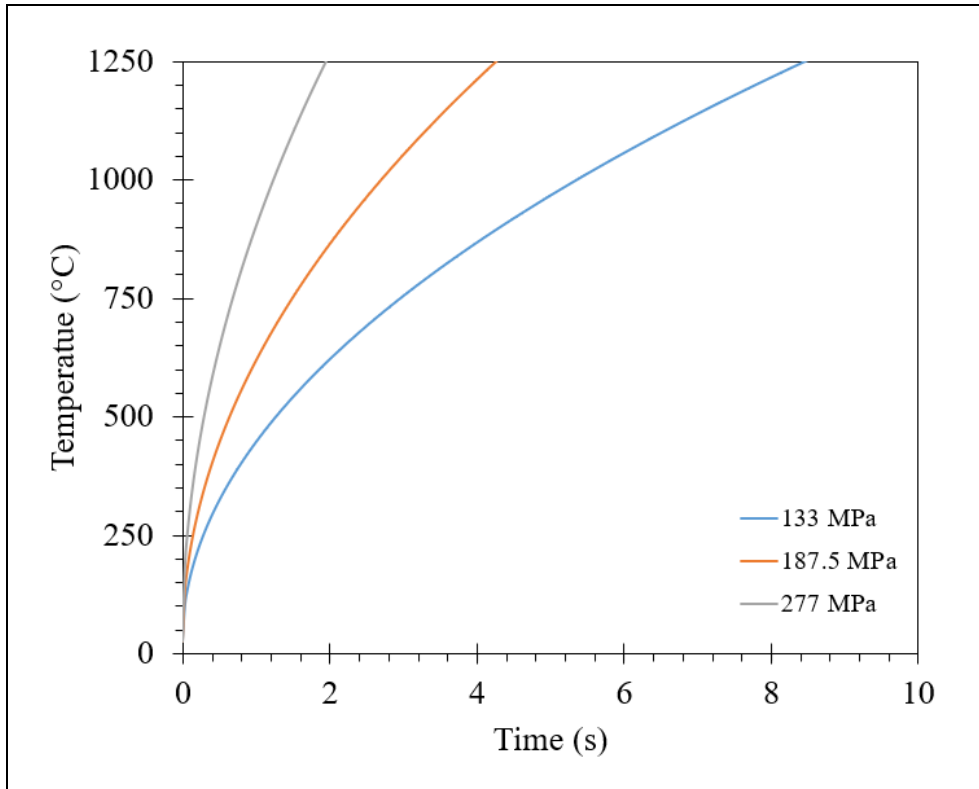


Figure 2.4 Temperature variation with time for different LFW process parameters of AD730<sup>TM</sup> superalloy at a = 3 mm and f = 40 Hz conditions

As reported by Masoumi et al. (Masoumi et al., 2019), the axial shortening should be in the range of ~ 2- 4 mm in order to produce a high quality joint for AD730<sup>TM</sup>. The axial shortenings that they achieved were ~ 2 mm and 3.1 mm by applying 187.5 MPa and 285 MPa as friction pressures; respectively and applied 265 MPa and 580 MPa as forge pressures, respectively.

The above analyses confirm that the proposed 1D analytical thermal analysis can be used to predict the temperature reasonably well, by taking into account the friction time. However, 2D or 3D numerical simulations are recommended to be employed to predict more accurately the axial shortening. In order to achieve that range of axial shortening and the maximum temperature at the interface of dissimilar LFW of SLM IN718 to AD730<sup>TM</sup>, according to the

optimum conditions during the friction stage for AD730<sup>TM</sup> (2.5 s), we need the friction pressure more than 187.5 and less than 277 MPa (i.e., to avoid liquation and melting at the interface). Regarding the successful joint after LFW of AD730<sup>TM</sup> after 10 s and thermal gradient in 3 directions, the processing time is estimated to be between 2.5 s and 10 s. Therefore, LFW parameters are defined in Table 2.1 and Table 2.2:

Table 2.1 Estimation of Linear friction welding parameters to use for SLM IN718 and AD730<sup>TM</sup> superalloys

Size (mm) (L-W-H)	Welding Area	Oscillation Direction	a (mm)	f (Hz)	Friction pressure (MPa)	Time of process (s)	Forge pressure (MPa)
26-13-37	L-W	L	2.5	40	133-277	2.5-10	265-404

Table 2.2 Linear friction welding parameters determined and used for SLM IN718 and AD730<sup>TM</sup> superalloys

Size (mm) (L-W-H)	Welding Area	Oscillation Direction	a (mm)	f (Hz)	Friction pressure (MPa)	Time of process (s)	Forge pressure (MPa)
26-13-37	L-W	L	3	40	220	10 (max)	390

The final parameters have been used by TWI Co. are changed for this dissimilar LDW due to the technical limitations. However, those used values are in the range of estimation Table 2.3.

Table 2.3 Final LFW parameters used by TWI Co. according to the estimation

Size (mm) (L-W-H)	Welding Area	Oscillation Direction	a (mm)	f (Hz)	Friction pressure (MPa)	Time of process (s)	Forge pressure (MPa)
26-13-37	L-W	L	3	40	228	15.4*	340

\* 7.7 s for friction stage and 7.7 s for forge stage.

The schematic of the processing stages and the details of the processing parameters are shown in Figure 2.5. The axial shortening after welding was 3.3 mm for both cases of LFWed SLM IN718 to AD730<sup>TM</sup> and homogenized SLM IN718 (H-SLM) to AD730<sup>TM</sup>.

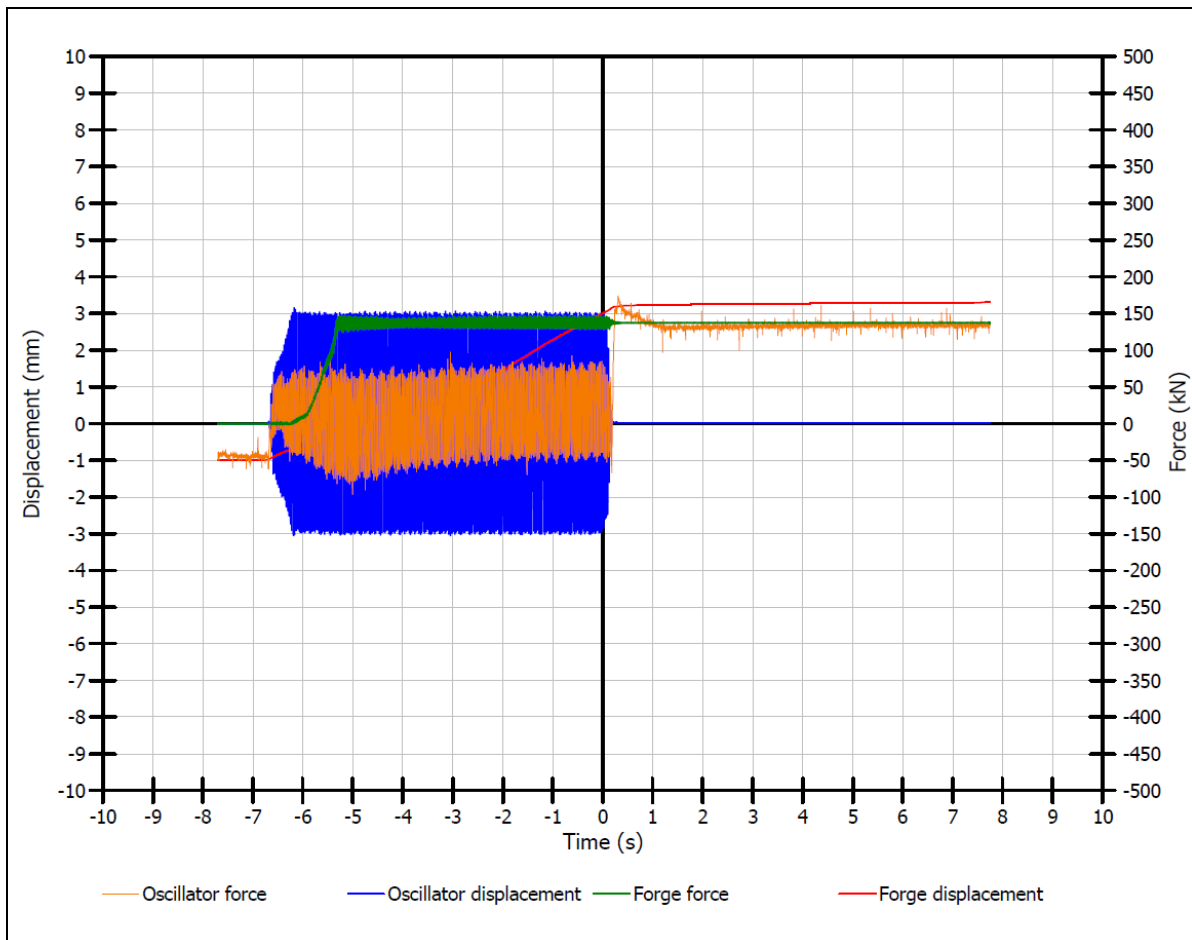


Figure 2.5 Linear friction welding cycle for dissimilar SLM IN718 to AD730<sup>TM</sup>

Figure 2.6 shows temperature variation at the weld interface versus time after applying friction pressure (228 MPa). It shows the maximum temperature could be achieved after  $\sim 2.5$  s. After time 7.7 s, the temperature at the weld interface of AD730<sup>TM</sup> and IN718 alloys, should reach 2027 °C and 2208 °C, respectively. Although the  $T_M$  in both alloys is between 1340-1365 °C, no melting and liquation were observed during LFW. As reported for LFW of forged IN718 (M. M. Smith, 2017b) and LFW of Waspalloy (Ahmad Chamanfar et al., 2015; A Chamanfar, Jahazi, Yue, Gholipour, & Wanjara, 2009) (same thermophysical properties for both alloys in

this study), the temperatures measured by the IR camera (with an indium antimonide detector) and thermocouples (K type) showed 1240 °C and 1220 °C; respectively, at the weld interface. It reveals that there is around 780-950 °C difference between the 1D estimation and the practical conditions due to the 3D thermal gradient and friction coefficient ( $\mu$ ), which change with temperature (i.e.,  $\mu$  reduces when the temperature increases).

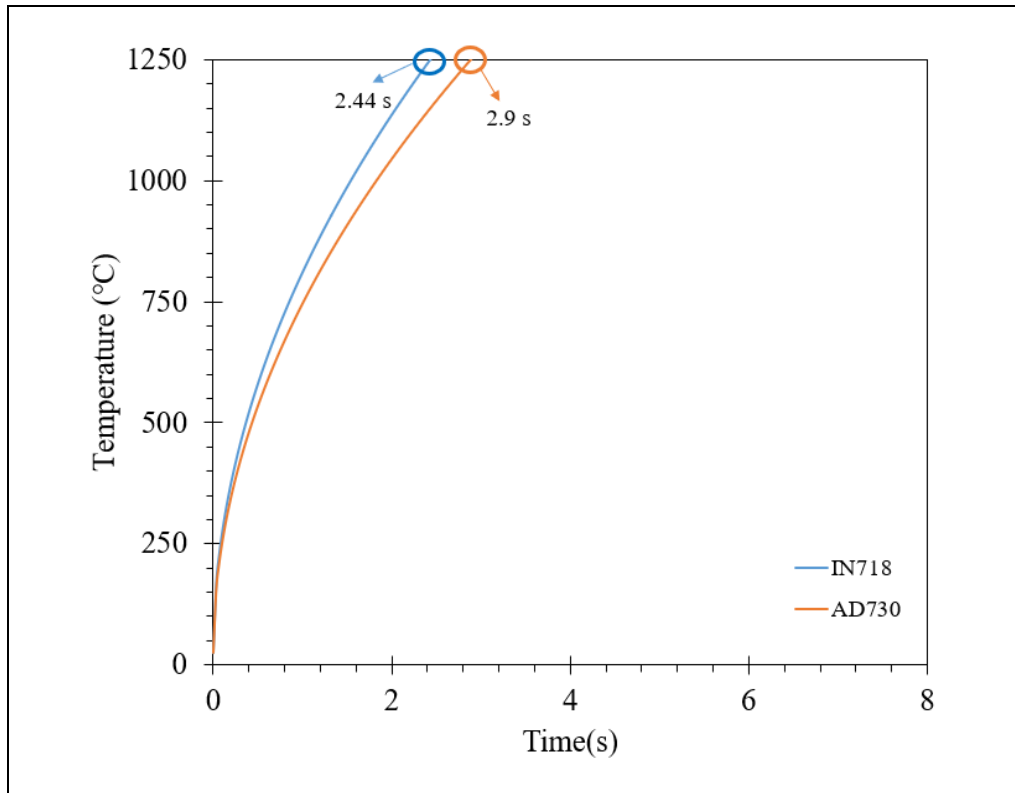


Figure 2.6 Variation of temperature as a function of time at the weld interface by applying friction pressure 228 MPa for 7.7 s

Considering this temperature difference ( $\sim 950$  °C for IN718 and  $\sim 780$  °C for AD730<sup>TM</sup> alloy) between the 1D estimation conditions and the expected real LFW conditions (due to the 3D thermal conductivity and variation of  $\mu$  with temperature), as well as assuming the maximum temperature range (1200-1250 °C) in the weld line, the temperature variation as a function of distance can be evaluated at a distance of 1 mm from the weld line (Figure 2.7). As a result, the microstructures, on both sides of the joint, were affected by thermal gradient and temperature distribution induced by heat generated at the weld line.

Therefore, the temperature distributions in near the LFW line and predicted values using the proposed 1D thermal analysis for two different superalloys, Waspaloy and GH4169 (Chamanfar et al., 2011a; Yang et al., 2015) show a reasonable agreement exists between the predicted values (as a possible maximum temperature at the weld line) and the measured ones (an error of about 3%) thereby confirming the good predictability of the 1D thermal model in the present investigation.

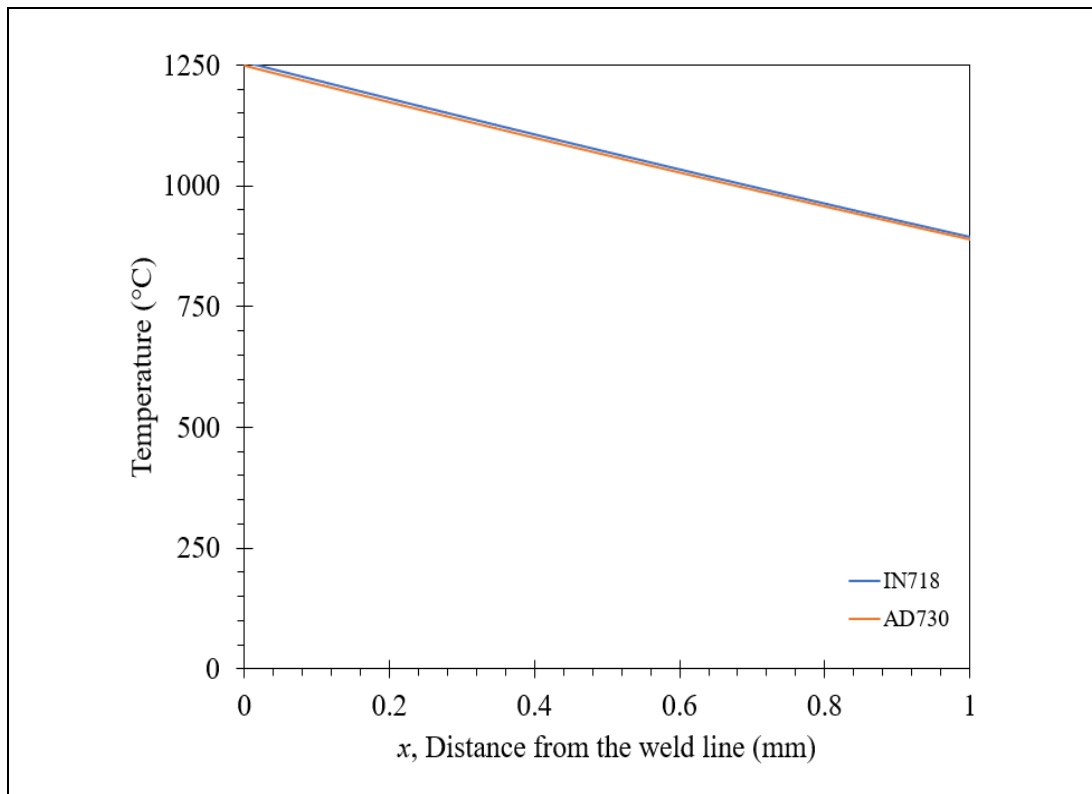


Figure 2.7 Temperature distribution along the x-axis with applied friction pressure 228 MPa after 7.7 s

## CHAPTER 3

### HOT DUCTILITY BEHAVIOR OF AD730™ NICKEL-BASED SUPERALLOY

Syedmohammad Tabaie <sup>a</sup>, Davood Shahriari <sup>a</sup>, Cléa Plouze <sup>a</sup>, Alexandre Devaux <sup>b</sup>, Jonathan Cormier <sup>c</sup>, Mohammad Jahazi <sup>a</sup>

<sup>a</sup> Department of Mechanical Engineering, École de Technologie Supérieure,  
1100 Notre-Dame West, Montreal, QC, Canada.

<sup>b</sup> Aubert & Duval, Site des Ancizes, BP1, 63770 les Ancizes Cedex, France.

<sup>c</sup> Département de Physique et Mécanique des Matériaux Institut Pprime, CNRS-ENSMA-  
Université de Poitiers, UPR CNRS 3346 Futuroscope-Chasseneuil Cedex, France.

Paper published in *Materials Science and Engineering: A*, September 2019

#### Abstract

Hot ductility of the newly developed AD730™ nickel-base superalloy was investigated in the temperature interval 1050-1240 °C. The nil strength and nil ductility temperatures were determined by hot tensile testing using the Gleeble™ 3800 weld thermal simulation method. The influence of heating rate, representing the weld thermal cycle, on hot ductility behavior of the alloy was also investigated. The microstructure and the fracture mode of samples were examined by optical and scanning electron microscopy. The influence of heating rate on the extent of grain boundary liquation and void formation was determined and it is shown that the significant ductility loss near the NDT point could be related to the reduction of surface tension at the grain boundary-matrix interface. In addition, the contribution of hard precipitates, such as grain boundary MC carbides, voids, and cavities as other damage mechanisms responsible for ductility loss at high temperature, are discussed.

**Keywords:** Hot Ductility Test; Nil Ductility Temperature; Nil Strength Temperature; Void Formation; Liquation.

### 3.1 Introduction

Investigations on hot-ductility behavior of materials are used to evaluate the susceptibility of an alloy to cracking at elevated temperatures, during solidification, hot deformation, or welding (J.L.Caron & J.W.Sowards, 2014). Considering that nearly all engineering alloys go through the above manufacturing processes; it is therefore of critical importance to quantify and better understand their hot ductility behavior. Nil ductility temperature (NDT) and nil-strength temperature (NST) are two key parameters when studying the hot ductility of metallic systems (Z. Huang, Shun, & Yao, 1990; Mandziej, 2005). NDT has been defined as the temperature at which the material experiences significant ductility drop (e.g. reduction in area) during tensile testing and NST is the temperature at which the alloy, under the effect of a very small constant tensile load, loses its strength (Z. Huang et al., 1990; Mandziej, 2005). NST is located in the temperature interval between the NDT point and the liquidus temperature ( $T_L$ ) and corresponds to the point where the alloy loses its strength (C.-W. Li, Yeh, Chen, & Wang, 2015; Montazeri & Ghaini, 2012; Ojo & Chaturvedi, 2005).

Segregation of solutes and formation of precipitates along grain boundaries have been identified as the main causes of ductility loss at high temperatures (Joel Andersson et al., 2010; Y. C. Lin, Deng, Jiang, Wen, & Liu, 2014b; Mejía, Bedolla-Jacuinde, Maldonado, & Cabrera, 2011; Qu et al., 2011; Raj & Ashby, 1975; Z. L. Zhao, Ning, Guo, Yao, & Fu, 2015). Therefore, alloy systems with a large number of alloying elements in their composition and microstructure are prone to hot cracking. Superalloys, as the most performant high temperature alloys, and particularly modern nickel-based superalloys have sometimes up to fifteen alloying elements in their composition and several types of precipitates and are therefore highly sensitive to hot cracking during forging or Heat Affected Zone (HAZ) liquation cracking of welded structures (Cieslak, Stephens, & Carr, 1988; J.L.Caron & J.W.Sowards, 2014; Noecker & DuPont, 2009; Qian & Lippold, 2002, 2003b; Ramirez, 2012).

Mejia et al. (Mejia et al., 2011) observed that hot ductility of an advanced high strength steel (AHSS) was mainly controlled by deformation induced matrix and grain boundary sliding by formation of the thin pro-eutectoid ferrite layer and the precipitation of carbides or nitrides particles at the austenite grain boundaries. Lee et al. (Lee, Um, Kim, Choi, & Lee, 2004) reported that the severity of the ductility loss of a GTD111 and Inconel 738LC (IN738LC) superalloys were dependent on the degree of grain boundary wetting due to constitutional liquation of MC carbide precipitates. Qian and Lippold determined NDT and NST points of Inconel 718 (IN718) (Qian & Lippold, 2003b) and Waspaloy (Qian & Lippold, 2002) and reported that MC-type carbide constitutional liquation and segregation induced grain boundary liquation are responsible for HAZ liquation cracking behavior. They considered that the grain size and grain boundary characteristics are the two primary factors influencing HAZ liquation cracking. Knock et al. (Knock, 2010) studied the weldability of IN718 and the fracture surfaces of samples after NDT and NST. They observed many carbides and voids in fracture surface which caused failure at NDT and NST points. Ramirez (Ramirez, 2012) reported on Inconel 740 susceptibility to liquation cracking and ductility-dip cracking and found NDT and NST for the alloy. Anderson et al. (Joel Andersson et al., 2010) investigated the hot ductility of Haynes 282 alloy using low heating rates with different solution heat treatments conditions. They found that the on-heating ductility drop occurred because of liquation of secondary phases and melting point depressant elements for all the applied heating rate. However, in the above studies, most, if not all, the heating rates used for the investigations were very low and are not well representative of the heating rates encountered during real welding conditions (100-400 °C/s (Ahmad Chamanfar et al., 2015; Masoumi et al., 2019; M. Smith et al., 2016; M. M. Smith, 2017b)), whether solid state such as Linear Friction Welding (LFW) or fusion welding.

In recent years with the advent of new manufacturing technologies, LFW has been considered as a very competitive technology for producing blade integrated disks (Blisks) compared to the conventional fir-tree disk-blade mechanical assembly (Caroline Mary & Jahazi, 2006; Nunn, 2005; Vairis & Frost, 2000). LFW is a solid-state joining process during which through the generation of frictional heat and application of a forge pressure, the mating interface is brought

to high temperature, high strain plastic deformation ( $1-20 \text{ s}^{-1}$ ) (Ahmad Chamanfar et al., 2015; Masoumi et al., 2019; M. Smith et al., 2016; M. M. Smith, 2017b), and welded together. Despite the fact that no melting is expected to occur at the interface; however, due to the large number of alloying elements in the composition of superalloys, liquation cracking could occur under some processing conditions resulting in significant ductility loss and produce unacceptable weld defects or even fracture. Specifically, weld regions between the HAZ and the weld line are prone to crack susceptibility due to possible liquation or void formation as a result of rapid and uneven thermal cycles (Caron & Sowards, 2014).

In the present work, the influence of some LFW process parameters (high temperature and high heating rate) on hot ductility behavior of a new generation nickel-based superalloy, AD730<sup>TM</sup> intended for blisk applications will be investigated. Specifically, the NDT and NST temperatures were determined, the fracture surfaces of the samples were examined and possible governing mechanisms for the observed behaviors are discussed. It should be mentioned that despite the above-mentioned studies on hot ductility loss of superalloys, few or none of them consider conditions similar to the ones observed during LFW and very few of them correlate the NDT and NST temperatures with the fracture surface of the alloy.

### **3.2 Materials and Experimental Method**

The AD730<sup>TM</sup> alloy was provided by Aubert & Duval. The alloy was produced through ingot casting using vacuum induction process followed by vacuum arc remelting and finally radial forging to produce a bar-round billet with a diameter of 86 mm (Fig. 3.1). An 84 mm in diameter and 110 mm in length bar was then cut from the center of the billet for the study. The bar was solutionized at 1080 °C for four hours followed by air cooling.

The chemical composition of the studied material is given in Table 3.1. The microstructure of the alloy is shown in Fig. 3.2 with an average grain size of  $51.36 \pm 9.14 \text{ }\mu\text{m}$  and  $\gamma'$  volume fraction of 40% (Devaux et al., 2014; Pérez, Dumont, Nodin, & Nouveau, 2018).

Table 3.1 Chemical composition of AD730™

Element	Ni	Fe	Cr	Co	Al	Ti	Mo	W	Nb	C
Wt. %	Bal.	4	15.8	8.0	2.4	3.8	2.9	2.0	1.2	0.02
At. %	Bal	4.08	17.31	7.73	5.07	4.52	1.72	0.62	0.74	0.094

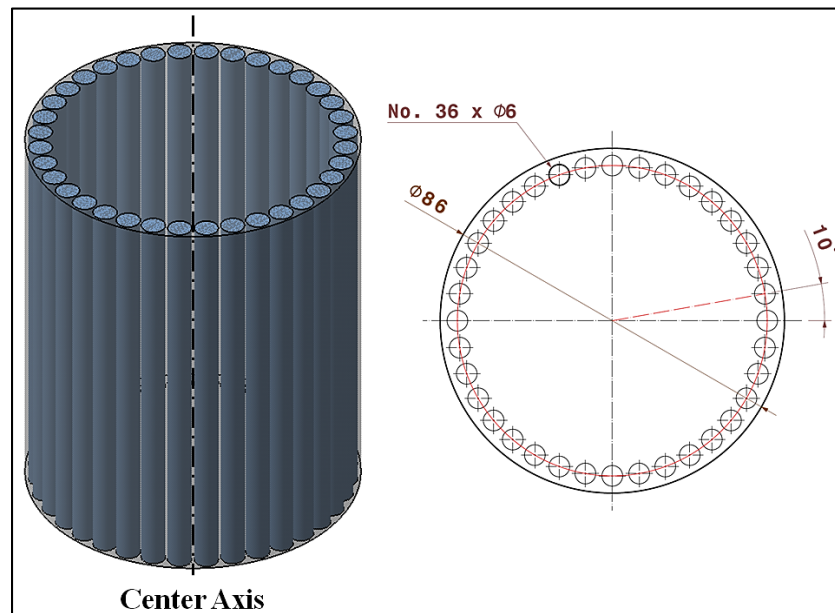


Figure 3.1 NDT and NST sample location in the as forged billet

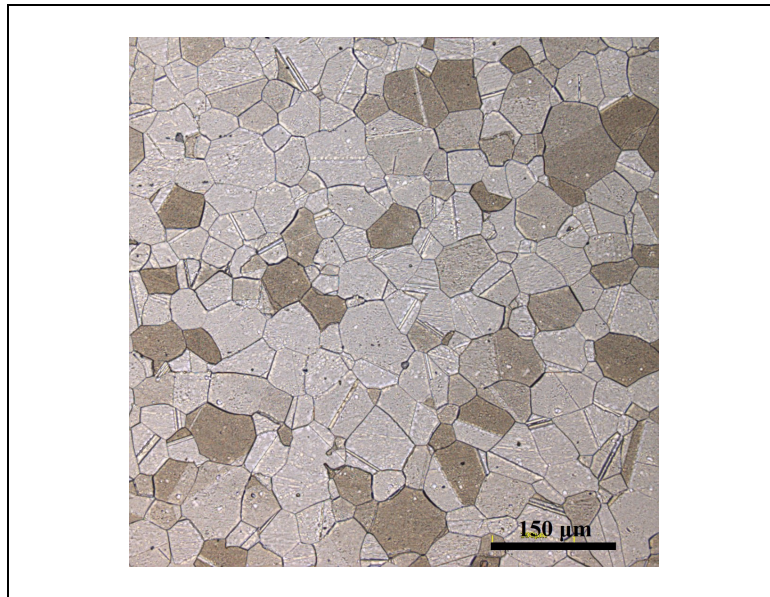


Figure 3.2 Initial microstructure of AD730<sup>TM</sup> superalloy

For NST and NDT experiments, 10 mm diameter and 120 mm long rods were prepared from the external diameter of the bar using electro discharge wire cut machining (wire-EDM). Figure 3.1 displays a schematic view of the bar and the location of the machined rods along with their dimensions.

The determination of the NDT and NST temperatures was made using the Gleeble<sup>TM</sup> 3800 thermomechanical simulator. Heating rates in the range, 5-100 °C/s in the temperature interval of 1050-1240 °C and a strain rate 2.5 s<sup>-1</sup> were used for the test, which were all carried out under vacuum. The thermal cycle consisted of two distinct steps: the heating and the cooling cycle. In the heating step, the heating rate, the peak temperature, and the holding at peak temperature were controlled with high precision (less than 0.2% variation) using the advanced control system of the Gleeble machine. During the cooling step, cooling rate and holding time at test temperature needed to be precisely controlled. A pair of specially designed grips was used in order to increase the accuracy of the results during testing and reduce to a minimum the temperature gradient along the sample gauge length.

Two series of tests with different sample geometries and experimental setup was conducted for the determination of the NST and NDT. For NST tests, 75 mm long and 6 mm diameter samples were used in a setup in the Gleeble<sup>TM</sup> system as shown in Figure 3.3. A pneumatic actuator equipped with the nil strength jaw system was employed to apply a nominal tensile loading of 90 N. This small load was applied before heating and was kept constant throughout the test until the fracture of the specimen. R-type thermocouple wires were welded within the span zone, in the middle of the sample. Samples were then heated in vacuum at  $10^{-6}$  torr using alternated current with heating rates of 5 °C/s, 25 °C/s, 50 °C/s, and 100 °C/s until rupture. The measured temperature at the rupture point is the NST of the alloy.

For the NDT tests (i.e. hot ductility tests), different specimen size and geometry as well as machine setup, as schematically illustrated in Figure 3.4 were used. The maximum peak temperature was selected approximately 50 °C lower than the determined NST. The specimens were heated therefore to temperatures in the range 1050°C-1240°C at a constant heating rate of 100 °C/s followed by two seconds holding time before it was strained at a rate of 125 mm.s<sup>-1</sup> ( $\sim 2.5$  s<sup>-1</sup>) until failure. Figure 3.5 shows the testing procedures used for the determination of the nil strength temperature and the hot ductility behavior of the AD730<sup>TM</sup> alloy.

Both NST and NDT experiments were repeated at least three times to validate repeatability of the results and the mean value were used for subsequent analyses. The fracture area was measured after each experiment using a digital caliper as well as profilometer to ensure accuracy and the average of the readings was considered as the reduced diameter of the fractured sample. In agreement with other published works, the limit of 5% reduction area was considered as the criteria for the determination of the NDT point (Mandziej, 2005).

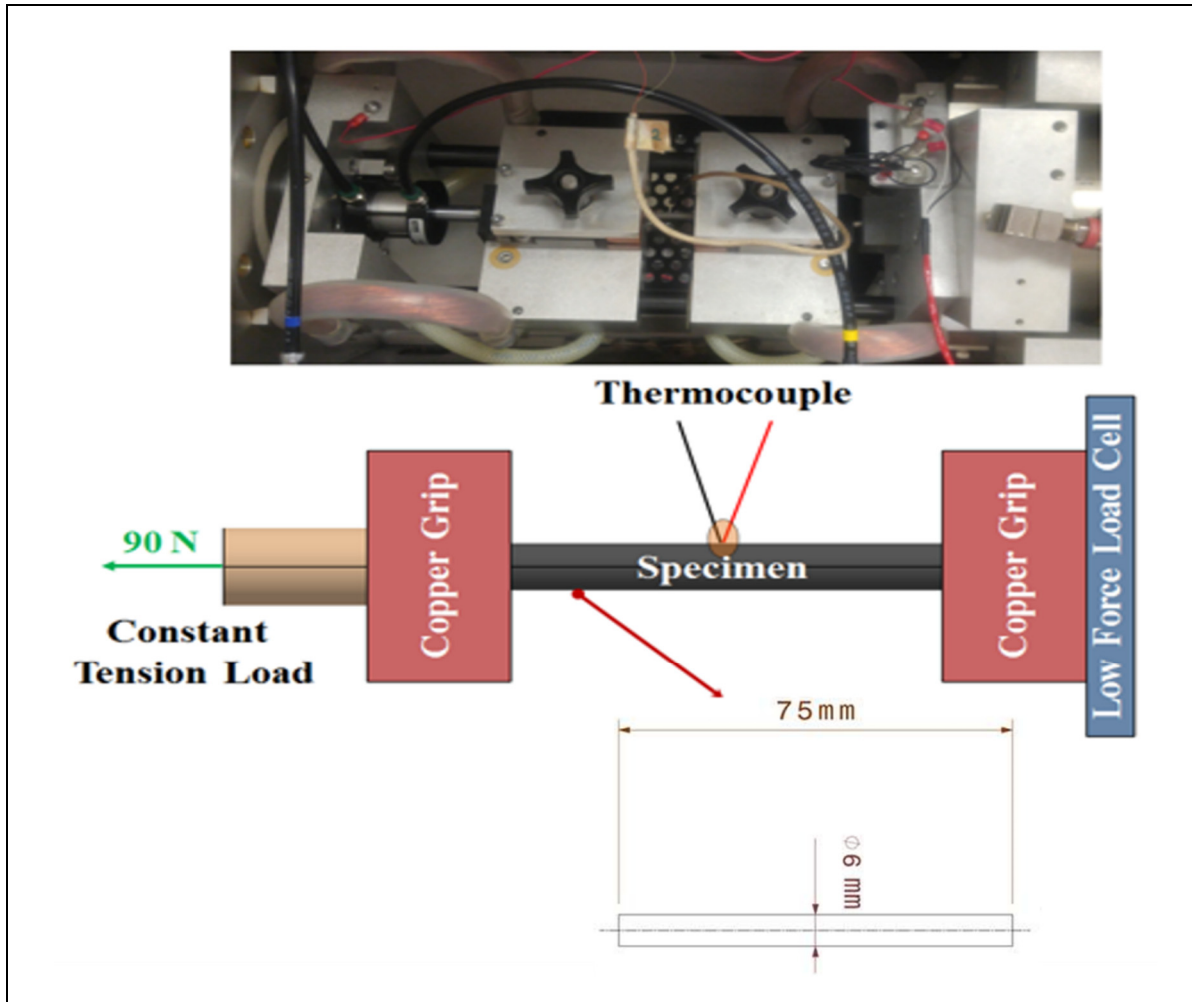


Figure 3.3 Gleeble™ 3800 physical simulator setup and adapted geometry for determining nil strength temperature. Using a special actuator allows maintaining a constant 90 N tensile load on sample throughout experiment. The specimen dimensions are 75 mm long and 6 mm diameter

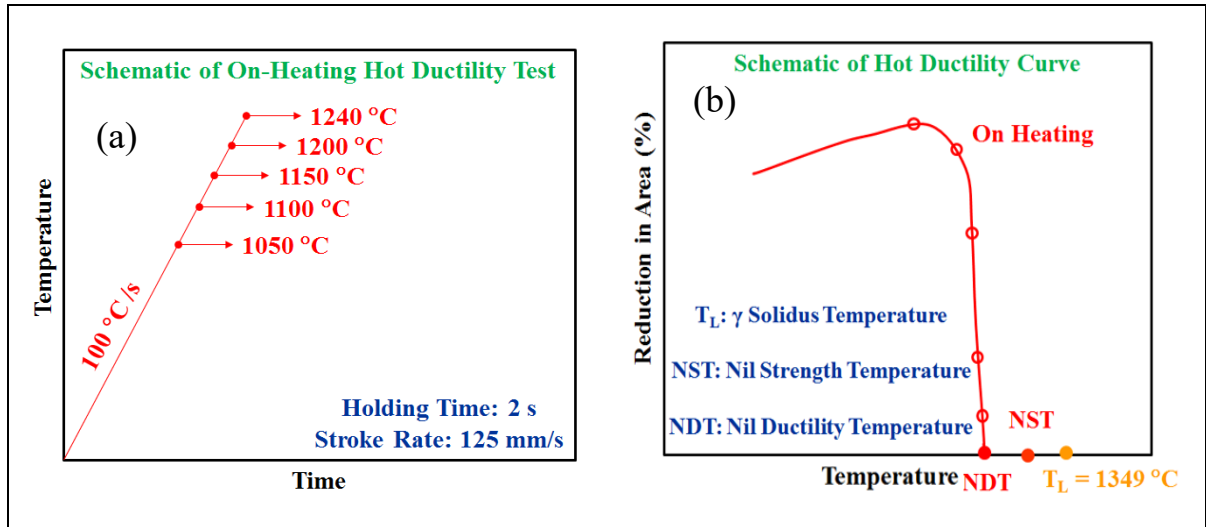


Figure 3.4 Schematic of Gleeble™'s procedure for hot ductility testing, (a) on-heating hot tensile test with constant heating rate, holding time and stroke rate at different temperature. (b) hot ductility curve with respect to testing temperature; note that the NDT is lower than the NST and  $\gamma$  solidus temperature of AD730™

The NST and NDT specimens were characterized using optical microscopy (OM) and scanning electron microscopy (SEM, TM3000, Hitachi) as well as the energy dispersive spectroscopy (EDS) technique in order to investigate fracture surface morphology, microstructural evolution, and chemical composition analysis. Examination of the NST and NDT samples was conducted in the transverse and longitudinal directions. The samples for OM and SEM observations were prepared using standard metallographic procedures and chemically etched in Kalling No.2's reagent (CuCl<sub>2</sub>: 5 g, HCl: 100 ml, and ethanol: 100 ml). The growth, coalescence and fraction of voids at the fracture surface of NST samples were determined according to ASTM standard, E1382-97 (ASTM-International, 2015) via images taken at 200× and 500× magnifications by OM and SEM. Digitized OM and SEM images were processed using GIMP and ImageJ software to quantify the size and fraction distribution of voids.

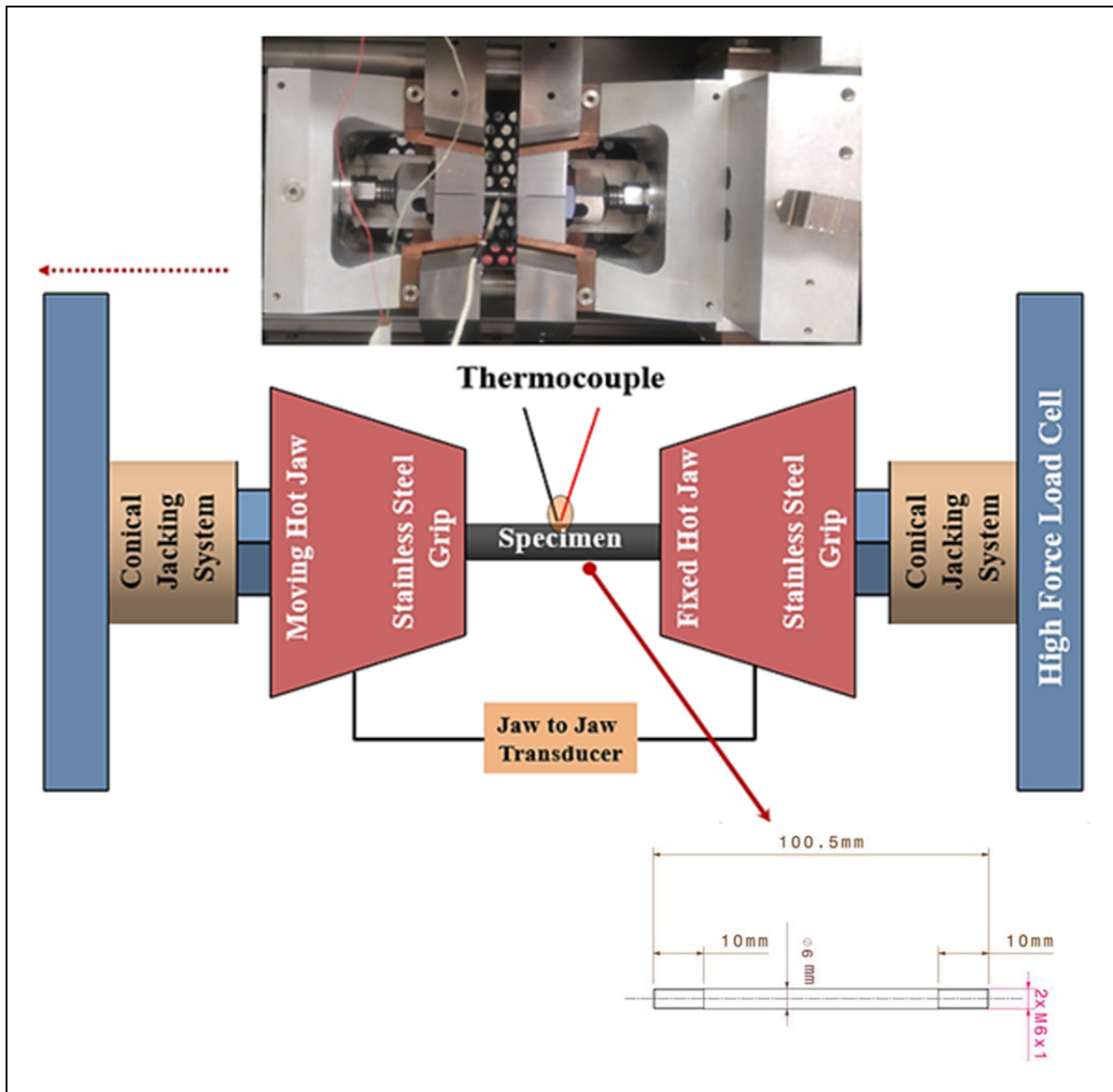


Figure 3.5 Gleeble<sup>TM</sup> 3800 physical simulator setup and adapted geometry for conducting hot ductility testing. Large load cell is used on the high force jaw system and the lengthwise change is controlled by longitudinal transducer

### 3.3 Results and Discussion

#### 3.3.1 Nil strength temperature

The NST was measured during on-heating experiments using four different heating rates and the obtained results were compared with the published NST of IN718 and Waspaloy (Qian, 2001; Qian & Lippold, 2003b), as shown in Figure 3.6. The lowest NST (1280 °C) was obtained for the heating rate of 5 °C/s and the highest (1295 °C) for the fastest heating rate of 100 °C/s. For the intermediate heating rates of 25 and 50 °C/s the NST values were very similar varying in the range 1289 °C and 1291 °C. The average NST value for AD730<sup>TM</sup> alloy was therefore determined to be 1290 °C. The nominal temperature tolerance during all the experiments was in the range of  $\pm 1$  °C.

Knorovsky et al. (Knorovsky, Cieslak, Headley, Romig, & Hammett, 1989) and Knock (Knock, 2010) reported that the average NST point for as-received IN718 for a heating rate similar of about 110 °C/s was 1276°C. Qian (Qian, 2001) reported an average value of 1302°C for Waspaloy in the as received condition and a heating rate of about 110 °C/s (From the literature no error bars given). It can be seen that the NST points of IN718 and Waspaloy are in the same range as the one determined for AD730<sup>TM</sup>. Differences in chemical composition and applied heat treatments are probably the main reason for the observed variations in NST values between the three alloys. For instance, Boron rich constituents and grain boundary liquation were more salient in NST samples of IN718 (Knock, 2010; Knorovsky et al., 1989) and Waspaloy (Qian, 2001). Furthermore, variation in heat treatment cycles may result in grain boundary segregation and/or increase the fraction of some secondary phases (e.g.  $\delta$ -phase in IN718) increasing the propensity for grain boundary liquation during nil strength experiments (Chou & Chao, 1988; Qian, 2001; Qian & Lippold, 2003b). On the basis of the obtained results, it could be said that the NST value does not seem to be very sensitive to the heating rate and that variations are more sensitive to chemical composition and thermal cycle applied to the alloy.

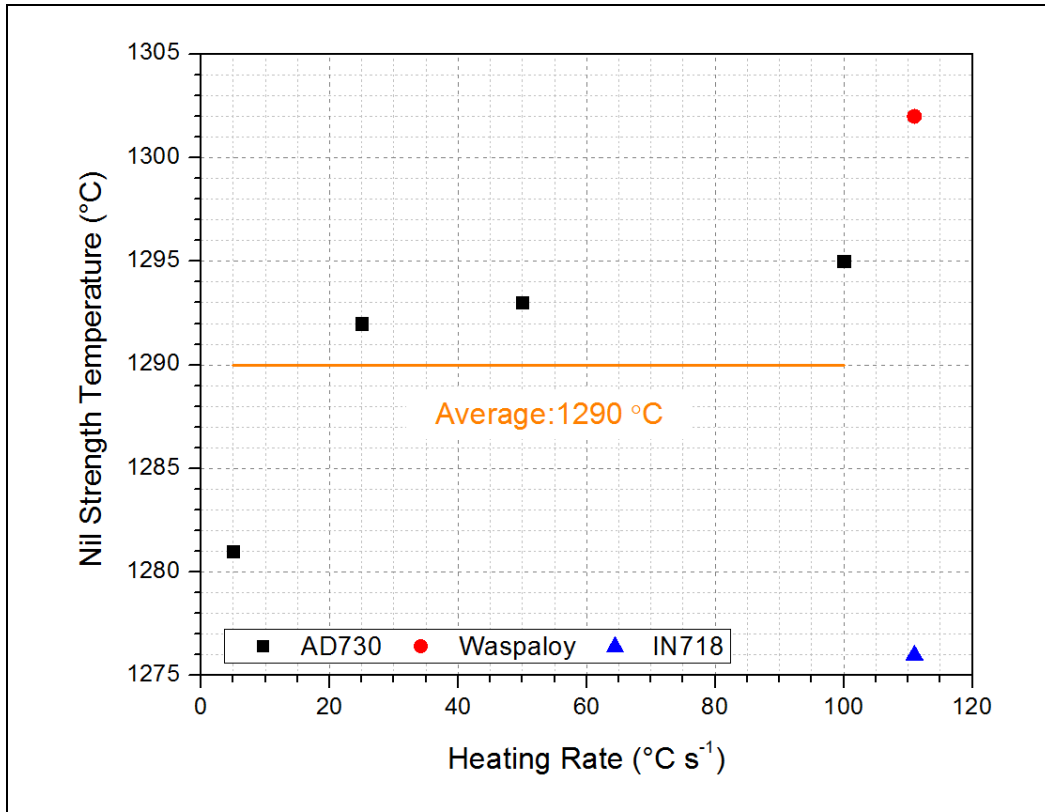


Figure 3.6 Variation of the NST point of AD730<sup>TM</sup> with heating rate when compared to the NST of IN718 and Waspaloy

### 3.3.1.1 Fracture surface analysis

Illustrative examples of the fracture surface of the NST samples are shown in Fig. 3.7a-d. A large number of voids were observed on the surface of the samples, as indicated by in each figure. The samples were fractured at high temperature (near to the melting point) at which the alloy had no ductility and strength. Examination of the fracture surface revealed a brittle characteristic with the presence of porosity, microvoids, and liquations for all four tested heating rates. Partial or total melting at the grain boundary was also observed in all samples, suggesting that the observed grain boundary cracks are the result of post-fracture liquid cooling. These findings corroborate with those reported by Knock in IN718 (Knock, 2010). It should be noted that liquation cracking is the forming, presence and persistence of liquid films at grain boundaries (GBs) and their inability to accommodate the thermally and/or

mechanically induced strain experienced during the loading at elevated temperature and weld cooling that subsequently reduce the grain boundaries strength (Qian & Lippold, 2002, 2003b).

Qian and Lioppold (Qian & Lippold, 2003b) reported that in IN718 alloy, boron carbide liquation produced a low melting eutectic, an extra low melting point constituent that further aggravates the liquation then led to cracking. Masoumi et al. (Masoumi et al., 2017) observed liquation in AD730<sup>TM</sup> and attributed it to the melting of carbides within GBs.

The porosities and voids observed in the above figures have been related to the application of stress during tensile test and the fracture phase through the creation of spaces as a result of grain boundary sliding or precipitate removal. Lin et al. (Y. C. Lin, Deng, Jiang, Wen, & Liu, 2014a) reported that interaction and accumulation of dislocations near the boundaries and particles result in strain concentration in these areas and leads to the nucleation of microvoids. In addition, the accumulation of slip bands in the boundaries causes the formation of voids; as a result, a loss of strength occurs due to decreased interface energy (Dieter, 1988). In the present work, the voids were counted and classified into different size categories to compare their distribution for each heating rate. Preliminary qualitative examination of the voids in different samples showed that at the heating rate of 5 °C/s (Fig. 3.7a), the number of microvoids is lower than the sample exposed to 100 °C/s (Fig. 3.7d); however, their sizes are significantly bigger indicating the occurrence of microvoid coalescence. An intermediate trend is observed for samples heated at 25 and 50 °C/s. Figure 8 shows the evolution of void size distribution as a function of heating rate obtained by counting the voids present on the fracture surface using ImageJ image analysis software. As mentioned in the experimental method section a total number of at least 50 voids were counted for the size estimation.

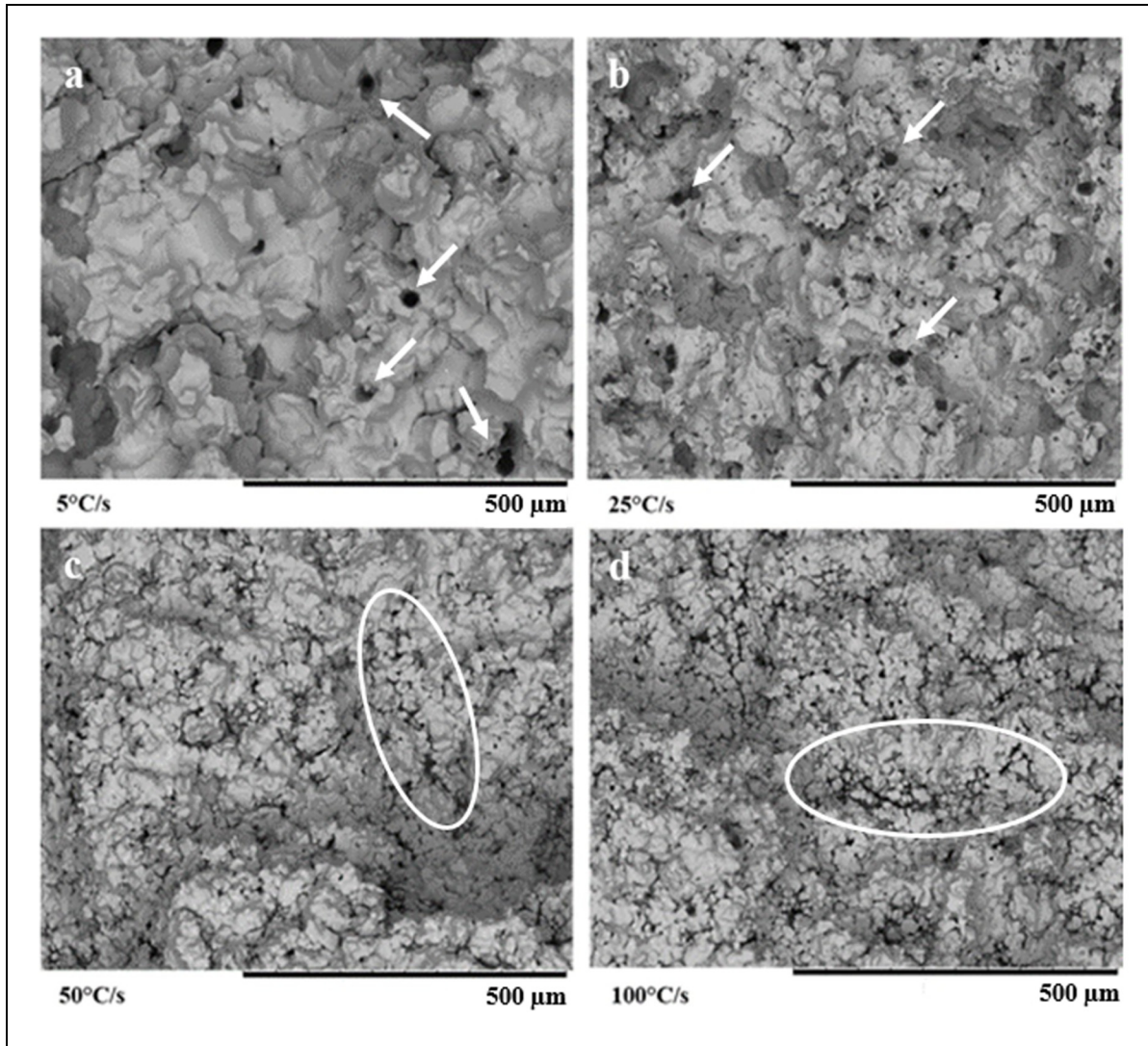


Figure 3.7 Fracture surface of NST samples at different heating rates. a) 5 °C/s, b) 25 °C/s, c) 50 °C/s, d) 100 °C/s. White arrows indicate the large voids and circled zones indicate small voids coalescence

As shown in Fig. 3.8, at higher heating rates (50 and 100 °C/s), the voids were smaller while by applying lower heating rates (5 and 25 °C/s), larger voids were formed (more than 100 μm). Considering the scatter in size distribution of the voids, they were categorized in two groups, from 0 to 10 μm and from 0 to 100 μm, and the results are shown in Figs. 3.9 and 3.10, respectively. As can be seen from these figures, a higher percentage of small voids with higher fraction could be associated to higher heating rates. In contrast, larger voids (20-100 μm) with lower fraction characterize the low heating rate conditions (5 and 25 °C/s) (Fig. 3.10). It should

be noted that applied temperature, heating rate (i.e., time factor) and stress are the main variables that affect the extent of damage during the test. For example, NST tests are characterized with a constant stress; however, at lower heating rates, more time is available and therefore, smaller voids coalesce into one another and form larger ones that cause damage. In contrast, as shown in Fig. 3.9, at higher heating rates the fracture surface is characterized by a large number of small voids indicating that nucleating was accelerated but there was not enough time for void growth under these conditions. The role of temperature, time, and applied stress on the nucleation rate and growth of voids will be discussed further in the upcoming sections.

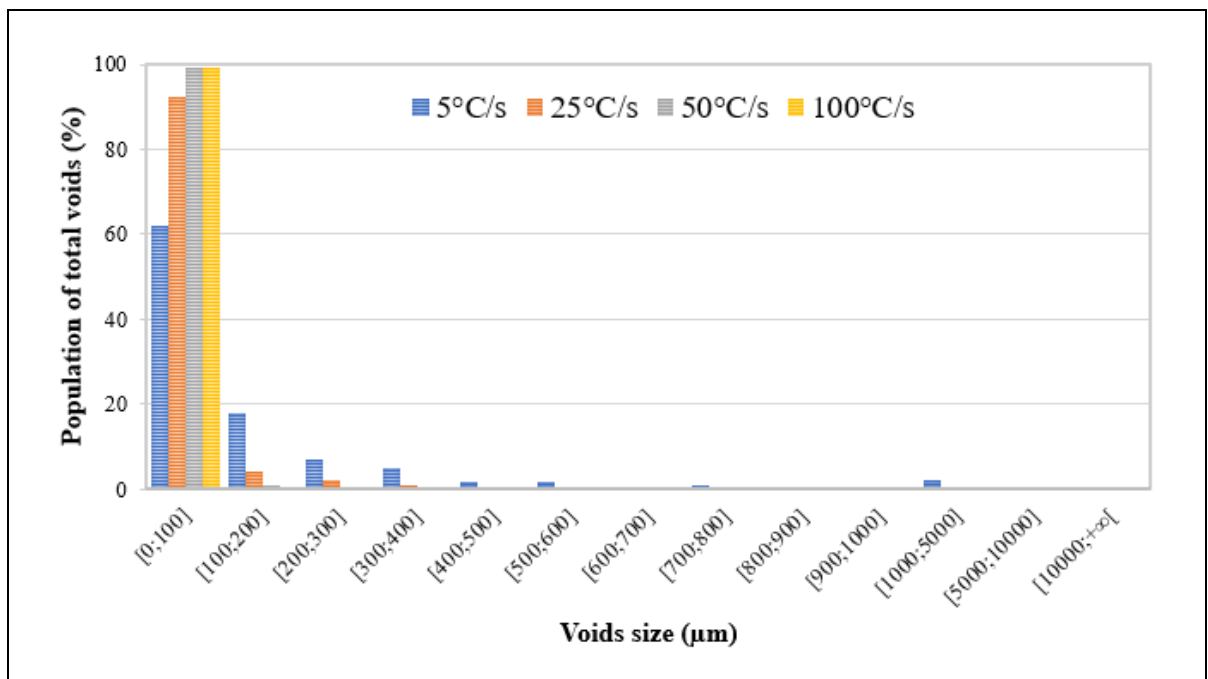


Figure 3.8 Voids fraction and size distribution as a function of the heating rate

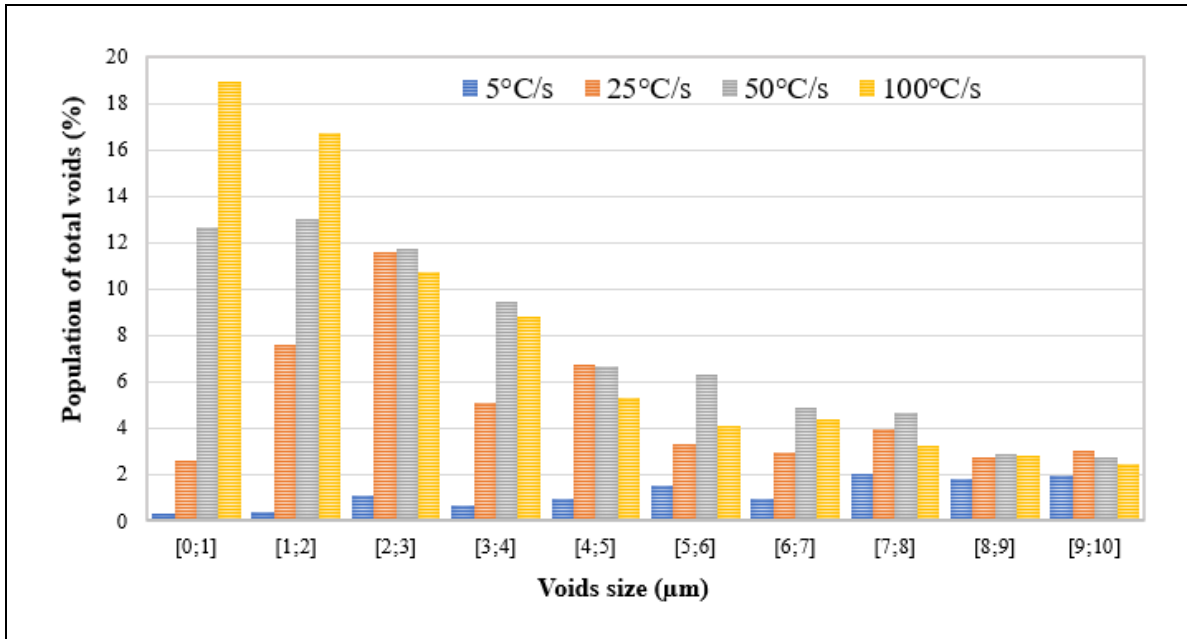


Figure 3.9 Distribution of void size fraction between 0 and 10 μm interval as a function of the heating rate

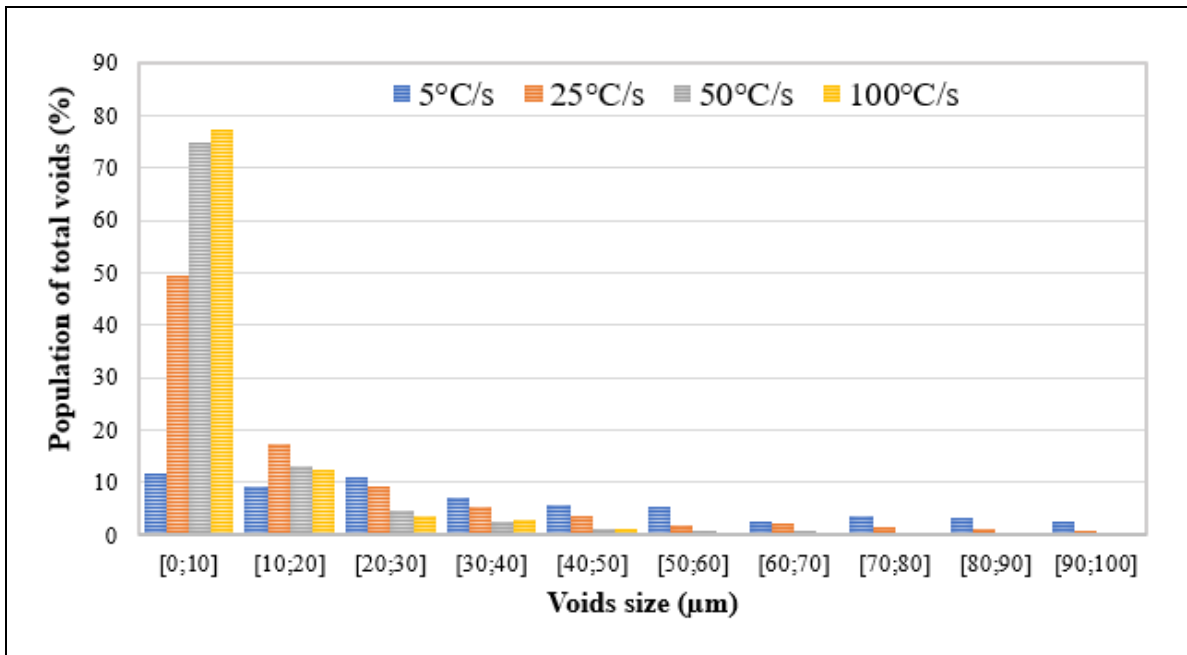


Figure 3.10 Distribution of void size fraction between 0 and 100 μm as a function of the heating rate

In the case of the investigated alloy, Masoumi et al. (Masoumi, Shahriari, et al., 2016a) observed that cavities initiated preferentially at the grain boundaries due to the nucleation of voids around the primary  $\gamma'$  or carbides. The NST results shown in Fig. 3.6 indicate that even for the lowest heating rate the NST (1280 °C) is above the dissolution temperature of primary  $\gamma'$  in AD730<sup>TM</sup> (1150 °C) (Masoumi, Jahazi, Cormier, & Shahriari, 2014; Masoumi, Jahazi, et al., 2016); thereby, confirming the origin of void formation in AD730<sup>TM</sup> and by extension to other nickel-based superalloys.

Finally, as shown in Fig. 3.7(a-d), a large number of dimples like features that are visible at the fracture surface. Such surface characteristics have already been also reported in other superalloys (Davies, Jeffs, Lancaster, & Baxter, 2017; Y. C. Lin, Deng, et al., 2014a; Masoumi et al., 2018). They have been related to the growth (Fig 3.7 a and b) and coalescence of voids (Fig. 3.7 c and d), and cavities nucleated at grain boundaries which have been connected to the surface and assisted surface crack growth due to the reduction of the surface area resulting in the formation of a large number of microvoids that produce a dimpled crack surface (Davies et al., 2017; Y. C. Lin, Deng, et al., 2014a; Masoumi et al., 2018; Sasajima, Akabane, Nagai, Chonan, & Onuki, 2009). For the low heating rate, void coalescence could take place and the dimples appear larger, while for the fast heating rate very small dimples are observed at the fracture surface. Furthermore, in general, surface tension decreases when temperature increases due to lower intermolecular cohesive forces between the grains (Mcnallan & Debroy, 1991). As a result, the adhesion between the grains in the boundary area is weakened, resulting in void connection and the growth of micro-cracks at the boundary and subsequent failure of the sample without any ductility. Therefore, the large number and distribution of voids which brought them closer led to the crack growth and likely easier to connect to each other and brittle fracture happened.

### 3.3.2 Nil Ductility Temperature

As explained in section 3.2, the hot ductility tests with the objective to determine the nil ductility temperature of the alloy were conducted between 1050 and 1240 °C using a heating rate of 100 °C/s.

#### 3.3.2.1 Analysis of the flow curves

Fig. 3.11 shows the stress-strain curves of hot tensile tests of AD730<sup>TM</sup> superalloy for the different temperatures of deformation. The flow behaviors are significantly affected by the deformation temperature and composed of three distinct stages, work hardening, flow softening, and the final fracture stage. A peak after the strain hardening, followed by a yield drop phenomena was also observed in all the specimens. The stress difference between the upper and lower yield points was nearly the same for the first four testing temperatures. For the 1240 °C, the lower yield point was not detectable due to the sample fracture under this condition. Several authors have also reported the occurrence of a yield drop phenomena during hot deformation of various types of superalloys (Jonas, Ghosh, Queleennec, & Basabe, 2013; Z. L. Zhao et al., 2015). Guimaraes and Jonas (Guimaraes & Jonas, 1981) attributed the stress peak to dislocation locking due to short range ordering of  $\gamma'$  forming elements (Ti and Al) while Chamanfar et al. (A. Chamanfar, Jahazi, Gholipour, Wanjara, & Yue, 2014) showed that carbides can act as an additional source for dislocation locking. Recently, Zhao et al. (X. Zhao, Chen, Lin, & Huang, 2008) associated the yield drop to the occurrence of softening phenomena such as dynamic recovery and dynamic recrystallization (DRX). However, considering that the yield drop occurs over a very short period of time, observing microstructural variations during yield drop becomes very challenging.

In the present work and at the tested temperatures, the slow increase of flow stress after the yield drop is mainly associated with the interaction of strain hardening and softening mechanism. The results show that the strain of the alloy increased with temperature until 1150 °C. High deformation temperature can promote the mobility of grain boundaries for dislocation

annihilation, and thus the flow stress decreases probably due to the grain boundaries mobility, more DRX and dissolving the secondary phase precipitates at temperatures higher than 1000 °C in AD730<sup>TM</sup> as reported by Masoumi et al. (Masoumi, Jahazi, et al., 2016; Masoumi, Shahriari, et al., 2016a). Consequently, with increasing strain, diffuse necking occurred during tensile test and led to sample fracture. Huang et al. (Y. Huang & Langdon, 2005) studied the failure behavior of IN718 superalloy and observed localized necking in the temperature range above 950 °C. They also found that cavitation was the main cause of localized necking, particularly at higher strain rates (strain rates above  $10^{-2} \text{ s}^{-1}$ ). Therefore, the combined effects of localized necking and microvoid coalescence and interlinkage (near the NST) appear to be the responsible mechanisms for intergranular and fracture of the hot tensile tested samples.

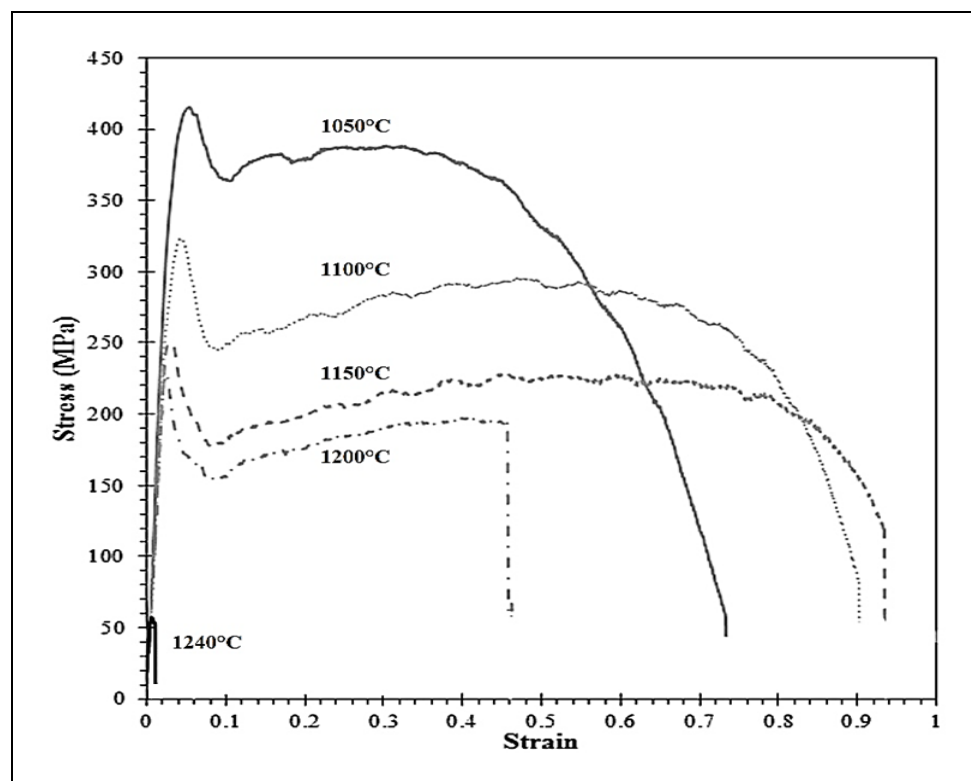


Figure 3.11 Stress-strain curves of hot tensile tests obtained by Gleeble<sup>TM</sup> 3800

Fig. 3.12 shows the evolution of the reduction in area with temperature obtained from the hot ductility tests. Based on the defined criteria for the NDT (point of 5% reduction area) the nil ductility temperature for AD730<sup>TM</sup> alloy is 1234 °C. This value is in agreement with those

obtained by other researchers for IN718 (1200 °C) (Knock, 2010), IN718Plus™ (1150 °C) (J. Andersson, Sjöberg, Viskari, & Chaturvedi, 2013), and Waspaloy (1250 °C) (Qian, 2001). As a result, by comparing the reported results for other alloys with the investigated alloy, it can be concluded that the difference between NST and NDT for all the above alloys is in the range of 40 to 90 °C.

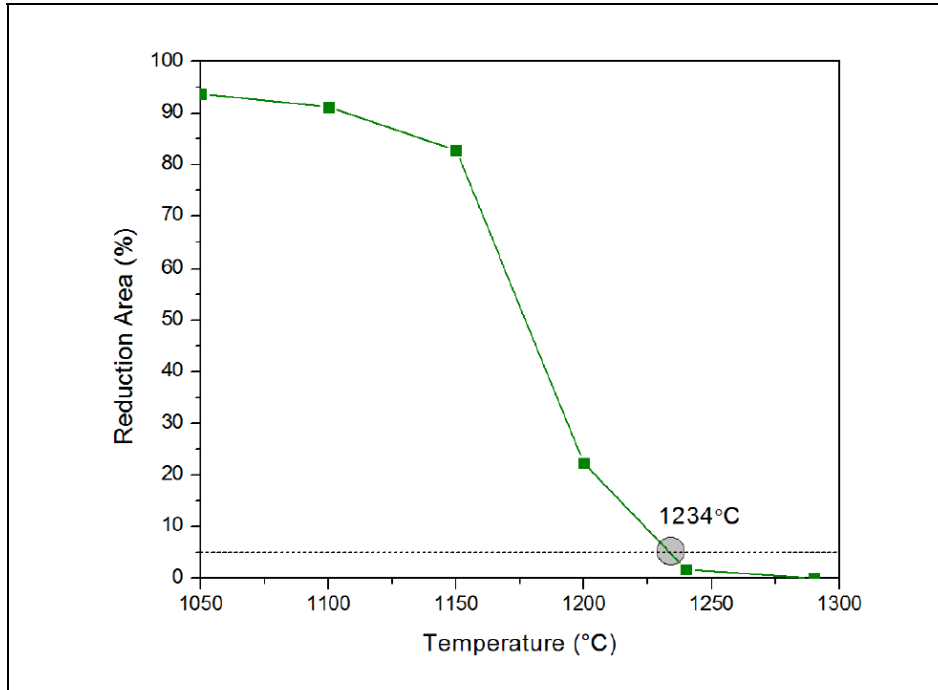


Figure 3.12 Hot ductility behavior during heating process at different temperatures. The standard deviation on the estimated reduction of area values is less than 2%

A comparison of the initial microstructure of the alloy (Fig. 3.2) with the one after the tensile test (for 1240 °C) revealed that the grains size behind the fracture zone did not change significantly passing from  $51.36 \pm 9.14 \mu\text{m}$  in the base material to  $58.13 \pm 15.43 \mu\text{m}$  (not shown here) for the samples exposed at 1240 °C. This is probably related to the limited time available for grain coarsening associated with the high strain rate and heating rate used in the experiments. Therefore, the effect of grain size variation on the hot ductility behavior of the alloy under these conditions could not be significant. Furthermore, above 1150 °C, the dissolution of  $\gamma'$  particles and carbides in the microstructure, especially the ones at the grain

boundaries, have a detrimental effect on mechanical properties as observed in the stress-strain curves of the samples tested at 1200 and 1240 °C.

The results obtained in the present work show (Fig. 3.12) that AD730<sup>TM</sup> superalloy has zero ductility under tensile loading above 1234 °C, where  $\gamma'$  precipitates are completely dissolved and liquation could occur under non-equilibrium conditions. Similar results have been reported by Ola et al. (Ola, Ojo, & Chaturvedi, 2013) for IN738LC. Specifically, the authors reported that the occurrence of liquation in the vicinity and within grain boundaries degraded the ductility of the alloy under tension and, as such, the alloy failed without plastic deformation (Ola et al., 2013). Furthermore, as reported by other investigators (Masoumi, Shahriari, et al., 2016a; Masoumi et al., 2017; Masoumi et al., 2018), complete dissolution of  $\gamma'$  particles in the matrix of AD730<sup>TM</sup> occurred at 1200°C which resulted in significant weakening of the grain boundaries in which liquation could occur. In general, intergranular cracking at high temperatures takes place at locations with localized stress or structural imperfections such as the grain boundary edges, triple points, and interface of brittle particles and are accompanied with grain boundary slipping and the formation voids (Aning & Tien, 1980; Dieter, 1988; Hertzberg, 1996). The possible operation of the above mechanisms in the present study will be discussed in the following.

Fig. 3.13 shows the fracture surface for the specimens exposed to 1050, 1100, 1150, 1200, and 1240 °C. A ductile fracture characterized with a large number of dimples and interstitial cavities (Fig.3.13 a-c). The presence of the larger voids may be due to the presence of large precipitates such as carbides that can be seen on the fracture surface of Fig. 3.15. By increasing the temperature to 1200°C and then to 1240 °C the fracture mode changed from intragranular to intergranular (Fig. 3.13d and e); however, the fracture is fully intergranular at 1240 °C. The presence of cracks along the grain boundaries and the clear definition of the grain limits in the fracture surface, and the differentiation of the shape of each grain during failure are signs of (quasi-) brittle fracture. The morphology of the fracture surface and the amount of reduction area for each specimen clearly revealed the transition from ductile to brittle fracture. The evolution of the fracture surface from 1050 °C to 1240 °C in Fig. 3.13 indicates that microvoids

and cavities are present along the tensile direction of the specimen and coalesce to become a continuous crack. The brittle fracture occurred when the temperature approached the NDT, whereas at lower temperatures the fracture was ductile.

The presence of grain boundary cracks and cavities within the microstructure is also reported in the zones below the fracture surface as shown in where cavities and microvoids formed due to the particle detachment (MC carbides) in the boundary areas can be observed. Fig. 3.14 (b) shows the formation of microcracks as a result of interconnection of previously formed cavities within the boundaries. Similar results have been reported also by Gifkins (Gifkins, 1994) and Greenwood (Greenwood, 1952). The above findings further confirm that cavitation and void nucleation and their growth during deformation at high temperatures are the main causes for grain boundary cracking and subsequent minimum ductility.

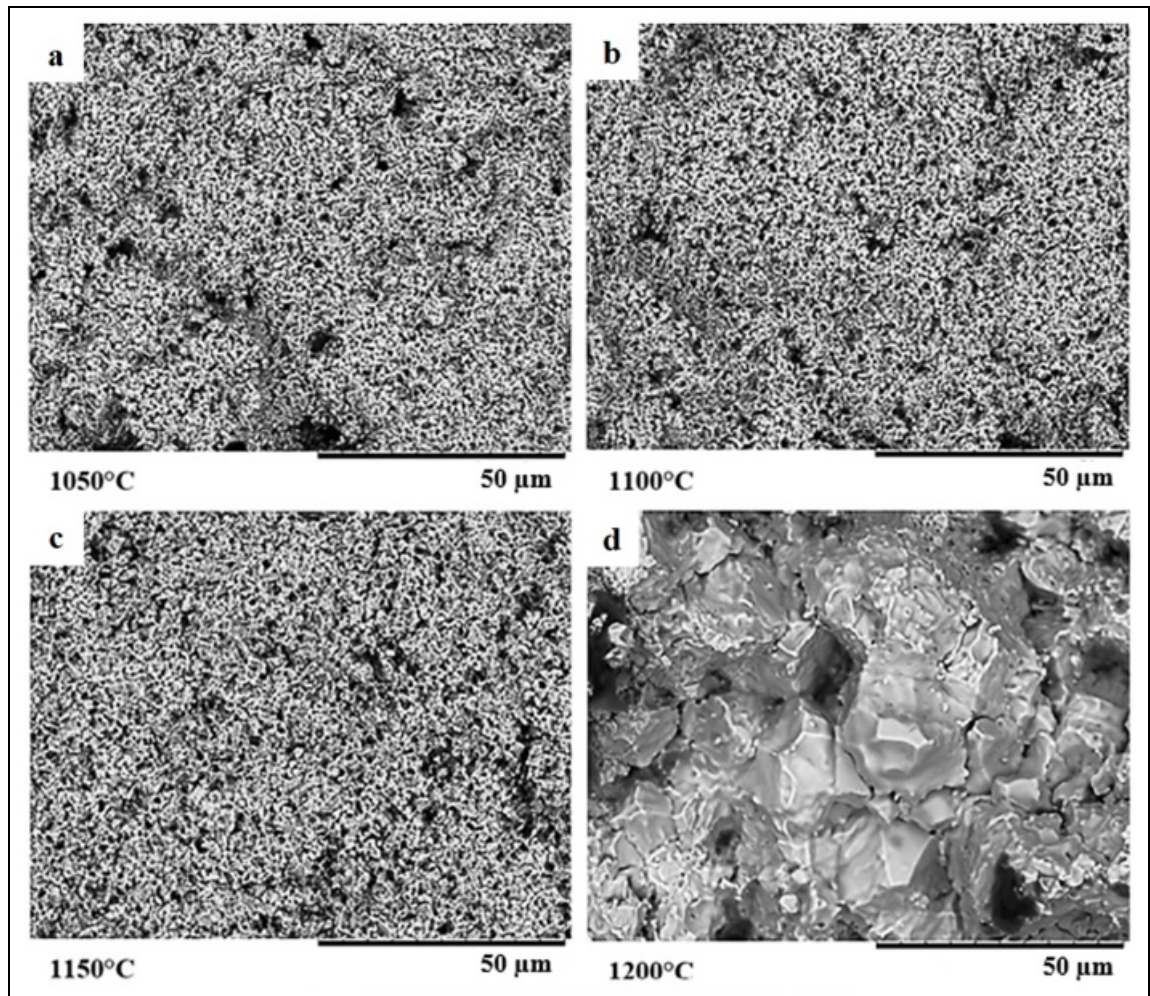


Figure 3.13 Fracture surface after NDT tests of AD730<sup>TM</sup> alloy, a) 1050 °C, b) 1100 °C, c) 1150 °C, d) 1200 °C

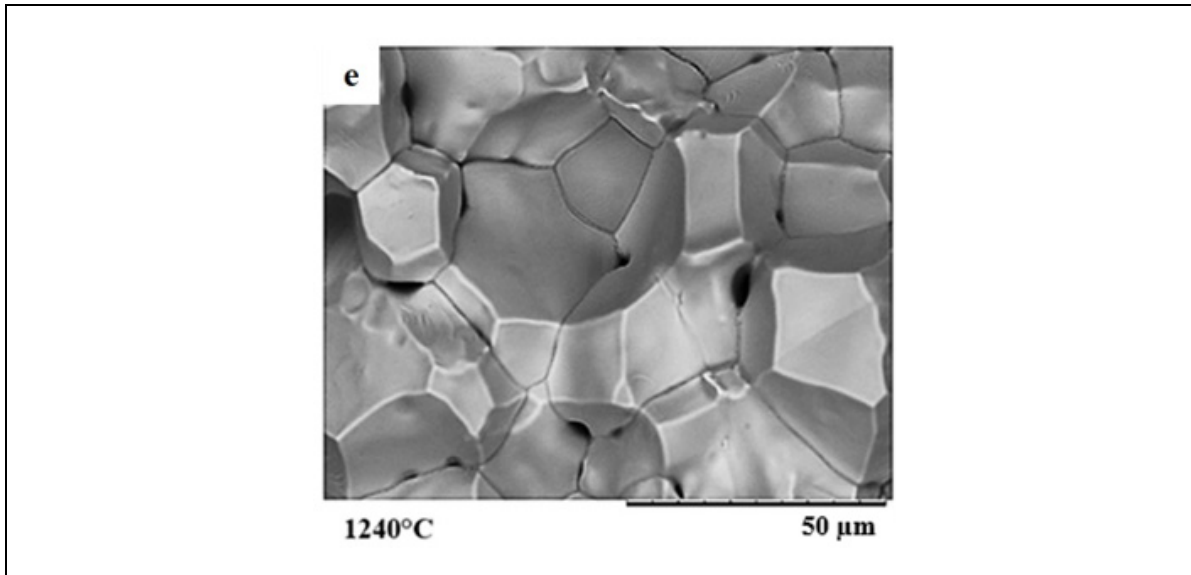


Figure 3.14 Fracture surface after NDT tests of AD730™ alloy, e) 1240 °C

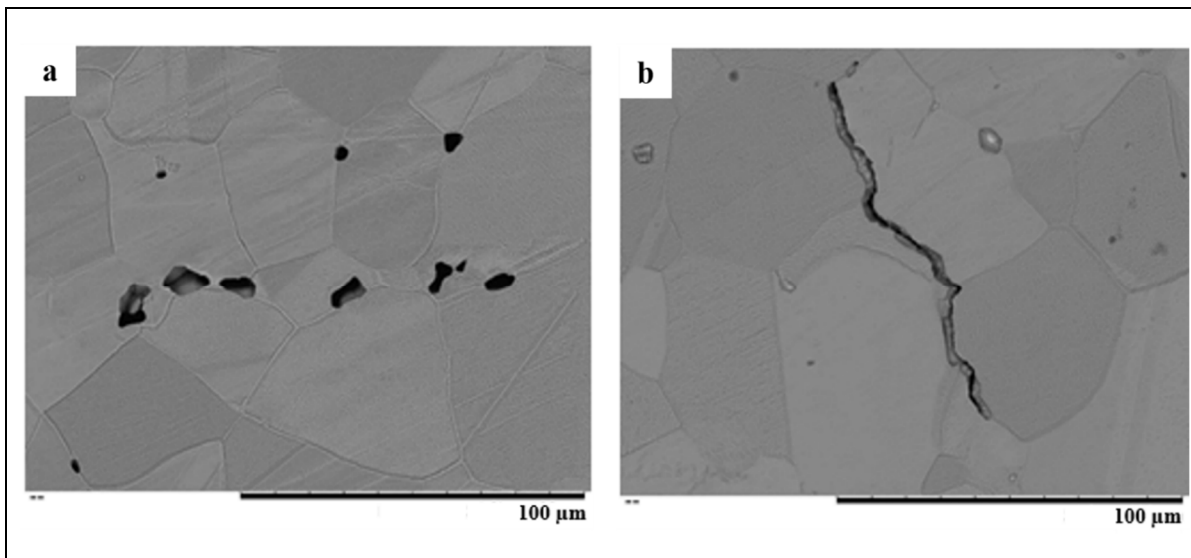


Figure 3.15 SEM images showing void formation and crack growth at grain boundaries in the fracture area obtained from cross-sectioned 1240 °C specimen

### 3.3.2.2 Characteristics and formation mechanism of cavities

Cavities or voids formed at grain boundaries can have different shapes depending on whether they formed at the junction of two grains, triple junctions, and four-grain junctions (voids in

inclusion-free boundaries) or at the interface of inclusions or precipitates present at the grain boundaries (Raj & Ashby, 1975; Riedel, 1987). All the above type of voids and cavities were observed in the examined fracture surface of samples as shown in Figs. 3.13 and 3.15, and internal microstructure, as shown in Fig. 3.14.

Gifkins (Gifkins, 1994) and Smith (R. W. Smith & Srolovitz, 1996) reported that the spacing between the cavities was about the same as that of the slip bands formed during the hot deformation process. Afterward, the slip bands formed ledges near the boundaries, which then nucleated the cavities through the grain boundary sliding (GBS) process by the applied stress. Moreover, cavities could also nucleate around the particles that are present at the grain boundaries (R. W. Smith & Srolovitz, 1996). As the temperature increases, the stress required to maintain a given strain-rate falls in such a way that the void growth rate increases while void nucleation rate decreases. In contrast, at low temperatures, the opposite occurs and higher nucleation rates and lower growth rates are observed (Raj & Ashby, 1975). The energy barrier ( $\Delta G_c$ ) for nucleation is function of the free surface energy ( $\gamma$ ) or surface tension and the volume of the void of critical radius ( $r_c$ ) (Raj & Ashby, 1975):

$$\Delta G_c = \frac{r_c^3 \cdot F_{v(\alpha)} \cdot \sigma}{2} \quad (3.1)$$

$$r_c = \frac{2\gamma}{\sigma} \quad (3.2)$$

Where  $\sigma$  is applied tensile stress,  $F_{v(\alpha)}$  is the function of void geometry and  $r_c^3$ .  $F_{v(\alpha)}$  is the volume of the void of critical size and  $\alpha$  is the angle formed at the junction of the void and the grain boundary.

If  $\rho_{max}$  is the maximum number of potential nucleation sites in the grain boundary per unit area, then the number of critical nuclei per unit area is:

$$\rho_c = \rho_{max} \cdot \exp\left(\frac{-\Delta G_c}{KT}\right) \quad (3.3)$$

Where  $\rho_c$  is the number of supercritical nuclei formed per second and it is time dependent. Using the above analysis the nucleation rate ( $\dot{\rho}$ ) can be described as (Raj & Ashby, 1975):

$$\dot{\rho} = \frac{4\pi\gamma}{\Omega^3 \cdot \sigma} \cdot D_B \delta \left(1 + \frac{\sigma\Omega}{KT}\right) (\rho_{max} - \rho) \times \exp\left[-\left(\frac{4\gamma^3 \cdot F_v(\alpha)}{\sigma^2 \cdot KT}\right)\right] \quad (3.4)$$

Where  $\Omega$  is the atomic volume (usually  $\sigma\Omega/kT \ll 1$ ) and  $D_B\delta$  is the boundary diffusion coefficient times the boundary thickness. The exponential factor is the dominant influence in the temperature dependence of nucleation. Therefore,  $F_{v(\alpha)}$ ,  $\gamma$  and  $\sigma$  are the critical parameters in determining the nucleation rate.

The above equation, which has been developed for pure copper, indicates that, void nucleation and growth depend on temperature; applied stress and time (i.e., strain rate and heating rate). The results obtained in the present study also confirm such dependence for the investigated nickel base superalloy. However, in order to quantitatively determine the nucleation rate of voids as a function of heating rate for AD730<sup>TM</sup> alloy, each of the variables in equation (3.4) need to be known. Such data (for example, void geometry, void critical radius, interface energy, etc.) is not available in the literature and their determination was out of the scope of the present study. Therefore, the time to fracture defines the area fraction of voids in a grain boundary, which could be attributed to the voids fraction and/or voids size during deformation. As different heating rates were used during the NST tests, it is expected that both void fraction and void size would vary during testing.

In general, nucleation is continuous with time i.e., the number of nuclei increases with time towards the number  $\rho_{max}$ . As shown in Fig. 3.15 (a) and (b), MC type carbides with M = Ti, Mo and Nb-rich carbides are present at the grain boundaries. These carbides are not coherent with the matrix and cause the formation of voids and cavities due to the difference in the shear modulus between the particles and the matrix (Davis, 2004; Y. Huang & Langdon, 2005). The stability of the cavity nuclei depends upon their growth to the critical size by absorbing

vacancies. As reported by Gifkins and Smith (Gifkins, 1994; R. W. Smith & Srolovitz, 1996) the growth of the cavity nucleus is opposed by the cavity surface tension which tends to shrink it and suppress it, unless the cavity growth rate is high enough and could reach the critical size. Once this step is successfully passed, the cavity continues to capture vacancies until cavities link to form *chains* (Gifkins, 1994; R. W. Smith & Srolovitz, 1996). Finally, these chains grow to form cracks over part or all of the grain boundary and joint other cracks in the neighbouring grains (Fig. 3.14 (a, b)).

The presence of liquation at the grain boundaries was also observed in all samples tested at 1200 and 1240°C, as illustrated in Figure 3.15 (a-d). Fig. 3.16 shows the liquation thickness in the different zones of the sample exposed to 1240°C. As it can be seen, the average measured thickness of the liquation film within the grain boundaries is maximum in the vicinity of the fracture zone and drops significantly as the distance from the fracture surface increases. Knock (Knock, 2010) reported that as the liquid forms around the grains, the material retains some of its strength due to capillary effects. As the fraction of liquid increases, the capillary effects are unable to support the forces on the interface of each grain. Afterward, the surface tension diminished and the grain boundary strength decreased which led to crack growth and ductility dropped in the alloy at high temperatures. In a previous investigation on liquation in a nickel-based superalloy with relatively similar composition to AD730<sup>TM</sup>, it has been reported that liquation of Cr-rich carbides (often containing some Co and W) within grain boundaries took place at the origin of the formation of the liquid zones (Xiao et al., 2008).

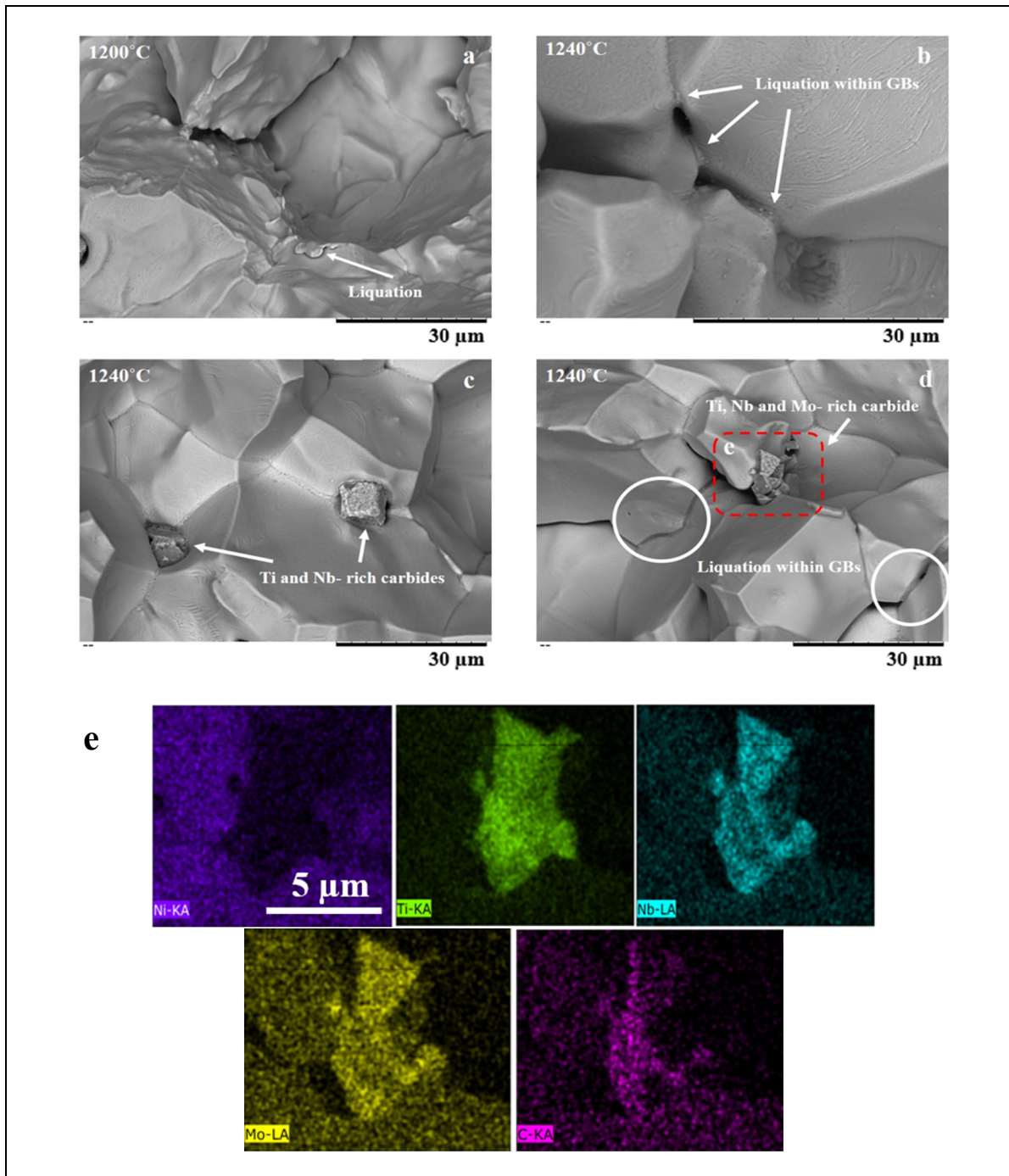


Figure 3.16 SEM images from samples exposed to 1200 and 1240 °C of AD730™ showing: a) liquation at the GB, b) GB liquation and joining of the voids, c) carbides at GB and triple junctions, d) liquation at GB and crack growth, e) map analysis of a carbide particle in image (d)

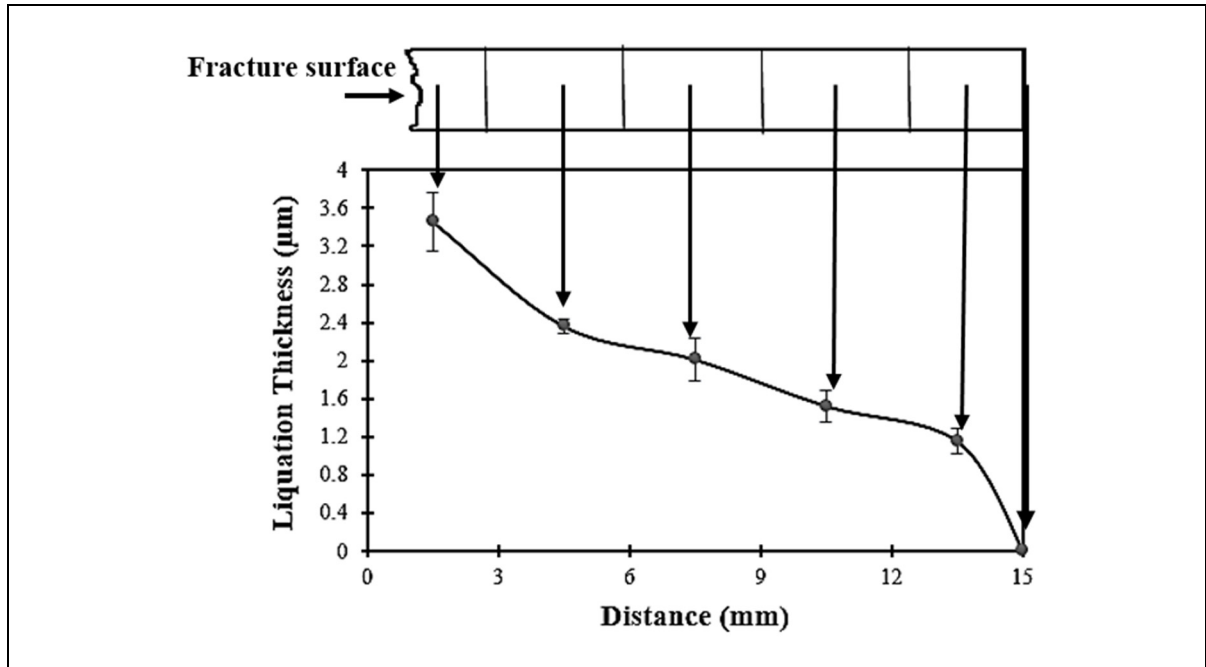


Figure 3.17 Variations of the liquation thickness from the fracture zone to the parent material in the sample. Obtained from the longitudinal cross section of the NDT test sample 1240 °C. Measurements positions in the fractured sample are indicated by arrows

Miller and Chadwick (Miller & Chadwick, 1967) studied on the effect of liquation on boundaries strength. They obtained the stress required for splitting the interface by overcoming surface tension at the solid-liquid interface on liquated grain boundaries (Eq. 3.5):

$$\sigma = \frac{2\gamma_{sl}}{h} \quad (3.5)$$

Where the tensile stress,  $\sigma$  the stress required to overcome the attraction due to surface tension,  $\gamma_{sl}$  is surface tension at the solid-liquid interface and  $h$  is the liquid film thickness (the meniscus for the case of complete wetting is given by  $\frac{h}{2}$ ). Furthermore, Xiao et al. (Xiao Feng, Fang Liang, & K., 2005) proposed the following equation to describe the evolution of the surface tension of an alloy with temperature (Xiao Feng et al., 2005):

$$\gamma_{sl} = \gamma_l + k(T - T_L) \quad (3.6)$$

Where  $\gamma_l$ , in mN/m, is the surface tension at liquidus temperature ( $T_L$ );  $k$ , in mN/(m.K), is the temperature coefficient of surface tension; and  $T$  is the temperature in Kelvin scale.

Equation (3.5) implies that the stress required separating the solid-liquid interface decreases with increasing thickness of the grain boundary liquid film. Accordingly, any factor that reduces the thickness ( $h$ ) of the intergranular liquid film, it could presumably reduce the susceptibility of the alloy to cracking (Egbewande, Zhang, Sidhu, & Ojo, 2009). On the other hand, based on equations (3.4) and (3.6), the closer the temperature is to the liquidus, the lower will be the surface tension. Therefore, reduction in surface tension decreases the critical size for the formation of a void resulting in increased formation and coalescence of the voids and cavities. It should be noted; a very accurate calculation would require the determination of the surface tension of the AD730<sup>TM</sup> alloy which is out of the scope of the present work.

Ojo et al. (Ojo & Chaturvedi, 2005) and Lin et al. (W. Lin, Lippold, & Baeslack III, 1993) reported that NDT usually occurs at the onset of grain boundary liquation, so the lower the GB liquation temperature the lower will be the NDT (W. Lin et al., 1993; Ojo & Chaturvedi, 2005). Generally, any factor that reduces the temperature of grain boundary liquation initiated during the welding heating cycle, increases material's susceptibility to liquation cracking. In the present study, it was found that the intergranular carbide particles present in the AD730<sup>TM</sup> superalloy decreased the liquation initiation temperature in the material and can be considered as the most detrimental phase in promoting cracking susceptibility. Similar results have been reported by Egbewande et al. (Egbewande et al., 2009) in IN738 and Montazeri et al. (Montazeri & Ghaini, 2012) in IN738LC that the melting and liquation of Cr-Mo rich carbides (or borides) at lower temperatures resulted in the higher susceptibility to liquation cracking with the effects being intensified by hard carbides such as MC (Ti, Mo, and Nb-rich) carbides.

The above findings demonstrate that, in addition to the voids and cavities, the formation of liquated zones at the grain boundaries, has a significant impact on the NDT point. Specifically, liquation at the boundaries acts as an accelerating factor for the interconnection of cavities

resulting in faster joining of the voids and cavities and the ensuing intergranular fracture. Evidently, faster damage is expected at higher temperatures due to the increased liquation at the boundaries and reduced surface tension between the grains.

### **3.4 Conclusions**

Hot ductility behavior of the nickel base alloy AD730<sup>TM</sup> was investigated using Gleeble<sup>TM</sup> thermomechanical simulator. Different heating rates representative of those observed during linear friction welding were used. The microstructure and fracture surface of the samples were examined and the possible mechanisms responsible for the loss of ductility were proposed. The following conclusions can be made from this investigation:

1. The nil strength and nil ductility temperatures of the alloy were determined to be 1290 °C and 1234 °C, respectively.
2. Variation of heating rates from 5 to 100 °C/s does not have a significant influence on the NST point. However, this variation changed the size and fraction of voids in the fracture surface.
3. The failure mechanism at nil strength temperature seems to be mostly controlled by void nucleation and growth.
4. Liquation within the grain boundaries and the reduction in surface tension at the grain boundary-matrix interface combined with the presence of Nb and Mo rich MC appear to be the main mechanisms for ductility loss at the NDT point.
5. The nucleation, growth, and coalescence of cavities and voids occur during hot deformation and the extent of material damage is a function of temperature, applied stress, and time.



## CHAPTER 4

### MICROSTRUCTURE EVOLUTION OF SELECTIVE LASER MELTED INCONEL 718: INFLUENCE OF HIGH HEATING RATES

Syedmohammad Tabaie <sup>a</sup>, Farhad Rézaï-Aria <sup>b</sup>, and Mohammad Jahazi <sup>a</sup>

<sup>a</sup> Department of Mechanical Engineering, École de Technologie Supérieure,  
1100 Notre-Dame West, Montreal, QC, Canada.

<sup>b</sup> Institut Clément Ader (ICA), Université de Toulouse, CNRS, IMT Mines Albi, INSA, UPS,  
ISAE, Campus Jarlard, 81013 Albi, France.

Paper published in *Journal of Metals*, April 2020

#### Abstract

Inconel 718 (IN718) superalloy samples fabricated by selective laser melting (SLM) were submitted to different heating cycles and their microstructural characteristics were investigated. The selected heating rates, ranging from 10 °C/min to 400 °C/s, represent different regions in the heat-affected zone (HAZ) of welded additively manufactured specimens. A combination of Differential Thermal Analysis (DTA), high-resolution dilatometry, laser confocal and electron microscopy were used to study the precipitation and dissolution of the secondary phases and microstructural features. For this purpose, the microstructure of the additively manufactured specimen was investigated from the bottom, in contact with the support, to the top surface. The results showed that the dissolution of  $\gamma''$  and  $\delta$  phases were delayed under high heating rates and shifted to higher temperatures. Microstructural analysis revealed that the Laves phase at the interdendritic regions was decomposed in specific zones near the surface of the samples. It was determined that the thickness and area fraction of these zones were inversely related to the applied heating rate. A possible mechanism based on the influence of heating rate on Nb diffusion in the interdendritic regions and core of the dendrites is proposed to interpret the observed changes in the microstructure.

**Keywords:** Selective laser melting; Inconel 718; High heating rate; Differential thermal analysis; Phase transformation.

## 4.1 Introduction

Selective laser melting (SLM) is an additive manufacturing (AM) process which uses a laser as a source to melt the metal powder in the form of deposited successive layers on top (Petersen-Øverleir, 2015). This technology has been used to fabricate components with complex geometries (e.g. gas turbine blades, injection molds, heat exchangers) with a close to full density (close to 99.7%) which is difficult and costly to acquire through conventional casting and /or forging routes (Deng et al., 2018; Kruth et al., 1998; Levy, Schindel, & Kruth, 2003; C. Li et al., 2017). IN718® alloy is the workhorse superalloy extensively used in energy and transportation industries and therefore is a promising candidate for an advanced manufacturing technology such as SLM method in aerospace applications (Jia & Gu, 2014; Knapp, Raghavan, Plotkowski, & DebRoy, 2019; Sufiiarov, Borisov, & Polozov, 2014). Despite its good weldability, IN718 is known for its susceptibility to welding defects such as strain age-cracking and hot cracking, particularly, hot cracking in the heat-affected zone (HAZ) during welding (Owczarski, Duvall, & Sullivan, 1966; Raza et al., 2019). Considering the continuous expansion of additively manufactured components from IN718 and the inherent heterogeneous nature of an AM microstructure, it is of both scientific and technological interest to better understand the evolution of an AM microstructure to rapid thermal cycling and characteristic of welding operations.

Typically, the low melting point compounds can liquate within the HAZ during conventional fusion welding operations such as Gas Tungsten Arc Welding (GTAW) and Electron Beam Welding (EBW). The temperature in the HAZ for wrought IN718 and SLM IN718 during fusion welding is in the range of 950-1200 °C (Manikandan, Sivakumar, Kamaraj, & Rao, 2012; Manikandan et al., 2015; Radhakrishnan & Thompson, 1993; Raza et al., 2019; Raza, Andersson, & Svensson, 2018), while it is between 950 and 1100 °C in solid-state welding methods such as linear or inertia friction welding (Ahmad Chamanfar et al., 2015; Z. W. Huang et al., 2007; Caroline Mary & Jahazi, 2006). At these temperatures, grain boundary liquation

in HAZ could cause the constitutional liquation of Niobium (Nb)-rich particles such as Laves phase, carbides, and interdendritic  $\gamma$ /Laves eutectic formed during rapid solidification. These phases are usually found in high concentrations in the interdendritic regions in the microstructure of conventionally as-printed parts (Y. Chen, Lu, et al., 2016; Knapp et al., 2019; Kumara et al., 2019; Sui, Chen, et al., 2019). Sui et al. (Sui, Chen, et al., 2019) investigated the formation of  $\delta$  phase and proposed two possible mechanisms. The first one relates the formation of the  $\delta$  phases around the interdendritic Laves phases to the existence of a chemical gradient that promotes the diffusion of Nb to the grain boundaries and become nucleation sites for the  $\delta$  phase. The second mechanism is based on the lack of coherency between Laves phase and matrix that promotes the diffusion of Nb and formation of Nb rich zones (~ 10 wt.%) that become nucleation sites for the  $\delta$  phase.

Qian and Lippold (Qian & Lippold, 2003a) related intergranular HAZ liquation cracking to the combined effects of  $\delta$  phase dissolution, boron carbide constitutional liquation, and grain boundary segregation. On the other hand, Zhang and Ojo (VishwakArma, Ojo, Wanjara, & Chaturvedi, 2014; H. R. Zhang & Ojo, 2009) reported that the  $\delta$  phase could actually constitutionally liquate in the HAZ during welding above their solvus (about 1010 °C in IN718) and enrich the grain boundary with Nb. Thrappel et al. (Tharappel & Babu, 2018) and Muralidharan et al. (Muralidharan, Shankar, & Gill, 1996) reported that during rapid heating, second phase eutectic grain boundary precipitates such as  $\gamma$ /Laves or  $\gamma$ /NbC (at 1200 °C) present in the HAZ of wrought IN718 melted due to the lack of time for dissolution into the matrix. In very recent studies, Raza et al. (Raza et al., 2019; Raza et al., 2018) studied the cracking in the HAZ of GTAWed SLM IN718 samples and related it to the melting of the Laves phase in the interdendritic regions. However, in the above works the influence of heating rate on microstructure evolution was not investigated.

The influence of heating rate on the evolution of the secondary phases in the microstructure of wrought IN718 has been investigated by many researchers. For instance, Roder et al. (Roder, Helm, Neft, Albrecht, & Luetjering, 2005) reported that  $\delta$  and  $\gamma''$  particles are dissolved in

HAZ zone during friction welding of wrought IN718. Niang et al. (Niang, Viguiet, & Lacaze, 2010) reported that the dissolution kinetics of  $\gamma''$  and  $\delta$  phases is quite sluggish in forged IN718 and not change by increasing the heating rate. Antonsson and Fredriksson (Antonsson & Fredriksson, 2005) reported that the diffusion rate and/or the solubility of Nb in the  $\gamma$  phase increased at higher cooling rates. Knorovsky et al. (Knorovsky et al., 1989) and Zhang et al. (H. R. Zhang & Ojo, 2009) reported that during rapid heating (more than 100 °C/s) the chemical composition of formed phases are under non-equilibrium thermodynamic states and can significantly deviate from the assumed solid-state equilibrium dissolution conditions, which may drastically contribute to HAZ micro-cracking. Under rapid heating conditions, due to limited available time for homogenization by diffusion of atoms,  $\delta$  phases can survive above their thermodynamic equilibrium solvus temperature which is beyond the  $\gamma$ -Laves eutectic temperature. However, no data is available on the influence of heating rate on the dissolution and reprecipitation kinetics of the above phases. It must be noted that the solidification thermal regime during conventional casting and additive manufacturing are expected to be very different and hence influence the phase changes. For example, the primary interdendritic distance in conventionally cast IN718 parts ranges between 80 to 220  $\mu\text{m}$  (primary dendrite arm spacing) (Sohrabi & Mirzadeh, 2019c) while it is expected to be much smaller (0.4 to 3  $\mu\text{m}$ ) in as-SLM parts due to the difference in the solidification and subsequent thermally induced regimes (W. Huang et al., 2019).

In the present investigation, the evolution of second phase particles in the microstructure of SLM IN718 submitted to rapid thermal cycling will be addressed. A better understanding of the response of an AM structure to rapid heating rates is crucial for predicting HAZ and HAZ cracking susceptibility in welded AM parts, where very little data is available. The obtained results will also help design optimized procedures for welding of additively manufactured components.

## 4.2 Materials and Methods

### 4.2.1 Materials

The recommended SLM parameters for fabrication IN718 superalloy specimens are reported in (Table 4.1). SLM-125HL machine at IMT-Mines Albi, France was used for the manufacturing of the specimens.

Table 4.1 SLM parameters to fabricate Inconel 718 alloy specimens

<b>P (W)</b>	<b>v (mm/s)</b>	<b>H (μm)</b>	<b>t (μm)</b>
<b>275</b>	760	120	50

In the above table, P is laser beam power, v is laser-scanning velocity, H, and t are respectively the hatch spacing and the thickness of the deposited layers. The volume energy density (VED) was estimated using the following relation:

$$\text{VED} \left( \frac{J}{\text{mm}^3} \right) = \frac{P}{v.H.T} = 60.307 \quad (4.1)$$

IN718 powders had spherical shape with a particle size distribution between 20-70 μm. Two cylindrical specimens with two different diameters (d = 6 mm and d = 3 mm) and identical length (L = 40 mm) were fabricated for the experiments. A thin disk-shaped specimen (d = 25 mm and thickness = 3 mm) was also fabricated for room temperature (RT) post-fabrication chemical analysis by Atomic Emission Spectroscopy (AES). The results are reported in Table 4.2 and are based on an average of five measurements in different locations of the disk shape sample. The laser beam scanning orientation and the building direction were collinear with the Z-direction displacement and perpendicular to fabrication platform. The laser beam scanning was rotated successively for 67° in each layer to reduce microstructural anisotropy.

Table 4.2 The average chemical composition of SLM IN718 (wt. %)

Ni	Fe	Cr	Co	Al	Ti	Nb	Mo	C	B	Zr	Si
Bal.	15.7	20.54	0.1	0.34	1.17	5.1	3.13	0.04	0.002	0.018	0.01

#### 4.2.2 Thermal analysis

The low to medium heat treatment cycles were performed using a Diamond PerkinElmer Differential Thermal Analysis (DTA). To this end, two mm thick disk-type samples were sliced by Electro Discharge Machining (EDM) from the top area of the fabricated cylinders. The samples were heated in platinum crucibles and flowing air up to 1200 °C with rates of 10, 15, 25, 50, 80, and 100 °C/min and then cooled down to room temperature with an identical rate. The DTA tests were repeated two times for heating rates lower than 80 °C/min (10, 15, 25, and 50 °C/min) and three times for the 80 and 100 °C/min.

For the high heating rate experiments, three thermal cycles with rapid heating rate of 100, 200, and 400 °C/s with an identical dwell time (10 s) and a quenching rate of 65 °C/s by Helium gas were applied, as schematically shown in Figure 4.1, using the high-resolution TA A/D 805 dilatometer. The 4 mm × 10 mm dilatometry samples were extracted by EDM from the 6 mm diameter fabricated bars. These samples were heated to 1000 °C by induction heating in the dilatometer machine and for each test; the heating and cooling profiles were recorded using a S-type thermocouple welded to the center of the specimen.

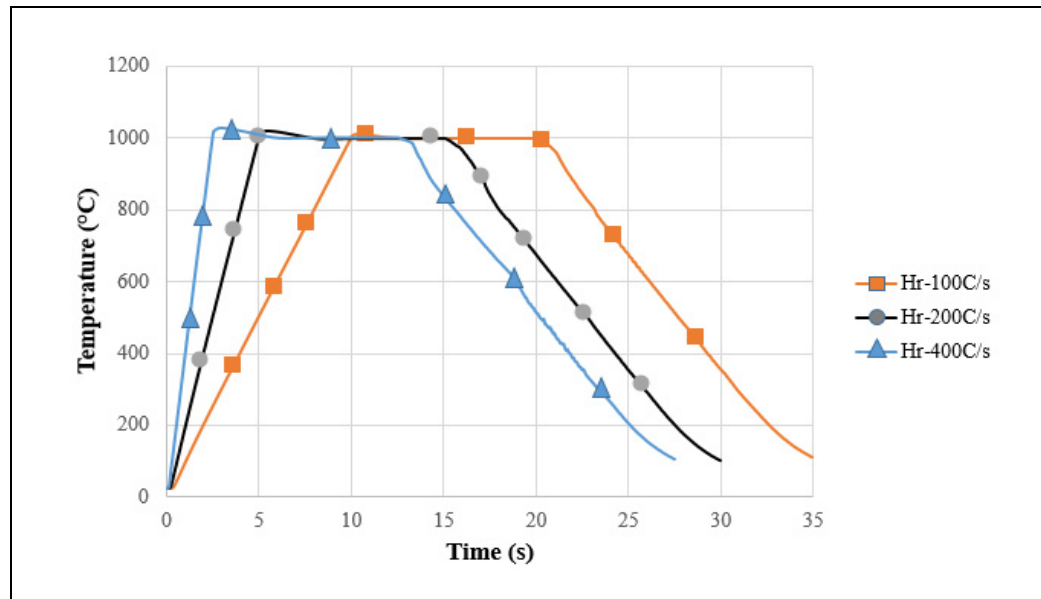


Figure 4.1 The time-temperature heating-cooling cycles of SLM IN718 specimens with three heating-up rates to achieve 1000 °C and a dwell time of 10 s and a final identical quenching constant rate of 65 °C/s

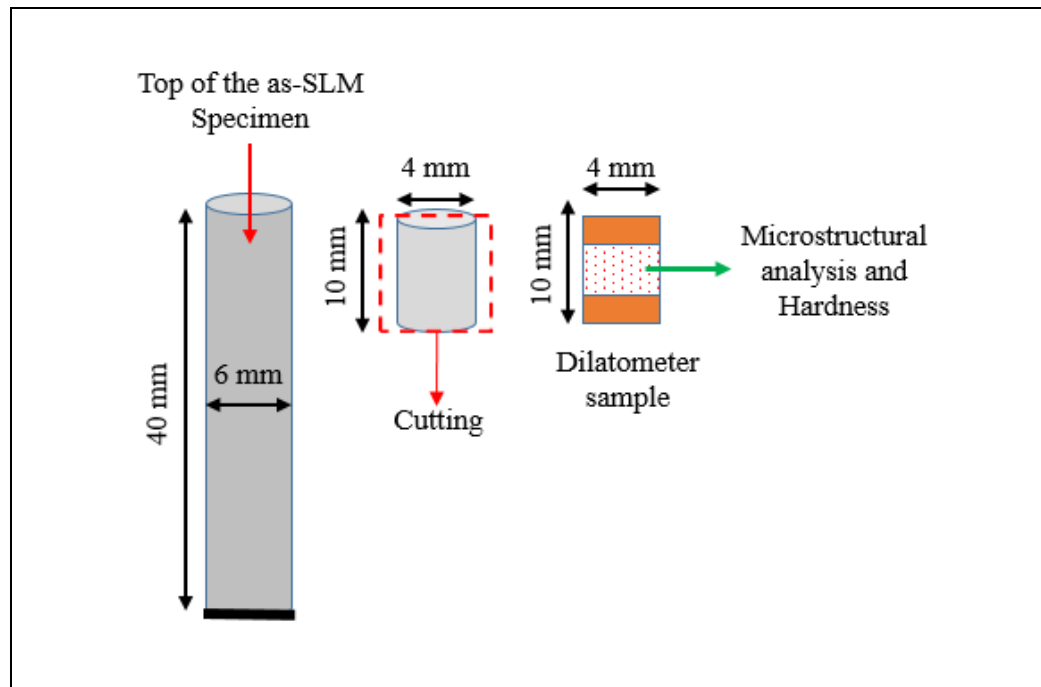


Figure 4.2 Schematic of dilatometer samples and their designated location for microstructural analysis and micro-hardness measurements

### 4.2.3 Microstructural investigations

The as-SLM IN718 and post-dilatometry tested specimens were characterized by LEXT OLS4100 laser confocal optical microscopy (OM) as well as scanning electron microscopy (SEM) (Hitachi TM3000 and SU-8230 Field Emission-SEM equipped with a Bruker EDS detector). Examination of the as-SLM samples was conducted in the transverse and longitudinal directions (Figure 4.2). The OM and SEM samples were cold etched to reveal the dendritic microstructure and precipitates using standard metallographic procedures in Kalling No.2's reagent (5 g CuCl<sub>2</sub>, 100 ml HCl, and 100 ml ethanol). The size and morphology of the precipitates was characterized at micro scales via OM and SEM images analysis. The average dendrite arm spacing (DAS) and volume fraction of all precipitates were quantified and calculated on the basis of digitized micrographs and standard image analysis software (Image J). Finally, hardness testing was conducted on the middle of longitudinal cross-section of as-fabricated samples after high heating rate tests (Figure 4.2). A Future-Tech Vickers micro-hardness machine under a dead-load of 200 gf and a dwell time of 15 s was used for the tests. The measurements were repeated at least three times for each condition and the average values are reported.

## 4.3 Results and discussions

### 4.3.1 Characterization of the as-SLM sample

The initial microstructure of the as-SLM fabricated, built-in the Z direction, is shown in Figure 4.3 where the periodic melt pools generated after each deposited layer is clearly revealed. For each layer, the melting pool embodies the molten powder particles of the freshly deposited layer along with the previously sub layer material already solidified. As an example, a melt pool along with its measured depth and width is shown in Figure 4.3 (a and b) where a fish-scale feature is revealed in the longitudinal cross-section of the sample. The wide columnar grains, crossing multiple layers are due to the thermal gradient along the SLM building

direction. The area fraction of the porosities measured all over the as-SLMed IN718 specimen after SLM was about 0.4 % in the bottom (B) and about 0.28 % in the top (T) layers.

Due to the steep temperature gradient and high solidification rate during the SLM process, a supersaturated solid-solution matrix is expected to be formed with Laves phase precipitating in the sub-grain boundaries. In addition, a gradient of microstructure along the build direction, as well as from the dendrite cores to the interdendritic regions was observed. Similar observations were also reported by Kumara et al. during solidification of electron beam melted IN718 alloy.

Figure 4.4 shows the variation of primary dendrite arm spacing (DAS),  $\lambda$ , along with the height of the as-printed specimen. The average DAS at the bottom (B) of the specimen is the lowest ( $0.789 \pm 0.136 \mu\text{m}$ ) and increased in the middle (M) ( $1.153 \pm 0.132 \mu\text{m}$ ) and then decreased again at the top (T) ( $0.820 \pm 0.130 \mu\text{m}$ ). The parallel white lines in each image are the remaining interdendritic Laves phase ( $\text{Ni}_2\text{Nb}$ ) that rapidly solidified after AM processing. Their volume fraction increased from 13.2 % (B) to 15.46 % (M) and then decreased to 14.6 % in the Top region (T). These variations could be explained by the equivalent time-temperature histories that are generated by the changes of the thermal gradients and the difference in cooling rate throughout the sample during the SLM fabrication process. In fact, the higher cooling rate at the bottom and top of the sample results in a finer dendritic (smaller DAS) structure leaving less time for elemental diffusion from the interdendritic zones to the core of dendrites. The high cooling rate normally results in the suppression (or at least reduction) of the segregation of elements and the formation of Laves phase in the interdendritic solidifying regions (Mostafa et al., 2017b). As a result, in the bottom and the top of the sample where DAS is smaller, the Nb concentration homogenizes faster and therefore the Laves ( $\text{Ni}_2\text{Nb}$ ) fraction decreased. This finding is further confirmed by examining Figure 4.5, where it can be seen that the volume fraction of the Laves phase increased from the bottom to the middle of the sample (Figure 4.5).

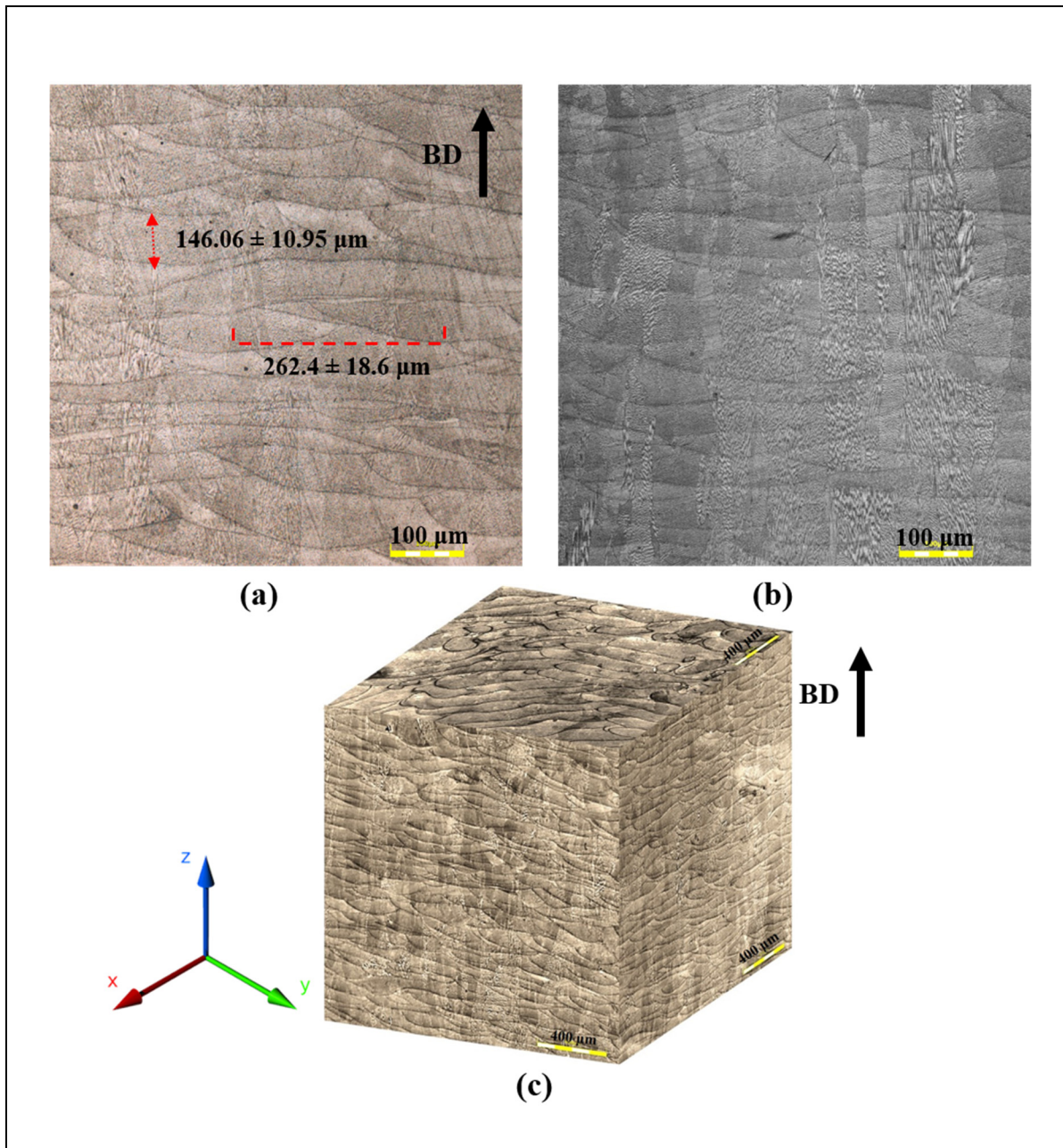


Figure 4.3 OM of as-Fabricated SLM-IN718 along the building direction (Z): (a) measured width and depth of a melt pool; (b) wide columnar grains elongated in the building direction; (c) 3D-reconstruction of cross-sectioned & polished planes of a SLM specimen

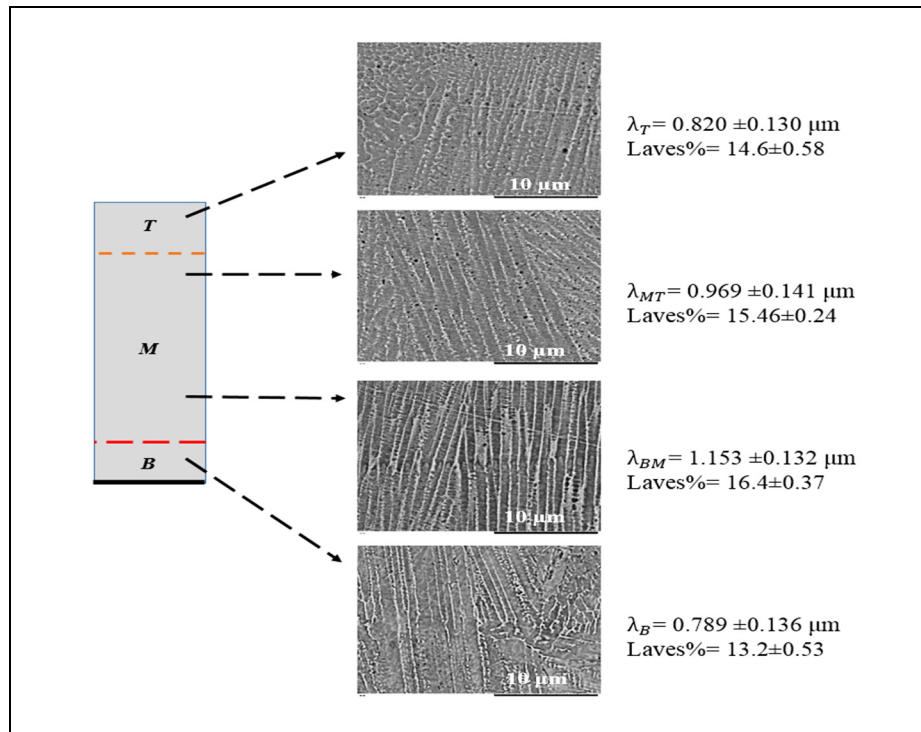


Figure 4.4 Variation of DAS and Laves fraction along the as-SLM IN718 specimen height. The BM to MT area is the middle region between the bottom (B) and the top (T) of the examined samples

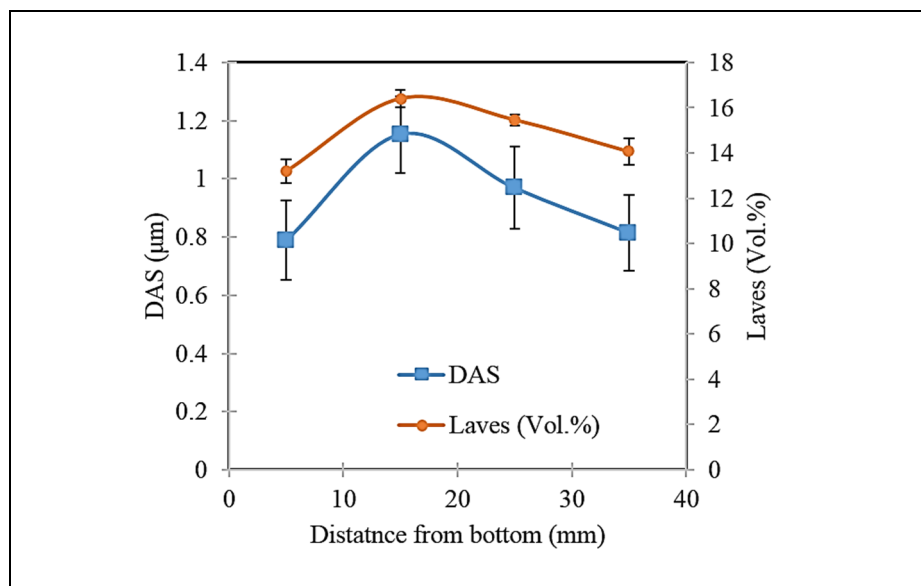


Figure 4.5 Variation of DAS and Laves phase along the height of the as-SLM IN718 samples

Figure 4.6 shows the microstructure of the as-SLM sample in the top (T) region. The microstructure in the bottom region (B) was similar to the top region and is not shown here to avoid repetition. The  $\gamma''$  and  $\delta$  particles observed in this study are similar in shape and size ( $80 \pm 34$  nm), which have also been observed in the works (Amato et al., 2012; G. H. Cao et al., 2018; Y. Cao, Bai, Liu, & Hou, 2019; Jia & Gu, 2014; J. Li et al., 2019; Mostafa et al., 2017b; Tucho et al., 2017). These phases are mostly confined at the bottom and top of the SLM samples by precipitation at the interdendritic zones close to the Laves. Jia et al. (Jia & Gu, 2014) reported that during the solidification of the upper layers, the previously solidified layers experience an aging heat treatment resulting in the precipitation of  $\gamma'$  and  $\gamma''$  ( $\text{Ni}_3\text{Nb}$ ) phases. Therefore, more  $\gamma'$  and  $\gamma''$  (less likely  $\delta$  particles (J. Li et al., 2019)) precipitate in the B region of the as-fabricated parts. Hence, the concentration of Laves in the B region is expected to be less than in the M or T regions. These microstructural differences could induce differences in hardness between the zones, as will be shown below.

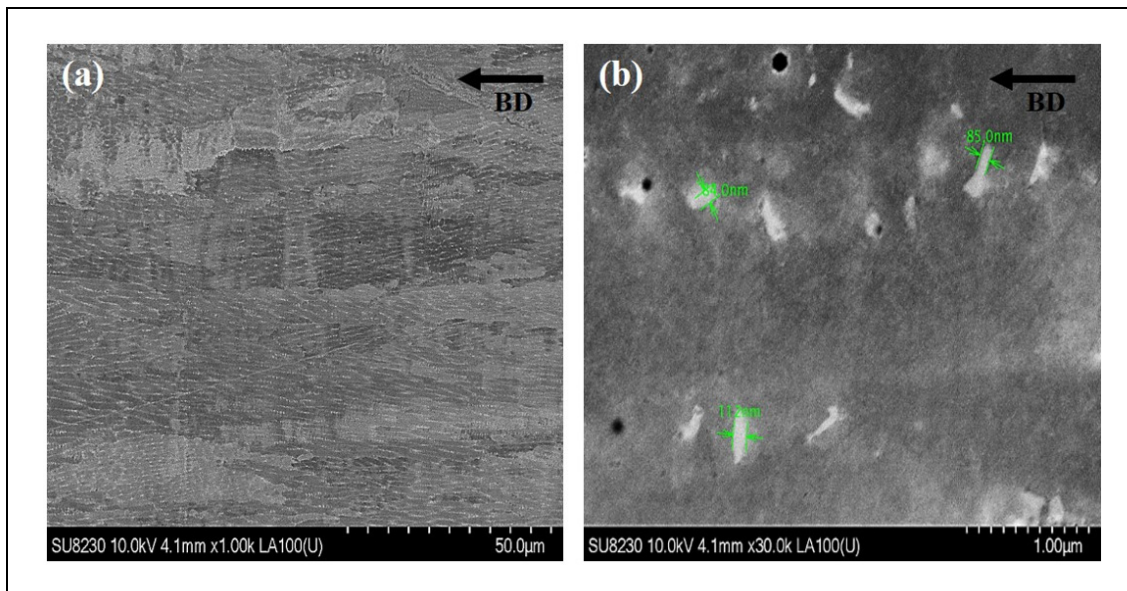


Figure 4.6 FE-SEM micrographs from the microstructure of the as-SLM IN718 sample. (a) Dendritic structure and (b) particles at the interdendritic regions

Figure 4.7 shows micro-hardness evolution from the bottom to the top of the as-SLM IN718 sample. The average hardness values decrease from  $\sim 290$  HV in B region to about 270 HV in M region and increases again to reach  $\sim 287$  HV in the T region. These considerable variations

of the hardness throughout the height of the sample could be induced by the thermal gradient in the Z-direction (vertical) and the presence of different microstructural features such as precipitates, DAS, and changes in Laves volume fraction. Indeed, as discussed in the previous section and shown in Figure 4.7, a more rapid heat extraction provokes as higher temperature drop rate ( $10^5$ - $10^6$  °C/s) and therefore smaller DAS as well as finer precipitation of strengthening phases,  $\gamma'$ ,  $\gamma''$ , and  $\delta$  in B and T regions which is contributing to the higher hardness in these regions. In contrast, for the middle layers, the cooling rate being slower, the material remained longer time at elevated temperatures ( $>900^\circ\text{C}$ ) which is high enough to dissolve, fully or partially, the strengthening phases formed during the printing process and ultimately reduces its hardness. The above findings are also in agreement with those reported by Chen et al. (Y. Chen et al., 2019), Moussaoui et al. (Moussaoui et al., 2018), and Bayerlein et al. (Bayerlein, Bodensteiner, Zeller, Hofmann, & Zaeh, 2018) who observed similar DAS values and precipitation of the strengthening phases in the regions with the highest thermal gradients.

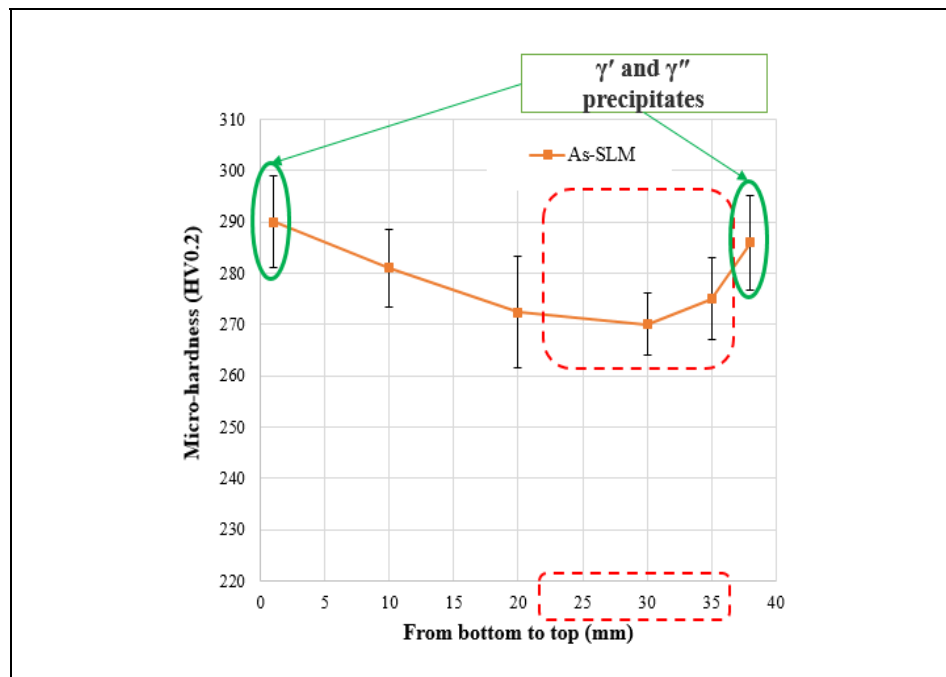


Figure 4.7 Variation of the microhardness measured from bottom to the top of as-SLM sample

### 4.3.2 DTA test

The DTA results are shown in Figure 4.8 where the precipitation and dissolution temperatures of phases are extrapolated according to the exothermic and endothermic peaks, respectively. The corresponding determined temperatures are also provided in Table 4.3. The results show that the first peak temperature is around 540 °C for the sample heated with the rate of 10 °C/min. Niang et al. (Niang et al., 2010) in their work on kinetics of precipitation in wrought IN718, reported that this peak corresponds to  $\gamma'$  precipitation (p). The other peaks correspond to the dissolution (d) of  $\gamma'$ , transformation of  $\gamma''$  to  $\delta$ , and finally dissolution of the  $\delta$  phase. It must be noted that the very small size of the  $\gamma'$  particles, suggests that they are most probably of tertiary type, as also reported in (Masoumi, Shahriari, et al., 2016a). The results also show that with increasing the heating rate from 10 to 100 °C/min, both the dissolution and precipitation reactions shift to higher temperatures. For example, the dissolution temperature of the  $\gamma'$  particles increased by 112 °C, and those of  $\gamma''$ , and  $\delta$  phases increased by 72 °C, and 73 °C, respectively. In this study, the focus was before liquation and melting because the melting temperature is principally independent of the heating rate.

Table 4.3 Variation of precipitation (p) and dissolution (d) temperatures of  $\gamma'$ ,  $\gamma''$ , and  $\delta$  phases in the SLM-IN718, for different heating rates

Heating rate (°C/min)	Temperature (°C)					
	$\gamma'$ - p	$\gamma'$ - d	$\gamma''$ - p	$\gamma''$ - d	$\delta$ - p	$\delta$ - d
10	540	589	736	801	886	984
15	557	595	741	817	926	1008
25	560	614	754	831	962	1024
50	572	663	761	840	948	1035
80	596	678	776	860	965	1051
100	600	700	798	873	990	1057

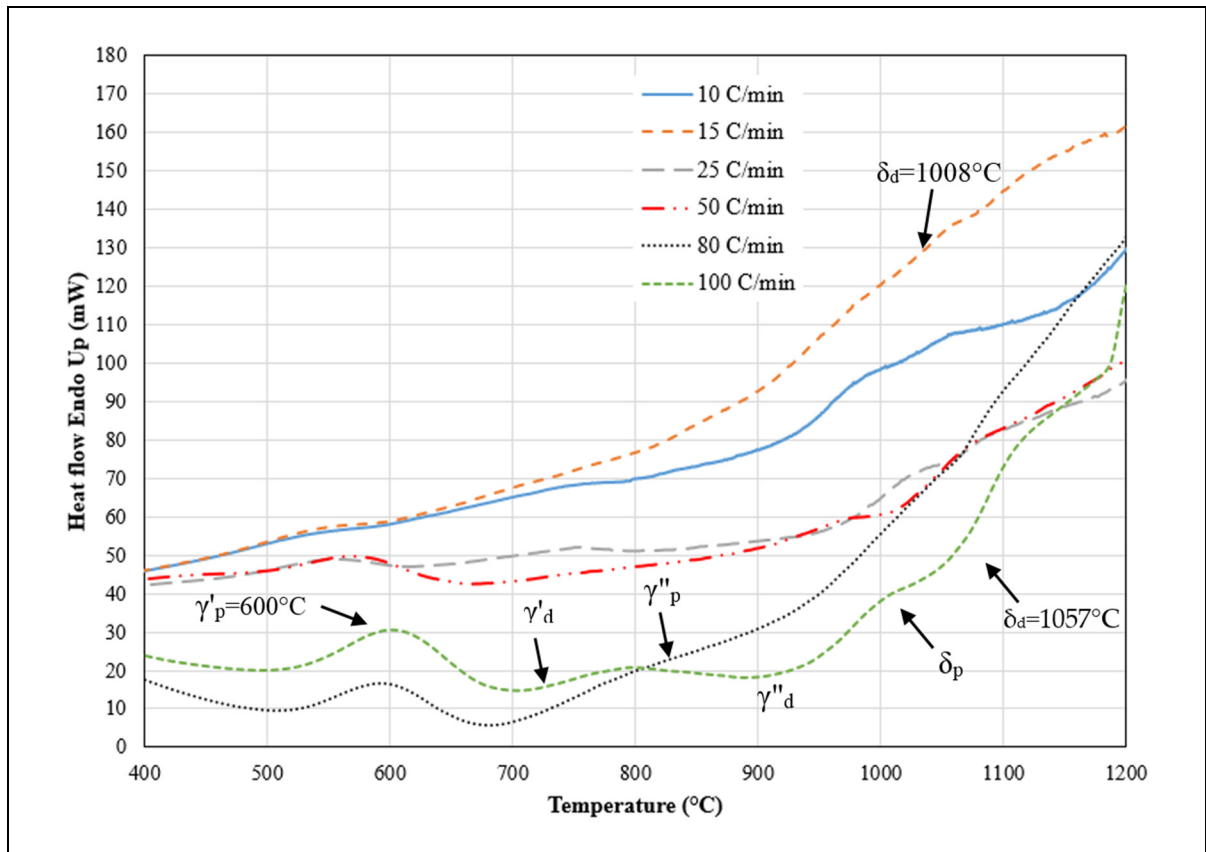


Figure 4.8 DTA records obtained on the as-SLM IN718 upon heating at scanning rates of 10, 15, 25, 50, 80, and 100 °C/min up to 1200 °C. The subscripts 'd' and 'p' represent the dissolution and precipitation temperatures of the corresponding phase

It has been reported (Chrostek, 2016; X.-Y. Wang, Wen, Cheng, Gu, & Lu, 2019; X. Wang & Chou, 2018) that changes in the heating rate modified the microstructure and the distribution of elements in the matrix resulting in changes in the chemical reaction temperatures and hence the DTA results. The results, reported in Table 4.3, quantify these changes for the examined samples in the present study and show that indeed the precipitation temperatures of  $\gamma'$ ,  $\gamma''$  and  $\delta$  phases increased by increasing the heating rate because there was less time for elemental diffusion and chemical reactions for precipitation of each phase at higher rates.

Based on the obtained results, the dissolution rate for the three precipitating phases were determined and the results are reported in Figure 4.9. The dissolution rate of  $\gamma'$  follows a parabolic pattern, as shown in figure 4.9 (a), and described by the following equation:  $T =$

$485.49 \times \text{Hr}^{0.0778}$ . The  $\gamma''$  dissolution evolution is shown in Figure 4.9 (b) where a parabolic ( $T = 742.61 \times \text{Hr}^{0.0339}$ ) trend can also be seen. This behavior can also be considered as two linear regimes ranging between 25 to 50 °C/min (S1) and 80 to 100 °C/min (S2). It must be noted that the  $\gamma''$  solvus temperature depends on the initial size of the precipitates; therefore, the greater the size of the precipitates, the larger the deviation will be. Soucail et al. (Soucail & Bienvenu, 1996; Soucail et al., 1992) observed similar behavior for the dissolution rate of secondary  $\gamma'$  in Astroloy during heating. In particular, they found that the departure from equilibrium dissolution temperature was lower for smaller secondary  $\gamma'$  precipitates but increased with the heating rate in the interval 1-300 °C/s. As shown in Figure 9 (c), the  $\delta$  phase dissolution temperature presents a non-linear dependence to the heating rate ( $T = 928.51 \times \text{Hr}^{0.0284}$ ).

It is also important to note that, the above relations indicate that  $\gamma''$  and  $\delta$  particles could still be present up to 1000 °C under high heating rates (e.g. 100 °C/s or more), while the much finer  $\gamma'$  particles dissolve. As reported by several authors (Beaubois, Huez, Coste, Brucelle, & Lacaze, 2004; Lalvani & Brooks, 2016; J. Li et al., 2019; Sui, Tan, et al., 2019),  $\gamma''$  particles as metastable phase, start to decompose to the more stable  $\delta$  phase at temperatures around 750 °C. However, their SEM examinations revealed that  $\gamma''$  phase was still present at 900 °C, which is above the  $\gamma''$  solvus temperature. Furthermore, the dissolution temperature of the  $\delta$  phase has been reported to be between 990 °C and 1020 °C (Beaubois et al., 2004; J. Li et al., 2019); however, this study shows that the initial dissolution temperature of  $\delta$  increased from 984 to 1057 °C when the heating rate was increased from 10 to 100 °C/min, respectively.

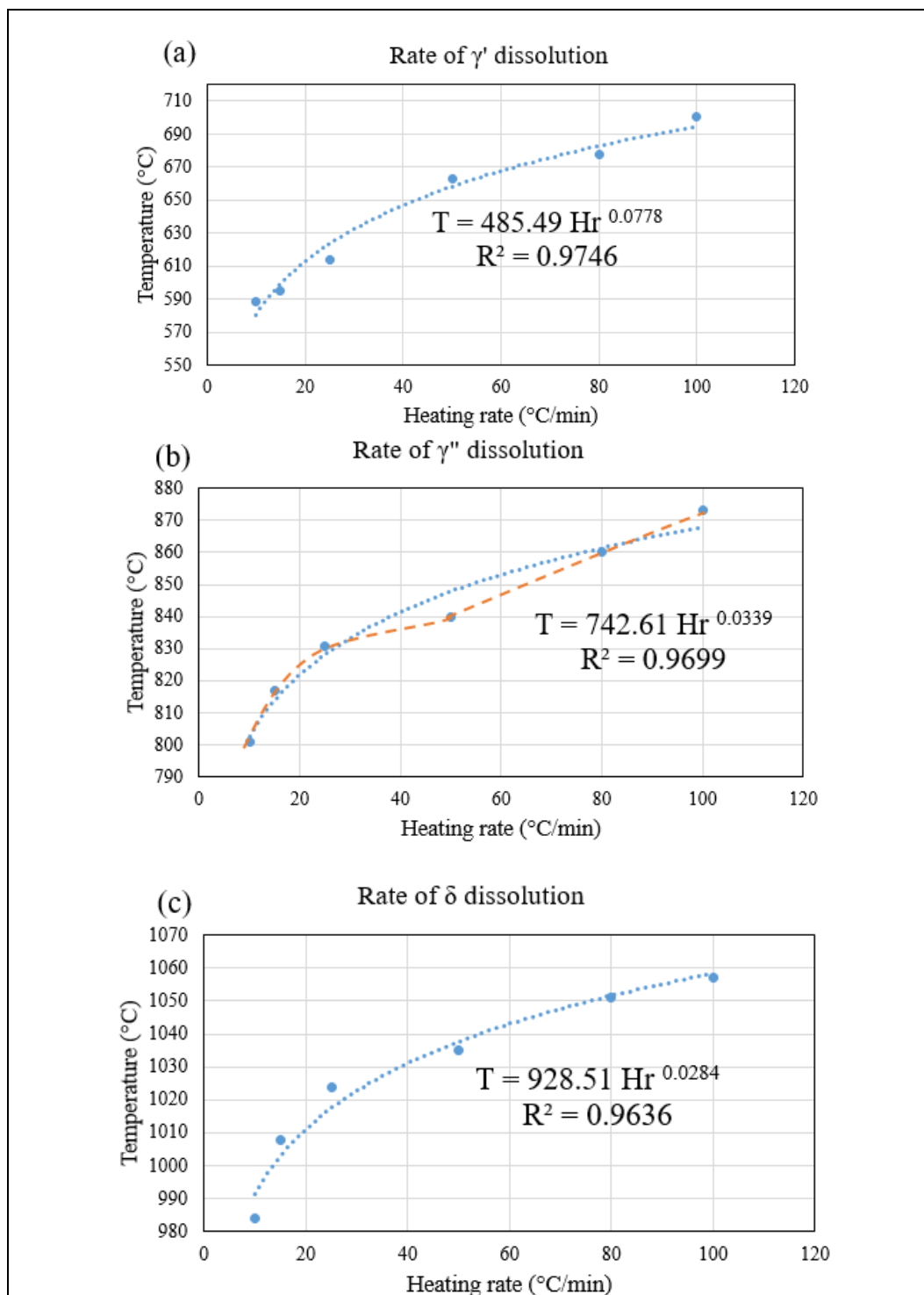


Figure 4.9 Variations of: (a)  $\gamma'$ , (b)  $\gamma''$ , and (c)  $\delta$  phase dissolution temperature (T) with heating rate (Hr) at the top section of the SLM IN718 sample

### 4.3.3 High heating rate tests

Microstructure examinations of the observed zones (identified in Figure 4.2) revealed a specific variation from the surface to the center, as indicated by the arrow in Figure 4.10. These features, located from just few micrometers below the surface until a depth of about 100  $\mu\text{m}$ , called blocky zones, appeared along the dendrites from the surface toward the center. Only dendritic microstructure was observed below this zone (yellow line) down to the center of the sample. This change could be attributed to the transient thermal gradient from the surface to the center of the samples during rapid heating.

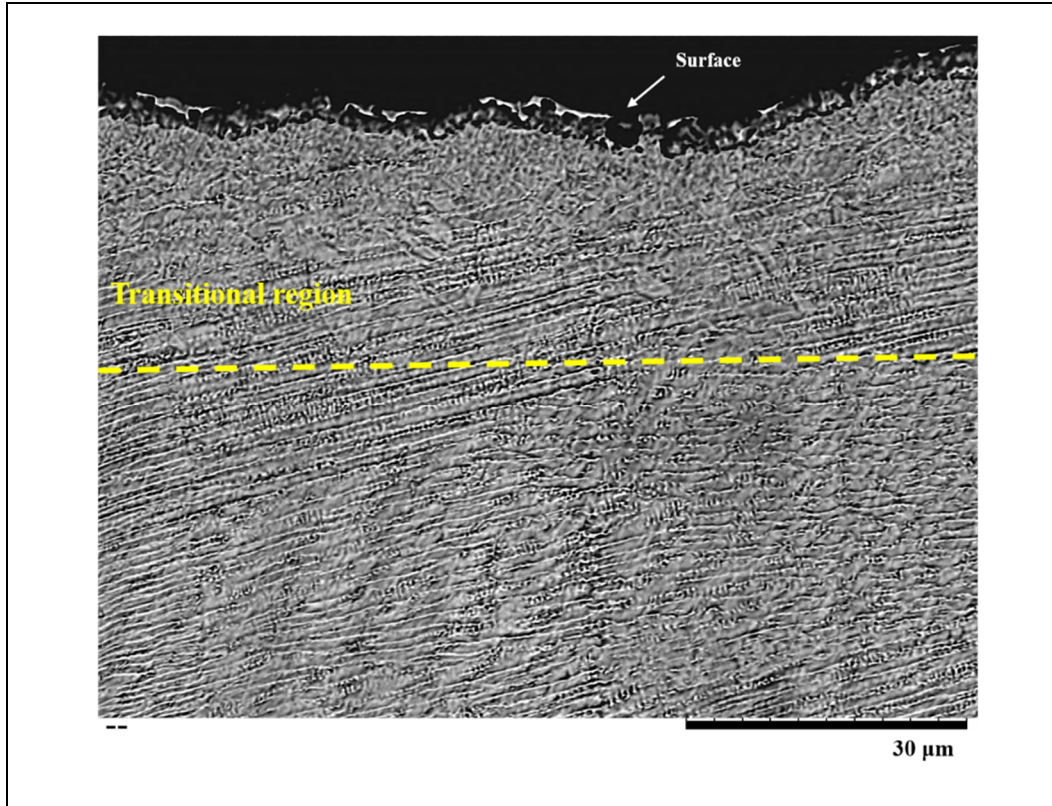


Figure 4.10 SEM image showing the microstructure near to the surface area of the sample heated to 1000  $^{\circ}\text{C}$  with 100  $^{\circ}\text{C}/\text{s}$  and dwell time 10 s followed by cooling at a constant rate of 65  $^{\circ}\text{C}/\text{s}$

In order to assess whether the presence of a temperature gradient could be the cause for the observed features, a model proposed by Semiatin et al. (Semiatin, Mahaffey, Levkulich, & Senkov, 2017) that predicts the radial temperature gradient developed in a round-bar sample

was used. The analysis was based on a one-dimensional heat conduction equation for a round bar of infinite length and used direct local temperature measurements corroborated by microstructural observations, as in the present study. Using the above model and considering similar physical properties for IN718 and SLM IN718 (e.g. thermal conductivity, thermal convection, and emissivity (Keller et al., 2015)) the radial thermal gradient from the surface to center was estimated for heating rates of 100 °C/s and 200°C/s and the results are reported in Figure 4.11. In this figure, ( $\Delta T$ ) represents the difference between the temperature applied to the sample surface (1000 °C, measured by the thermocouple) and the center of the sample during the heating cycle defined in the radial direction (based on the model proposed in reference (Semiatin et al., 2017)). It can be seen that  $\Delta T$  is very small in the first 250  $\mu\text{m}$  below the surface and starts to increase afterward, reaching its maximum value at the center. Therefore, the microstructural features observed in the near surface region of samples are most probably not related to a temperature gradient effect.

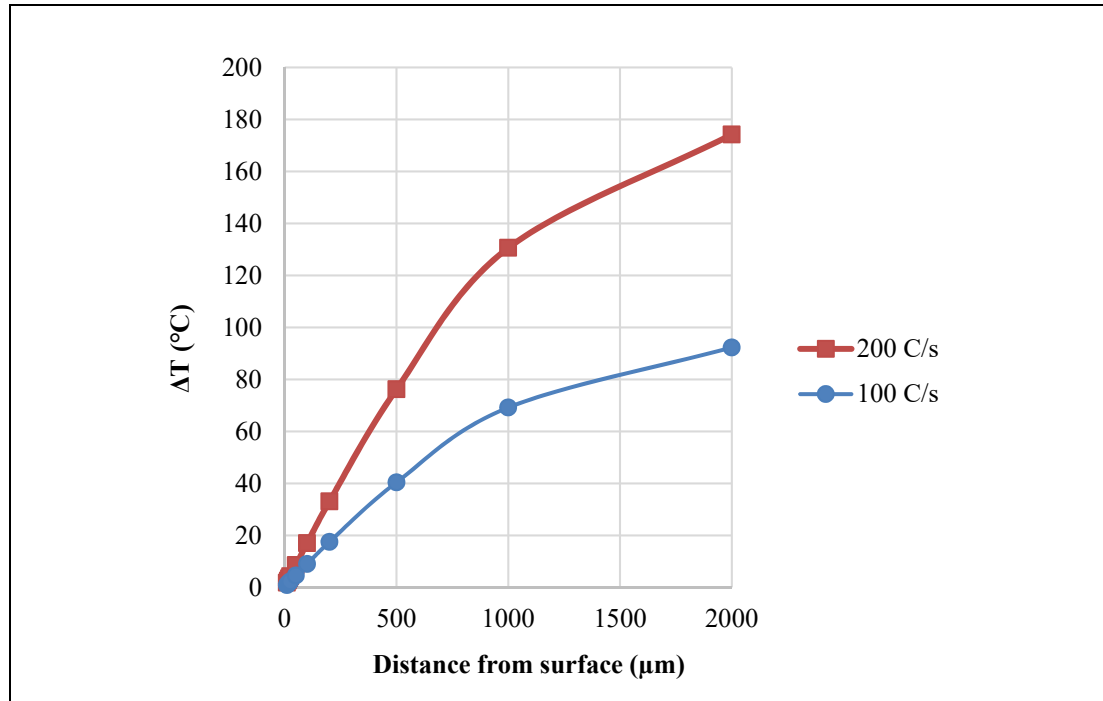


Figure 4.11 Estimated radial temperature gradients in 4-mm diameter SLM IN718 dilatometer samples for two heating rates. Surface temperature is 1000 °C

Figure 4.12 (a-c) shows the microstructural features revealed along the longitudinal direction near the surface at mid-span of dilatometer SLM-IN718 samples (as indicated in Figure 4.2) exposed to heating rates of 100, 200, and 400 °C/s, respectively. The blocky zones are circled in the three micrographs and were observed in between the dendrites as well as very close to them. The Laves phase (white particles) were also observed at interdendritic regions close to these zones and even elongated into them.

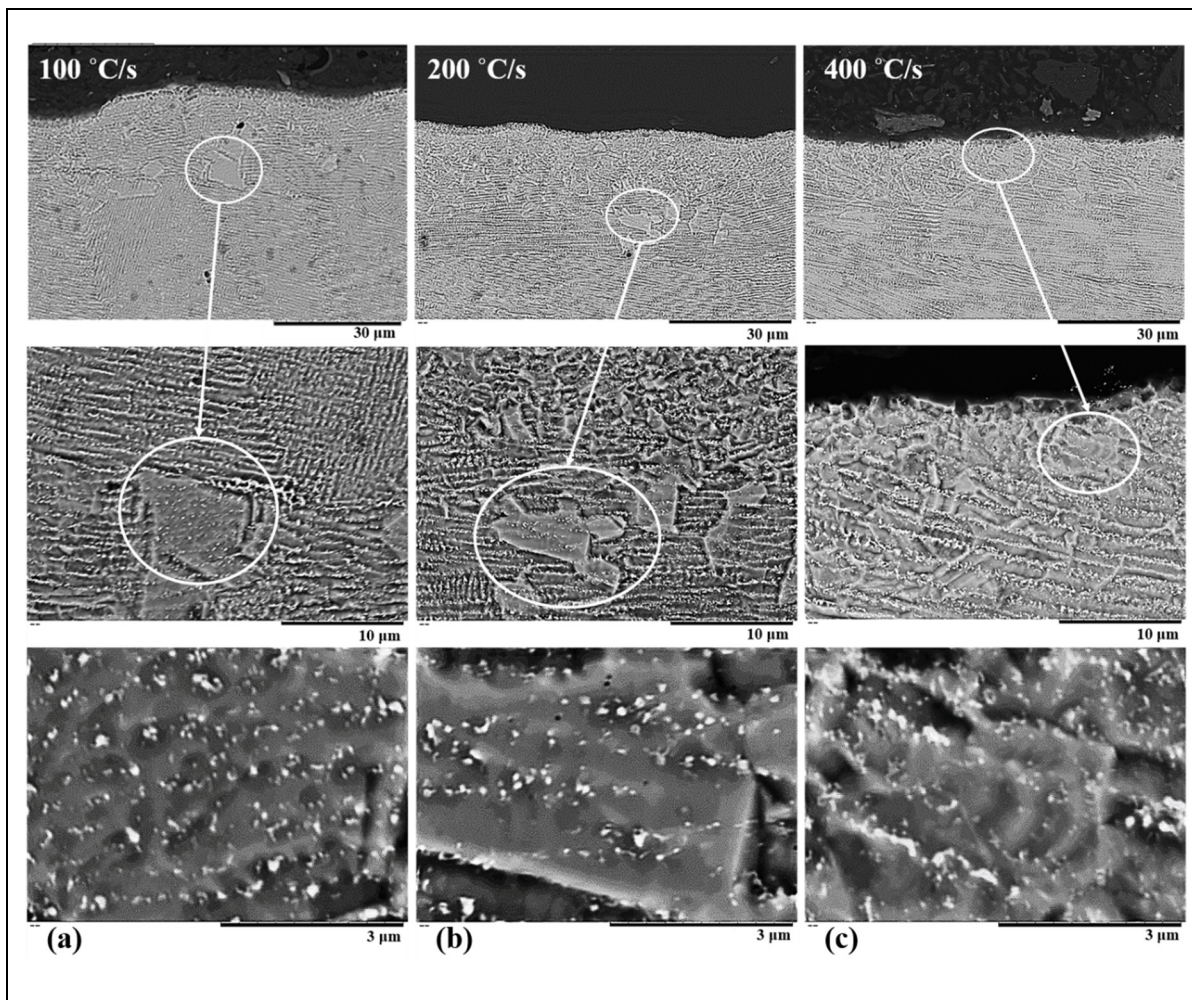


Figure 4.12 SEM images showing blocky zones in the sub-surface area at the mid-span of longitudinally cut samples heated to 1000 °C at the rates of (a) 100, (b) 200, (c) 400 °C/s and 10 s holding time, and cooled by constant rate 65 °C/s

These blocky zones contain different particles that were analyzed by EDS and the results are reported in Table 4.4. The map analysis, Figure 4.13, shows the presence of Nb and Mo-rich particles within these zones and at their boundaries for all different heating rates. The Laves (white particles) were detected and had fine and granular shaped for 100 and 200 °C/s heating rates, while they became irregular and long-striped shaped particles for the 400 °C/s. As reported by Sui et al. (Sui, Tan, et al., 2019), this change (Laves phases from long-striped to granular shapes) could be related to Laves phase dissolution process during heating. Indeed, the interdendritic Laves phases contain a certain amount of micro-segregated niobium that could dissolve and diffuse into the matrix or contribute to the formation of  $\gamma''$  precipitates (for longer time exposure). Furthermore,  $\delta$  and  $\gamma''$  particles were observed alongside the Laves particles at higher magnifications in transitional zones, as reported in Figures 4.12 and 4.14. A comparison between the average size of  $\gamma''$  particles prior to the heating ( $80 \pm 34$  nm) and after heating ( $96 \pm 30$  nm) in the top of SLM samples reveals that the smaller  $\gamma''$  particles were dissolved for the heating rate of 100 °C/s.

Table 4.4 Chemical composition (wt.%) in sample heated at 100 °C/s

<b>Phases</b> \ <b>Elements</b>	Ni	Cr	Fe	Nb	Mo	Ti	Al
Matrix in blocky zone	Bal.	16.56	16.21	4.98	2.89	1.28	0.31
Laves in interdendritic region	Bal.	10.98	10.80	34.05	5.85	3.98	0.0
MC carbide	Bal.	3.08	2.96	47.71	6.10	10.78	0.0
$\delta$ - precipitate	Bal.	17.93	17.26	9.09	5.06	1.68	0.06
$\gamma''$ - precipitate	Below the EDS detection limits						

The formation and dissolution of precipitates such as  $\gamma''$ , Laves, and  $\delta$  phases are directly related to the amount of the Nb in the microstructure (Rafiei, Mirzadeh, Malekan, & Sohrabi, 2019; Sohrabi & Mirzadeh, 2019b). The stress field induced by dislocations and vacancy inside the Laves phase act as driving forces for generating the migration of the dislocations and solute atoms (e.g. Nb and Mo) (Sui et al., 2020). Moreover, the non-coherent interface between the Laves phase and  $\gamma$ -matrix enhances the concentration of vacancies, which facilitates the movement of solute atoms of constitutional elements to  $\gamma$  matrix thereby increasing the dissolution rate of the Laves phase. Nb and Mo are also the most severely segregated elements in the IN718 alloys, and thus it is relatively easy to measure their segregation (Kumara et al.,

2019). Examination of the microstructure in the blocky zones revealed that the interdendritic Laves phase is dissolved in the  $\gamma$ -matrix. Similar findings were also reported by Raza et al. (Raza et al., 2019) and Owczarski et al. (Owczarski et al., 1966) in a fusion welded IN718 alloy by GTAW. It is interesting to note that, partial or even full dissolution of the Laves phase has also been reported; however, such dissolution was not observed under the experimental conditions examined in the present study.

Based on the above analysis, it is expected that Nb and Mo, as the two main constituent elements, diffuse back into the matrix and stay in solid solution or could participate in the composition of  $\delta$  and  $\gamma$ " due to the change the precipitation and the dissolution temperatures of these phases. However, despite it is intuitively evident that heating rate should influence the dissolution process through the diffusion distance ( $x$ ); this needs to be quantified if microstructure evolutions are to be modeled. Soucail and Bienvenu (Soucail & Bienvenu, 1996) proposed an additive time-temperature incremental approach that takes into account the contributions from the dwell time and heating (and/or cooling) rates. Specifically, they used an "effective diffusion" time using the classical "equivalent time" ( $t_e$ ) and activation energy concepts.

The equivalent time  $t_e$  was estimated by the integration of an Arrhenius type diffusion law from an initial time ( $t_i$ ) and initial temperature  $T_i$  to a final time ( $t_f$ ) and final temperature  $T_f$ :

$$t_e = \int_{t_i}^{t_f} \exp\left(-\frac{Q_e}{R}\left(\frac{1}{T} - \frac{1}{T_h}\right)\right) dt \quad (4.2)$$

In the above equation,  $R$  is the universal gas constant,  $Q_e$  is the equivalent activation energy for the diffusion process, and  $T_h$  is the temperature at holding time ( $t_h$ ). The influence of the heating rate ( $H_r$ ) is represented as:

$$t_e = \int_{t_i}^{t_f} \exp\left(-\frac{Q_e}{R}\left(\frac{1}{H_r(t-t_f)+T_h} - \frac{1}{T_h}\right)\right) dt \quad (4.3)$$

$$t_e = \int_{t_i}^{t_f} \exp\left(-\frac{Q_e}{RT_h} \left(\frac{1}{\frac{H_r(t-t_f)}{T_h} + 1} - 1\right)\right) dt \quad (4.4)$$

Because:

$$\left|\frac{H_r(t-t_f)}{T_h}\right| = \left|\frac{T-T_h}{T_h}\right| \text{ and } \left|\frac{T-T_h}{T_h}\right| \ll 1 \quad (4.5)$$

Equation (4.4) simplifies into:

$$t_e = \frac{T_h^2 R}{Q_e H_r} \left(1 - \exp\left(\frac{Q_e(T_i - T_h)}{RT_h^2}\right)\right) \quad (4.6)$$

A similar equation for the cooling cycle will be obtained by replacing  $H_r$  by  $C_r$ . Thus, the total equivalent time including the heating stage, holding time and cooling would be obtained by summing the two  $t_e$  times for heating and cooling and the for the ( $t_h$ ) for the holding time. In the present case, the exponential term could be neglected, as it is very small, when considering the examined temperatures. Therefore,  $t_e$  for heating becomes ( $t_e \approx \frac{T_h^2 R}{Q_e H_r}$ ), and ( $t_e \approx \frac{T_h^2 R}{Q_e C_r}$ ) for cooling. The equivalent holding time for the entire diffusion process becomes:

$$t_e = \frac{T_h^2 R}{Q_e} \left(\frac{1}{H_r} + \frac{1}{C_r}\right) + t_h \quad (4.7)$$

On the basis of the above discussion, the diffusion distance ( $x$ ) of Nb from the Laves phase in the interdendritic regions to the  $\gamma$ -matrix (core of the dendrites) is controlled by  $t_e$  which can be determined using Fick's second law,  $x = \sqrt{D_e t_e}$ .

In the above equations, the diffusion coefficient of Nb in Ni was calculated according to the following equation, obtained from the literature (Keller et al., 2015; Rafiei et al., 2019; Sohrabi & Mirzadeh, 2019b, 2019c; Sui et al., 2020):

$$D_e \text{ (m}^2\text{/s)} = 1.04 \times 10^{-6} \exp(-201700/RT_h) \quad (4.8)$$

where  $D_e$  is the diffusion coefficient of the considered element during the equivalent time. Using the above equations, the diffusion distance ( $x$ ) of Nb at 1000 °C was calculated. For example, this value was estimated to be in the interval 260 to 230 nm for heating rates from 100 to 400 °C/s and equivalent time ( $t_e$ ) values ranging between 11.7 to 11.1 s, respectively. These values could justify the small transitional areas (~one third of DAS or interdendritic zone) and localized dissolution of the Laves phase. It should be noted that the average DAS ( $\lambda$ ) of all samples was about  $0.832 \mu\text{m} \pm 0.147$ , which was close to the DAS value measured within MT and T regions in the as-SLM specimens (as reported in Figure 4.4).

From Equations (4.7) and (4.8) as well as relation,  $x = \sqrt{D_e t_e}$ , a logarithmic relation (Equation (4.9)) between diffusion distance ( $x$ ) and heat rate ( $H_r$ ) can be established:

$$x \text{ (}\mu\text{m)} = -0.006 \times \log^{H_r} + 0.2827 \quad (4.9)$$

The TTT diagram presented by Ning et al. (Niang et al., 2010) also confirms that even at rapid heating (1–10 °C/s) and at appropriate temperatures (>900 °C),  $\gamma''$  and  $\delta$  phases can form and therefore delay the dissolution of existing second phase particles. These findings are in contrast with those of Roder et al. (Roder et al., 2005) who did not observe any delay in the dissolution of the  $\gamma''$  and  $\delta$  phases in a wrought IN718 after the application of high heating rates, thus demonstrating the difference in the response of SLM material as compared to a wrought one.

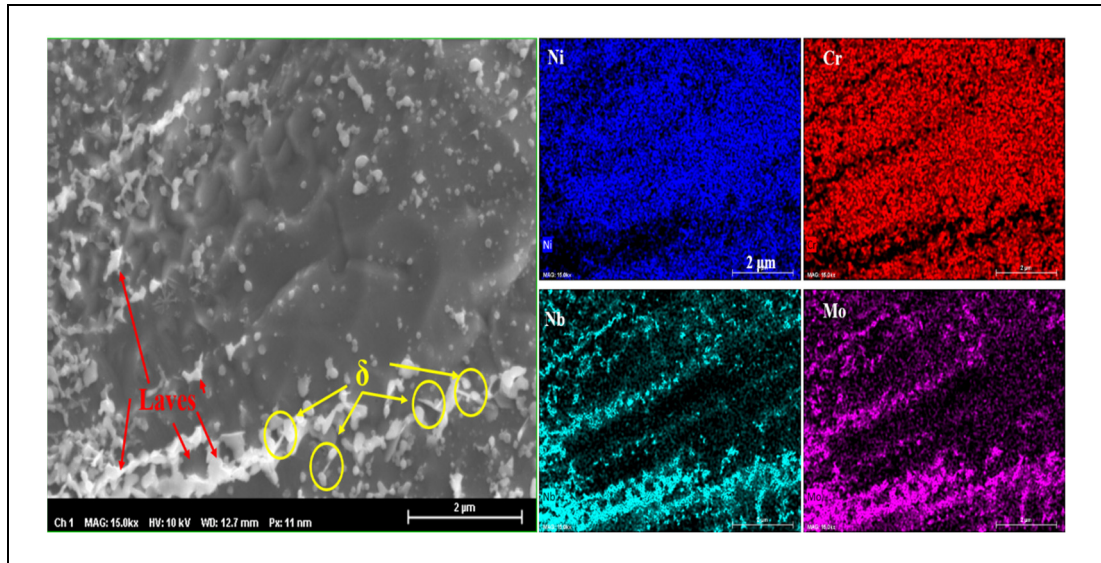


Figure 4.13 Chemical EDS mapping of some principal elements of as-SLM IN718 sample heated to 1000 °C for 200 °C/s

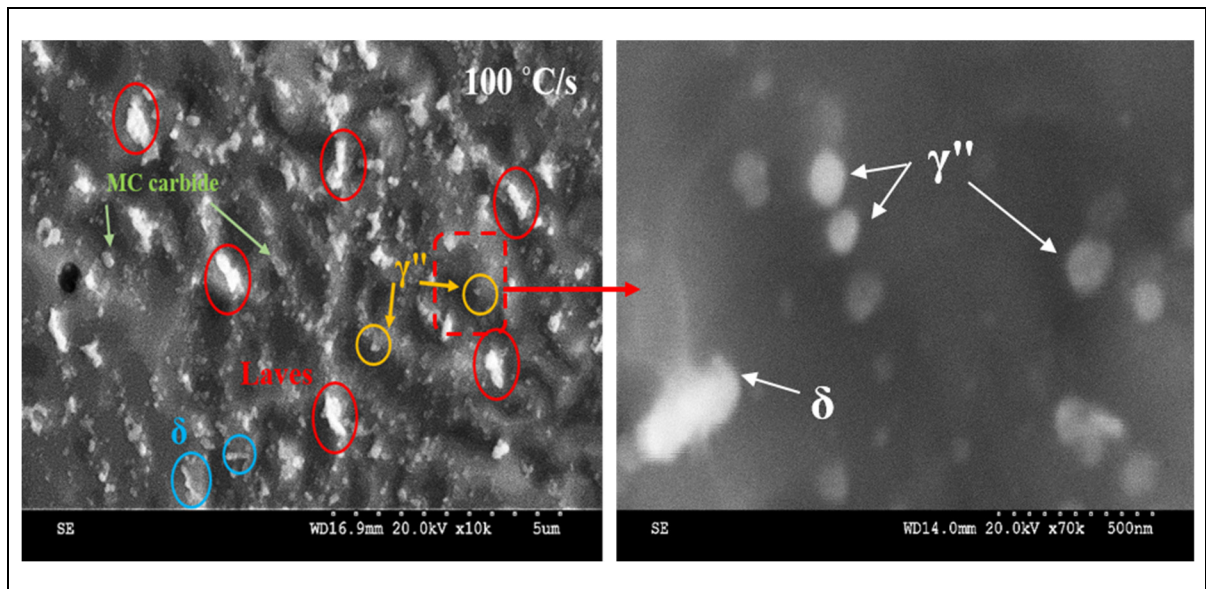


Figure 4.14 SEM images of the blocky zone show the presence of different precipitates such as semi-spherical  $\gamma''$  and  $\delta$  particles for sample heated to 1000 °C at a rate of 100 °C/s

Table 4.5 shows the influence of the heating rate on microstructural features. For example, the thickness of the zone over which blocky zones were observed decreased from  $12.08 \pm 2.01$  to  $4.23 \pm 1.01$   $\mu\text{m}$  when the heating rate increased from 100 to 400 °C/s, respectively. This trend was also observed in the average area fraction of the blocky zones with increasing heating

rates. The data reported in Table 4.5 also shows that Nb concentration in Laves phase with spherical shape in the interdendritic region was significantly higher than in the blocky region. For instance, for the 100 °C/s heating rate, this concentration is around 34.05 wt.%, while it decreases to  $15 \pm 3.8$  wt.% in white Laves particles within the blocky zones. The concentrations of Nb and Mo (wt. %) at the center of the dendrite core in the top section of the SLMed samples were measured to be 3.33 wt.% and 1.75 wt.%, respectively. These amounts increased to 4.98 wt.% (Nb) and 2.89 wt.% (Mo) after heating at a rate of 100 °C/s in the matrix of the transitional region (about 100  $\mu\text{m}$  below the surface). However, for the heating rate of 400 °C/s, the intensity of these changes was reduced, so that the level of Nb and Mo in the matrix of the transitional region reached 4.51 and 2.46 (wt. %), respectively. Due to the increased heating rate, the time is much shorter for Nb diffusion from the Laves phase into the matrix or to  $\gamma$  and  $\delta$  phases. Hence, the measured average concentration of Nb in the Laves phase was higher for higher heating rates ( $15 \pm 3.8$  % to  $17 \pm 3.9$  wt.% for 100 and 400 °C/s, respectively). The changes in Nb concentration exhibited an inverse relationship to the variations in the Laves volume fractions. This probably indicates that the Nb trapped inside the Laves phase in the “solidified” microstructure was released and diffused back into the dendrite core as a consequence of the very fast heating and cooling (Kumara et al., 2019). Therefore, there was still enough time for elemental diffusion for high heating rates (i.e. 20 s for 100 °C/s) but its severity decreased for the higher rate of 400 °C/s (12.5 s).

Table 4.5 Microstructural characteristics of the SLMed IN718 for different heating rates

<b>Heating rate (°C/s)</b>	<b>Thickness (<math>\mu\text{m}</math>)</b>	<b>Area of blocky zones (<math>\mu\text{m}^2</math>)</b>	<b>Laves (wt.%)</b>	<b>Nb<sub>Laves</sub> (wt.%)</b>	<b>Shape of Laves phase</b>
100	$12.08 \pm 2.01$	$13.5 \pm 10.24$	$5.45 \pm 0.67$	$15 \pm 3.8$	Fine and granular
200	$9.61 \pm 1.97$	$6.65 \pm 3.64$	$4.14 \pm 0.28$	$14 \pm 4.6$	Fine and granular
400	$4.23 \pm 1.01$	$5.76 \pm 4.49$	$3.25 \pm 0.53$	$17 \pm 3.9$	Irregular and long-stripped

#### 4.3.4 Hardness variations

Figure 4.15 shows the hardness distribution curves measured from the surface to the center of the dilatometer specimens for three heating rates (100, 200 and 400 °C/s) in the area considered to be the possible HAZ after the welding processes. The hardness was higher in the transitional region located near the surface (100  $\mu\text{m}$ ) affected by heating compared with the rest of the SLM part. The hardness decreased when moving out of the transitional region and become very close to the hardness value measured in the dashed line area in Figure 4.7 (before applying the heating). The higher hardness in the transitional region is probably due to the combination of three mechanisms: (1) the decomposition of Laves phase at the blocky zones; (2) the diffusion of Nb and Mo into the  $\gamma$ -matrix resulting in  $\gamma''$  and  $\delta$  precipitations, and (3) the stability of the  $\gamma''$  and  $\delta$  precipitates for temperatures up to 1000 °C.

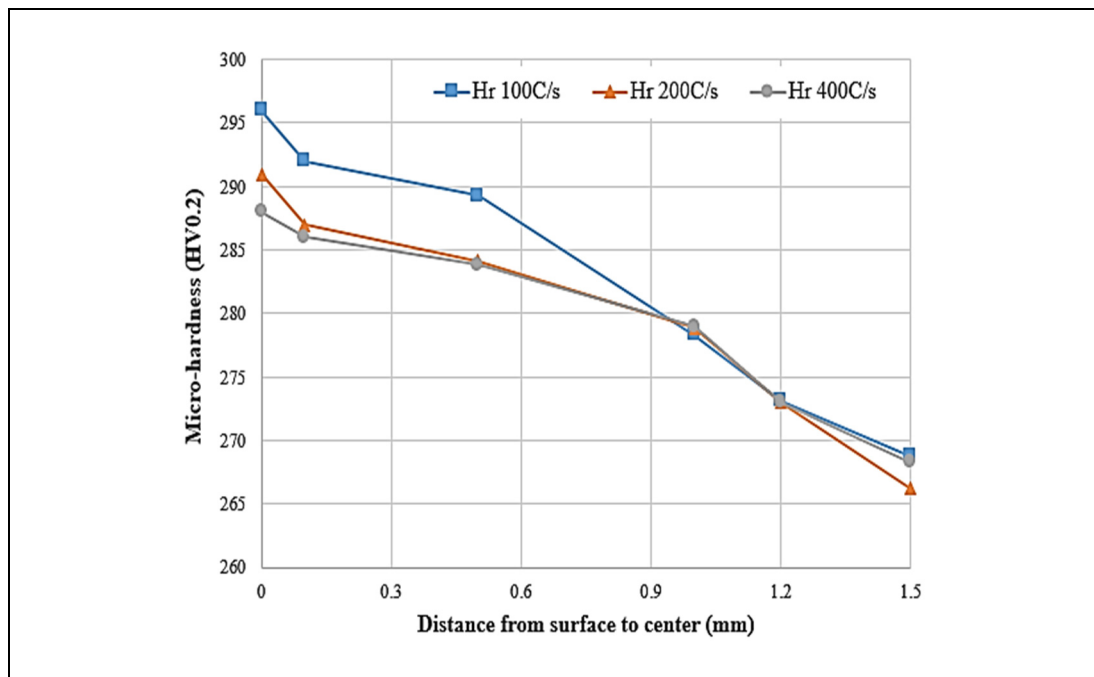


Figure 4.15 Hardness distribution curves of the SLMed IN718, from the surface to the center of the sample for different heating rates in area showed in Figure 4.7.

#### 4.4 Conclusions

In this study, various heating rates were applied to additively manufactured IN718 samples. The evolution of the microstructure, hardness, and phase changes were analyzed and discussed before and after heating for different heating rates. The main findings are:

1. A transitional zone characterized with the presence of blocky zones was identified in the subsurface region of the samples.
2. It was demonstrated that the transitional zone was not due to a thermal gradient in the sample but to microstructural changes.
3. The evolution of  $\gamma''$  and  $\delta$  phases in the SLM samples is different when compared to wrought materials when submitted to high heating rates.
4. The diffusion rate and/or the solubility of Nb in the  $\gamma$  phase increased at higher heating rates. The remaining Nb content in the interdendritic areas was determined to be insufficient for the Laves phase to form. The morphology of the Laves phase changed from fine and granular for 100 °C/s to long-stripped for 400 °C/s demonstrating that less time was available for Nb dissolution of in the matrix and/or precipitation.

## CHAPTER 5

### GRAIN SIZE AND MISORIENTATION EVOLUTION IN LINEAR FRICTION WELDING OF ADDITIVELY MANUFACTURED IN718 TO FORGED SUPERALLOY AD730™

Seyedmohammad Tabaie <sup>a</sup>, Farhad Rézaï-Aria <sup>b</sup>, Bertrand C.D. Flipo <sup>c</sup>, Mohammad Jahazi <sup>a</sup>

<sup>a</sup> Department of Mechanical Engineering, École de Technologie Supérieure,  
1100 Notre-Dame West, Montreal, QC, Canada.

<sup>b</sup> Institut Clément Ader (ICA), Université de Toulouse, CNRS, IMT Mines Albi, INSA, UPS,  
ISAE, Campus Jarlard, 81013 Albi, France.

<sup>c</sup> TWI Ltd., Granta Park, Great Abington, Cambridge CB21 6AL, United Kingdom.

Paper published in *Materials Characterization*, November 2020

#### Abstract

Selective Laser Melted (SLM) Inconel718 (IN718) superalloy was linear friction welded (LFWed) to forged AD730™ Nickel-based superalloy. Successful joints free of micro-porosity, micro-cracking, and oxides were obtained. Microstructure variations across the weld line developed during LFW were examined using different techniques, including laser confocal microscopy, scanning electron microscopy, energy dispersive spectroscopy (EDS) and electron backscatter diffraction (EBSD). The microstructure was also evaluated, particularly in terms of grain size and misorientation changes were determined and correlated with microhardness evolution in different regions of the weld joint. The characteristics of the microstructure on both sides of the weld joint was analyzed and related to the deformation and temperature paths imposed during the LFW process. Dynamic recrystallization (DRX) occurred on both sides of the dissimilar weld line, and it was found that Discontinuous DRX (DDRX) and Continuous DRX (CDRX) took place in the WZ and in the TMAZ, respectively. In order to study the influence of the starting microstructure in the LFW experiments, LFW of a homogenized SLM IN718 sample was analyzed and compared with the non-homogenized sample. A clear change in the size and grain misorientation levels of the heat and thermomechanical affected zones were observed between the two conditions. The differences were related to a greater degree of strain induced in homogenized sample and the increasing

effect of the solid solution strengthening mechanism caused by a partial dissolution of the second-phase strengthening particles in the matrix.

**Keywords:** Additive manufacturing; Dissimilar linear friction welding; Ni-based superalloys; Dynamic recrystallization; Misorientation; Microhardness.

## 5.1 Introduction

LFW is a modern solid-state welding technique initially introduced for manufacturing and repairing blade integrated disks (blisks) in the compressor section of gas turbines made of titanium alloys (Ahmad Chamanfar et al., 2015). In recent years, LFW has also been applied to the assembly of components made of Nickel (Ni)-based superalloys, as well as in many other engineering applications, ranging from automotive to agriculture, and allowing for new designs and applications (Ahmad Chamanfar et al., 2015; Ma et al., 2018). In addition to overcoming the disadvantages associated with mechanical assembly techniques, such as fretting fatigue and thermomechanical fatigue (Arakere & Swanson, 2001; Cortés et al., 2019; Ghorbanpour et al., 2020) observed in conventional blade-disk setups, or cracking and distortions in fusion-based welding assemblies, LFW joints are characterized by higher mechanical properties and extended component life in service (B. Gan et al., 2012; Homma, Takano, & Ozaki, 2019).

During the LFW process, a reciprocating movement, along with a normal pressure, is imposed on the two surfaces to be joined. The frictional force increases the temperature in a limited zone and removes surface imperfections and impurities such as oxides from the interface and allows a fresh contact between the two surfaces, which are joined in the last step by the application of a forge pressure. Therefore, the technique is ideally suited for assembling dissimilar materials tailored for specific designs and applications (Ahmad Chamanfar et al., 2015). The thermomechanical cycle imposed during the LFW process produces three distinct zones, namely, the Weld Zone (WZ), where the highest temperatures and deformations are imposed; the thermomechanical affected zone (TMAZ), characterized by deformed grains; and

the heat affected zone (HAZ), where only the heat of the welding has affected the material (Ahmad Chamanfar et al., 2015).

Additive manufacturing is of great interest for the fabrication of components and structures with complex geometries for the aerospace and power generation industries, as well as an advanced technique for component repair (Vairis & Frost, 1998). Selective laser melting (SLM) as a laser powder bed fusion method is a widely applied powder bed additive manufacturing process being developed as an economically viable solution for processing of Ni-based superalloy (Attallah et al., 2016). In SLM, a laser beam is directed at deposited fine layers of metal powder, which are locally and rapidly heated up to fusion, together with part of the already deposited layers, and cooled down. The process is repeated layer by layer until the desired component, for example a blade, is fabricated (called *printing*) (Balbaa, Mekhiel, Elbestawi, & McIsaac, 2020; Hariharan et al., 2019; Jia & Gu, 2014). Gas turbine blades are known for their complex geometries and high time to market. SLM is therefore an excellent alternative to conventional fabrication techniques as it allows achieving new designs and significantly reducing the time to market constraints (Masoumi et al., 2017). Therefore, the combination of LFW and SLM as two advanced techniques could open new possibilities for both the gas turbine industry and other high value-added industries.

Very limited information is available on the dissimilar solid-state welding of superalloys and for LFW of a forged microstructure to an additively manufactured superalloy, it is actually non-existent. Even that limited information covers only forged to forged superalloys joined by Inertia Friction Welding (IFW), where a rotational movement is imposed at the interface, different from the linear sliding movement in LFW. Huang et al. (Z. W. Huang et al., 2007) welded IN718 to U720Li alloy by IFW and reported substantial microhardness differences in the HAZ and the WZ. They interpreted their results in terms of variations in grain size, diffusion of alloying elements, and different volume fractions of strengthening phases on both sides of the weld line. Muralimohan et al. (Cheepu & Che, 2020) investigated the intermixing of the ferrite and Ni phases in the weld interface during friction welding of IN718 with SM45C steel. Senkov et al. (Oleg N. Senkov et al., 2014) used IFW to join Mar-M247 and LSHR Ni-

based superalloys. They found that Mar-M247 alloy, which has a higher strength at high temperatures, presented a larger grain size at the WZ, but the thickness of this zone was narrower as compared to that of the softer alloy LSHR (Ma et al., 2016; Oleg N. Senkov et al., 2014). In addition to grain size, they reported that the level of stored energy induced by the grain rotation/misorientation compatibilities and changes in dislocations density, were significant parameters that could influence the mechanical properties of joints; the fraction of secondary phases were similarly significant parameters (Karadge, Preuss, Withers, & Bray, 2008; Ye et al., 2020).

In the present study, the LFW and SLM techniques were used to study the dissimilar welding of two superalloys with the ultimate goal of evaluating the possibility of manufacturing new generation of blisks. Specifically, the LFW of additively manufactured Inconel 718 (IN718) to forged AD730<sup>TM</sup> Ni-based superalloy is investigated. IN718 is a high strength superalloy extensively used for blade applications in gas turbines due to its good weldability and excellent resistance to cracking (X. Cao, Rivaux, Jahazi, Cuddy, & Birur, 2009; Damodaram, Ganesh Sundara Raman, & Prasad Rao, 2014; Radhakrishnan & Thompson, 1993). AD730<sup>TM</sup> is a Ni-based alloy recently developed by Auber & Duval Company as a new forged Ni-based superalloy for turbine disk applications, and its mechanical properties are comparable to those of other Ni-based superalloys such as Waspaloy, Udimet720 and IN718Plus (Z. W. Huang et al., 2007; Masoumi et al., 2017; Masoumi et al., 2019; Masoumi et al., 2018; Tabaie et al., 2019).

## 5.2 Experimental Procedures

The as-received forged AD730<sup>TM</sup> alloy was provided by Aubert & Duval. The alloy was produced by vacuum induction melting, followed by vacuum arc remelting (VAR), and was then radially forged to produce a bar-round billet. The bar was solutionized at 1080 °C for 4 hours, followed by air cooling. Rectangular samples (37 (L: length) × 26 (W: width) × 13 (H: height) mm<sup>3</sup>) were wire-electro discharge machined (EDM) from the as-received material for

LFW. The average grain size of the alloy microstructure was  $41.36 \pm 9.14 \mu\text{m}$ , with a  $\gamma'$  volume fraction of 40%. The chemical composition of the alloys is provided in Table 1.

Very similar rectangular samples ( $40$  (L: length)  $\times$   $26$  (W: width)  $\times$   $13$  (H: height)  $\text{mm}^3$ ) of IN718 superalloy, were fabricated by an SLM-125HL machine at IMT-Mines Albi, France, for LFW in as-fabricated conditions. Spherical-shape alloy powders with a particle size distribution between  $15$  and  $50 \mu\text{m}$  were used for SLM processing. The laser beam scanning orientation and the building direction were collinear with the Z-direction displacement and perpendicular to the fabrication platform. The laser beam scanning was rotated successively for  $67^\circ$  in each layer to reduce microstructural anisotropy. The area fraction of the porosities was measured all over the as-SLMed IN718 specimen after SLM and was determined about  $0.4\%$  in the bottom and about  $0.28\%$  in the top of the part. Post-fabrication chemical analysis was carried out by Atomic Emission Spectroscopy (AES). The results are reported in Table 5.1 and are based on an average of five measurements.

Table 5.1 Chemical compositions of AD730<sup>TM</sup> and SLM IN718 alloys

Alloy	Element (Wt. %)												
	Ni	Fe	Cr	Co	Mo	W	Al	Ti	Nb	B	C	Zr	Si
<b>AD730-Forged</b>	Bal.	4	15.7	8.5	3.1	2.7	2.25	3.4	1.1	0.01	0.015	0.03	-
<b>IN718-SLM</b>	Bal.	15.7	20.54	0.1	3.13	-	0.34	1.17	5.1	0.002	0.04	0.018	0.01

The LFW process was conducted using an FW34-E20 LFW machine at TWI, Cambridge, UK. Figure 1 shows a schematic of the LFW process, where it can be seen that the pressure was applied perpendicular to the cross-section defined by the length (L) and the width (W, i.e., area of L-W). The oscillations on the top of the SLM-IN718 samples were perpendicular to the SLM building direction and the surface in contact with the AD730<sup>TM</sup> was the surface on the top of the building direction. Table 5.2 and Figure 5.1 present the details of the LFW processing conditions.

Before LFW, faying surfaces were grinded by SiC paper up to 800 grades and cleaned out by acetone to remove any oxidation and contamination. The height reduction after LFW (called axial shortening) is used as a reliable indication of the combined effects of frequency ( $f$ ), oscillation amplitude ( $a$ ), friction and forge pressures, and the welding time on the quality of a LFW joint (A. Chamanfar et al., 2012a; M. Smith et al., 2016). LFW process was carried out based on an estimation of high temperature mechanical properties of IN718 alloy and optimum welding parameters for defect free joints in AD730<sup>TM</sup> (Masoumi et al., 2019) were determined to be a friction pressure of 228 MPa, an oscillation frequency of 40 Hz, and an amplitude of 3 mm for the friction phase and a forge pressure of 340 MPa is applied in the last stage.

SLM-IN718 samples were used in two conditions: as-fabricated SLM condition (as-SLM IN718) and after homogenization treatment at 1100 °C for 1 hour (H-SLM IN718).

Table 5.2 LFW processing parameters in the current study

LFW	$a$ (mm)	$f$ (Hz)	Friction pressure (MPa)	Processing time (s)	Forge pressure (MPa)	Heat Input (W.m <sup>-2</sup> )
<i>Test 1</i> SLM IN718 /AD730	3	40	228	15.4	340	6.74×10 <sup>7</sup>
<i>Test 2</i> H-SLM IN718 /AD730						

After welding, to detect possible presence of porosity formed around the weld zones, X-ray Computed Tomography (XCT) by XCT Scan and an XTH-225 Nikon machine were employed. XCT scans were carried out along weld lines (Figure 5.2) with high resolution scanning (9 to 25  $\mu$ m) from the sample edges toward the center of the joint. By changing the XCT resolutions, the full-size range of pore sizes could be seen in different positions. Data analysis was conducted using a dedicated image analysis software.

For metallographic and microstructural analyses, the welded samples were EDM-cross-sectioned perpendicular to the welding direction from the center of the sample along the longitudinal axis (the rectangular area as shown in Figure 5.2 (a)). The cross-sectioned samples were prepared by standard metallographic techniques for microstructure investigation and

using waterless Kalling and Marble solutions for etching. A LEXT OLS4100 laser confocal microscope was used for light microscopy (OM) and scanning electron microscopy (SEM) examinations were carried out using a Hitachi TM3000 tabletop SEM, as well as a Hitachi SU-8230 Field Emission-SEM equipped with a Bruker Electron Backscatter Diffraction (EBSD) and Quad EDS detectors.

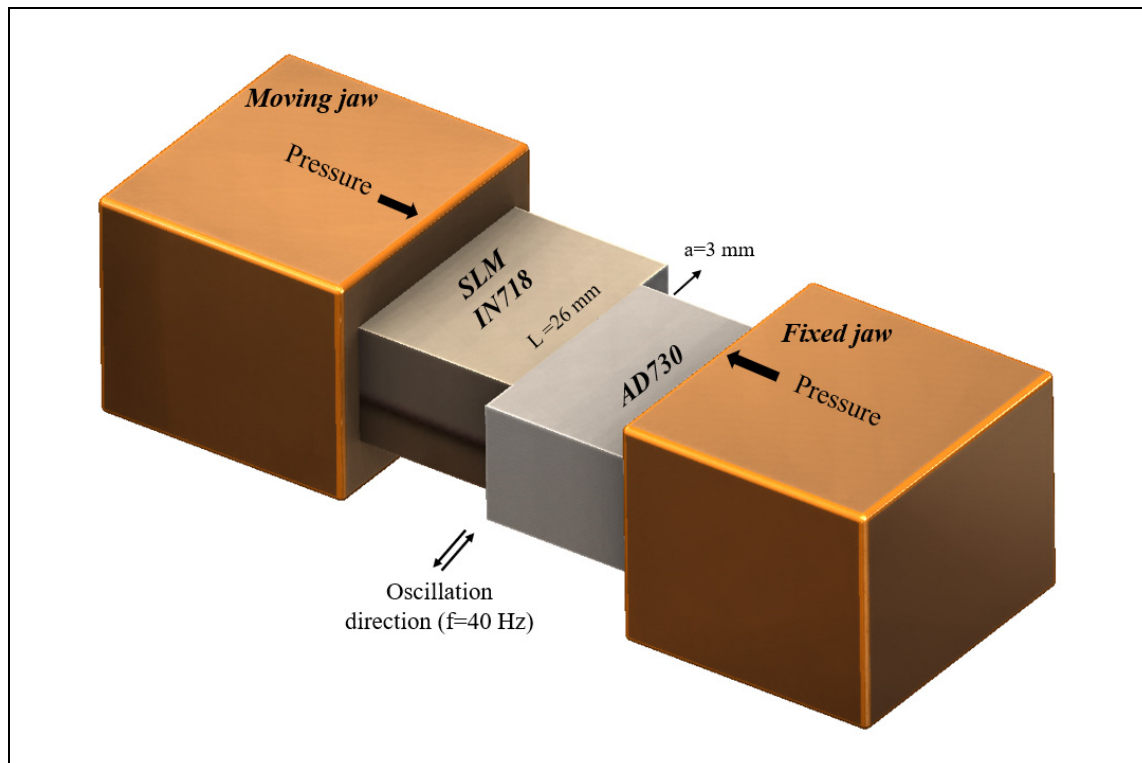


Figure 5.1 Schematic presentation of process for LFW of dissimilar welding of forged Ni-based superalloy AD730<sup>TM</sup> to as-SLM IN718 and H-SLM IN718 superalloys

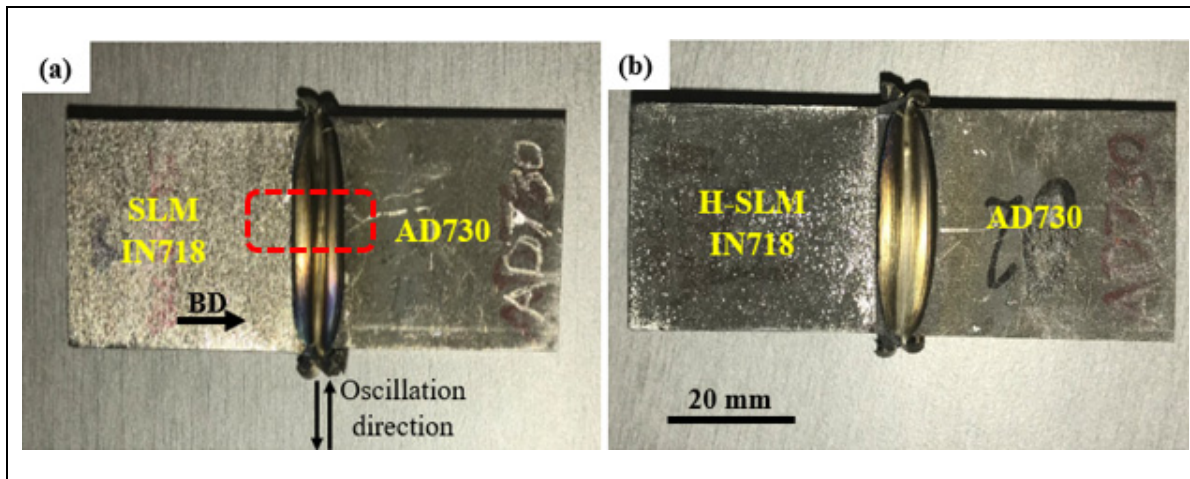


Figure 5.2 Linear friction welded samples: (a) SLM IN718 to AD730<sup>TM</sup>, (b) Homogenized SLMed IN 718 (H-SLM IN718) to AD730<sup>TM</sup> alloy. The building direction (BD) in the SLM samples is shown with a black arrow. The dashed rectangular area applies to the microstructural analysis

Specimens for EBSD examinations were prepared on a Buehler VibroMet<sup>TM</sup> polisher using a 0.05  $\mu\text{m}$  colloidal silica suspension. Then, the specimens were ion-milled by an Ion Beam Milling System (IM 400Plus, Hitachi). To illustrate grain size variations in the weld regions, a 0.41  $\mu\text{m}$  step size was selected for EBSD mapping. Because grain size variations or recrystallizations are expected to take place during LFW, a quantitative measurement of the grain size on the IN718 side was carried out using step sizes ranging between 90 nm and 0.47  $\mu\text{m}$ . The finer step size of 90 nm was used for the dynamic recrystallized region close to the weld lines or WZ, and the coarser step size of 0.47  $\mu\text{m}$  was used for the non-recrystallized regions (TMAZ, HAZ, and BM). In order to evaluate the grain size at each location, an average of at least 300 grains was characterized for each microstructure. The EBSD data were analyzed using Esprit software developed by Bruker, to obtain grain size and misorientation distributions, as well as for EDS analysis.

The microhardness (HV) profiles were measured on cross-sectioned LFWed samples using a Future-Tech Vickers device to evaluate the weld strength. The measurements were carried out under a load of 200 g and a dwell time of 15 s, and over a distance of approximately 3 mm from the weld interface to the base materials, to identify variations in strengths across the weld

regions in both superalloys. The measurements were repeated at least five times for different distances and the average values are reported.

## **5.3 Results and Discussion**

### **5.3.1 Microstructural evolutions across the weld line**

Figure 5.3 (a) shows the XCT-Scan of the as-SLM IN718/AD730<sup>TM</sup> LFWed joint. A defect-free joint is clearly visible, showing no presence of oxides or cavities. Figure 5.3 (a & b) show a macroscopic view of the weld joint, with no oxides or gap visible at the interface. It is also important to note that the flash shape and amount are not symmetrical and identical for the two materials, which indicates that the material response to the imposed LFW thermomechanical cycle had been different on each side of the joint. For instance, as reported in Table 5.3, the axial shortening from the IN718 side was thicker than that from the AD730<sup>TM</sup> side for both starting IN718 microstructures (i.e., as-SLM or H-SLM). It should be also noted that the axial shortening (3.3 mm) was identical for both starting microstructures. The higher axial shortening on the IN718 alloy side can be explained by the difference in high-temperature mechanical properties of the two alloys as the strength of as-printed IN718 dropped more rapidly than that of AD730<sup>TM</sup> alloy in the high-temperature process when compression force was applied. This behavior could be attributable to the difference in some of the strengthening phases between the two alloys. Indeed, the matrix of AD730<sup>TM</sup> is solid solution-hardened by W and Co (elements absent in IN718), which may contribute to the maintenance of a higher resistances and therefore to a resistance loss for IN718 at these temperatures. Another possible source could be the difference in thermal capacity between the two alloys resulting in higher heat conduction in IN718 as compared to AD730<sup>TM</sup>. Furthermore, the distance from the weld line affected by the heat seems to be greater, as will be discussed in sections 5.3.2 and 5.3.4, which cover respectively grain size evolution and hardness.

In Figure 5.3b, the magnified view of the weld interface (as indicated by dashed lines in Figure 5.3a) is reported, with the geometry of the weld line and of the different zones on both sides

of the joint identified. As illustrated, the microstructure of the WZ on the AD730™ side is very smooth, with only a few large particles still visible in the WZ. The very smooth nature of the interface indicates a significant dissolution of second-phase particles, which are probably  $\gamma'$ . It must be noted that, the melt pool boundaries as well as the columnar grains in the TMAZ and the WZ of SLM IN718 were eliminated due to the thermomechanical cycle applied during the LFW process.

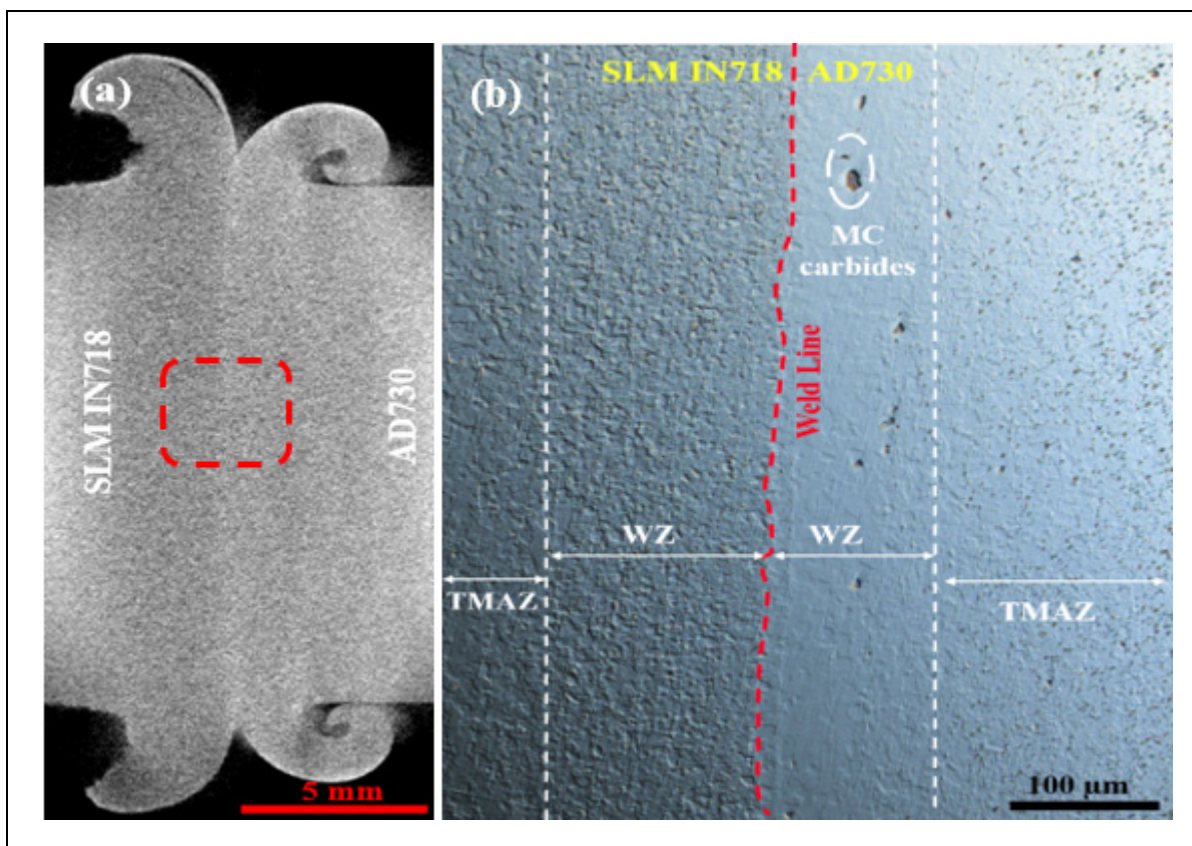


Figure 5.3 (a) XCT-Scan image from weld area, and (b) OM image of the weld interface rotated counter clockwise relative to (a) shows a crack free weld area. The black particles in the WZ are MC-type carbides

The temperature on the weld line reported for these two alloys could be in the range of 1200-1250 °C (Ma et al., 2016; Masoumi et al., 2017; Masoumi et al., 2019; Ye et al., 2020). At these temperatures, the main strengthening precipitates  $\gamma''$ ,  $\gamma'$  and/or  $\delta$  phases in as-SLM IN718

as well as  $\gamma'$  particles in the AD730<sup>TM</sup> superalloy are expected to be completely dissolved. Since the strengthening precipitates have been dissolved, it is reasonable to assume that each part will exhibit very low flow stress and that the material will be ejected into the flash. As a result, different macro- and microstructural characteristics are to be expected near the weld line region, on either side of the weld. Considering that the dissolution temperature of the strengthening phases in IN718 ( $\gamma''=930^{\circ}\text{C}$ ,  $\gamma'=970^{\circ}\text{C}$ , and  $\delta=1020^{\circ}\text{C}$ ) (Q. Li et al., 2016; M. Smith et al., 2017) are lower than in AD730<sup>TM</sup> ( $\gamma'=1200^{\circ}\text{C}$ ) (Masoumi, Shahriari, et al., 2016b; Tabaie et al., 2019), more material will be ejected from the weld region of as-SLM-IN718 (and H-SLM) into the flash at a lower temperature than for AD730<sup>TM</sup>.

Table 5.3 Axial shortening of samples after forging stage in LFW

Sample	Axial shortening (mm)		
	Total	AD730	IN718
As-SLM IN718 /AD730	3.3	1.16	2.14
H-SLM IN718 / AD730		0.83	2.47

### 5.3.2 Grain size evolution

Grain size variations across the weld interface were investigated by electron backscatter diffraction (EBSD) and FE-SEM. Figure 5.4 shows the grain size distribution in different regions of the weld area. The average grain size evolution from the weld interface to the base metal was measured according to the ASTM: E11 2-12 standard.

EBSD mapping (Figure 5.5) shows dynamic recrystallization (DRX) on both sides of the weld, including fully (at the WZ) and partially (at the TMAZ) recrystallized zones. For the as-SLM IN718 material, grains were refined from 51.8  $\mu\text{m}$  in the base metal (BM) to 2.25  $\mu\text{m}$  in the WZ. A similar trend was observed for the H-SLM IN718 samples, where it was found that the grain size decreased from 67  $\mu\text{m}$  to 7.54  $\mu\text{m}$  from the BM to the weld line. On the AD730<sup>TM</sup> side, the 45  $\mu\text{m}$  grain size in the BM was reduced to 2.5  $\mu\text{m}$  in the WZ of the joint with the as-

SLM IN718 (7.9  $\mu\text{m}$  in the joint with H-SLM sample), further confirming the significant grain size reduction on both sides of the dissimilar weld joint.

In the TMAZ, which is the zone adjacent to the WZ, the grain size became progressively larger over a distance of about 1500  $\mu\text{m}$  on the IN718 side and 1000  $\mu\text{m}$  on the AD730<sup>TM</sup> side, indicating that the kinetics of recrystallization on the AD730<sup>TM</sup> side were significantly slower. This grain size evolution indicates that applying an linear oscillation movement and a friction force along with compression stress (forging stage) can modify significantly the size and crystallographic orientations of the original grains in the initial microstructure in the WZ and the TMAZ by recrystallization mechanisms, thanks to severe plastic deformation at high temperature within the weld interface regions (M. M. Smith, 2017a).

In the as-SLM IN718 part between the TMAZ and the BM, the HAZ with a thickness ranging from 20-60  $\mu\text{m}$  was observed (cannot be seen in Figure 5.3b), and contained some blocky zones in the middle of columnar grains as reported also by (Tabaie, Rézaï-Aria, & Jahazi, 2020). According to the latter's report, this zone was only affected by a high heating and cooling rate during the LFW process. In the HAZ, not only was there a partial dissolution of Laves particles, but delta and  $\gamma''$  phases were also able to remain in the blocky zones. However, the HAZ was not observed in the AD730<sup>TM</sup> alloy, just as was the case in a similar investigation for the LFW of this alloy by Masoumi et al. (Masoumi et al., 2019).

The heat input ( $HI$ ) in the friction phase could be estimated for the selected LFW process parameters by the following equation, as also reported by others (Fratini, Buffa, Campanella, & La Spisa, 2012; Geng, Qin, Li, et al., 2019; Masoumi et al., 2019):

$$HI = \mu \cdot v_r \cdot P_{Fr} \quad (5.1)$$

where  $\mu$  is the friction coefficient,  $v_r$  and  $P_{Fr}$  are the rubbing velocity (plastic deformation due to the friction) and friction pressure (220 MPa), respectively. A fixed rubbing velocity of 480  $\text{mm}\cdot\text{s}^{-1}$  was considered and the friction coefficient was taken equal to 0.6, as reported in the

literature (Geng, Qin, Li, et al., 2019; Masoumi et al., 2019; M. Smith et al., 2017). On the basis of the above values, a heat input of  $6.74 \times 10^7 \text{ W.m}^{-2}$  was calculated for the present study. Furthermore, using an analytical procedure reported by Masoumi et al. (Masoumi et al., 2019), and considering the effect of adiabatic heating by mechanical deformation ( $\Delta T = \frac{0.95\eta}{\rho C_p} \int_0^\epsilon \sigma. d\epsilon$ ) (Chadha, Bhattacharjee, & Jahazi, 2016), the maximum temperatures at the interface of *similar* friction welding were estimated to be about  $1220^\circ\text{C}$  for the SLM IN718 and  $1250^\circ\text{C}$  for the AD730<sup>TM</sup> alloy during the LFW process. Therefore, the temperature at the interface of the *dissimilar* weld (SLM IN718 to AD730<sup>TM</sup>) is expected to fall within this interval ( $1220\text{-}1250^\circ\text{C}$ ).

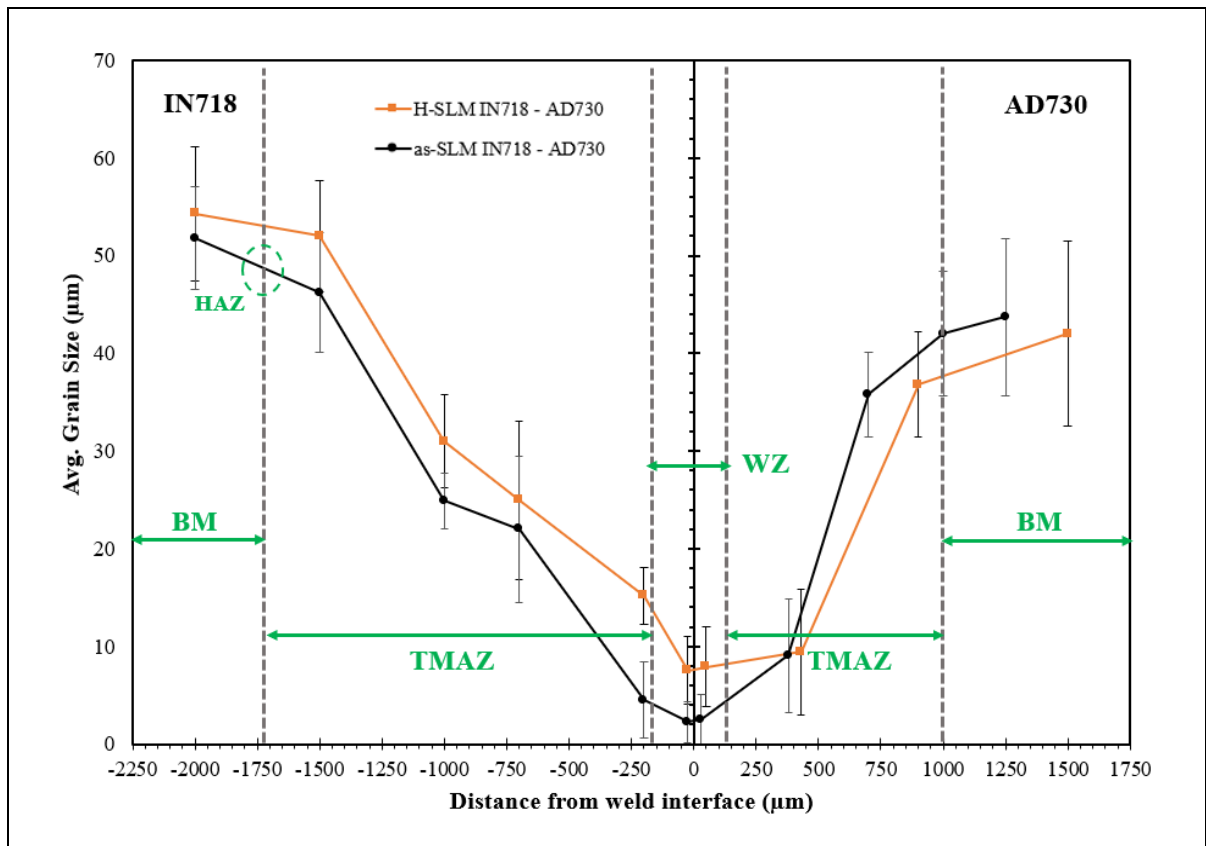


Figure 5.4 Grain size at various locations from the weld interface in the LFW of SLM and H-SLM IN718 to AD730<sup>TM</sup>

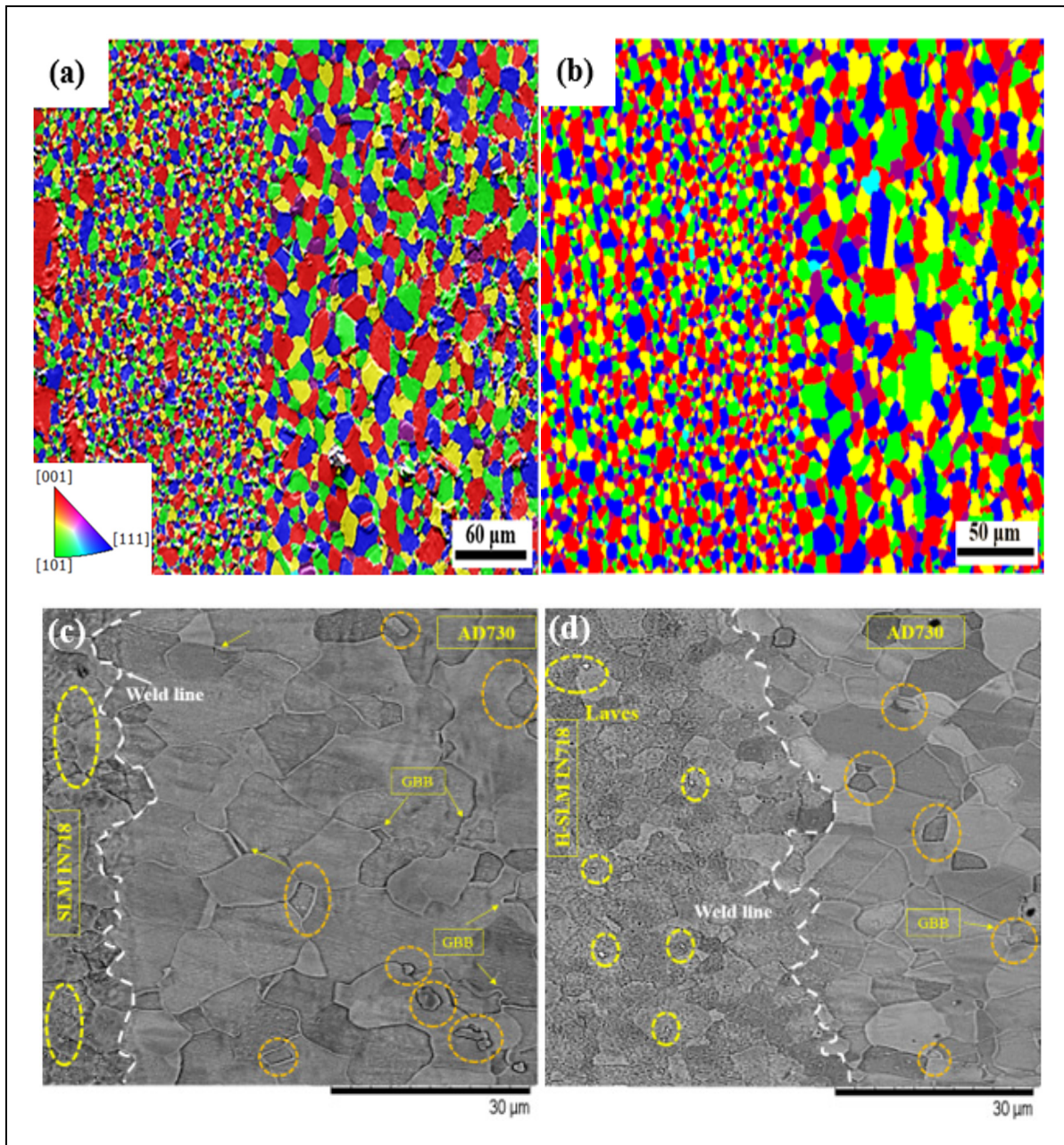


Figure 5.5 (a), (b) EBSD grain map and inverse pole figure (IPF) map from the weld line for LFW of SLM IN718 and H-SLM IN718 to AD730<sup>TM</sup> alloy, respectively. (c) and (d) SEM micrographs from the weld line for LFW of SLM IN718 and H-SLM IN718 to AD730<sup>TM</sup> alloy, respectively. Laves particles on IN718 side and the GBB on AD730<sup>TM</sup> side are illustrated by yellow circles

Since exposure to such high temperatures, severe plastic deformation, and rapid cooling induces significant changes in the microstructure across the weld, the occurrence of dynamic recrystallization (DRX) is noticeable, as shown in Figure 5.5. DRX has been frequently observed during hot deformation processes in low stacking fault energy materials such as Ni-based superalloys (e.g., AD730<sup>TM</sup> and IN718), where the recovery or dynamic recovery (DRV) process is slow and the material retains large amounts of thermomechanically induced stored energy (Azarbarmas, Aghaie-Khafri, Cabrera, & Calvo, 2016; Hatherly, 2004; W. Li et al., 2016; M. M. Smith, 2017a; Y. Wang, Shao, Zhen, & Zhang, 2008) (1100 °C for IN 718 (Y. Wang et al., 2008)). During the DRV process, thanks to the combination of generated stress and high temperature, the dislocations are sufficiently activated, leading to a rearrangement of the edge dislocations of the same symbol in a small angle of the boundary along the direction perpendicular to the sliding surface, resulting in the formation of subgrains (Ma et al., 2017). These subgrains become the nuclei of recrystallization and the newly formed grains grow under the high temperature. However, in the present case, as the heating and cooling rates of the LFW process were very fast, the growth of the recrystallized grains was restricted, leading to the formation of fine grains in the weld zone, as shown in Figure 5.5 (a & b).

Regarding the characteristics of recrystallized grains in the WZ, the DRX that occurred in this zone could be categorized as DDRX. Lin et al. (X.-M. Chen, Lin, Wen, Zhang, & He, 2014; Y. C. Lin et al., 2015) reported that dominant recrystallization mechanism was DDRX for the GH4169 superalloy (as same as IN718), and CDRX had a minor contribution to the overall recrystallization process. The DDRX process is based on the nucleation of new grains through a mechanism called grain boundary bulging (GBB). The presence of wavy grain boundaries and grains with serrated edges in the microstructure indicates that GBB has taken place. GBB occurs on the initial high angle grain boundaries (HAGBs) which are characterized with high dislocation density (Hatherly, 2004; Y. Wang et al., 2008). Illustrative examples are marked by arrows in Figure 5.5 (c & d). When the accumulated difference in strain energy in the HAGB reaches a critical value, the DRX nucleus (marked by circles in Figures 5.5 c & d) can grow and result in the migration of the grain boundary.

As the grain boundary moves (driven by the difference in the dislocation density of the recrystallized and non-recrystallized grains), the dislocation density behind the boundary is reduced to near-zero values (as a result of the recrystallization process). However, with continued straining, the dislocation density behind the moving boundary increases, approaching that of the non-recrystallized material, and thus, the driving force for continued grain growth decreases. In addition, the bulges along the original grain boundaries can be the actual nucleation sites for DRX as reported in (Geng, Qin, Li, et al., 2019). Finally, the nucleation of the DRX can also occur at a triple grain boundaries junction because the high strain concentrations at these junctions stimulate DRX nucleation (Geng, Qin, Li, et al., 2019; Y. C. Lin, Wen, Deng, Liu, & Chen, 2014).

As mentioned above, LFW thermomechanical parameters (i.e., temperature, strain, and strain rate) were lower in the TMAZ than in the WZ. They were therefore less effective in promoting the recrystallization. Fully recrystallized grains were formed in the WZ, while only partial recrystallization was observed in the TMAZ. Furthermore, the grains in the TMAZ were highly deformed along the linear oscillation direction, while their average grain size in this area was similar to that of the BM. However, the TMAZ grains did not show the very intense deformed morphology as reported in TMAZ of LFWed Titanium alloys (Karadge et al., 2007). This could be related to the high plastic flow stresses of superalloys at high temperatures.

The EBSD map of low angle grain boundary misorientation (LAGBs,  $2^{\circ}$ - $15^{\circ}$ ) and high angle grain boundaries (HAGBs,  $>15^{\circ}$ ) of different weld regions is shown in Figure 6. The figure also provides an insight into the evolution of the microstructure at different locations from the weld line by presenting the evolution of the LAGBs, HAGBs, and  $\Sigma 3$  twin boundaries on both sides of the joint. The fine grains in the WZ are characterized by a very low scattering in misorientation. The WZ is dominated by HAGBs with a percentage of 96.5 and 95.8% on both sides of as-SLM-IN718 and AD730<sup>TM</sup>, respectively, which indicates that extensive recrystallization occurred in this zone. This result is consistent with the SEM analysis, as mentioned above. The proportion of the LAGBs in the TMAZ increases as compared to the WZ, which is more obvious on the IN718 side (both as-SLM and H-SLM). The higher

proportion of LAGBs in the TMAZ of IN718 alloy is indicative of possibly different recrystallization mechanisms as compared to AD730<sup>TM</sup>.

In AD730<sup>TM</sup> alloy, at approximately 1 mm from the weld line, LAGBs start to develop within the parent grains or near the parent grain boundaries. Therefore, this zone could be considered as the outer edge of the TMAZ. The LAGBs have very low misorientations, and the HAGB fraction in this region is close to that of BM. Closer to the weld zone, LAGBs are observed within the most of the original grains, and are frequently concentrated close to the original grain boundaries. Furthermore, according to the coincident site lattice (CSL) model, the  $\Sigma 3$  boundaries, as a type of HAGBs (primary twins are a subset of this boundary (H. Zhang et al., 2018)), appear to have been transformed into random boundaries as evidenced by an increase in their fraction from 48.7% to 86.4% (from the WZ to the BM). This increase in the fraction of twin boundaries has been attributed not only to the strain-induced crystallographic rotations forming the mechanical twins in the surrounding matrix, but also to the generated annealing twins. These twins are deviated from the ideal  $\Sigma 3$  misorientation because of cyclic thermo-mechanical loading applied during LFW (Masoumi et al., 2018).

Figure 5.7 shows the EBSD map of the welded joint. The microstructure of as-SLM IN718 was mainly composed of coarse columnar grains elongated in the building direction in the BM zone (Figure 5.7a). The grains contained certain number of dendrites having the same growth direction. These dendrites were separated by LAGBs, while adjacent grains were separated by HAGBs. In addition, the columnar grains had higher amounts of LAGBs than the TMAZ and the WZ. In the TMAZ, the microstructure was composed of both columnar and fine grains (Figure 5.7b & c). Moreover, both fine and elongated grains were observed in the TMAZ making HAGB with the adjacent grains. In the BM, HAZ and in some grains at the end of the TMAZ, coarse columnar grains were observed. The above findings are in agreement with those reported by Tucho et al. (Tucho et al., 2017) and Huang et al. (W. Huang et al., 2019).

However, in the WZ and the TMAZ, the columnar grains were recrystallized due to the high temperature (1050-1250°C) and high strain rate (3.5-1000 s<sup>-1</sup>). As can be observed in Figures 6 and 7, the microstructure in the TMAZ transformed progressively from the LAGBs into high HAGBs during hot deformation. This evolution, which was manifested by the formation of finer grains without the nucleation of fine grains at the interfaces, is characteristic of the occurrence of continuous dynamic recrystallization (CDRX) (K. Huang & Logé, 2016; H. K. Zhang et al., 2020). CDRX by lattice rotation near grain boundaries (LRGB), as well as sheared micro-bands (elongated grains induced by shearing force during the friction movements) could be the governing mechanisms responsible for CDRX in this zone.

A large number of new  $\Sigma 3$  boundaries were obtained in the newly formed DRX grains, whose fraction increases with the increasing strain. In other words, as the cumulative cyclic strain increases, there is a decrease in the total LAGBs fraction, and a simultaneous increase in the fraction of HAGBs, many of which have a  $\Sigma 3$  twin relationship. However, in the WZ, the  $\Sigma 3$  twin relationship is lower than in the TMAZ, probably due to the higher deformation temperature and removal of the twins in the WZ. It was reported by Zhang et al. (H. Zhang et al., 2018; H. Zhang et al., 2015) that a concomitant rotation of grains during high-temperature deformation of Ni-based superalloys continuously changed the orientation of original twin boundaries, and that most of the original  $\Sigma 3$  boundaries lost their  $\Sigma 3$  relationships at relatively low strain, leading to a reduction of  $\Sigma 3$  boundary fractions. A similar trend is observed in the present work, where as reported in Figure 6, the fraction of  $\Sigma 3$  boundaries was reduced from 63 to 30.5% near to the BM zone (1500  $\mu\text{m}$  from weld line) of as-SLM and H-SLM IN718 after the LFW process.

The proportion of the LAGBs in different regions could be an indication of the difference in deformation conditions between BM and other regions. However, as reported in Figure 5.6, the LAGB fraction in the TMAZ of the SLM parts was higher than in the WZ. This could be due to the lower deformation temperature and lower plastic strain rate that the material experiences in the TMAZ than in the WZ, which leads to incomplete DRX in the TMAZ. Hence, the percentage of HAGBs in the TMAZ tends to decrease.

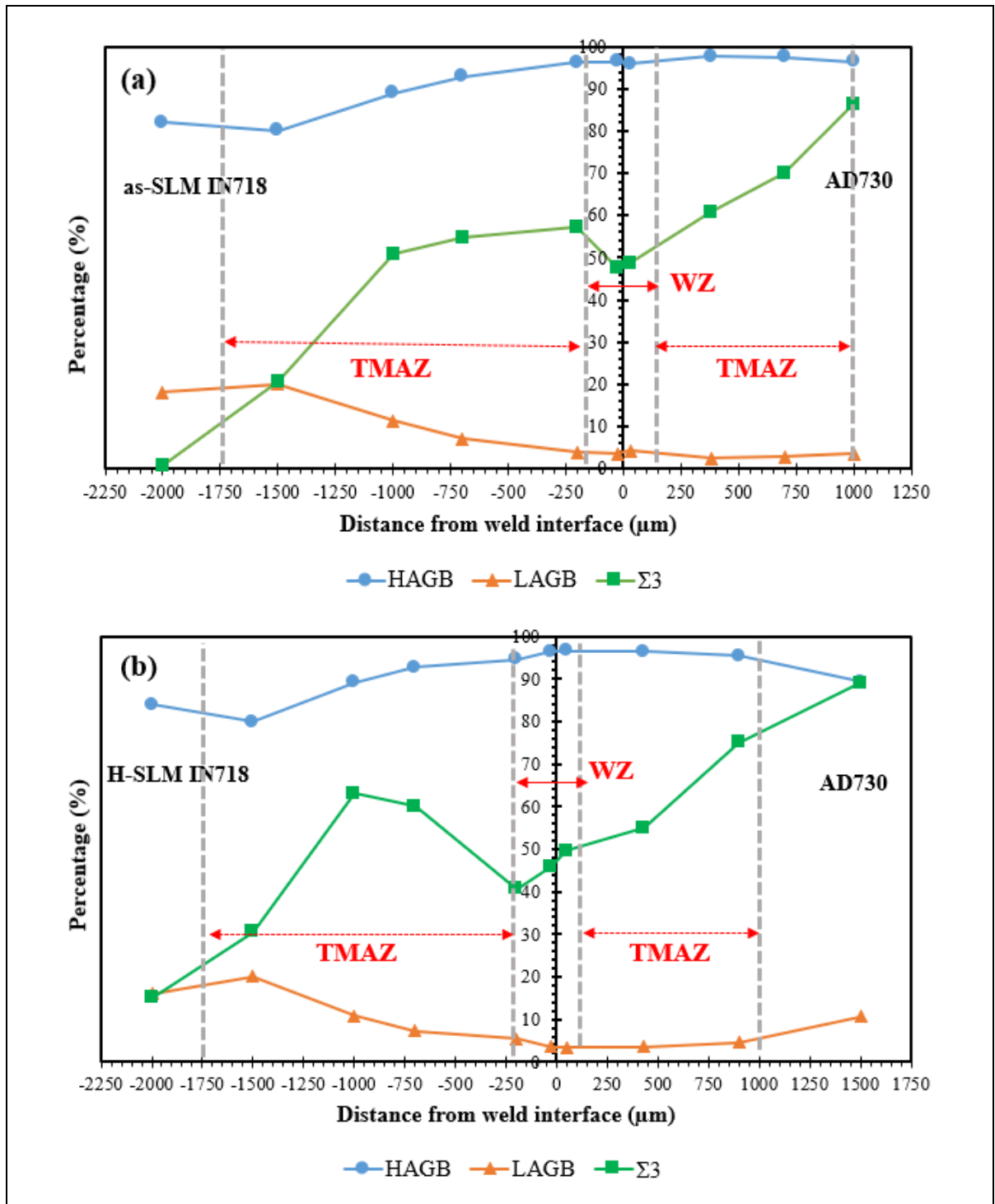


Figure 5.6 Variation of HAGB, LAGB, and  $\Sigma 3$  twin boundaries from the weld interface to the BM on both sides in LFWed samples: (a) as-SLM IN718-AD730<sup>TM</sup> and (b) H-SLM IN718-AD730<sup>TM</sup>

In the WZ, where the strain is the highest, the growth of DRX grains is promoted, and there is a significant decrease in the dislocation substructure arrangements, while the fraction of HAGBs increases. At small strain levels, in the TMAZ, the stored deformation energy is relatively low, and insufficient for the annihilation and rearrangement of most of the dislocation substructures. So, the fraction of HAGBs in the TMAZ is less than in the WZ (Figure 5.6). With increasing strain, the high dislocation network is gradually converted to substructures, and then transformed into DRX grains (Y. C. Lin et al., 2016; Y. C. Lin et al., 2015). The EBSD results reported in Figures 5.5 and 5.7 appear to confirm the above analysis in both as-SLM and H-SLM IN718.

The plastic deformation induced by the LFW process results in the introduction and movement of dislocations (Y. C. Lin et al., 2015; C. Zhang, Jahazi, & Tremblay, 2020). Huang and Loge (K. Huang & Logé, 2016) studied the generation and reorganization of dislocation networks during dynamic recrystallization. They reported that dislocations are rapidly generated during the early stages of hot deformation, resulting in the formation of a high dislocation density network. Comparing changes in the TMAZ of as-SLM IN718 with AD730<sup>TM</sup>, in Figure 5.5, it can be seen that microstructure of the as-SLM IN718 has a higher sensitivity to process parameters (e.g., strain and strain rate) than that of AD730<sup>TM</sup>.

The third factor that could influence the grain size evolution on each side of the dissimilar joint is the strain rate during the LFW process, which reaches its highest value during the forge phase. The strain rate can be estimated using an average velocity ( $a \times f$ ) over the total length ( $l$ ) (as reported in Table 5.2) (A. Chamanfar et al., 2013; Vairis & Frost, 1998):

$$\dot{\varepsilon} = \frac{\partial \varepsilon}{\partial t} = \frac{a \cdot f}{l} = 4.61 \text{ s}^{-1} \quad (5.2)$$

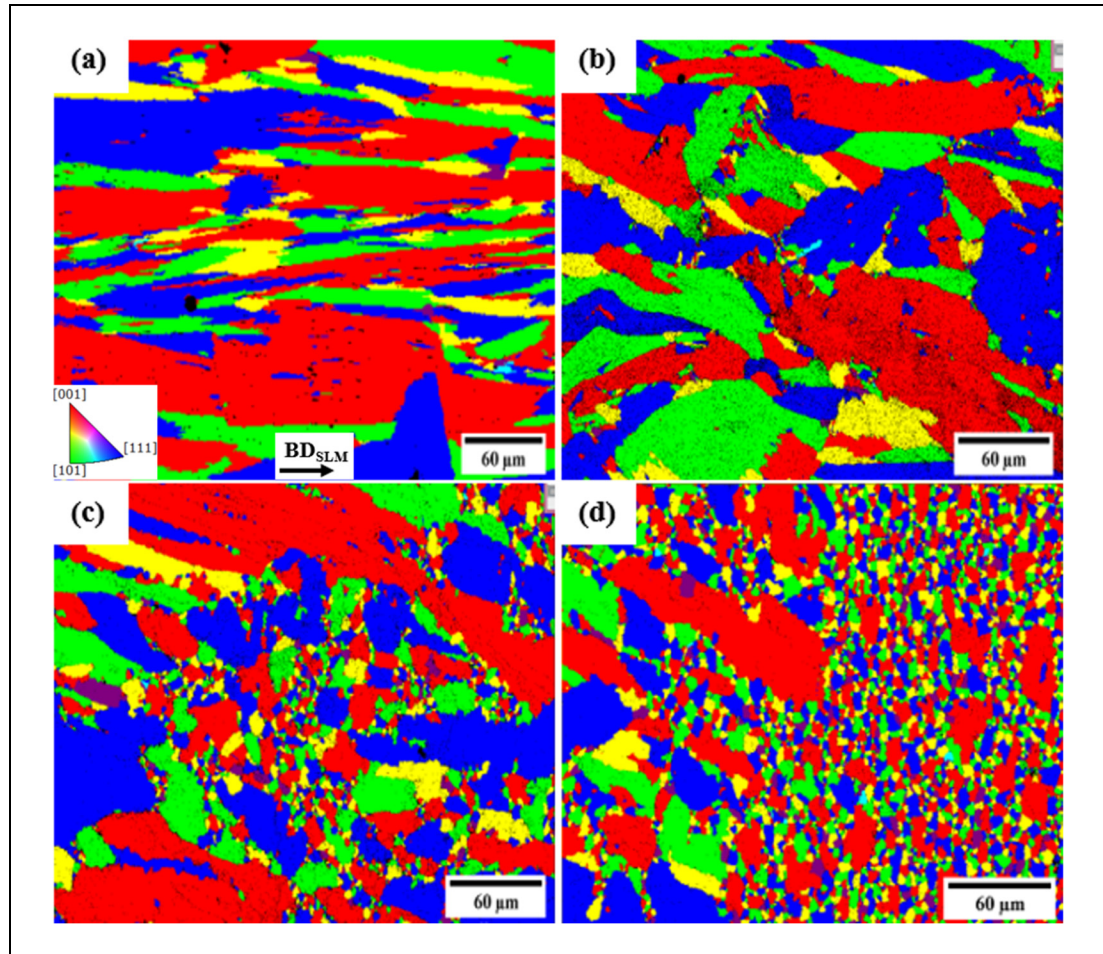


Figure 5.7 EBSD grain map in the as-SLM IN718 after the LFW to AD730<sup>TM</sup> alloy: (a) in the BM zone, (b) in the BM+TMAZ, (c) in the TMAZ, and (d) in the TMAZ+WZ. IPF map and building direction of as-SLM part are shown

Turner et al. (Turner et al., 2011) estimated the strain rates for different amplitudes of oscillations using finite element modeling (FEM) for LFW of Ti-6Al-4V alloy. According to their estimation, the strain rate could be in the range of  $1000-1500 \text{ s}^{-1}$  in the weld area. Chamanfar et al. (A. Chamanfar et al., 2013) modeled the grain size evolution during LFW of Waspaloy and reported that the strain rate in the weld area was in the range of  $1520 \text{ s}^{-1}$ . However, the model provided by Masoumi et al. (Masoumi et al., 2019), mostly based on equation (2), predicts a strain rate in the  $3.85-10 \text{ s}^{-1}$  range for LFW of AD730<sup>TM</sup> alloy. The grain refinement could be associated with the occurrence of DRX, according to Zener-Hollomon equations  $Z = \dot{\epsilon} \exp\left(\frac{Q}{RT}\right)$  and  $d_{DRX} = AZ^{-\beta}$ , where  $Z$  is the Zener-Hollomon

parameter,  $Q$  is the activation energy for dynamic recrystallization,  $\dot{\epsilon}$  is strain rate,  $T$  is the temperature (in Kelvin) and  $A$  and  $\beta$  are material constants. These equations show that recrystallization is accelerated at higher temperatures (Masoumi et al., 2019; Medeiros, Prasad, Frazier, & Srinivasan, 2000). Mostafa et al. (Mostafa et al., 2018) reported that, in SLM IN718, the high strain rate (0.1 and 1 s<sup>-1</sup>) observed is associated with the occurrence of very localized DRX, followed by hardening and short-range ordering of solute atoms (Nb, Al, and Ti). Moreover, they noted that the effect of the strain rate was greater than that of the temperature. However, in the present study, the higher strain rate (e.g., LFW conditions), in addition to a very short process time (15 s) and high temperature (higher than the dissolution temperature of strengthening phases), did not lead to a significant change in the grain size (grain coarsening) probably due to the occurrence of meta-dynamic recrystallization (MDRX), static recrystallization (SRX), and grain growth. In the present case it appears that the SLM-IN718 is more influenced by the strain rate applied in the process and showed more recrystallization as compared with AD730<sup>TM</sup>.

### 5.3.3 Misorientation

The misorientation angles were defined as <15° for LAGBs and above 15° for HAGBs. Figure 5.8 provides the average of misorientation angles value (based on the color bar) between all pairs of neighbouring points in the grains. The color-coded map is shown at the bottom, with the blue and red colors representing the minimum and maximum misorientation levels, respectively. The grain reference misorientation deviation (GROD) was used to analyze the misorientation induced by the dislocation arrangements in the deformed and non-deformed grains after the LFW. This map is a parameter that was calculated from the EBSD data to assess misorientation distribution (according to the strain distribution), as well as the dislocation density. The GROD shows the orientation deviation between a reference point in a grain and all other points within the grain, which can reflect and quantify the dislocation density in the deformed part in each zone. The evolution of the misorientation angle or GROD is closely associated with the evolution of DRX, and ultimately, with the volume fraction of DRX grains. It must be noted that, recrystallized and non-recrystallized grains have different dislocation

densities, which induce different intragranular misorientation levels and can also be analyzed by Kernel Average Misorientation (KAM) (Nicolay et al., 2019).

Figure 8a represents the misorientation map of the BM region of the as-SLM samples. The misorientation in the BM regions after LFW represents the misorientation in the initial microstructure of as-SLM and H-SLM IN718. It should be noted that this region is considered as not having been affected by the thermomechanical cycle of the LFW process. The results show that higher strains or dislocation densities were concentrated near the grain boundaries (GBs) in the as-built IN718 (Figure 5.8 a), the BM of AD730<sup>TM</sup> (Figure 5.8 e) and the TMAZs (Figure 5.8 b, c, & d) in weldment. Figure 5.8 (a & e) show many grains with significant levels of intragranular misorientation, indicating that high geometrically necessary dislocation constitutes the main fraction of LAGBs and twin boundaries. In Figure 5.8 c, most grains are blue in color, and are likely recrystallized. There are isolated grains with less intragranular misorientation than the others. These observations are in agreement with those of Li et al. (X. Li et al., 2019), who associated the isolated grains to the presence of Laves phases in GBs providing heterogeneous local misorientation distributions.

As reported in Figure 5.8, the misorientation decreased from the BM (Figure 5.8 a & e) to the WZ (Figure 5.8 c) indicating the decrease of subgrains sizes and the increased extent of dynamic recrystallization. The Figure also shows that the distribution of misorientation angles on both sides was affected by both temperature and strain rate. These findings are in agreement with those reported by Salishchev et al. (Salishchev, Mironov, Zhrebtssov, & Belyakov, 2010) who found that the misorientation angle increased with an increase of the strain rate. Figures 5.8 b, c, & d, show that the misorientation angle in as-SLM IN718 is more sensitive to deformation conditions (e.g., temperature, strain, and strain rate) than AD730<sup>TM</sup> alloy.

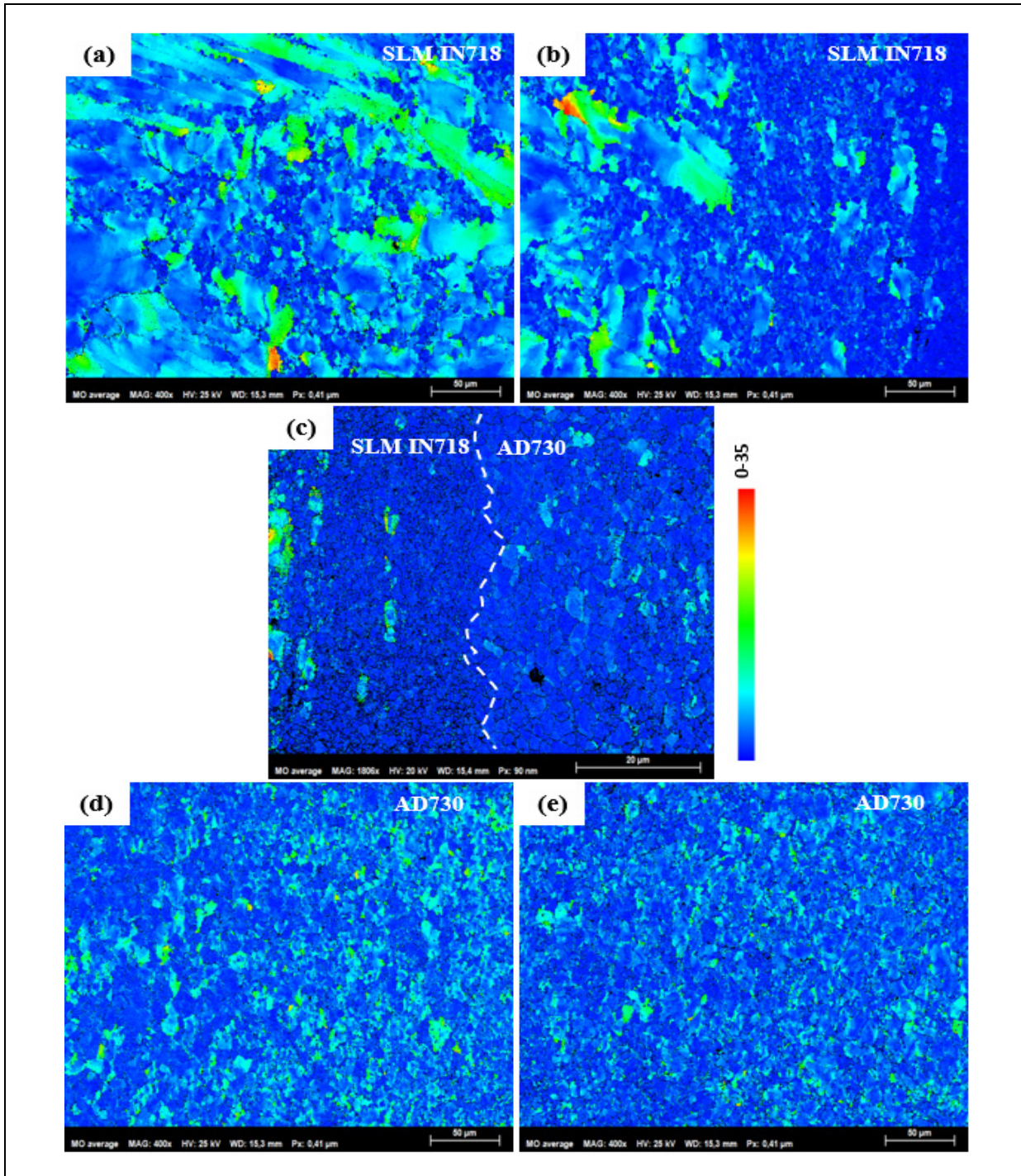


Figure 5.8 Local misorientation (LM) or average misorientation maps of the analyzed areas from the BM region in the as-SLM IN718 toward the BM region in AD730<sup>TM</sup> after LFW. (a) and (b) are the BM and the TMAZ on the side of as-SLM IN718, respectively. (c) is the weld line and the WZ on both sides. (d) and (e) are the TMAZ and the BM on the side of AD730<sup>TM</sup>

### 5.3.3.1 Effect of recrystallization on misorientation

The evolution of substructures during hot deformation under LFW can be evaluated by the changes in the point-to-point (short-range local) misorientations inside the grains and the point-to-origin misorientations between the non-deformed and deformed grains generated by cumulative plastic shear straining (long-range change in shape or morphology of grains). The cumulative misorientations both along the original grain boundaries and within the grains increase when the deformation temperature decreases. This process took place from the WZ toward the BM (from Figure 5.8c to 5.8a and 5.8e). This evolution of the substructure could be related to the dislocation motion and the rotation of subgrains, which intensifies when the temperature increases. Lin et al. (Y. C. Lin et al., 2016) reported that the local misorientation hardly exceeds  $5^\circ$ , and the variations of local misorientation with deformation temperature are limited. This indicates that the misorientation gradient is relatively steady within grains and slightly sensitive to deformation and temperature. However, the above EBSD analysis revealed that the AD730<sup>TM</sup> superalloy was free of subgrain micro-structuring, while the as-SLM IN718 superalloy was composed of HAGBs and a larger fraction of subgrain boundaries. The large fraction of HAGB results in higher instability of the microstructure, as also reported in (Shtrikman, 2010).

In the WZ, of both AD730<sup>TM</sup> and SLM IN718 sides, grains have lower intragranular misorientations and dislocation densities, illustrating that the occurrence of DRX rapidly diminished dislocation entanglements and reduced the dislocation density, as also reported in (Zouari, Bozzolo, & Loge, 2016; Zouari, Logé, & Bozzolo, 2017). Conversely, the old grains (in the BM) and the growing nuclei which may readily increase in misorientation to become a new DRX grain (in the TMAZ) have higher GROD values and dislocation accumulation. Under these conditions, the DRX would be initiated once the critical dislocation density is attained in the higher GROD regions (H. Zhang et al., 2018). Meanwhile, the higher dislocation density manifested by higher misorientation near the deformed grains, as shown in Figure 5.8 (b, c, & d) indicates that new DDRX grains have been formed, mainly along the deformed grain boundaries. By easy cyclic slipping or climbing, dislocations can move towards the

newly formed grain boundaries which act as sinks. The DRX would be triggered, once the critical dislocation density is attained in the higher GROD regions (H. Zhang et al., 2018).

Meanwhile, as shown in Figure 5.8, a higher dislocation density, manifested by higher misorientations, can be observed near the grain boundaries of the deformed grains. This indicates that new DDRX is mainly an intergranular driven phenomena and mechanisms. Huang et al. (Z. W. Huang et al., 2007) measured the level of plastic deformation stored in a dissimilar weld of two superalloys by analyzing the stored energy across the weld line. They found that the stored energy is proportional to the boundary misorientation and the HAGB energy while it has an inverse relationship with the level of misorientation at which a boundary is considered to be an HAGB. In the present work, it was found that the WZ region which contained refined grains by recrystallization, had the lowest level of the stored energy indicating that the material was sufficiently hot enough to be readily plastically deformed during LFW and to recrystallize.

In the TMAZ, both AD730<sup>TM</sup> and SLM IN718, were exposed to lower deformation rates compared to the WZ, which delays the accumulation of the plastic strain for triggering the DRX (Kumar, Raghu, Bhattacharjee, Rao, & Borah, 2016). In addition, as reported by Huang et al. (Z. W. Huang et al., 2007) and (Agnoli et al., 2015; Hatherly, 2004) the presence of secondary-phase particles (Laves phase in SLM IN718 and  $\gamma'$  phase in AD730<sup>TM</sup>) in the TMAZ could hinder boundary migration, due to the Smith-Zener pinning effect. As a result of the above processes the dislocation density increases in the TMAZ and produces high degree of misorientation within the grains in this region as reported in Figure 5.8.

#### 5.4 Microhardness

Figure 5.9 shows microhardness variations across the weld line as a function of the axial position. The BMs in AD730<sup>TM</sup>, as-SLM IN718, and H-SLM IN718 superalloys have average microhardness values of 393, 340, and 275 Vickers, respectively. The hardness values on the as-SLM IN718 side exhibited a decreasing trend, changing from  $281 \pm 9$  HV at the -500  $\mu\text{m}$

location to  $236 \pm 4$  HV at the weld interface, and the lowest hardness value (236 HV) was observed at  $\sim 115$   $\mu\text{m}$  from the weld interface.

In the H-SLM IN718 specimen, the lowest hardness value, 234 HV, was measured at 300  $\mu\text{m}$  from the weld interface. The measured hardness on the side of AD730<sup>TM</sup> increased from  $364 \pm 11$  HV at the +1000  $\mu\text{m}$  location to  $443 \pm 7$  HV at the weld interface. The highest hardness value of 443 HV was found at 85  $\mu\text{m}$  from the weld interface while in the case of LFWed joint with H-SLM IN718, the highest hardness of AD730<sup>TM</sup> was  $428 \pm 5.7$  HV at  $\sim 60$   $\mu\text{m}$  from the WZ.

Figure 5.9 also shows that AD730<sup>TM</sup> displays a strain hardening behavior while IN718 alloy (as-SLM or H-SLM) strain softening. These findings are in agreement with those reported by other authors on dissimilar solid-state welding of IN718 to an alloy with higher strength (B. Gan et al., 2012; Ma et al., 2016; Ye et al., 2020). It must also be noted that in all welded joints, the strengthening phases were found to be completely dissolved in the WZ. This means that no precipitation hardening is expected in this region and therefore, the observed hardness variation in the WZ can be attributed to grain size changes.

On the AD730<sup>TM</sup> side, the hardness decreased from the WZ toward the TMAZ (until  $\sim 1000$   $\mu\text{m}$ ) and then increased towards the BM up to  $393 \pm 4.5$  HV. Though this trend was similar whether as-SLM or H-SLM IN718 was used for welding; however, the hardness drop in the TMAZ was lower ( $362 \pm 8$  HV) in the joint with as-SLM than in the joint with H-SLM IN718 ( $390 \pm 13$  HV).

On the IN718 side, interestingly, after the TMAZ, two different behaviors were observed: In the as-SLM condition, the hardness continuously increased from the WZ ( $236 \pm 4$  HV) to the TMAZ ( $281 \pm 9$  HV), and then up to the BM to reach  $341 \pm 8$  HV. In the case of H-SLM material, after an initial increase of 234 HV over a 300  $\mu\text{m}$  distance from the weld line, the hardness remained nearly stable through the TMAZ and into the BM. As shown in Figure 5.9,

close to the BM in the as-SLM IN718, the hardness increases in the HAZ in a thin layer (20-60  $\mu\text{m}$ ), and then decreases again toward the BM.

The decrease in hardness in the BM of the H-SLM sample is probably due to the dissolution of secondary phases such as Laves,  $\gamma'$ ,  $\gamma''$ , and  $\delta$  during the homogenization before welding (Gargani, 2019; Mostafa, Picazo Rubio, Brailovski, Jahazi, & Medraj, 2017a). This decline could also be attributed to the columnar grains that tend to grow and change in orientation to form an equiaxed texture (Mostafa et al., 2017b) as also reported by Gargani et al. (Gargani, 2019). They reported that grain coarsening during homogenization had a detrimental effect on the strength and hardness of AMed IN718. In this study, both factors seem to have contributed to the evolution of the hardness.

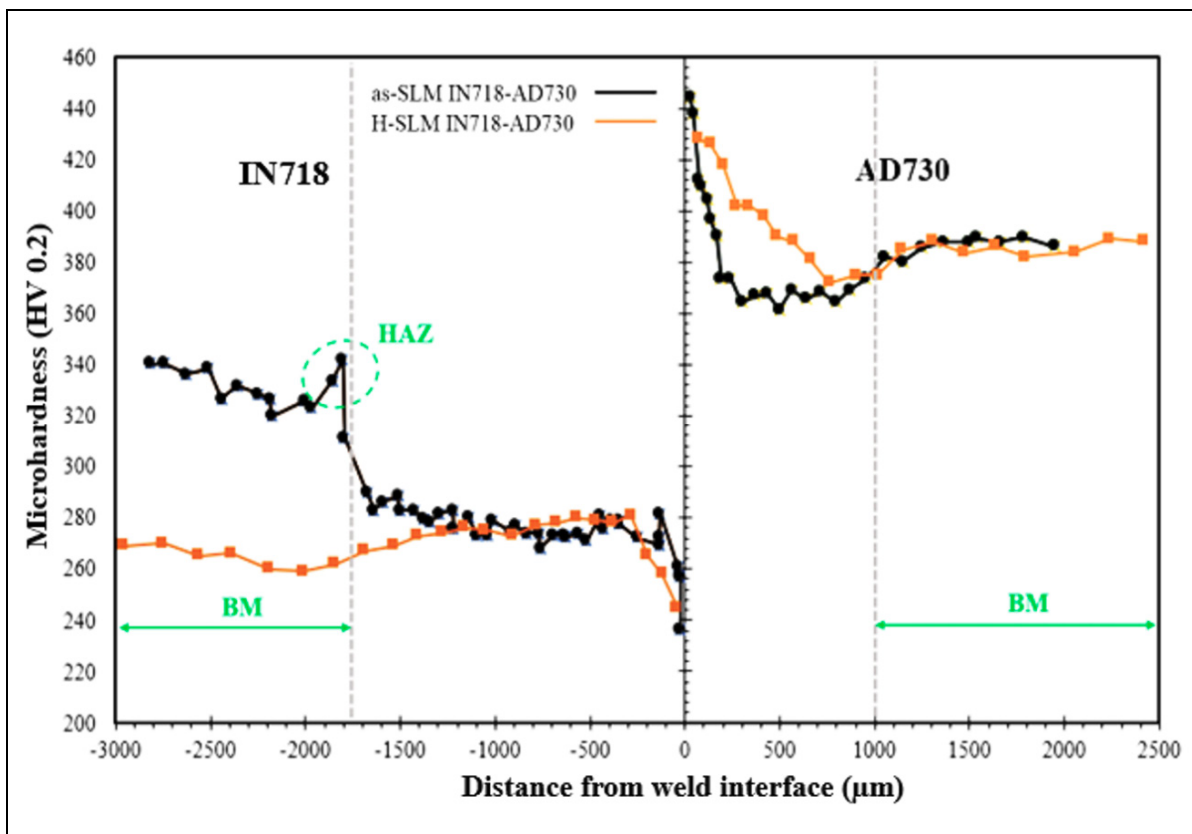


Figure 5.9 Microhardness profiles of two LFWed samples

Figures 5.4 and 5.9 show that the  $\gamma$  grain size and hardness were decreased  $\sim 79\%$  and  $\sim 20\%$ ; respectively, over a distance between  $\sim 250 \mu\text{m}$  and  $\sim 350 \mu\text{m}$  from the weld interface on the IN718 sides of the weld joint (either as-SLM or H-SLM). In contrast, in the case of AD730<sup>TM</sup>, and for both welds, the yield strength and hardness increased with decreasing the grain size, in accordance with the well-known Hall-Petch relationship. These results indicate that other microstructural features such as the grain size, solid solution strengthening in matrix, misorientation or pile-up dislocations, and precipitates, are contributing to the hardness evolution as will be discussed below.

The grain size evolution in the weld area is a function of the temperature and strain rate experienced by the material during LFW. Therefore, the initial grain size and mechanical properties of the alloy during the LFW process will influence the analysis of the progressive grain refinement by increasing axial shortening, which affect the final hardness. As shown in Figure 9, the highest hardness is in the WZ of AD730<sup>TM</sup>. Considering that the main strengthening phase  $\gamma'$  was dissolved in this zone during LFW (Masoumi et al., 2017; Masoumi et al., 2019), the increase in strength could only come from grain refinement. Nevertheless, in the TMAZ, the hardness in the AD730<sup>TM</sup>/H-SLM joint is higher than that in the AD730<sup>TM</sup>/as-SLM IN718 joint. This could be related to the smaller axial shortening (Table 5.3) obtained in AD730<sup>TM</sup> when H-SLM material is used, as less deformation and heat are needed to dissolve the secondary phases (e.g., primary  $\gamma'$  particles) (A. Chamanfar et al., 2013, 2014; Masoumi et al., 2017; Masoumi et al., 2019). It must be emphasized that, although the grain size increased after the TMAZ and towards the BM (Figure 5.4), the hardness is higher in the BM than in the TMAZ. This finding indicates that the hardness is less affected by the temperature and deformation (strain and strain rate) where secondary phases (primary, secondary, and tertiary  $\gamma'$ ) could remain undissolved during the LFW process.

In contrast to the AD730<sup>TM</sup>, as illustrated in Figure 5.9, the lowest hardness was measured in the WZ of as-SLM and H-SLM IN718 samples. This observation could be explained in terms of the selected LFW parameters for dissimilar welding. Indeed, due to the high temperature (1200-1250°C) generated in the WZ during the LFW, the microstructure could be

homogenized. As a result, the dendritic microstructure in the as-SLM IN718 and all the secondary and precipitation hardening phases (in as-SLM and H-SLM conditions) are expected to be dissolved completely. This behavior shows that the mechanical properties, specifically hardness, were significantly affected by precipitation hardening phases. The obtained results are in agreement with those reported by Ye et al. (Ye et al., 2020), who, in a recent publication, studied the LFW of IN718 to IN713LC and observed a similar trend for the hardness evolution.

In the TMAZ, the hardness in the as-SLM and H-SLM IN718 are very similar, despite the fact that all secondary and precipitation hardening phases were dissolved during the homogenization process in the H-SLM. As a result of this dissolution, it is expected that the constitutional elements of the secondary phases (e.g., Ni, Mo, Al, and Ti) that diffused to the matrix, slightly increased the hardness by the solid solution strengthening (Franke, Durst, & Göken, 2011; Pouranvari, 2015). Furthermore, as noted in section 3.3, the fraction and severity of misorientation in H-SLM were higher than in the as-SLM condition, thus indicating that the differences observed in the misorientations between the two initial conditions of the IN718 material did not affect the hardness level in the TMAZ. Based on the above analysis, it could be said that the secondary phases, the solid solution, strain, and grain size affect the hardness in the TMAZ.

In the as-SLM IN718, in the narrow HAZ, between the TMAZ and the BM, the hardness increased as compared to the BM. This is due to the partial dissolution of Laves phase, the diffusion of Nb and Mo to the matrix (solid solution), and the remaining strengthening phases ( $\gamma''$  and  $\delta$ ) in the blocky zones as also reported by (Tabaie, Rézaï-Aria, & Jahazi, 2020).

In the BM zone, secondary precipitates such as Laves phase plus  $\gamma'$ ,  $\gamma''$ , and  $\delta$  phases are present in the microstructure (Q. Li et al., 2016). Therefore, on the as-SLM IN718 side as the distance is increased from the weld line the hardness increases continuously until reaching that of the base metal. In the case of the H-SLM IN718 samples, all these phases were dissolved during homogenization, which in addition to producing larger grains, reduced the hardness.

## 5.5 Conclusions

In the present study, the linear friction welding method was applied to weld as-SLM and homogenized SLM IN718 (H-SLM) samples to forged and treated AD730<sup>TM</sup> Ni-based superalloy. The evolution of the microstructure and microhardness were analyzed and discussed before and after the welding process in all regions. The main findings are:

1. Compared to AD730<sup>TM</sup> superalloy, larger TMAZ is observed on both as-SLM and H-SLM IN718 sides, which is due to the lower strength of as-SLM and H-SLM IN718 at high temperatures.
2. DDRX occurred as a dominant grain refinement mechanism in the WZ while CDRX was the dominant recrystallization mechanism in the TMAZ in the as-SLM or H-SLM IN718 superalloy. In contrast, for the AD730<sup>TM</sup> superalloy, DDRX was the only grain refinement mechanism for both the WZ and the TMAZ.
3. Grain refinement was the main mechanism in increasing the hardness of AD730<sup>TM</sup> alloy in the WZ despite the dissolution of the secondary phases.
4. Hardness decreased in the WZ of both as-SLM and H-SLM IN718. This behavior was related to the lower misorientation and the dissolution of secondary phases that neutralize the effect of grain refinement.
5. Although the hardness of the as-SLM IN718 part is generally higher than that of the H-SLM part, it was approximately the same in the TMAZ. This is due to the higher effect of solid solution strengthening in the H-SLM material and the resulting higher strains (e.g., more misorientation) induced during welding.



## CHAPTER 6

### DISSIMILAR LINEAR FRICTION WELDING OF SELECTIVE LASER MELTED INCONEL 718 TO FORGED Ni-BASED SUPERALLOY AD730™: EVOLUTION OF STRENGTHENING PHASE

Syedmohammad Tabaie <sup>a</sup>, Farhad Rézai-Aria <sup>b</sup>, Bertrand C.D. Flipo <sup>c</sup>, Mohammad Jahazi <sup>a</sup>

<sup>a</sup> Department of Mechanical Engineering, École de technologie supérieure,  
1100 Notre-Dame West, Montreal, QC, Canada.

<sup>b</sup> Institut Clément Ader (ICA), Université de Toulouse, CNRS, IMT Mines Albi, INSA, UPS,  
ISAE, Campus Jarlard, 81013 Albi, France.

<sup>c</sup> TWI Ltd, Granta Park, Great Abington, Cambridge CB21 6AL, United Kingdom.

Paper publication in *Journal of Materials Science and Technology*, March 2021

#### Abstract

The continuous growth in the manufacture of aerospace components such as blisks has led to an increase in the application of different hybrid materials fabricating methods, and thus the requirements for joining and strengthening of dissimilar welds. According to this goal, selective laser melted (SLM) Inconel 718 was joined with forged AD730™ Nickel-based superalloy through linear friction welding (LFW) in this study. Microstructure variation, specifically with respect to secondary phases precipitation was investigated. The microhardness and strengthening mechanisms of the weldment were also studied. The precipitation (volume fraction and size of particles) at different regions of both sides of the weld line was characterized. Close to the weld line, the dissolution of  $\gamma'/\gamma''$  and Laves phases and grain refinement occurred which reveals the effects both compression strain and high temperature on recrystallization and high degree of elemental diffusion in the weld zone (WZ). It is shown that the size, volume fraction, and shape of secondary phases increased and changed (from spherical to long-stripped for Laves particles) as we went from the WZ toward the base metal. However, the measured microhardness indicated that the strength of AD730™ alloy depends significantly on the grain size, while strength in SLM Inconel 718 was dominated by shape (or size) and the presence of secondary phases ( $\gamma'/\gamma''$  and Laves).

**Keywords:** Additive manufacturing, Linear friction welding, Ni-based superalloy, Precipitation, Microhardness, Strengthening mechanisms.

## 6.1 Introduction

The demand for joining different components by welding dissimilar materials is growing continuously for the aerospace industry. Among the various techniques, friction based solid-state welding processes are well suited for joining dissimilar alloys as they do not suffer from weld shrinkage and cracking which are very common in fusion based techniques (Ahmad Chamanfar et al., 2015; Cheepu, Muthupandi, & Che, 2018). The welding can be realized by rotating or linear movement of one part against another part that is maintained stable in a static position while a compressive load is exerted. During linear friction welding (LFW), a reciprocating movement and a normal pressure are, imposed on the two surfaces to be joined. Due to the frictional force and accumulated micro-plastic mechanical strain under the contact surface, the heat generated increases the temperature at contact surfaces. When the temperature becomes high enough to decrease the plastic flow limit and increase the ductility of the two materials, a forging pressure is applied in the last step to weld them together. Hence, this technique can be suitable for assembling dissimilar materials (Ahmad Chamanfar et al., 2015; McAndrew, Colegrove, Bühr, Flipo, & Vairis, 2018). This thermomechanical deformation process imposes three different zones away from the weld interface: weld zone (WZ), where the highest deformation and temperature are achieved, the thermomechanical affected zone (TMAZ) where material experiences small scale thermo-plastic yielding, and the heat-affected zone (HAZ) where the material is only affected by the heat of welding, respectively. Beyond the HAZ, the base metal (BM) is remained free of thermomechanically-induced changes (Ahmad Chamanfar et al., 2015; McAndrew et al., 2018).

Selective laser melting (SLM) as a laser powder bed fusion (LPBF) method is being developed as an economically viable technology for fabricating Ni-based superalloy with the complex geometries in aerospace industries and also as an advanced technique for component repair. Gas turbine blades are known for their complex geometries and high time to market delay

(Adegoke, Andersson, Brodin, & Pederson, 2020; Y. Cao et al., 2019; Hosseini & Popovich, 2019; Mostafa et al., 2017b). To be able to fully utilize the SLM process as a commercial production process, welding of its components with complex geometries will be an issue (Oliveira, Santos, & Miranda, 2020; Raza et al., 2019). Welding is the main joining method for metallic materials and thus, a combination of LFW and SLM which are two advanced techniques could open new possibilities for the gas turbine industry as well as for other high value-added industries. The behavior of SLM-manufactured material during welding is an important concern that needs to be investigated.

The Ni-based superalloys are used extensively for the aerospace engine, gas turbines, and nuclear applications due to their excellent mechanical properties at high temperatures. These alloys are mainly strengthened by precipitation mechanisms, either by  $\gamma'$ ,  $\text{Ni}_3(\text{Al}, \text{Ti})$  in AD730<sup>TM</sup>, Waspaloy, and U720Li or by a combination of  $\gamma''$  ( $\text{Ni}_3\text{Nb}$ ) and  $\gamma'$  ( $\text{Ni}_3(\text{Al}, \text{Ti})$ ) in Inconel 718 (IN718) (M. C. Chaturvedi & Han, 1983; Kozar et al., 2009). In addition, alloying elements such as Co, Fe, Cr, Ti, Al, Nb, Mo, W, and Ta provide an extra strengthening of the gamma phase matrix by solid solution mechanism ( $\sigma_{ss}$ ) (Franke et al., 2011; Harte et al., 2020; Kamikawa et al., 2015; Ma et al., 2018; X. Xie et al., 2005).

To date, some similar LFW of Ni-superalloys such as IN718 (C. Mary & Jahazi, 2008), AD730<sup>TM</sup> (Masoumi et al., 2019), Waspaloy (A. Chamanfar et al., 2012a), and GH4169 alloy (Geng, Qin, Li, et al., 2019) have been successfully joined by LFW, while few works have been reported for LFW of dissimilar Ni-based superalloys. Compared to similar materials welding, dissimilar welds are generally more difficult to be successfully achieved due to the different thermomechanical properties of the two base materials (Z. W. Huang et al., 2007; Lalam, Reddy, Mohandas, Kamaraj, & Murty, 2013; H. Y. Li et al., 2007; O. N. Senkov et al., 2018; Oleg N. Senkov et al., 2014; Ye et al., 2020). LFW conditions, such as friction and forge pressures, strain, strain rate, temperature, heating and cooling rates, could affect the microstructure of materials during the welding process at different zones. Karadge et al. (Karadge et al., 2008) reported the specific difficulties encountered when welding a single-crystal superalloy CMSX4 to polycrystalline a Ni-based superalloy RR1000 having extremely

different microstructures. The authors also briefly mentioned the variation of microstructure across the weld line, but no mechanical properties of the weldment were reported. Huang et al. (Z. W. Huang et al., 2007) applied the inertia friction welding (IFW) method to weld 720Li superalloy to IN718 alloy. Their results showed weld free of micropores and microcracks with no significant chemical migration of alloy elements across the weld line. The authors observed a significant variation of the microstructure, which resulted in a partial or full dissolution of secondary precipitates ( $\gamma'$ ,  $\gamma''$ , and  $\delta$  phases) in the region close to weld because of drastic thermal-mechanical solicitation experiencing by sever high plastic deformation loading. It has been reported (Ahmad Chamanfar et al., 2015; A. Chamanfar et al., 2013; Oleg N. Senkov et al., 2014; Ye et al., 2020) that for some IFW or LFW of Ni-based superalloys, the WZ is free of secondary precipitate phases. Jokisch et al. (Jokisch et al., 2019) reported that the dissolution of Laves,  $\gamma'$ , and  $\gamma''$  phases have occurred near the weld line region because the temperature reached in the range of the homogenization and forging temperatures. Ye et al. (Ye et al., 2020) reported the dissolution of  $\gamma'$  and  $\gamma''$  close to the weld line on both sides of a dissimilar LFW of IN713LC and IN718. However, the re-precipitation of  $\gamma'$  was only observed in IN713LC in as-LFW state. All these material evaluations and changes could have a huge impact on the mechanical properties of the weldment.

It should be noted that it is not clear whether liquation of second phases, which often induces microcracking during fusion welding of Ni-based superalloys, also takes place in LFW. Liquation and liquation cracking have been observed by Smith et al. (M. M. Smith, 2017a) and Vishwakarma et al. (VishwakAarma et al., 2014) for LFW of as-serviced IN718 and Allvac 718 Plus, respectively. In addition, Raza et al. (Raza et al., 2018; T. Raza et al., 2019) reported liquation cracks in the HAZ microstructure of gas tungsten arc-welded SLM IN718. However, for LFW of AD730<sup>TM</sup> (Masoumi et al., 2017), Waspaloy (A. Chamanfar et al., 2012a), and dissimilar IN713LC-IN718 (Ye et al., 2020) liquation have not been reported. Besides, no liquation was observed by Jokisch et al. (Jokisch et al., 2019) for dissimilar laser welding of SLM IN718 and IN625.

In the present study, a detailed microstructural analysis of LFW joints of two dissimilar Ni-based superalloys SLM IN718 and forged AD730<sup>TM</sup> is carried out, with a particular focus on the evolution of the strengthening phases and liquation. Microstructural evolutions, such as changes in volume fraction and size of precipitates in different zones and liquation are correlated with the evolution of microhardness, which could be useful to assess their impacts on strengthening mechanisms and mechanical properties of the joint. The obtained results will help in designing pre- and post-weld procedures and controlling the mechanical properties of weldments of dissimilar additively manufactured components to the conventional polycrystalline parts produced by the dissimilar welding of additively manufactured components to the alloy is fabricated by traditional method.

## 6.2 Experimental procedure

The forged AD730<sup>TM</sup> alloy was provided by Aubert & Duval. The alloy was vacuum induction melted (VIM) and then refined by vacuum arc remelting (VAR) in the form of an ingot that was then radially forged into a bar-round billet. The billet was cut into disks. The as-received disk of AD730<sup>TM</sup> alloy is first solutionized (at 1080 °C for 4 hours) and then wire electro-discharge machined (EDM) to produce rectangular coupons (L: length=37 mm, W: width=26 mm, and H: height= 13 mm) for LFW. The initial average grain size of the microstructure was  $41.36 \pm 9.14 \mu\text{m}$  with a  $\gamma'$  volume fraction of 40% (the total volume fraction of all types of  $\gamma'$ ). Its chemical composition is provided in Table 6.1.

Similar rectangular coupons ( $40 \text{ (L: length)} \times 26 \text{ (W: width)} \times 13 \text{ (H: height)} \text{ mm}^3$ ) of IN718 superalloy were selective laser melted by an SLM-125HL machine at IMT-Mines Albi, France, and used in as-fabricated conditions for LFW. Spherical shaped powders with a particle size distribution between 15-50  $\mu\text{m}$  were used for SLM processing. The building direction was along with the Z-direction perpendicular to the fabrication platform. Laser beam scanning orientation in building direction was rotated successively for  $67^\circ$  in each layer to reduce microstructural anisotropy. Post-fabrication chemical analysis was carried out by Atomic

Emission Spectroscopy (AES). The results are reported in Table 6.1 and are based on an average of five measurements.

Table 6.1 Chemical compositions of bulk of alloys (Wt.%). Chemical potentials for driving the elements by diffusion near the weld line is indicated by positive sign that means element diffusion from AD730<sup>TM</sup> to SLM IN718 and negative sign in the opposite direction

Alloy	Elements												
	Ni	Fe	Cr	Co	Mo	W	Al	Ti	Nb	B	C	Zr	Si
<b>AD730-Forged</b>	Bal.	4	15.7	8.5	3.1	2.7	2.25	3.4	1.1	0.01	0.015	0.03	-
<b>IN718-SLM</b>	Bal.	15.7	20.54	0.1	3.13	-	0.34	1.17	5.1	0.002	0.04	0.018	0.01
<b>AD730-IN718</b>	+5.35	-11.7	-4.84	+8.4	-0.03	+2.7	+1.91	+2.23	-4	No significant changes			

The FW34-E20 LFW machine at TWI, Cambridge, UK was used for LFW of coupons from these dissimilar alloys. Figure 6.1 shows a schematic of LFW processing. The pressure (both friction and forge) was applied perpendicular to the cross-section defined by the length and the width (i.e. area of L-W) of coupons. The direction of oscillations during LFW, was perpendicular to the SLM building direction of as-SLM-IN718 sample (on the top part of the as-SLM sample) and parallel in-plane of the contact the surface in contact with the AD730<sup>TM</sup>. In order to remove any oxidation and contamination, the contact surfaces were grinded by SiC paper up to 800 grade and cleaned out by acetone. Details of the LFW processing conditions are provided in Table 6.2 and Figure 6.1. Axial shortening or height reduction after LFW is a reliable indication of the combined effects of LFW process parameters such as frequency ( $f$ ), oscillation amplitude ( $a$ ), friction and forge pressures, and the welding time, which all affect the quality of the joint.

Table 6.2 LFW processing parameters in the current study

LFW Sample	$a$ (mm)	$f$ (Hz)	Friction pressure (MPa)	Time of process (s)	Forge pressure (MPa)	Heat input ( $W.m^{-2}$ )	Axial shortening (mm)
SLM IN718 & AD730	3	40	228	15.4	340	$6.74 \times 10^7$	3.3

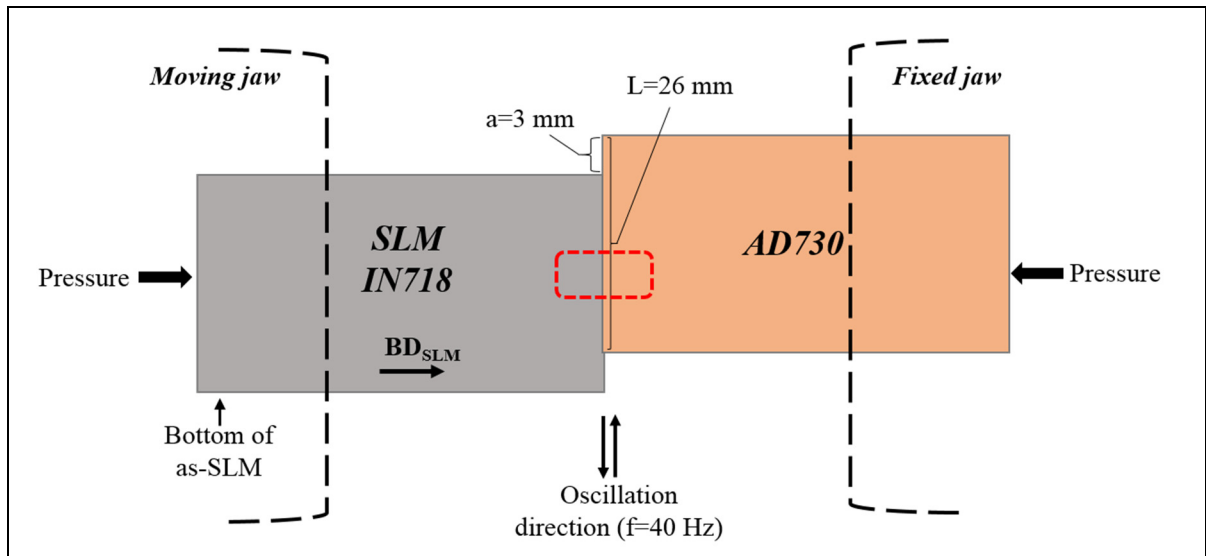


Figure 6.1 Schematic presentation of LFW process for dissimilar Ni-based superalloys of AD730<sup>TM</sup> and as-SLM IN718 and H-SLM IN718 alloys. The building direction (BD) in the SLM sample is shown with black arrow. The dashed rectangular area is EDMed for the microstructural analysis

Following the welding the sample was EDM cross-sectioned perpendicular to the welding line in the center of the sample along the longitudinal axis (the red rectangular area in Figure 1). The cross-sectioned samples were polished by standard metallographic preparation techniques and etched by waterless Kalling and Marble solutions for microstructure investigations. A LEXT OLS4100 laser confocal microscope was used for light microscopy (OM) investigation. Scanning electron microscopy (SEM) examinations were carried out on a Hitachi TM3000 tabletop SEM as well as a Hitachi SU-8230 Field Emission SEM equipped with a Bruker Electron Backscatter Diffraction (EBSD) and Quad Energy Dispersive Spectroscopy (EDS) detectors.

The particles size and volume fractions (Vf) of all precipitates ( $\gamma'$ ,  $\gamma''$ , and Laves) were analyzed and measured by digitized microscopic images using ImageJ analysis software. The size and/or volume fraction are an average of 3-5 measurements. In each case, area measurements were carried out on more than 50 precipitates.

The specimen for EBSD examinations was prepared on a Buehler VibroMet™ polisher using a 0.05  $\mu\text{m}$  colloidal silica suspension. Then, the specimen was ion milled by an Ion Beam Milling System (IM 400Plus, Hitachi). Grain size variations in each alloy in the weld region, was measured with a step size of 0.47  $\mu\text{m}$  in EBSD grain mapping (Figure 6.2). The step size was changed between 90 nm and 0.47  $\mu\text{m}$  because of the grains size variations or recrystallization taking place in LFW. The step size was 90 nm in regions having finer grain (close to the weld line or the WZ). It was changed to 0.47  $\mu\text{m}$  in non-recrystallized regions with coarse grains (TMAZ, HAZ, and BM). At least 300 grains were characterized for evaluating the average grains size at each zone of each alloy (see (Tabaie, Rézaï-Aria, Flipo, & Jahazi, 2020) and section 6.3.4, hereafter). The EBSD data were analyzed using Esprit software developed by Bruker for grains size distributions and EDS analysis.

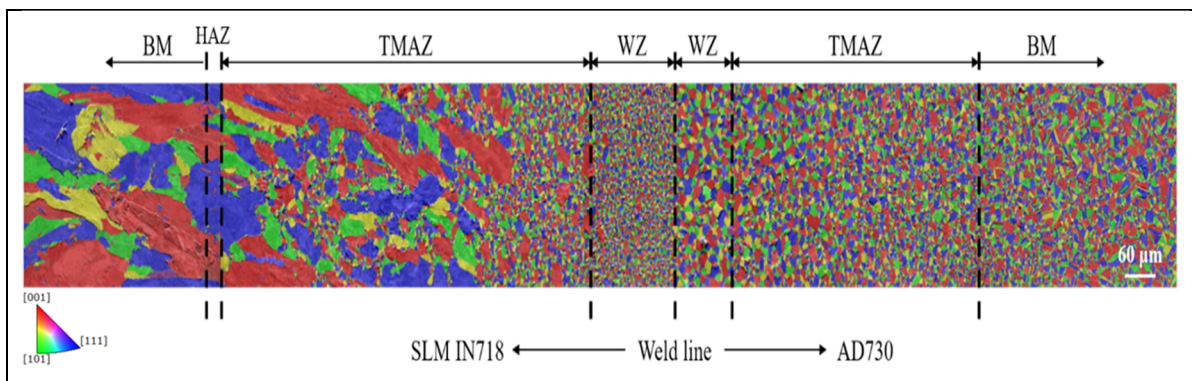


Figure 6.2 EBSD grain map from different zones after LFW on both sides. The HAZ on the side of AD730™ was not observed

The microhardness (HV) was measured over approximately 3 mm distance from the weld line to the BM (load of 200 g and a dwell time of 15 s) by a Future-Tech Vickers instrument was used to measure the microhardness (HV) in order to evaluate the weld strength variations on the across-sectioned the weld regions LFWed in both superalloys. Measurements were done over a distance of approximately 3 mm from the weld interface to the BM. At least five-line measurements were carried out at different distances.

## 6.3 Results and discussion

### 6.3.1 Chemical compositional change

The compositional changes in each matrix were micro-analyzed by EDS across the weld line. EDS map scanning of major elements (Ni, Fe, Al, Ti, Nb, and Mo) was carried out at 90  $\mu\text{m}$ , Figure 6.3. The diffusion profile of each element could be seen as a “plateau” for the as-LFWed bi-metallic welds. The distribution of elements such as Ni, Fe, Al, Ti, Nb, and Mo, in the intermixed region near the weld line is and evidence of their diffusion profiles revealed by the EDS line scan across the interface. Atoms were displaced from alloy with the higher content to alloy with the lower content. The diffusion per se depends on the inherent diffusion coefficient of each atom. As an example, Figure 6.3 (b), presents the diffusion of Nb from SLM IN718 alloy over a distance of about 13.2  $\mu\text{m}$ .

The combination of rapid heating and sever plastic deformation during LFW assisted the diffusion of these elements on both sides of the contact surfaces and the formation of the transition regions. That is why Fe, Mo, and Nb atoms migrated from SLM IN718 towards AD730<sup>TM</sup> and Ni, Al, and Ti diffused from AD730<sup>TM</sup> to IN718 resulting in the bonding at the weld interface. Senkov et al. (Oleg N. Senkov et al., 2014) reported the same trends for IFW of dissimilar Mar-M247 and LSHR superalloys.

The mutual diffusion of elements between dissimilar alloys could provide a strong metallurgical bonding without forming any harmful intermetallic compounds such as  $\gamma/\gamma'$  eutectic and/or liquation under LFW high temperature compression. Such elemental diffusion could alter the local chemical composition of precipitates like Laves phase close to the weld line of SLM IN718, which is commonly found in friction-welded Ni-based superalloys (Ye et al., 2020). The diffusion of heavy elements such as Nb and Mo as constitutional elements of the Laves phase in IN718 decrease the volume fraction of this phase near the weld line in WZ due to their dissolution at high temperatures (1200-1250 °C) and drastic plastic staining in the weld region. As a consequence, the mechanical properties of both SLM IN718 and AD730<sup>TM</sup>

can be altered (through the increasing solid solution strengthening mechanism). AD730<sup>TM</sup> alloy experienced less deformation and mechanical mixing than SLM-IN718, resulting in less extended transition region on the AD730<sup>TM</sup> side. Similar results were also found in dissimilar inertia friction welding of Mar-M247 to LSHR (Oleg N. Senkov et al., 2014), U720Li to IN718 (Z. W. Huang et al., 2007), IN718 to SM45C steel (Cheepu & Che, 2020), and IN718 to Ti6Al4V (Priti Wanjara et al., 2016), where the transition regions were larger in alloys presenting a lower volume fraction of strengthening phase.

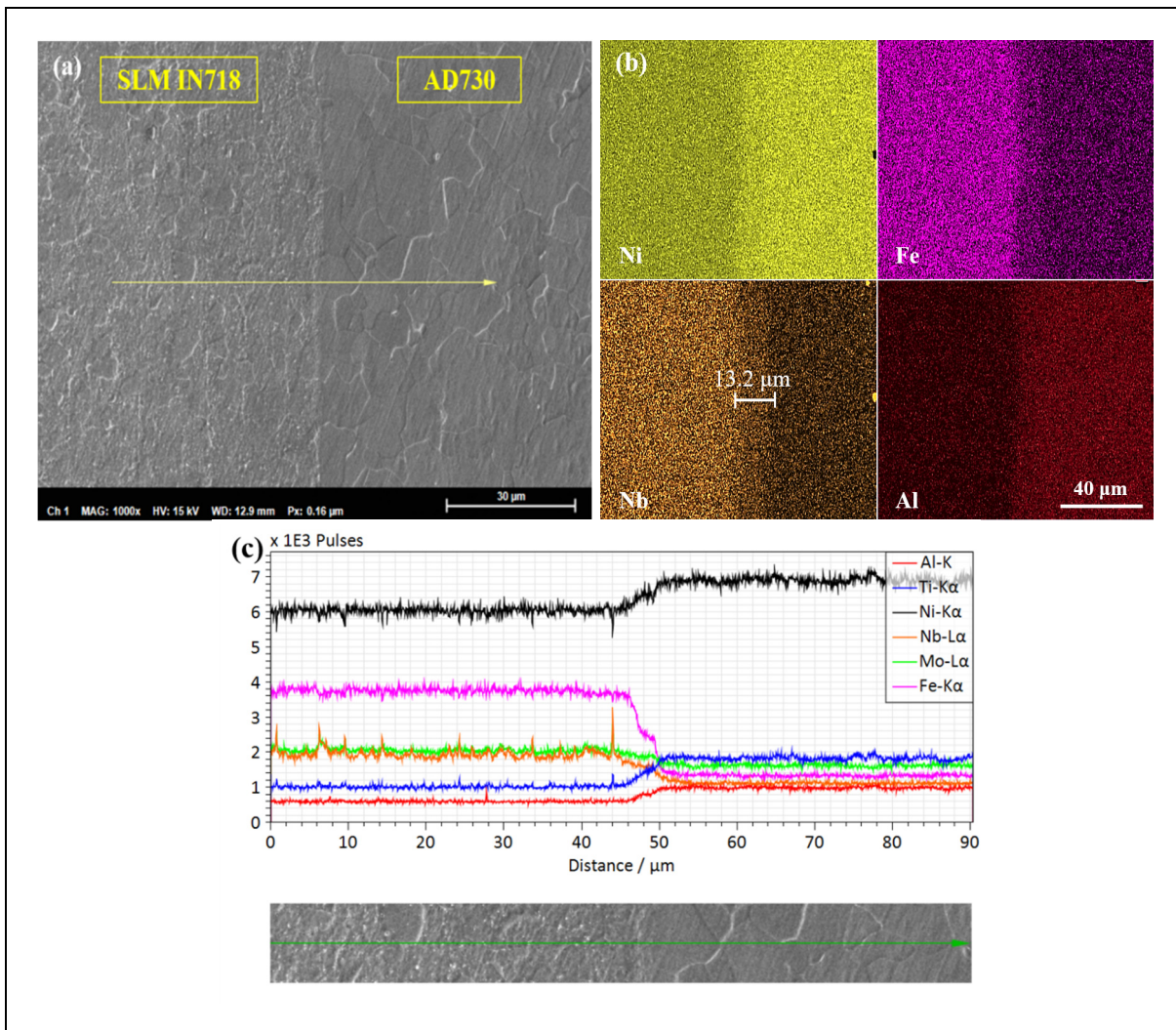


Figure 6.3 (a, b) SEM image and EDS map of the analyzed regions in both superalloys across the weld line. (c) Line analysis with length 90 μm corresponding element profiles across the weld line

### 6.3.2 Precipitation distribution analysis

Apart from variations in grain size and misorientations in different zones of the LFW joint on both sides (Tabaie, Rézaï-Aria, Flipo, et al., 2020), significant changes were also observed in the volume fraction, morphology, and distribution of the second phases (e.g.,  $\gamma'$  and Laves) were significantly changed. Figures 6.4 and 6.5 (a) illustrate size and volume fraction variations of different  $\gamma'$  vs distance from the weld interface. A trimodal distribution of  $\gamma'$  particle fractions ( $\gamma_p'$  (9%),  $\gamma_s'$  (27%), and  $\gamma_t'$  (2%)) was revealed in the BM zone in forged AD730<sup>TM</sup> alloy where the microstructure prior LFW was unaltered.

Masoumi et al. (Masoumi, Jahazi, et al., 2016; Masoumi, Shahriari, et al., 2016b; Masoumi et al., 2017) investigated the precipitation of secondary phases (all types of  $\gamma'$ ) in LFW of AD730<sup>TM</sup>. They reported that the gradient in deformation rates affected the kinetics of dissolution and re-precipitation of  $\gamma'$  phases. Furthermore, the different primary, secondary, and tertiary  $\gamma'$  sizes could also affect their solvus temperatures.

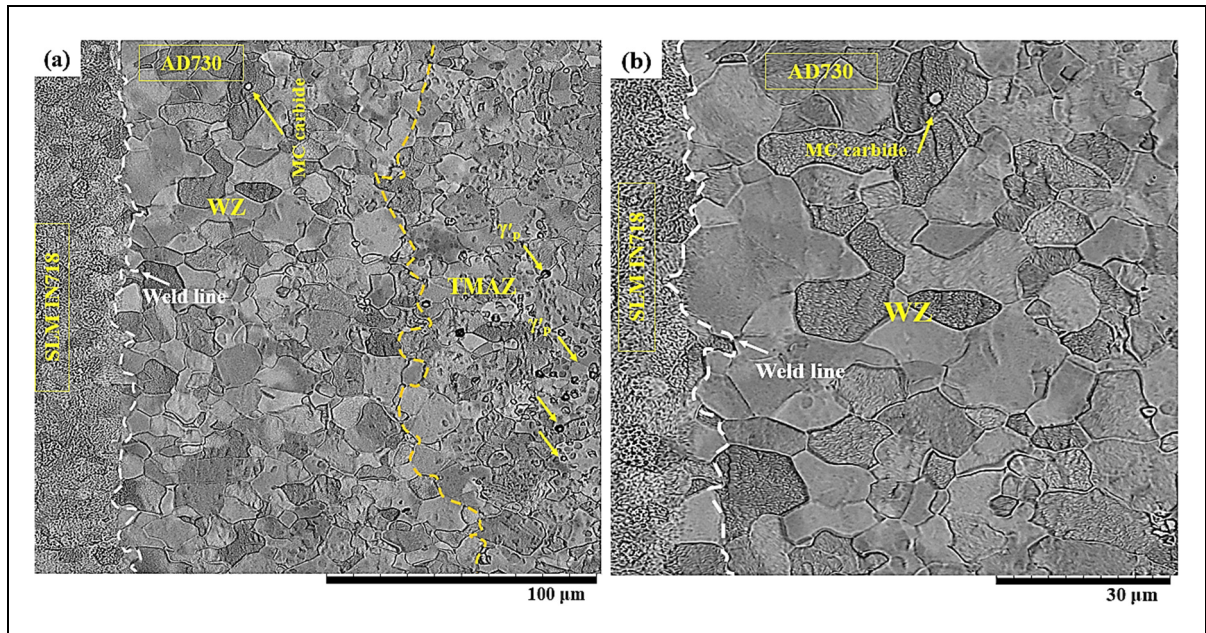


Figure 6.4 FE-SEM images of different  $\gamma'$  precipitates in LFWed AD730<sup>TM</sup> and SLM-IN718 (a, b) at the WZ and weld interface

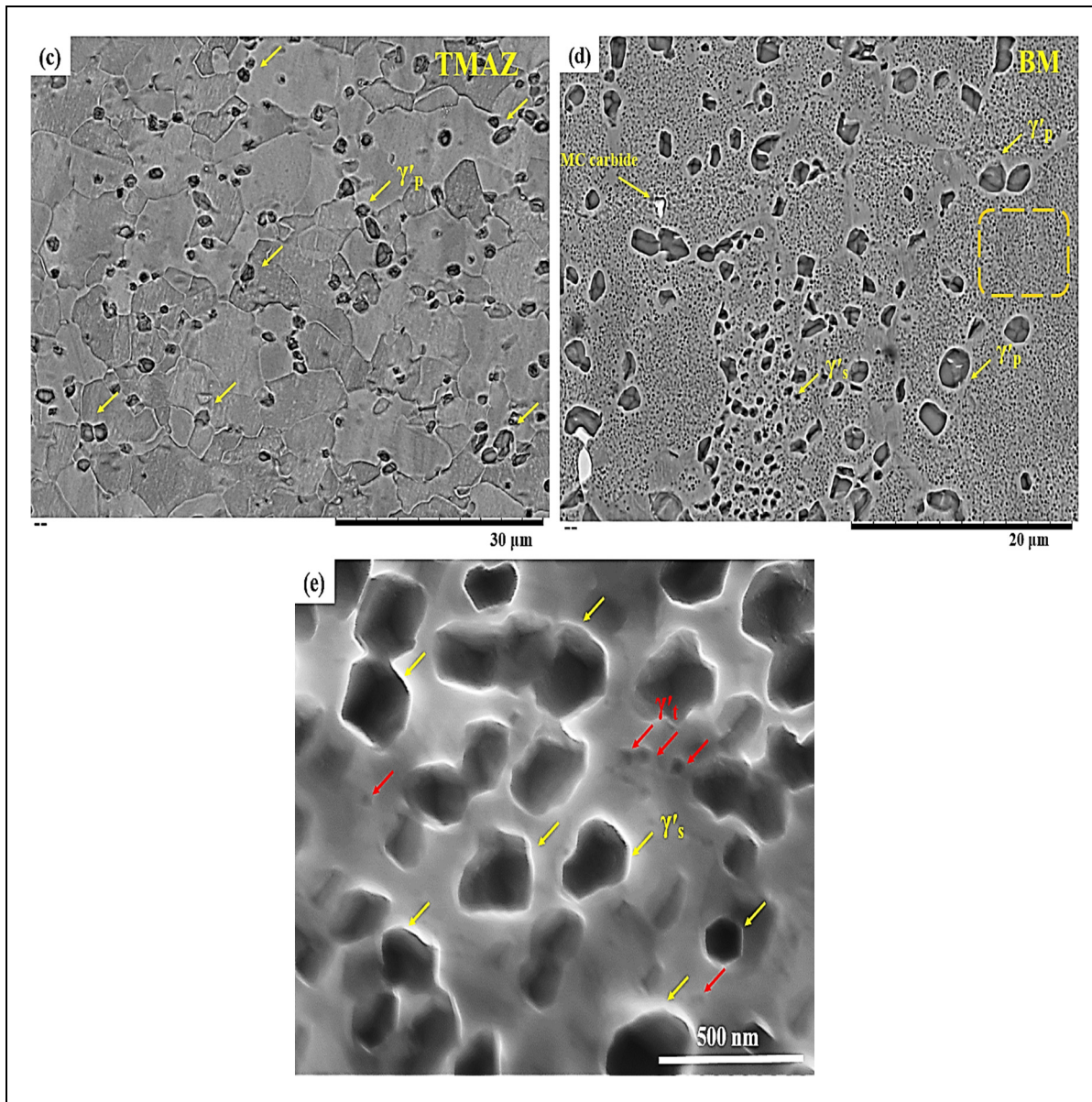


Figure 6.5 FE-SEM images of different  $\gamma'$  precipitates in LFWed AD730<sup>TM</sup> and SLM-IN718, (c) in the TMAZ or  $\sim 0.2$  to 1 mm from the weld interface, and (d) (e) secondary ( $\gamma'_s$ ) and tertiary ( $\gamma'_t$ )  $\gamma'$  in the BM of AD730<sup>TM</sup>

With a decrease in distance from the weld interface, the  $\gamma'$  precipitates volume fraction and size were decreased. As shown in Figure 6.4 (a) and (b), close to the WZ and in the TMAZ, primary  $\gamma'$  precipitates are located mostly on grain boundaries. The  $\gamma_p'$  particles started to be dissolved from 0.3 mm, while  $\gamma_s'$  and  $\gamma_t'$  were dissolved at a distance of 1 mm from the weld line. The total volume fraction of all forms of  $\gamma'$  precipitates at 1 mm from the weld interface was similar to that of the initial BM.

As shown in Figures 6.4 (d & e) and 6.5 (a), both intergranular and intragranular  $\gamma'$  were distributed in the BM as a function of the distance between the weld line and beyond 1 mm from it. The particle size distribution for  $\gamma_p'$  typically varied between 0.7 and 3.2  $\mu\text{m}$  from the WZ to the BM; respectively, 200 to 700 nm for  $\gamma_s'$ , and 30 to 90 nm for  $\gamma_t'$  in the BM zone. Figure 6.5 (a) demonstrates that the LFW process has caused significant dissolution of all forms of  $\gamma'$  in the WZ. It is observed that toward the weld line, first,  $\gamma_t'$  was dissolved, followed by  $\gamma_s'$  and finally, fine  $\gamma_p'$ . This finding indicates that TMAZ width is around 1 mm (Figures 6.4 & 6.5), where an increase of the fraction of  $\gamma_p'$  was revealed from the WZ. It must be emphasized that it is very difficult to fully suppress  $\gamma'$  precipitation while cooling from a partially/fully solutionized temperature to the room temperature. The dissolution behavior of different  $\gamma'$  reveals the existence of different thermal gradients exist from the weld line to the BM. Masoumi et al. (Masoumi et al., 2014; Masoumi, Shahriari, et al., 2016b) reported that, in AD730<sup>TM</sup> alloy, the full dissolution temperatures of primary, secondary, and tertiary  $\gamma'$  are around 1220 °C, 1120 °C, and 850 °C, respectively. As a result, it is supposed that the welding temperature at the WZ, which can be affected because of a high heating rate ( $\sim 350 - 400$  °C/s (Masoumi et al., 2019; VishwakAarma et al., 2014)), which was achieved at least 1220 °C (1200-1250 °C).

Figures 6.5 (b) and 6.6 show the evolution of Laves particles and microstructure in SLM IN718 at different locations from the weld line to the BM region. The distribution of Laves particles in the IN718 was investigated in both pre-weld (in HAZ and BM zones (Tabaie, Rézai-Aria, & Jahazi, 2020)) and post-weld conditions. Figure 6.6 (a & b) shows spherical (or semi-spherical) Laves particles within the grains in the WZ. From the WZ to the BM, the shape of

the Laves phase was changed from spherical to long-striped in the interdendritic regions in the HAZ and BM. In the TMAZ (Figure 6.6 c), the volume fraction of this phase increased. In the HAZ (Figure 6.6 d & e), both spherical and long-striped shapes precipitates could be observed in the blocky zones which is in agreement with the investigation reported in (Tabaie, Rézaï-Aria, & Jahazi, 2020).

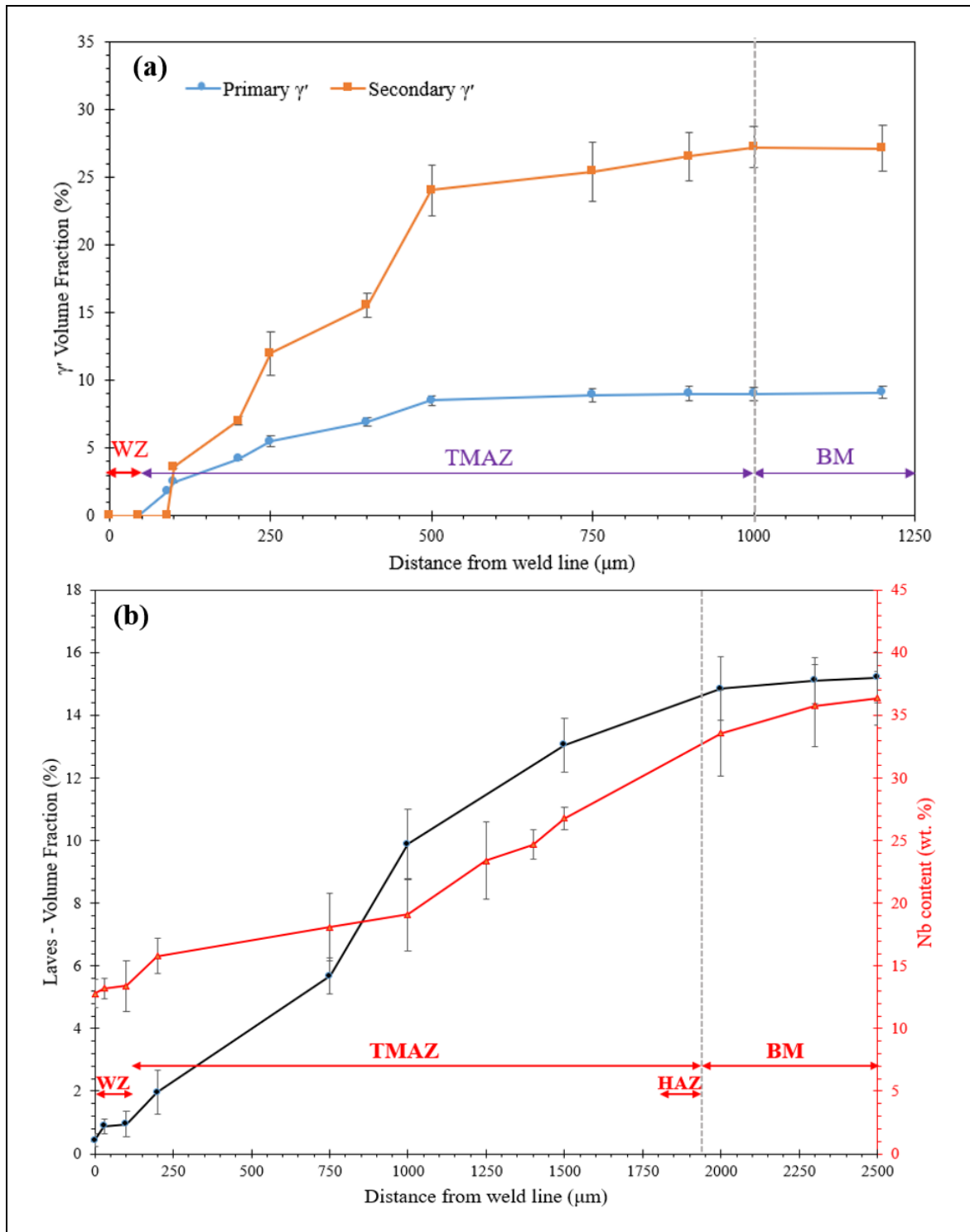


Figure 6.6 Variation of (a) volume fraction of  $\gamma'$  in AD730™, and (b) Laves phase and Nb content in the Laves particles in SLM IN718 as a function of the distance from the weld interface

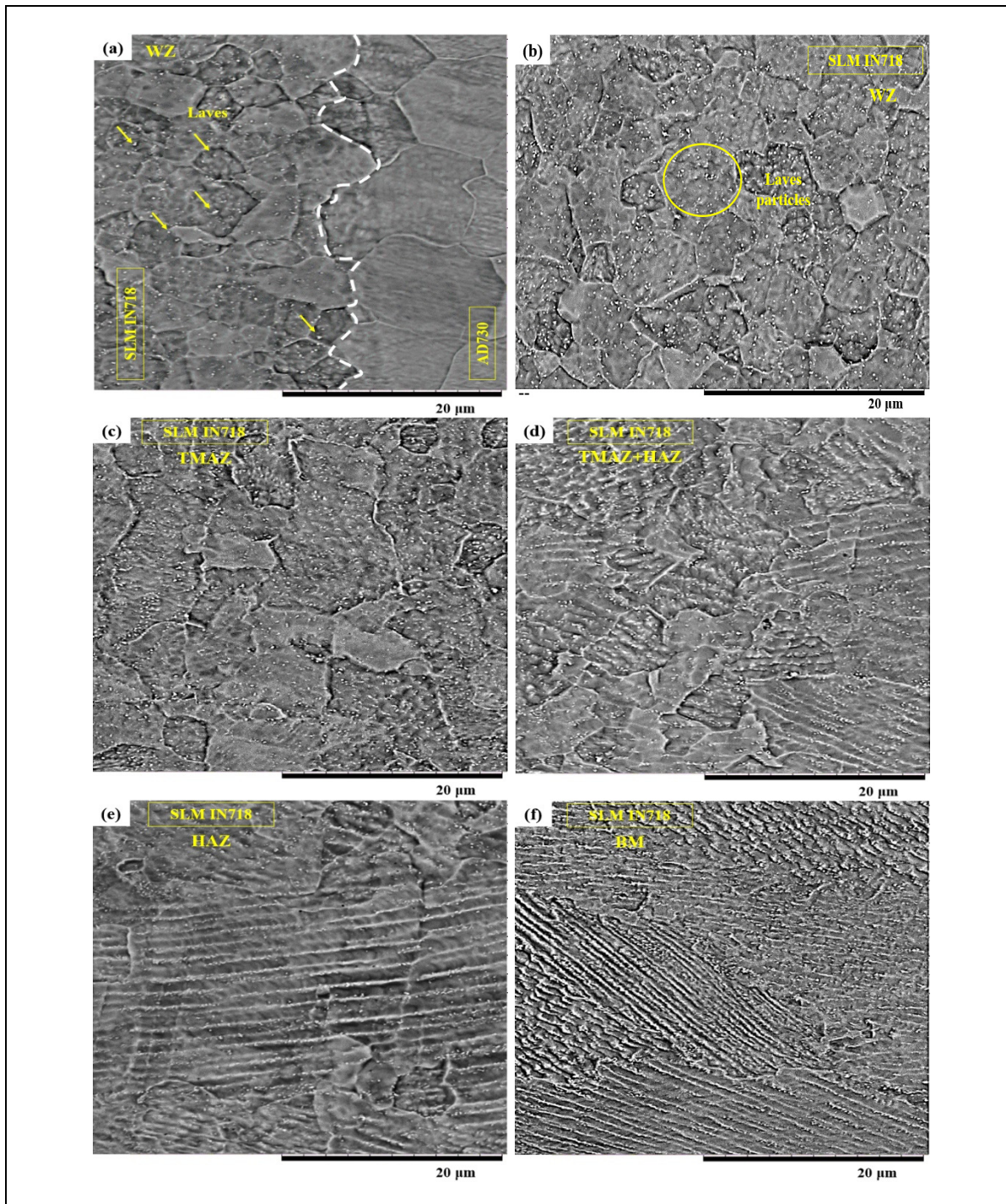


Figure 6.7 SEM images of microstructural evolution in SLM-IN718 after LFWed to AD730<sup>TM</sup> alloy: (a, b) the weld line and spherical Laves particles formed in the WZ, (c, d) the TMAZ, (d, e) HAZ with mixed spherical and long-stripped Laves particles, and (f) the BM with long-stripped interdendritic Laves

As well AD730<sup>TM</sup> side, in addition of grain size and misorientation changes in different zones of the LFW joint, a significant change was also observed and the volume fraction and distribution of the Laves particles (white particles) as well as the Nb content in them were quantified. As shown in Figure 6.5 (b), the volume fraction of the Laves phase and Nb content were increased from the WZ to the BM.

The laves phase volume fraction was increased as a function of the distance from the weld line. Furthermore, the amount of Nb as one of the constitutional elements of Laves phase  $(\text{Ni,Cr,Fe})_2(\text{Nb,Ti})$  was increased. The Laves phase particles were dissolved within the matrix at the WZ. The lower amount of Nb in the Laves and also the lower fraction of this phase at the WZ reveal that during LFW, the temperature was high enough beyond 1150 °C and led to dissolve the Laves and redistribution of Nb by short-range diffusion to the matrix.

### 6.3.3 Effects of thermomechanical compressive strain

In the TMAZ, in addition to grain size, the volume fraction of the Laves phase was higher than the WZ due to their different thermal gradients, heating and cooling rates, and drastic reductions in compression effects (or strain). It has been reported (Cowern, Zalm, van der Sluis, Gravesteijn, & de Boer, 1994; Suzuki, Ito, Inoue, & Miura, 2009) that the diffusion of solutes in the matrix increases exponentially with compressive strain as:

$$D_s = D \cdot \exp\left(-\frac{Q'S}{KT}\right) \quad (6.1)$$

where  $D_s$  and  $D$  are respectively the diffusion coefficients under strain and free loading conditions.  $Q' = dQ/dS$  is the variation of activation energy of diffusion ( $Q$ ) due to the change of the strain ( $S$ ) (negative for compressive strain and positive for tensile strain).  $K$  and  $T$  as the Boltzmann's constant and the temperature (in Kelvin), respectively. Kringhøj (Kringhøj, Larsen, & Shirayev, 1996) reported that the vacancy-assisted mechanisms are dominant for elemental diffusions at high temperatures in the matrix. Energy calculations (A. Chamanfar et

al., 2012b; Kringhøj et al., 1996) showed that the formation energy of the vacancies decreases with applied compressive strain. According to equation (6.1), at high temperatures, the application of compressive forging loads (strain at forging stage is equal to  $\sim -24.9$ ) can enhance the diffusion processes of the solute elements into the matrix at high temperatures whereas imposing tensile strain slow down the processes.

It should be noted that recrystallization was not observed in the HAZ. However, in some zones the so-called blocky zones, with interdendritic Laves precipitates were partially dissolved leading the diffusion of Nb and Mo into the  $\gamma$  matrix of SLM IN718 (Figure 6.6 (d & e)). As reported by (Tabaie, Rézaï-Aria, & Jahazi, 2020), the thickness of HAZ was controlled by the heating and cooling rates and the shape of the Laves phase was changed from long-stripped to spherical within the blocky zones. Hence, due to enough equivalent time ( $t_e$ ) and temperature ( $T$ ) controlling the diffusion of elements from the core of the dendrite into interdendritic regions, no liquation and eutectic composition were found in the HAZ. The influence of the heating/ cooling rates, time (15.4 s), and temperature (1200-1250 °C), on the diffusion distance ( $x$ ) in the HAZ, was reported by Tabaie et al. (Tabaie, Rézaï-Aria, & Jahazi, 2020). In this model  $x$  can be estimated by considering the strain assisted diffusion changes in the TMAZ:

$$x = \sqrt{D_e t_e} \quad (6.2)$$

$$D_e = D \text{ (m}^2\text{/s)} = 1.04 \times 10^{-6} \exp(-201700/RT) \quad (6.3)$$

where  $t_e$  is the equivalent holding time for the entire diffusion process acting at different stages (heating + holding + cooling cycle).  $R$  is the universal gas constant,  $Q$  (201700 J.mol<sup>-1</sup>) is the equivalent activation energy for the diffusion process of Nb in Ni,  $T$  is the equivalent temperature during LFW. For the HAZ, the diffusion coefficient of Nb in Ni can be estimated from  $D_e$  (Eq. 6.3). As a result, in the TMAZ, where is affected by both the temperature (high heating rate) and compressive strain, the diffusion distance can then be estimated as:

$$x = \sqrt{D_s t_e} \quad (6.4)$$

$$\rightarrow x = \sqrt{D_e \cdot \exp\left(-\frac{Q'S}{KT}\right) \cdot t_e} \quad (6.5)$$

On the basis of equation 6.5, it was found that the diffusion distance ( $x$ ) increased during the forging stage of the LFW process where important compressive strains are applied to the interface. In the above calculations, it was assumed that the weld line temperature was in the 1200-1250 °C range and the heating and cooling rates were 350-400 °C/s and 50-80 °C/s, respectively. Specifically, the maximum value of  $x$ , in the absence of any applied strain, was 385 nm, while this value was increased by almost 7-10 times after applying the compressive strain.

The Nb contents, in the bulk of the matrix, were measured for 5.1 and 1.1 (wt.%) in as-SLM IN718 and AD730<sup>TM</sup>, respectively. However, by segregating Nb and Mo at interdendritic regions during the solidification, the Laves phase could form in SLM IN718. Hence, the Nb concentration in the matrix close to the Laves phase in dendrite (3.33 wt.%) was lowered. As shown in Figure 6.7, the amount of Nb in the matrix of the SLM IN718 side increased from  $4.48 \pm 0.32$  (wt.%) at a distance of 60  $\mu\text{m}$  to  $4.81 \pm 0.18$  (wt.%) at distance of 20  $\mu\text{m}$  from the weld line (in the WZ), while the Nb concentration decreased close to the weld line ( $4.3 \pm 0.3$  wt.% at 10  $\mu\text{m}$ , point 1). In AD730<sup>TM</sup> alloy, the Nb content close to the weld line was higher than the bulk and decreased as we move away from the weld line. Therefore, it indicates that the Nb concentration in the matrix increased from the BM to the WZ (in SLM IN718) due to the dissolution of the Laves phase and its diffusion back to the matrix. However, very close to the weld line, the compressive strain was more effective than temperature on elemental diffusion, leading to a more extended diffusion distance ( $x$ ) and a migration into AD730<sup>TM</sup>.

High compressive strain levels leading to a total axial length shortening of about 3.3 mm (2.14 mm for SLM IN718 and 1.16 mm for AD730<sup>TM</sup>) increase the diffusivity (by 7-10 times) of constituent elements of secondary phases (e.g., Nb in Laves phase) into the  $\gamma$  matrix, as

reported in Table 6.2 and Figure 6.7 b. As the presence of  $\gamma'$  and Laves particles above their solvus temperatures (i.e.,  $\sim 1200$  °C and  $1150$  °C, respectively) is a prerequisite for their liquation, the “accelerated” dissolution of these particles can reduce or even suppress the propensity for  $\gamma'$  and Laves liquation.

In the present study, the liquation phenomenon was not observed on the AD730<sup>TM</sup> side of the joint. On the SLM IN718 side, although liquation was expected, due to the applied high temperature (greater than the eutectic Laves/ $\gamma$  temperature), no liquation was observed in the WZ, the TMAZ, and the HAZ. This behavior can be attributed to the high heating and cooling rates and applied compressive strain during LFW.

The local elastic field in the vicinity of the interfacial dislocations may promote the acceleration of the diffusion processes and of the  $\gamma + \gamma' \rightarrow \gamma$  reaction. Giraud et al. (Giraud et al., 2012) reported that the applied stress/strain at high temperature enhances the secondary phase ( $\gamma'$ ) dissolution kinetics.

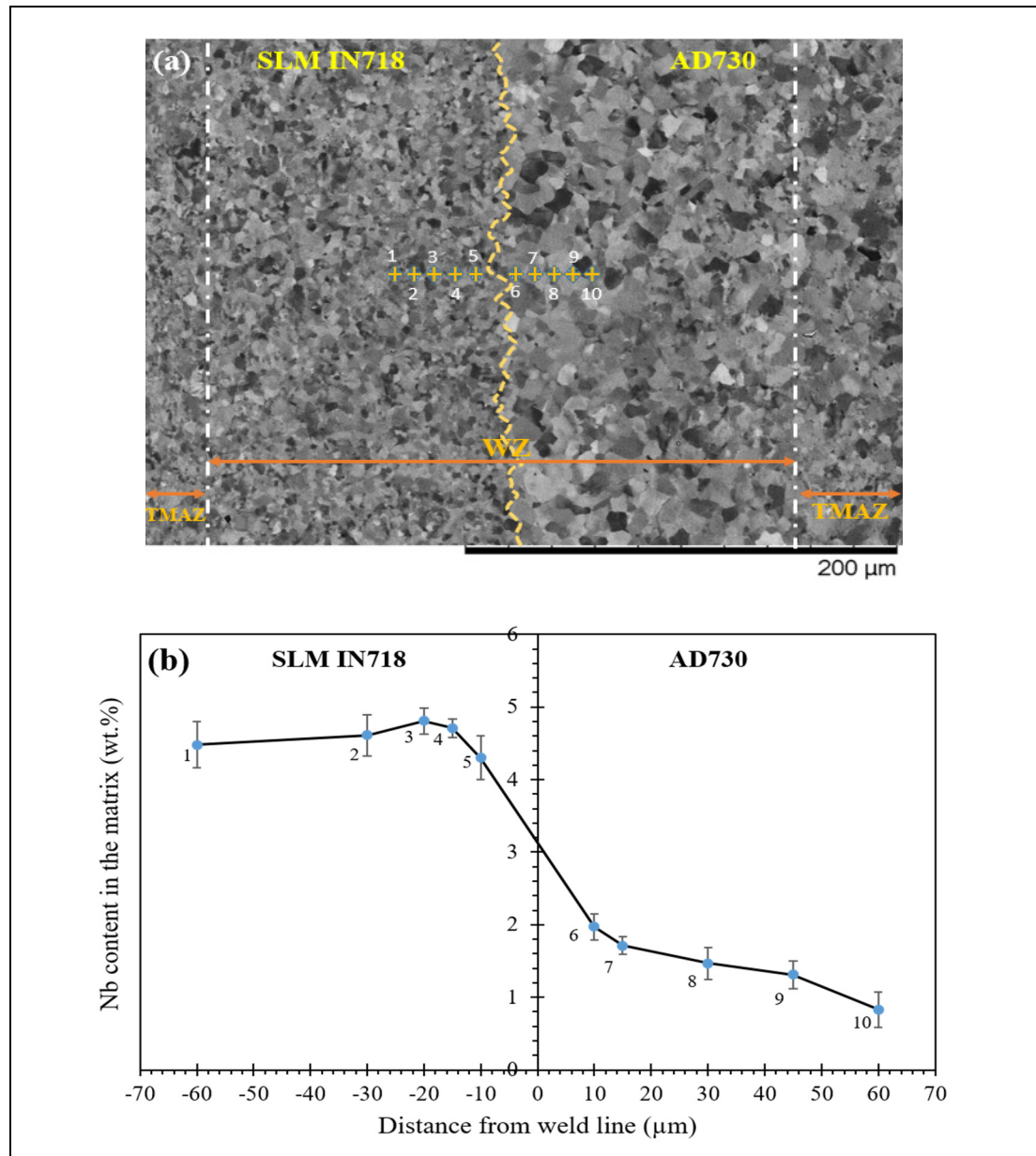


Figure 6.8 (a) SEM micrograph from the weld line, (b) variation of Nb in the  $\gamma$  matrix obtained from different EDS spot analysis in two superalloys close to the weld line after LFW

At low temperatures, solute atoms have a low mobility within the lattice, while at higher temperatures, they become mobile along with dislocations (Ghorbanpour et al., 2020). The accumulation of solute atoms in mobile dislocations further strengthens the obstacles (e.g., pile-up dislocations), raising the critical stress needed to overcome these obstacles. When the

applied flow stress exceeds the critical stress, these mobile dislocations move to the next obstacles (with increased strain and relaxed stress). Therefore, increased high temperature plastic deformation, in combination with the applied stress, promote precipitate dissolution and increase dislocation density ( $\rho_d$ ) (see equation 6.6). This, in addition to lattice diffusion, enhances the effective pipe diffusion coefficient ( $D_{peff}$ ), particularly at the  $\gamma/\gamma'$  interfaces (Giraud et al., 2012; Legros, Dehm, Arzt, & Balk, 2008):

$$\rho_d = \frac{10}{b^2} \left( \frac{\sigma}{\mu} \right)^2 \quad (6.6)$$

$$D_{peff} = \rho \cdot a_p \cdot D_p \quad (6.7)$$

where  $\rho_d$ ,  $b$ , and  $\mu$  are the dislocation density, the Burger's vector, and the shear modulus of the alloy under applied stress, respectively. The parameter of  $a_p \cdot D_p$  is pre-exponential term of pipe diffusion for Ni alloys ( $3.1 \times 10^{-23} \text{ m}^4 \cdot \text{s}^{-1}$ ).  $a_p$  is the cross-sectional area of the dislocation pipe in which fast diffusion is taking place. The values of applied frictional and forge pressures ( $\sigma$ ) during linear friction welding were 220 and 340 MPa (total process time  $t_p = 15.4 \text{ s}$ ), respectively. As reported by (Masoumi et al., 2017), lattice and pipe diffusion can enhance the self-diffusivity of the elements and influence the extent of liquation in the LFW process. According to equations 6.6 & 6.7, the application of compressive stress during LFW (at maximum temperature of 1250 °C) results in by 33 and 31 times increase in the diffusivity in the matrix of SLM IN718 and AD730<sup>TM</sup>, respectively. On LFW of AD730<sup>TM</sup>, Masoumi et al. (Masoumi et al., 2017) reported that with an applied forge pressure of 265 MPa ( $t_p = 10 \text{ s}$ ), the diffusivity increased by around 25 times, and no liquation was observed. While for LFWed IN738 (Ola et al., 2011a) with an applied forge pressure 90 MPa ( $t_p = 21.6 \text{ s}$ ), the diffusivity increased by 3.35 times and intergranular liquation, caused by non-equilibrium phase reactions, occurred in the microstructure. However, the occurrence of liquation was suppressed in LFW of Waspaloy (A. Chamanfar et al., 2012b) by applying specific LFW conditions which increased the diffusivity by 3.7 times (applied friction pressure 90 MPa,  $t_p = 4.4 \text{ s}$ , and temperature in the weld line measured at 1220 °C). As a result, the increase in the dissolution kinetics of secondary phase with the level of plastic deformation (friction and forge pressures)

may be due to an enhanced diffusion by dislocation pipe diffusion mechanism. In addition to an applied higher stress (e.g., in this study and similar welding of AD730<sup>TM</sup>), a shorter process time at high temperatures during the LFW process (e.g., similar to LFW of Waspaloy) can reduce the liquation in the microstructure.

Although less strain (35% of total axial shortening) was applied to AD730<sup>TM</sup> alloy as compared to SLM IN718, the effect of compressive strain was more significant on the dissolution of its secondary phases than of the Laves phase in SLM IN718, due to the complete dissolution of the  $\gamma'$  phases in the WZ on the AD730<sup>TM</sup> side. It should be noted that the complete dissolution of the Laves phase needs higher temperature and more time for inter-diffusion of Nb and Mo, as compared to the diffusion of Al and Ti to the matrix, as also reported by (Sohrabi & Mirzadeh, 2019a; Tucho et al., 2017). Therefore, the impact of this phenomenon on the mechanical properties of the joint needs to be investigated, and this is done in section 6.3.4.

In addition, the absence of liquation (and liquation cracking) and eutectic compositions ( $\gamma/\gamma'$  and  $\gamma/\text{Laves}$ ) could be explained by the parameters that influence particle liquation and subsequent cracking during friction welding. As reported by Smith et al. (M. M. Smith, 2017a), rapid heating-up in LFW (300-500 °C/s) altered the thermodynamic equilibrium conditions that can favor the early re-melting of grain boundaries, and later, their rapid solidification (non-equilibrium) through an increase of elemental diffusion (intergranular liquid film migration). Moreover, Ola et al. (Ola et al., 2011a, 2011b), who simulated the LFW of superalloy Inconel 738 (IN738) and a single crystal superalloy by Gleeble, reported the effect of stress-induced compressive strain (in the WZ and the TMAZ) on back-diffusion, which controls the isothermal re-solidification of intragranular metastable liquid. They observed that imposing compressive strain significantly aided the re-solidification of the intragranular liquid, where increased the diffusivity of solute atoms resulted in enhanced back-diffusion and healing. Therefore, under compressive strain (at the forging stage of LFW), the diffusion of a solute atom can be enhanced in the WZ and the TMAZ.

Despite the absence of a compression strain in the HAZ, no liquation was observed in that region due to the influence of the high heating rate (100-200 °C/s) on increasing the elemental diffusion (Nb and Mo) at the interdendritic region (Tabaie, Rézaï-Aria, & Jahazi, 2020). Moreover, Ojo et al. (Ojo et al., 2004a) and Vishwakarma et al. (VishwakAarma et al., 2014) reported another mechanism for suppressing liquation by the diffusional coherency strain in the HAZ due to the atomic size mismatch between secondary phase constituent elements and matrix atoms in IN738 alloy. This mechanism can cause intergranular liquid film migration (LFM), where no externally applied stress is involved. On the contrary, by applying externally compressive stress/strain during LFW, the initiation of LFM is controlled by lattice solute back-diffusion and can be aided by strain-enhanced diffusivity. As a result, eliminating both intergranular and intragranular liquid films in the HAZ during LFW was achieved by a combination of rapid heating and cooling, solute back-diffusion, and LFM.

#### 6.3.4 Microhardness

The effects of grains size and misorientation on the microhardness of this joint are reported in (Tabaie, Rézaï-Aria, Flipo, et al., 2020). The microhardness variations across the weld line toward the BM zone on both sides are shown in Figure 6.8. The average microhardness of the BMs in AD730<sup>TM</sup> and SLM IN718 superalloys is respectively 393 and 340 HV. The hardness in SLM IN718 decreased from  $281 \pm 9$  HV at -500  $\mu\text{m}$  from the weld line to  $236 \pm 4$  HV close to it. The lowest hardness (236 HV) was measured at  $\sim 115$   $\mu\text{m}$  from the weld line. The average measured hardness on the AD730<sup>TM</sup> side increased from  $364 \pm 11$  HV at +1000  $\mu\text{m}$  from the weld line to  $443 \pm 7$  HV close to it. The highest hardness (443 HV) was found at 85  $\mu\text{m}$  from the weld line.

The hardness in AD730<sup>TM</sup> decreased from the WZ toward the TMAZ (until  $\sim 1000$   $\mu\text{m}$ ), and then increased towards the BM up to  $393 \pm 4.5$  HV. In SLM IN718, after the TMAZ, the hardness continuously increased from the WZ ( $236 \pm 4$  HV) to the TMAZ ( $281 \pm 9$  HV), and then increased up to  $341 \pm 8$  HV in the BM. As shown in Figure 6.8, close to the BM in SLM

IN718, the hardness increased in the HAZ, having a thin layer (20-60  $\mu\text{m}$ ), and then decreased again toward the BM.

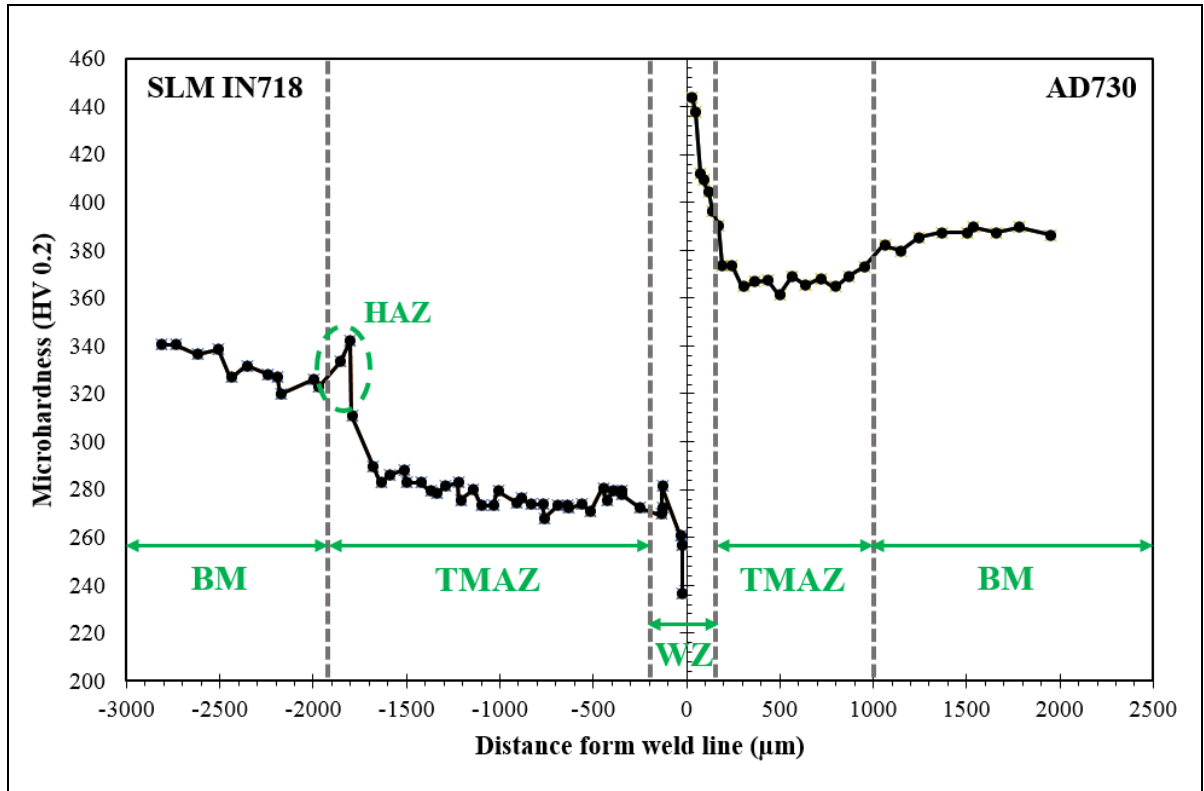


Figure 6.9 Microhardness profiles as a function of distance from the weld line of two LFWed samples

The microstructure in the WZ could be homogenized due to the high temperature generated during LFW (1200-1250  $^{\circ}\text{C}$ ). AD730<sup>TM</sup> presents the strain hardening behavior, while SLM IN718 presents strain softening, as also reported by other authors when IN718 is welded to other alloys with higher strengths (B. Gan et al., 2012; Ma et al., 2016; C. Mary & Jahazi, 2008). As mentioned, the strengthening phases were completely dissolved in the WZ. This means that no precipitation hardening was expected in this region. Therefore, the observed hardness variation in the WZ can be attributed to grain size changes according to the Hall-Petch relationship (Ye et al.):

$$\sigma_y = \sigma_0 + k_y \cdot d^{-1/2} \quad (6.8)$$

where  $\sigma_y$  is the yield stress,  $\sigma_0$  is the friction resistance for dislocation movements in the slip bands,  $k_y$  is the Hall-Petch parameter and  $d$  is the average grain size. It is known that the yield stress can be empirically related to the microhardness. As the WZ is free of secondary phases, microhardness variations can basically be related to the grain size. However, the evolution of the microhardness in the WZ is different in SLM IN718 as compared to AD730<sup>TM</sup> superalloys. In the WZ of SLM IN718 at 250  $\mu\text{m}$  from the weld line, the grains size increased from 2.25 to 5  $\mu\text{m}$ , but the reduction of the hardness did not obey the Hall-Petch relationship, whereas in AD730<sup>TM</sup>, the microhardness increased with the grains size reduction according to this relationship. Although all precipitates (except MC carbides) were dissolved in the WZ on both sides of the weld line, the different hardness behavior variations reveal that the contribution of second phase to the strength of IN718 alloy is higher than the one from grains size refinement as also reported by (Tucho et al., 2017). The same trends are also found in dissimilar joint after LFW of IN718 to IN713LC (Ye et al., 2020). The effect of other hardening mechanisms (e.g., matrix solid solution strengthening, grains misorientation, and pile-up dislocations at grain boundary) has been discussed in a recent publication by the present authors (Tabaie, Rézaï-Aria, Flipo, et al., 2020).

In the TMAZ, the hardness in the SLM IN718 is lower than the BM (-21 %) and higher than the WZ (+16 %). It is expected that elements such as Ni, Mo, Al, and Ti forming the secondary phases (Laves,  $\gamma'/\gamma''$  and  $\delta$ ) diffused to the matrix, will slightly increase the hardness by solid solution strengthening (Franke et al., 2011; Pouranvari, 2015). In the TMAZ, the effect of compressive strain is less than WZ. However, the diffusion distance ( $x$ ) at 1000-1150 °C, even without considering the strain, could reach 294-306 nm (knowing that the dendrite arm spacing is  $820 \pm 130$  nm). Therefore, the secondary phases, the solid solution, plastic strain, and grain size can affect the hardness of the TMAZ. The hardness of AD730<sup>TM</sup> showed a decrease in the TMAZ due to the dissolution of  $\gamma'$  particles, and an increase in hardness by the grain refinement in the WZ. It must be emphasized that although the grain size increased after the TMAZ toward the BM (from 5 to 52  $\mu\text{m}$  for SLM IN718 and 10 to  $41.36 \pm 9.14$   $\mu\text{m}$  for AD730<sup>TM</sup>), the hardness is greater in the BM than in the TMAZ. This indicates that in these regions the

hardness is less affected by the temperature and deformation (strain and strain rate), and here, secondary phases ( $\gamma'$ , Laves, and  $\gamma'/\gamma''$ ) remained undissolved during the LFW process.

In SLM IN718, in the narrow HAZ, between the TMAZ and the BM, the hardness increased as compared to the BM presumably due to the partial dissolution of Laves phases (mixture of spherical and long-stripped shapes), the diffusion of Nb and Mo in the matrix (solid solution), and the remaining strengthening phases (e.g.,  $\gamma''$  in size of  $\sim 80 \mu\text{m}$ ) in the blocky zones, as also reported by (Tabaie, Rézaï-Aria, & Jahazi, 2020). Therefore, the effect of the Laves phase on the yield strength is achieved by influencing the volume fraction, the size, and the distribution of  $\gamma''$  phase due to the effect of high heating rate (Y. Cao et al., 2019; Sui, Tan, et al., 2019; Tabaie, Rézaï-Aria, & Jahazi, 2020).

In the BM zone, secondary precipitates such as Laves phase plus  $\gamma'$  and  $\gamma''$  phases could remain in the microstructure, as also reported by (Q. Li et al., 2016). On the SLM IN718 side, as the distance is increased from the weld line, the hardness increases continuously until reaching that of the BM. Furthermore, despite the larger grain size in the BM, its hardness is more than the WZ and the TMAZ, which can be attributed to the formation of cellular substructures and dendritic/cellular segregation occurred due to the high cooling rates during the SLM process. The grain boundaries and the sub-grain boundaries are highly decorated with micro-segregated particles (Laves phases and to some extent MC carbides) (Figure 6.6 f, white particles) (Tucho et al., 2017). These sub-grain boundaries contained precipitated particles and high density of dislocation networks (Heep et al., 2021; Tucho et al., 2017). The boundaries between cellular microstructure induce more dislocation interactions and hamper dislocation movements which can increase the hardness of the alloy by dislocation strengthening mechanism. However, the hardness in the BM was lower ( $\sim 7\%$ ) than in the HAZ, due to the long-stripped shape of Laves particles in the BM, which can reduce the strength and ductility of the alloy, as also reported by (Tabaie, Rézaï-Aria, & Jahazi, 2020) and Sui et al. (Sui, Tan, et al., 2019).

As a result, in the SLM IN718, the contribution of precipitation hardening mechanism (plus contribution of dislocation strengthening) is more than grain refining effects. On the contrary, on the AD730<sup>TM</sup> side, although the grains size in the BM is larger than in the TMAZ, its hardness was higher (by ~10%) due to the presence of primary, secondary, and tertiary  $\gamma'$  phases. This points to a significant effect of precipitation on the strength ( $\sigma_{ppt}$ ) and its impact on dislocation movement or strengthening by dislocation ( $\sigma_{dis}$ ). However, the effects of solid solution ( $\sigma_{ss}$ ) and grain size or grain boundary movement ( $\sigma_{gb}$ ) mechanisms are generally higher than others in AD730<sup>TM</sup> alloy. The possible contribution of ultrafine  $\gamma'$  precipitate ( $\gamma'_p$ , 2-10 nm) to the strength of the alloy should also be considered in the WZ. As reported by several authors (Masoumi, Shahriari, et al., 2016b; Panella, Signor, Cormier, Bernacki, & Villechaise, 2020) the complete dissolution of  $\gamma'_p$  in AD730<sup>TM</sup> in the temperature range experienced during the LFW process is unlikely. On the other hand, it is also possible that some ultrafine  $\gamma'$  precipitate form during the post weld cooling step. However, in the present work such precipitates were not observed in the microstructure indicating that the selected LFW conditions resulted in the absence of precipitates in the final microstructure of the WZ. Therefore, in the analysis of the results, no contribution to the hardness of the alloy is considered. It must be noted that, even if some precipitates are present, undissolved during heating or formed during cooling, the contribution to the strength should be negligible. Finally, it is well known (Kong, Cheepu, & Kim, 2020; Masoumi et al., 2018; M. Smith et al., 2017; Ye et al., 2020) that the hardness and other mechanical properties of similar and dissimilar alloys LFWed can be enhanced by applying proper post-weld heat treatment cycles through precipitation hardening.

#### 6.3.4.1 Effects of secondary phases

According to equations (6.9-14), the changes in the volume fraction (in accordance with the portion of elements in the composition of the Laves and  $\gamma'/\gamma''$  phases and without  $\delta$  phase) and the size of secondary phases (Figure 6.9 a & b) can alter the hardness.

In as-SLM IN718 (Sui, Tan, et al., 2019):

$$x_{Al-matrix}(1 - f_{Laves} - f_{\gamma'} - f_{\gamma''}) + x_{Al-Laves}f_{Laves} + x_{Al-\gamma'Ni3Al}f_{\gamma'-Ni3Al} = x_{Al-total} \quad (6.9)$$

$$x_{Ti-matrix}(1 - f_{Laves} - f_{\gamma'} - f_{\gamma''}) + x_{Ti-Laves}f_{Laves} + x_{Ti-\gamma'Ni_3Ti}f_{\gamma'-Ni_3Ti} = x_{Ti-total} \quad (6.10)$$

$$x_{Nb-matrix}(1 - f_{Laves} - f_{\gamma'} - f_{\gamma''}) + x_{Nb-Laves}f_{Laves} + x_{Nb-\gamma''}f_{\gamma''} = x_{Nb-total} \quad (6.11)$$

$$f_{\gamma'} = f_{\gamma'-Ni_3Al} + f_{\gamma'-Ni_3Ti} \quad (6.12)$$

In AD730<sup>TM</sup> for different types of  $\gamma'$  phase:

$$x_{Al-matrix}(1 - f_{\gamma'}) + x_{Al-\gamma'Ni_3Al}f_{\gamma'-Ni_3Al} = x_{Al-total} \quad (6.13)$$

$$x_{Ti-matrix}(1 - f_{\gamma'}) + x_{Ti-\gamma'Ni_3Ti}f_{\gamma'-Ni_3Ti} = x_{Ti-total} \quad (6.14)$$

where  $x_{Al-matrix}$ ,  $x_{Al-Laves}$  and  $x_{Al-\gamma'Ni_3Al}$  are the concentration of Aluminum (Al) element in the matrix, Laves phase and  $\gamma'$ -Ni<sub>3</sub>Al phase, respectively;  $x_{Ti-matrix}$ ,  $x_{Ti-Laves}$  and  $x_{Ti-\gamma'Ni_3Ti}$  are the concentration of Titanium (Ti) in the matrix, Laves phase and  $\gamma'$ -Ni<sub>3</sub>Ti phase, respectively;  $x_{Nb-matrix}$ ,  $x_{Nb-Laves}$  and  $x_{Nb-\gamma''}$  are the concentration of Nb element in the matrix, Laves phase and  $\gamma''$  phase, respectively;  $x_{Al-total}$ ,  $x_{Ti-total}$  and  $x_{Nb-total}$  is the concentration of Al, Ti, and Nb in the material, respectively;  $f_{Laves}$ ,  $f_{\gamma''}$ ,  $f_{\gamma'-Ni_3Al}$  and  $f_{\gamma'-Ni_3Ti}$  is the volume fraction of Laves phase,  $\gamma''$  phase,  $\gamma'$ -Ni<sub>3</sub>Al phase and  $\gamma'$ -Ni<sub>3</sub>Ti phase, respectively.

As mentioned in section 6.3.3, the accumulation of solute atoms in mobile dislocations around precipitates could further strengthen the obstacles and raise the critical stress needed to overcome these obstacles (Hansen, 2004; Kozar et al., 2009). The obstacles could temporarily or permanently block dislocation movements. During the LFW process, solute atoms can free themselves from forest/pile-up dislocations to help dislocation movements via pipe diffusion. Several factors, such as anti-phase boundary energy ( $\gamma_{APB}$ ) (207 and 378 mJ/m<sup>2</sup> for  $\gamma'$  and  $\gamma''$ , respectively, in IN718 (Ghorbanpour et al., 2020; Ling et al., 2019) and 264.8 mJ/m<sup>2</sup> (Thébaud, 2017) for and AD730<sup>TM</sup>, respectively) as a function of ordered  $\gamma'$  and coherent  $\gamma''$ , volume fraction ( $V_f$ ) and size ( $r$ ) of  $\gamma'/\gamma''$ , may affect the precipitation strengthening mechanism (Y.-T.

Chen, Yeh, Li, & Kuo, 2017; Ling et al., 2019; Ma et al., 2018; Masoumi, Jahazi, et al., 2016; Masoumi, Shahriari, et al., 2016b; Xu, Li, Yang, & Gu, 2020; Ye et al., 2020), which is generally characterized by a critical resolved shear stress ( $\Delta\tau_{total}$ ). The strength of the material can be adequately accounted for mainly by the coherency hardening mechanism (Orowan looping being the other mechanism). According to equations (6.15 & 6.16), the critical resolved shear stress increases with increasing  $\gamma_{APB}$  and particle size for underaged particles (ordered secondary and/or tertiary  $\gamma'$  in AD730<sup>TM</sup> and ordered-coherent  $\gamma'/\gamma''$  in SLM IN718), whereas for overaged or large particles (ordered primary  $\gamma_p'$  in AD730<sup>TM</sup>), the critical resolved shear stress increases with increasing  $V_f$ ,  $\gamma_{APB}$ , and decreases with increasing particle size (Eq. 6.17). Furthermore, based on the coherent strain strengthening mechanism (Ghorbanpour et al., 2020; H. Yang, Zhu, Zhang, Zhou, & Sun, 2020), the interaction of the dislocations and the stress field generated around the  $\gamma''$  precipitates in IN718 plays a crucial role in the strengthening (more effective than  $\gamma'$  (M. C. Chaturvedi & Han, 1983)) (Eq. 6.18) (M. C. Chaturvedi & Han, 1983; Y.-T. Chen et al., 2017; Ling et al., 2019; J. M. Zhang, Gao, Zhuang, & Zhong, 1999). The effect of the size of strengthening phases on the hardness results for both alloys is shown in Figure 6.9.

$$\Delta\tau_c = \frac{\gamma_{APB}}{2b} \left[ \left( \frac{6\gamma_{APB}V_f r}{\pi T} \right)^{\frac{1}{2}} - V_f \right] \quad (\text{in both alloys}) \quad (6.15)$$

$$\Delta\tau_c = \frac{\gamma''_{APB}}{2b} \left[ \left( \frac{4\gamma''_{APB}V_f \gamma''}{\pi T} \right) \left( \frac{\sqrt{6Rh}}{3} \right)^{1/2} - \beta V_f \gamma'' \right] \quad (\text{in IN718}) \quad (6.16)$$

$$\Delta\tau_c = \sqrt{\frac{3}{2}} \left( \frac{Gb}{r} \right) V_f^{1/2} \frac{w}{\pi^{3/2}} \left( \frac{2\pi\gamma_{APB}r}{wGb^2} - 1 \right)^{1/2} \quad (\text{in AD730}^{\text{TM}}) \quad (6.17)$$

$$\Delta\tau_{coherency} = 1.7G(\varepsilon)^{3/2} \left( \frac{V_f \gamma''(1-\beta)}{2b} \right)^{1/2} \frac{h}{R^{1/2}} \quad (\text{in IN718}) \quad (6.18)$$

where  $b$  is the Burger's vector for the  $\langle 110 \rangle$  dislocations (2.492 Å for IN718 alloy (Ghorbanpour et al., 2020; Ling et al., 2019) and 2.45 Å for AD730<sup>TM</sup> (al., 2014)),  $r$  is the size of the  $\gamma'/\gamma''$  particle,  $T$  is the dislocation line tension which is equal to  $0.5Gb^2$ ,  $G$  is the shear

modulus (average 75.4 GPa for  $\gamma'/\gamma''$  in IN718 alloy (Ghorbanpour et al., 2020; Ling et al., 2019) and 76.3 GPa for AD730<sup>TM</sup> (al., 2014)), and  $w$  is a dimensionless constant ( $\sim 1$ ).  $\epsilon$  is (= 0.498-0.632 %) the lattice misfit between the  $\gamma''$  precipitate and the matrix.  $\beta$ ,  $R$ , and  $h$  represent the constant ( $\frac{1}{3}$ ) related to the distribution of  $\gamma''$  precipitates, the semi-major, and semi-minor axis lengths of the  $\gamma''$  precipitates, respectively (Ling et al., 2019). The increased yield strength value is  $\Delta\tau_{total}$  (sum of Eqs. (6.15-18) for each alloy). Therefore, the higher strength (hardness) of the material can be achieved by the coherent strain strengthening of the matrix, the precipitation of nanoscale  $\gamma'/\gamma''$  and microscale  $\gamma_p'$  phases (optimum size and number of particles (Lachowicz, Dudziński, & Podrez-Radziszewska, 2008)), and the dislocation interactions with particles.

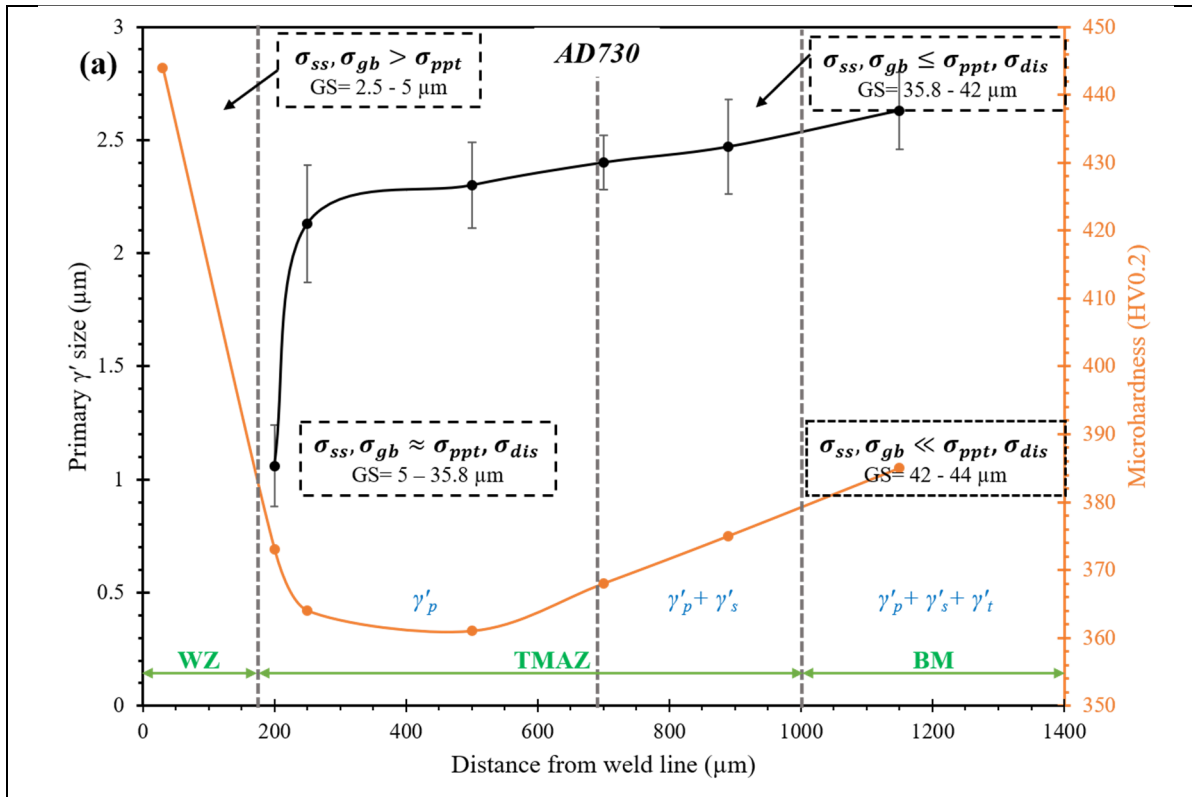
A large volume fraction and fine particle size are generally beneficial for strengthening. The total strength can therefore be obtained as (Hansen, 2004; Kamikawa et al., 2015; Kozar et al., 2009; Ma et al., 2018):

$$\sigma_y = \sigma_0 + \sigma_{ss} + \sigma_{gb} + \sigma_{ppt} + \sigma_{dis} \text{ (MPa)} \quad (6.19)$$

where  $\sigma_{ss}$ ,  $\sigma_{gb}$ ,  $\sigma_{dis}$ , and  $\sigma_{ppt}$  are contributions from solid solution strengthening, grain boundary strengthening, dislocation strengthening and precipitation strengthening, respectively. According to the Figures 6.5, 6.8, & 6.9, the effects of the precipitation (size and volume fraction) mechanisms can be realized.

As mentioned above, and shown in Figure 6.9 (a), in the WZ of AD730<sup>TM</sup>, the impact of grain size (and/or possible ultrafine undissolved precipitates) on the hardness of the material was more than precipitation. However, the effect of precipitation was more than grain size toward the BM due to increasing the size and volume fraction) of  $\gamma_p'$  (close to the grain boundaries) and  $\gamma_s'$  and the presence of  $\gamma_t'$  in the matrix (Figure 6.5 a). In Figure 6.9 (b), in the WZ of SLM IN 718, the grain size reduction could not increase the hardness and the strength of the material (according to the Hall-Petch relation). It reveals the significant impact of precipitation and the secondary phase dissolution (Laves and  $\gamma'/\gamma''$ ) on the strengthening of this alloy. From the WZ

to the BM of SLM IN718, the hardness and probably strength of the alloy increased due to both undissolved secondary phases and small grains size (in the TMAZ). However, as revealed in the HAZ (Figures 6.5 b and 6.6 d & e), the observed increase in hardness can be attributed to the sum of the contributions from the Laves phase, Nb micro-segregation, and  $\gamma''$  phase.



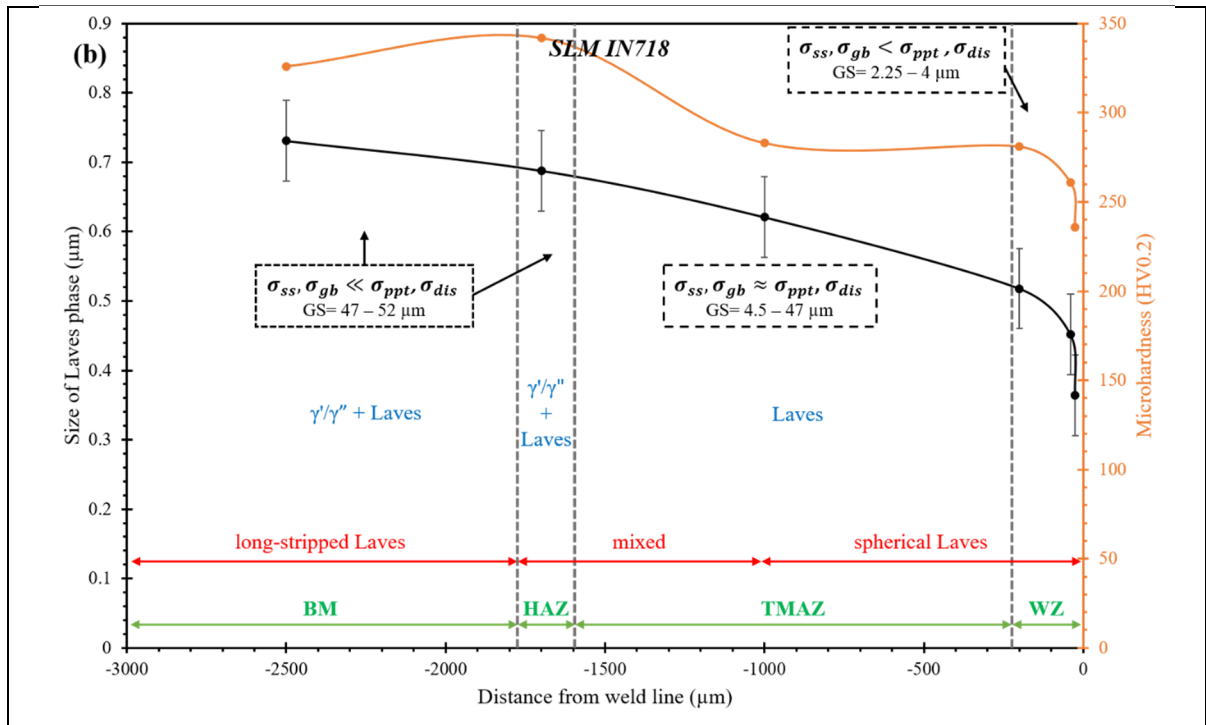


Figure 6.10 Variation of hardness and the size of secondary phases with distance from the weld line on (a) AD730<sup>TM</sup> and (b) SLM IN718 sides

## 6.4 Conclusions

In this study, two Ni-based superalloys fabricated by two different methods, SLM IN718 and a forged AD730<sup>TM</sup>, were linear friction welded. Variations of secondary phases across the weld line have been studied following welding. The impact of the evolution of the microstructure on the microhardness has also been evaluated. Various evolutions of microstructural features of SLM IN718 and AD730<sup>TM</sup>, specifically the dissolving of secondary phases, alter the mechanical properties of LFWed parts. The main findings of this study can be summarized as follows:

1. The different zones of LFWed joints were determined. The evolution of the precipitation or dissolution of secondary phases and microhardness as a function of strengthening mechanisms was found to be related to fundamental metallurgical features such as grain size variations and secondary phases.

2. The microhardness evaluation of LFWed samples showed a drop in the hardness of the TMAZ in AD730<sup>TM</sup> due to the dissolution of 90 % of secondary  $\gamma'$  and all tertiary  $\gamma'$  volume fractions. On the other hand, with a decrease in distance from the weld line, the microhardness gradually increased due to grain refining in the microstructure.
3. The strength of the SLM IN718 is more dependent on the secondary phases and their morphology as precipitation hardening mechanism than the grain size, whereas on the AD730<sup>TM</sup> side, the effect of grain size (and/or even possible presence of ultrafine  $\gamma'$ ) on the strength of the alloy is more significant than that of secondary phases. This could be attributed to the absence of solid solution elements (e.g., Nb, Mo, W, Co, and Cr) in the chemical composition of secondary phases. However, both the size and the volume fraction of all phases affect the hardness and mechanical properties of the joint.
4. A critical stress/strain is required to initiate plastic deformation at an appropriate process time range (10-15 s) to generate enough temperature ( $\sim 1200$  °C or higher than solvus temperature of secondary phases) to overcome the strength of the material during LFW.

## CHAPTER 7

### POST-WELD HEAT TREATMENT OF ADDITIVELY MANUFACTURED INCONEL 718 WELDED TO FORGED NI-BASED SUPERALLOY AD730™ BY LINEAR FRICTION WELDING

Syedmohammad Tabaie <sup>a</sup>, Farhad Rézaï-Aria <sup>b</sup>, Bertrand C.D. Flipo <sup>c</sup>, Jonathan Cormier <sup>d</sup>,  
Mohammad Jahazi <sup>a</sup>

<sup>a</sup> Department of Mechanical Engineering, École de technologie supérieure,  
1100 Notre-Dame West, Montreal, QC, Canada

<sup>b</sup> Institut Clément Ader (ICA), Université de Toulouse, CNRS, IMT Mines Albi, INSA, UPS,  
ISAE, Campus Jarlard, 81013 Albi, France

<sup>c</sup> TWI Ltd, Granta Park, Great Abington, Cambridge CB21 6AL, United Kingdom

<sup>d</sup> Institut Pprime, UPR CNRS 3346, Département de Physique et Mécanique des Matériaux,  
ISAE-ENSMA, BP 40109, 86961 Futuroscope-Chasseneuil Cedex, France

Paper publication in *Journal of Metallurgical and Materials Transactions A*, May 2021

#### Abstract

A new post-weld heat treatment (PWHT) cycle was designed for a novel dissimilar linear friction welding (LFW) of selective laser melted (SLM) Inconel 718 (IN718) to AD730™ forged Nickel-based superalloy. The microstructure and hardness of the joints after the PWHT are investigated and compared with those of as-LFWed samples. The precipitation of  $\gamma' + \gamma''$  is determined the main mechanism to increase the mechanical properties of SLM IN718 alloy. These particles coarsened during heat treatment at 980 °C and double aging. The thermomechanical history of LFWed joints can affect the microstructure of IN718 alloy such as morphology of  $\delta$  phase after solution treatment (ST) from the plate-like in the weld zone (WZ) to the needle-like in the base material (BM). It was found that in AD730™, nanometric size  $\gamma'$  particles re-precipitated close to the weld line during rapid cooling after welding. The presence of ultrafine  $\gamma'$  particles and coarsening the remained particles in the microstructure of the alloy, during the PWHT, can enhance the strength and hardness. The developed PWHT resulted in uniform hardness across the new dissimilar joint.

**Keywords:** Linear friction welding; selective laser melting; Ni-based superalloy; Post-weld heat treatment; Precipitation; Strengthening mechanisms.

## 7.1 Introduction

Linear friction welding (LFW) is a type of solid-state friction welding whose processes were introduced to overcome fusion defects induced by different fusion welding methods. This joining process is very fast and highly adaptable to automation in high-rate productions and in repairing blades and disks (blisks) in the aerospace industry as well as in other turbine applications (Addison, 2010; Bhamji et al., 2011; Ahmad Chamanfar et al., 2015; P Wanjara & Jahazi, 2005). Most nickel-based superalloys used in gas turbine blades are precipitation-hardened. Given that these alloys are usually solidly welded together, they are prone to crack formation in either the weld metal or in the heat-affected zone (HAZ) during welding or post-weld heat treatment (PWHT) (X. Cao et al., 2009; Ahmad Chamanfar et al., 2015; Masoumi et al., 2017). Most modern Ni-based superalloys which contain a high volume fraction of  $\gamma'$  (> 40%) (Ahmad Chamanfar et al., 2015; Ye et al., 2020) are considered to be “unweldable” by conventional fusion welding due to the occurrence of micro-shrinkage, intergranular liquation cracking, and/or strain-age cracking associated with melting, solidification, and PWHT, respectively.

Selective laser melting (or laser powder bed fusion (LPBF)) is an additive manufacturing (AM) process that offers several advantages over conventional technologies, by reducing the number of production steps, increasing the high flexibility in geometry, low material consumption, and most importantly, the possibility of manufacturing parts with high geometrical complexity and relative dimensional accuracy (Y. Chen, Zhang, Huang, Hosseini, & Li, 2016; Herderick, 2011; Moussaoui et al., 2018). The microstructure of fabricated parts contains inhomogeneity in fraction of precipitates arising from the high thermal gradient of the part during fabrication. Any inhomogeneity can be controlled by applying different post-heat-treating cycles. However, such PWHT may not be enough to erase tailored microstructure build-up (Y. Chen, Zhang, et al., 2016; Fayed et al., 2021; W. Huang et al., 2019; Ni et al., 2019; Popovich et al., 2017b; Sui, Tan, et al., 2019; Tabaie, Rézaï-Aria, & Jahazi, 2020).

As reported by (Tabaie, Rézai-Aria, Flipo, et al., 2020), a hybrid technique (SLM+LFW) involves some difficulties, such as controlling and tailoring the microstructure of the alloy after SLM and after joining. A number of research studies (Astarita et al., 2016; Cheepu et al., 2018; Z. W. Huang et al., 2007; Masoumi et al., 2019; Oleg N. Senkov et al., 2014; Ye et al., 2020) have reported that changes in the microstructure of the as-LFWed alloy take place that can affect the chemical composition, grain sizes, strengthening phases, and can induce undesirable eutectic compounds and liquation. The above changes could result in different mechanical properties such as hardness in different regions. Hence, to enhance the microstructure stability and to tackle undesirable variation in hardness and residual stresses, a PWHT cycle is required to restore the hardness in the weld regions (A. Chamanfar, Jahazi, Bonakdar, Morin, & Firoozrai, 2015; Ahmad Chamanfar et al., 2015; A. Chamanfar, Jahazi, Gholipour, Wanjara, & Yue, 2015; Kong et al., 2020; Sarrat, Chamanfar, & Jahazi, 2012; Xu et al., 2020).

The high temperature exposure and high heating (400-500 °C/s) and cooling (150-250 °C/s) rates present in the LFW process lead to a decrease in the average size and volume fraction of strengthening precipitates, resulting in a reduction in the hardness of the weld zone (WZ) as compared to the base material (BM) (A. Chamanfar, Jahazi, Gholipour, Wanjara, & Yue, 2011; Damodaram, Ganesh Sundara Raman, Satyanarayana, Madhusudhan Reddy, & Prasad Rao, 2014). In the case of the friction welding of dissimilar superalloys (Z. W. Huang et al., 2007; Ye et al., 2020), the significant differences existing between the microstructures, particularly in terms of the type and volume of the strengthening phase ( $\gamma'/\gamma''$ ) and grain size, could make it very difficult to achieve a sound dissimilar joint. Roder et al. (Roder et al., 2005) reported on tensile tests on IN718 alloy inertia friction welded to Incoloy 909 at different temperatures. In these tests, failure occurred in the WZ of IN718 alloy due to the absence of  $\gamma''$  strengthening precipitates. However, in the case of the LFW of AD730<sup>TM</sup>, Masoumi et al. (Masoumi et al., 2019; Masoumi et al., 2018) revealed that failure initiated in the BM and a final fracture occurred in the zone adjacent to the TMAZ during tensile testing at room temperature. They reported that the observed higher strength of the WZ as compared to that of the thermomechanical affected zone (TMAZ) resulted from finer grain microstructure and re-precipitation of fine secondary phase in the WZ. The  $\gamma'$  particles (in the range of a few

nanometers) re-precipitated in the WZ (Masoumi, Shahriari, et al., 2016b; Panella et al., 2020) after LFW during cooling at a higher portion than did those of the TMAZ and the BM. They noted that the PWHT cycle led to the re-precipitation of  $\gamma'$  particles in the TMAZ and restored the tensile properties of the LFWed joint (Masoumi et al., 2019).

Smith et al. (M. Smith et al., 2017; M. Smith et al., 2016) reported that the PWHT of LFWed IN718 samples improved the room temperature hardness and tensile properties of the weldment, likely partially due to an increase in the volume fraction of  $\gamma''$  phase resulting from complete  $\delta$  phase dissolution. It was observed that the PWHT re-solutionized the  $\delta$  phase uniformly even when the starting materials varied significantly in terms of  $\delta$  phase volume fraction. Therefore, the PWHT was compatible for use on LFWed samples. Chaturvedi et al. (Mahesh C. Chaturvedi, 2007; M. C. Chaturvedi & Han, 1983) reported that the precipitate strengthening mechanisms in IN718 varied (changing between precipitate shearing and coherency strain strengthening mechanisms) based on the size, morphology and volume fraction of the primary strengthening precipitates (i.e., spheroidal  $\gamma'$  and ellipsoidal  $\gamma''$ ), which were highly influenced by the aging duration and heat treatment peak temperature. In many studies (W. Cao, 2008; Kong et al., 2020; Kuo et al., 2017; Ling et al., 2019), in the case of cast and wrought or AM IN718, the dissolution/coarsening of strengthening precipitates and the formation of  $\delta$  phase are microstructure evolutions that have been shown to play a major role in the degradation of mechanical properties such as tensile strength, stress-rupture life, creep resistance (Rafiei, Mirzadeh, & Malekan, 2021) and cycle fatigue life. Damodaram et al. (Damodaram, Ganesh Sundara Raman, Satyanarayana, et al., 2014) reported that strengthening precipitates ( $\gamma''$ ) dissolved in the weld metal and the HAZ during welding. The HAZ was weaker than the weld metal due to coarser grains in the former, and therefore, there was failure in the HAZ. However, PWHTed samples (solution-treated (ST) and ST+ aged (STA)) failed at the BM. The STA sample after welding exhibited the best stress-rupture properties. The authors explained that this could be attributed to homogenization as well as a moderate coarsening of the grain structure of the WZ and a fine and uniform distribution of strengthening precipitates throughout the weldment.

As a laser powder bed fusion (LPBF) fabrication method, selective laser melting (SLM) can be combined with the LFW process to develop and to accelerate the manufacture and/or repair of blisks with dissimilar alloys. The main objective of the present study was to develop specific PWHT cycles for LFWed dissimilar joints of polycrystalline Ni-based superalloy AD730<sup>TM</sup> to as-SLM IN718 and to homogenized SLM IN718 (H-SLM IN718) in order to achieve uniform microstructure and to enhance the microhardness on both sides of the weldment. The obtained hardness measurements are compared with other reported results in the literature.

## 7.2 Experimental procedures

### 7.2.1 Post-weld heat treatment

An as-received forged AD730<sup>TM</sup> alloy with an average grain size of  $41.36 \pm 9.14 \mu\text{m}$  and with a  $\gamma'$  volume fraction of 40% (for all  $\gamma'$  classes) was provided by Aubert & Duval. IN718 superalloy was fabricated by an SLM-125HL machine at IMT-Mines Albi, France, with a Z-direction displacement and perpendicular to the fabrication platform for LFW in as-fabricated conditions. Two rectangular AD730<sup>TM</sup> samples ( $37$  (L: length)  $\times$   $26$  (W: width)  $\times$   $13$  (H: height)  $\text{mm}^3$ ) were LFWed to an as-SLM IN718 and an H-SLM IN718 (homogenized at  $1100^\circ\text{C}$  for 1 h and water-quenched) with the same dimensions. Their chemical compositions are provided in Table 7.1.

Table 7.1 Chemical compositions of bulk of alloys (wt.%)

Alloy	Elements												
	Ni	Fe	Cr	Co	Mo	W	Al	Ti	Nb	B	C	Zr	Si
<b>Forged AD730</b>	Bal.	4.00	15.70	8.50	3.10	2.70	2.25	3.40	1.10	0.010	0.015	0.030	-
<b>SLM IN718</b>	Bal.	15.70	20.54	0.10	3.13	-	0.34	1.17	5.10	0.002	0.040	0.018	0.01

The LFW process was conducted using an FW34-E20 LFW machine at TWI, Cambridge, UK. The process was run by applying a constant friction pressure of 228 MPa, with an oscillation frequency of 40 Hz, and an amplitude of 3 mm of cyclic frictional displacement. A forge

pressure of 340 MPa was applied at the last stage of LFW. Pressure was applied perpendicular to the cross-section defined by the length (L) and the width (W, i.e., area of L-W). The oscillations on the top of the SLM-IN718 samples were perpendicular to the SLM building direction. The surface in contact with the AD730™ was the surface on the top of SLM fabricated samples. Three welds were PWHTed in this study: two as-SLM IN718-AD730™ (W1) and one H-SLM IN718-AD730™ (W2).

In order to relieve the residual stress and restore the hardness on both sides of the weldments, post-weld heat treatments (PWHTs) were conducted in an air circulating furnace, as shown in Fig. 7.1. Depending on the microstructure of the SLM IN718 and the precipitation hardening treatment for the IN718 and AD730™ alloys, one of samples of W1 was solution-treated (ST) at 980 °C for 1 h and water-quenched. It should be noted that the ST heat treatment is a solution treatment for IN718 alloy. The samples were then aged at 730 °C for 12 h, furnace-cooled (55 °C/h), and held at 620 °C for 10 h, followed by air cooling (W1-STA). The second sample of W1 and the W2 sample were directly aged and are identified as W1-DA and W2-DA, respectively. Dependence on industrial aging treatment of AD730™ alloy at 730-760°C for 8 h and two-step aging for SLM IN718 alloy, in this study, the temperatures and time of the first aging step are modified (i.e., 8 h to 12 h). It should be noted that the second aging step (620 °C for 10 h) cannot affect the precipitation hardening in AD730™. However, the time was increased from 8 h (as usually aging time for IN718 alloy) to 10 h to compare the results with the literature.

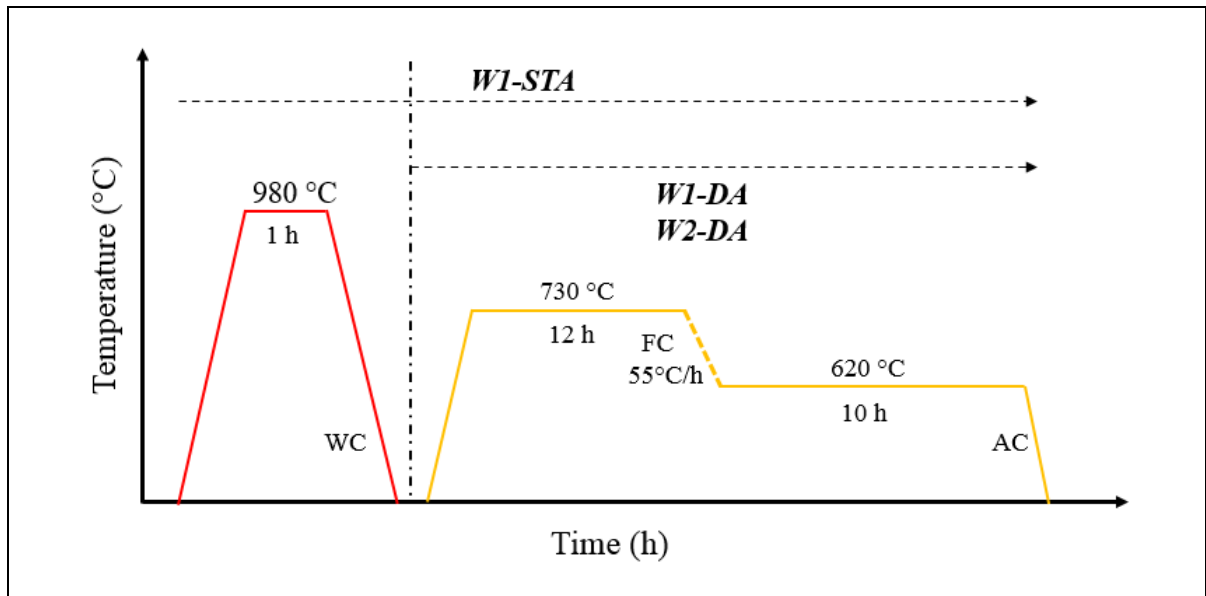


Figure 7.1 Schematic of the PWHT cycle for all LFWed samples

## 7.2.2 Microstructural analysis

For metallographic and microstructural analyses, the welded samples were EDM-cross-sectioned perpendicular to the welding direction from the center of the sample along the longitudinal axis, as fully reported in (Tabaie, Rézaï-Aria, Flipo, et al., 2020). The cross-sectioned samples were prepared by standard metallographic techniques for microstructure investigation and using waterless Kalling and Marble solutions for etching. A scanning electron microscopy (SEM) examination was carried out using a Hitachi TM3000 tabletop SEM, as well as a Hitachi SU-8230 Field Emission-SEM (FESEM) equipped with a Bruker Electron Backscatter Diffraction (EBSD) and Quad energy-dispersive X-ray spectroscopy (EDS) detectors.

To analyze possible grain size evolutions, W1-STA, and W1-DA specimens for EBSD examination were prepared on a Buehler VibroMet™ polisher using a 0.05  $\mu\text{m}$  colloidal silica suspension. Then, the specimens were ion-milled by an Ion Beam Milling System (IM 400Plus, Hitachi). To illustrate grain size variations in the weld regions, a 0.41  $\mu\text{m}$  step size was selected for EBSD mapping. A finer step size of 90 nm was used for the recrystallized region close to

the weld lines (or WZ), and a coarser step size of 0.47  $\mu\text{m}$  was used for the non-recrystallized regions (TMAZ, HAZ, and BM). In order to evaluate the grain size at each location, an average of at least 300 grains was characterized for each microstructure. The EBSD data were analyzed using the Esprit software developed by Bruker, in order to obtain grain size changes, as well as for EDS analysis.

### **7.2.3 Microhardness**

The microhardness (HV) profiles were measured on cross-sectioned PWHTed samples using a Future-Tech Vickers device to evaluate the weld strength and were compared with as-LFWed samples (W1 & W2). The measurements were carried out under a load of 200 g and a dwell time of 15 s, and over a distance of approximately 3 mm from the weld interface to the BM, to identify and compare variations in strength across the weld regions in both superalloys after LFW and PWHT. The measurements were repeated at least five times for different distances, and the average values are reported with errors between 0.4% (in the WZ and the BM) and 2.1% (in the TMAZ).

## **7.3 Results and discussion**

### **7.3.1 Microstructure evolution**

Grain size (GS) variation across the weld line was investigated by SEM and EBSD. Fig. 7.2 (a-d) shows that no grain growth is expected in SLM IN718 after the DA due to the prevailing low temperature (max. 730 °C). However, in the W1-STA IN718 sample, the columnar grains partially recrystallized due to the 1-hour heat treatment at 980 °C before aging, leading to a slight decrease in the average grain size in the BM (Fig. 7.2 e). It should be noted that the microstructures of SLM IN718 (in the BM of W1-STA) specimen mostly retained the columnar grains and cellular structures of the as-fabricated materials, which was important for improving the mechanical properties (Fig. 7.2 a & c). In the W2-DA (Fig. 7.2 d), the columnar

grains and cellular structures that were observed in the as-fabricated condition were partially removed after homogenization (before LFW) and replaced with equiaxial grains; however, highly an oriented structure could be observed inside the grains. Ni et al. (Ni et al., 2019) reported that partial recrystallization is beneficial in decreasing the anisotropy for mechanical properties. However, on AD730<sup>TM</sup>, no grain size change was observed since the heat treatment at 980 °C was too cold to induce any grain growth or recrystallization (Katnagallu et al., 2021; Pérez et al., 2018).

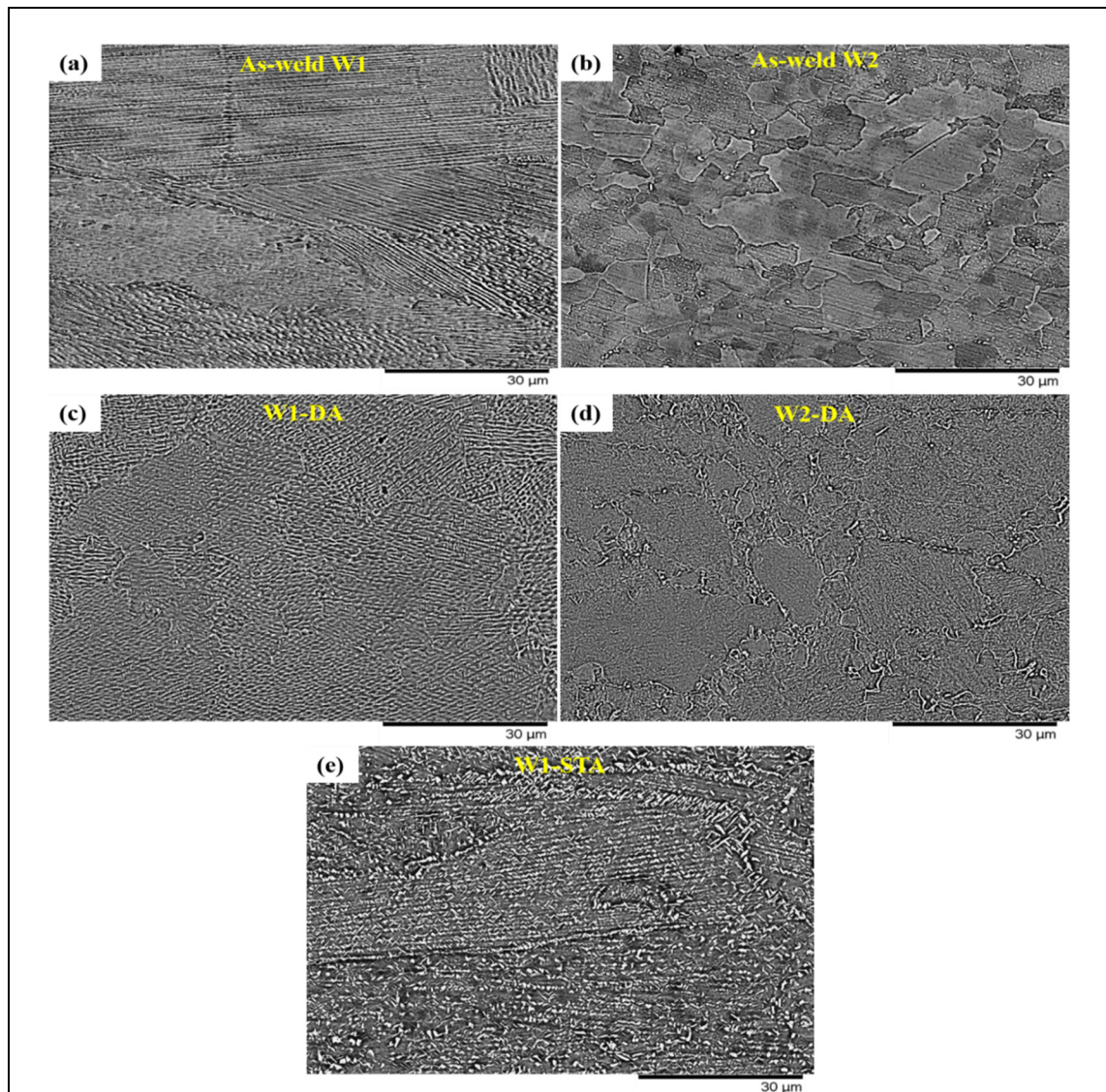


Figure 7.2 SEM micrograph in the BM zone of IN718 alloy after LFW and PWHT for: (a) W1, (b) W2, (c) W1-DA, (d) W2-DA, and (e) W1-STA

As shown in Figs. 7.2 & 7.3, in addition to grain size, different types of secondary phases precipitated after PWHT in different regions. Fig. 7.3 shows the evolution of the shape, location, and volume fraction ( $V_f$ ) of the  $\delta$  phase in IN718 alloy (W1-STA) from the BM zone to the WZ. In the BM, two  $\delta$ -phase morphologies were observed, namely, intragranular needle-like and plate-like  $\delta$  phases at grain boundaries (intergranular) in the vicinity of granular and long-stripped Laves particles (Nb: 21.58, Mo: 1.88, Ti: 1.77 (at %) on average). The presence of  $\delta$  phase particles (Nb: 9.92, Mo: 1.74, Ti: 1.75 (at %) on average) of varied sizes can be observed within the grains (larger) and at grain boundaries (smaller). Furthermore, the dimensions of the  $\delta$  particles (e.g., length and width) decreased from the BM to the WZ. This evolution was also observed in the microstructures of W1-DA and W2-DA on the IN718 side, where the fraction of the  $\delta$  phase was less than that of W1-STA (Fig. 7.4). As shown in Fig. 7.4,  $\delta$  particles are larger and plate-like or semi-spherical in the WZ and in the TMAZ (from the weld interface to  $\sim 1700 \mu\text{m}$ ).

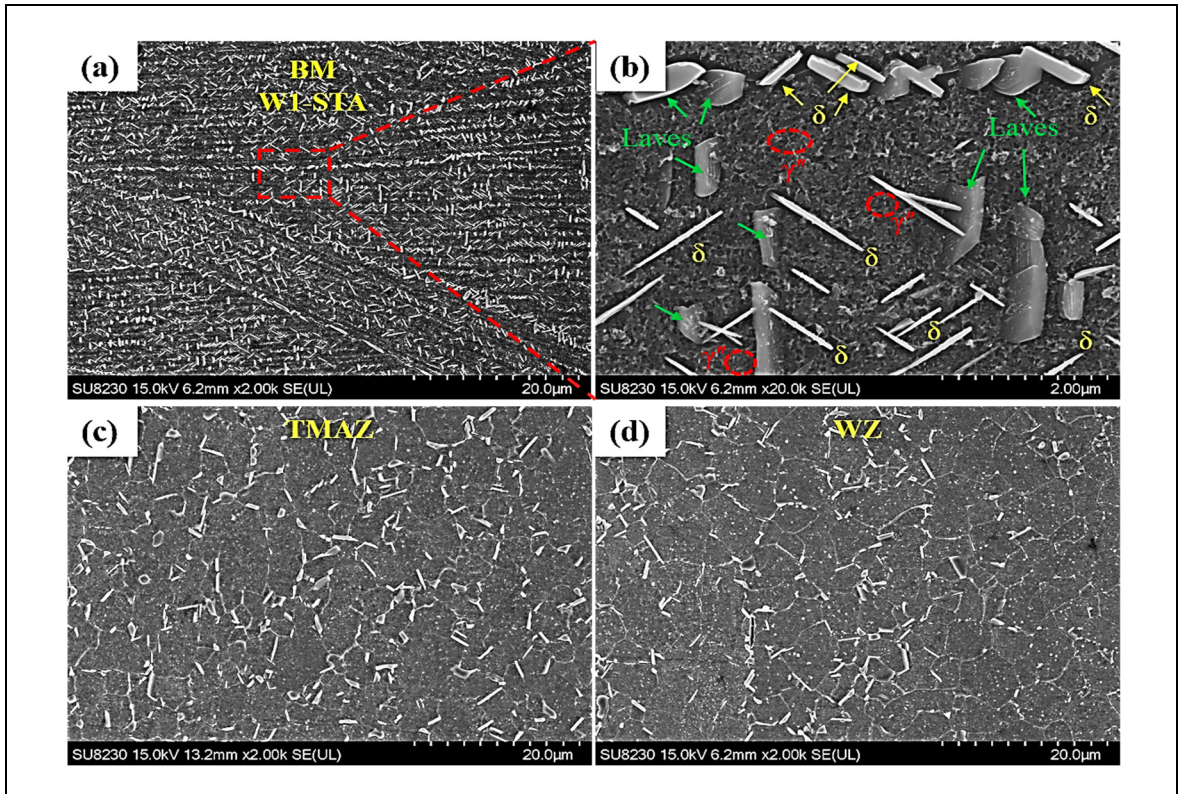


Figure 7.3 SEM images from sample W1-STA on the side of SLM IN718 alloy in the: (a) BM, (b) intergranular and intragranular  $\delta$  phase in the BM, (c) the TMAZ, and (d) the WZ

On the IN718 side, due to the heat treatment at 980 °C and aging on W1-STA, the microstructure contains more  $\delta$  phase within the grain and at the grain boundaries. Moreover, in the BM, this phase experienced greater  $\delta$  precipitation than in the TMAZ and the WZ (Figs. 7.3 & 7.4).

The  $\delta$  phase formed in the segregated (interdendritic) regions where the Laves phase (enriched Nb) precipitated after fabrication and solidification, but not so in the dendrite cores having a low Nb content. This indicates that the formation of this phase is a function of the local concentration in Nb (Sohrabi & Mirzadeh, 2020). Since the amount and the size of the  $\delta$  phase depends on the thermomechanical history of the alloy, the dissolution and precipitation of plate-like and spherical  $\delta$  phase particles both occurred during the deformation (H. Y. Zhang, Zhang, Cheng, & Li, 2010), and underwent a transformation during thermomechanical process such as the one in LFW (Fig. 7.4). The level of deformation during the LFW decreases from the WZ to the BM (A. Chamanfar et al., 2012a, 2013). As shown in Fig. 7.4 a, the volume fraction of  $\delta$  phase increased from the WZ to the BM in all samples. As a result of deformation and dissolution (due to the higher temperature close to the weld line), the plate-like  $\delta$  phase that had been formed during SLM process (and before STA) in grain boundaries was transformed, as precursor, dissolved/transformed into short granular rods or semi-spherical  $\delta$  phase particles (Fig. 7.4 b & c). The other plate-like particles could be formed during the ST (H.-y. Gan et al., 2020).

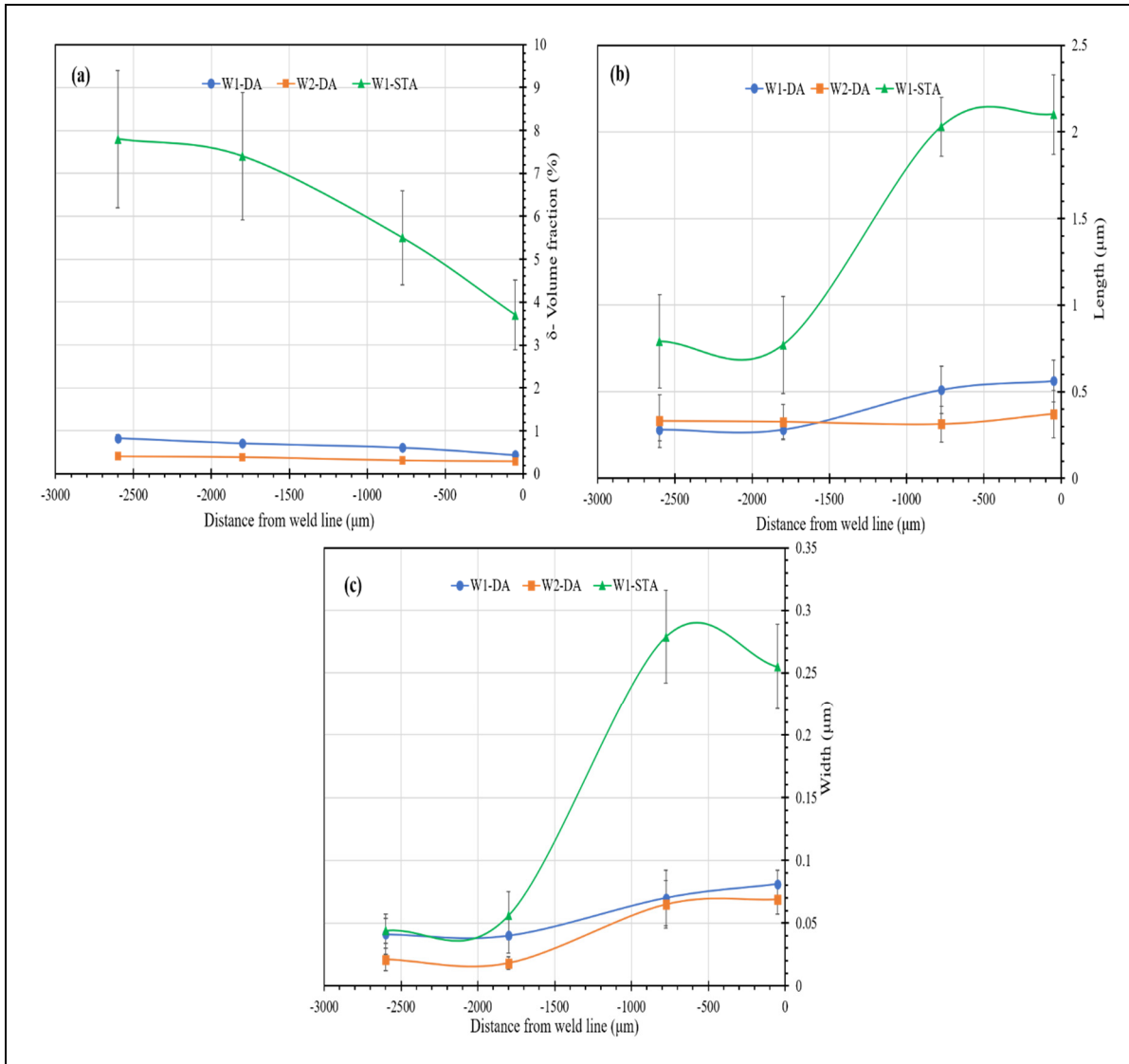


Figure 7.4 Size and volume fraction ( $V_f$ ) evolution of the  $\delta$  phase from the WZ to the BM, on SLM IN718 side, in different samples after PWHT: (a) volume fraction, (b) length, and (c) width of  $\delta$  particles

As also reported previously (Tabaie, Rézaï-Aria, Flipo, et al., 2020), there is an evolution in size, shape, and volume fraction of precipitates as we go from the WZ to the BM, on both sides. Fig. 7.5 (a & b) shows the microstructure in the WZ in the W1 and W1-DA samples, on the AD730<sup>TM</sup> side, before and after the PWHT, respectively.

In the WZ, on the AD730<sup>TM</sup> side,  $\gamma'$  phase was completely dissolved during LFW. Fig. 7.5 (a) shows no secondary phase precipitates close to the weld line after welding. However, the ultrafine  $\gamma'$  which could have re-precipitated due to the high cooling rate after LFW, were coarsened (primary  $\gamma'$ ) or newly-precipitated (secondary + tertiary  $\gamma'$ ) ( $44 \pm 12.2$  nm) within grains (as well as W2-DA sample) (Fig. 7.5 c & d) after the PWHT. In W1-STA,  $\gamma'$  particles are larger ( $189$  nm  $\pm$  29) due to the heat treatment (or ST) before aging (Fig. 7.6). The heat treatment temperature ( $980$  °C) used for W1-STA is less than the solvus temperature of the  $\gamma'$  phase ( $\sim 1105$ - $1110$  °C) and of secondary  $\gamma'$  particles ( $1050$ - $1080$  °C) in a fine grain AD730<sup>TM</sup> (Masoumi, Jahazi, et al., 2016; Masoumi, Shahriari, et al., 2016b). Therefore, on the AD730<sup>TM</sup> side, fine secondary  $\gamma'$  dissolved during the heat treatment at  $980$  °C, while undissolved or large particles coarsened, potentially affecting the volume fraction of  $\gamma'$  in the microstructure (from  $\sim 160$  nm in W1-DA to  $\sim 250$  nm W1-STA at the BM). The variation of the volume fraction and the size of  $\gamma'$  in AD730<sup>TM</sup> is provided in Fig. 7.7 for W1-DA and W1-STA. It should be noted that primary  $\gamma'$  was not observed in the WZ of the samples (Fig. 7.5 a & b and Fig. 7.6 a), and the  $V_f$  is reported for all categories.

Due to the temperature gradient between the WZ and the BM during LFW, almost all of  $\gamma'$  dissolved in the WZ where the temperature had reached  $1200$ - $1250$  °C and  $\gamma'$  primary and secondary were partially dissolved in the TMAZ where temperature had reached  $850$ - $1100$  °C. After PWHT (DA), ultrafine  $\gamma'$  ( $2$ - $10$  nm (Masoumi, Shahriari, et al., 2016b; Masoumi et al., 2019)) remained in the WZ of as-LFWed samples (in AD730<sup>TM</sup>), coarsened slowly during the first step of DA at  $730$  °C (for 12 h) in W1-DA and W2-DA samples. However, these particles could be re-precipitated and further coarsened (by 3 times close to the WZ and by 1.6 times in the BM) during the heat treatment at  $980$  °C and during double aging (W1-STA). However, the ST time and temperature are not long enough for the precipitation of primary  $\gamma'$ , although comparing W1-STA with W1-DA shows that it was coarsened, as shown in Fig. 7.7 b. According to Lifshitz–Slyozov–Wagner (LSW) well-known law (Lifshitz & Slyozov, 1961), which describes the growth kinetics of the  $\gamma''/\gamma'$  precipitate, these precipitates coarsen gradually with the aging time (Devaux et al., 2008; S. Zhang et al., 2021). As also reported by (Grosdidier, Hazotte, & Simon, 1998; Masoumi et al., 2017; Ricks, Porter, & Ecob, 1983), on

AD730™ side, the shape of the  $\gamma'$  precipitate could change from spherical to quasi-spherical and cubic (more rounded edges) as a result of coarsening that occurs during heat treatment at 980 °C and/or aging (Fig. 7.6 c & d).

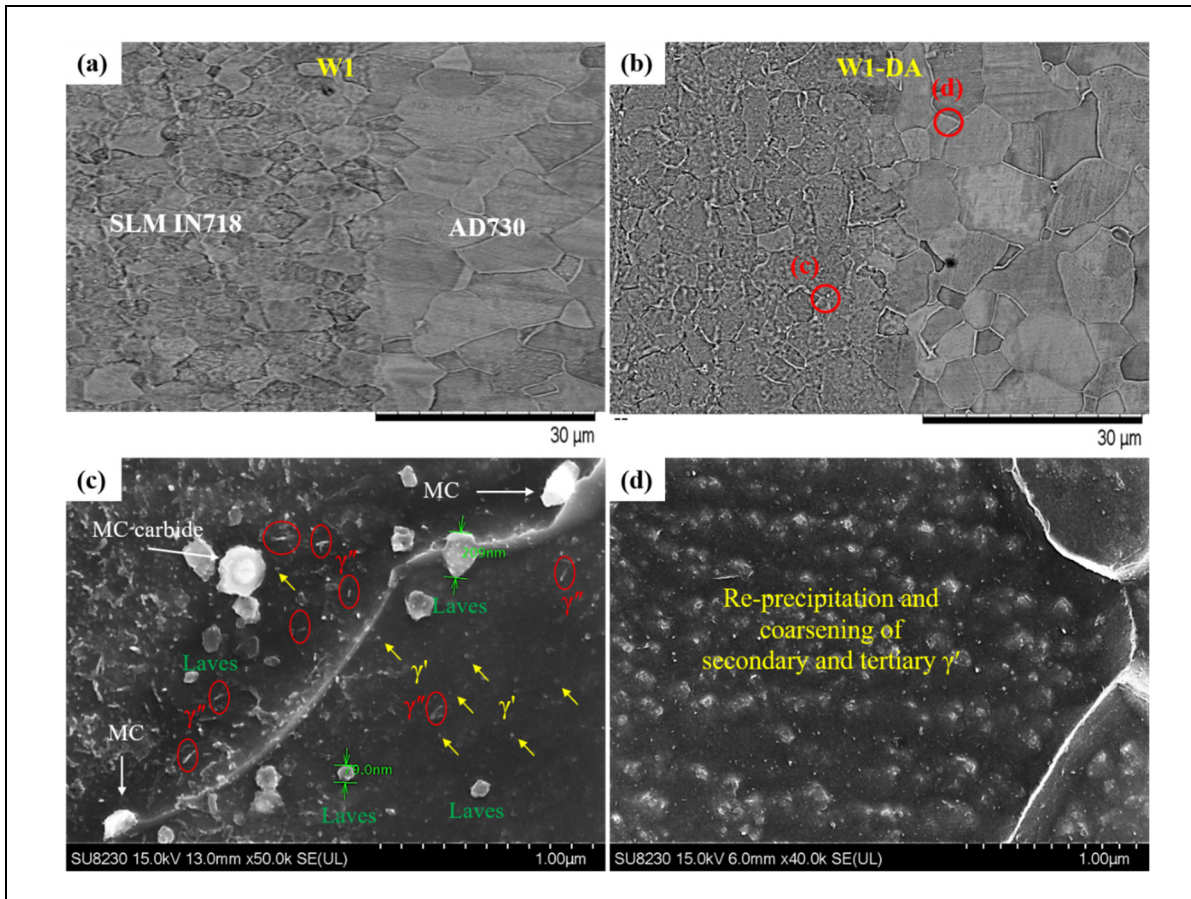


Figure 7.5 Precipitation of secondary phases in the weld interface of W1 sample after PWHT: (a) as-welded, (b) W1 direct-aged, (c) on DA-SLM IN718 side in the WZ, and (d) very fine secondary and probably tertiary  $\gamma'$  in DA-AD730™ in the WZ

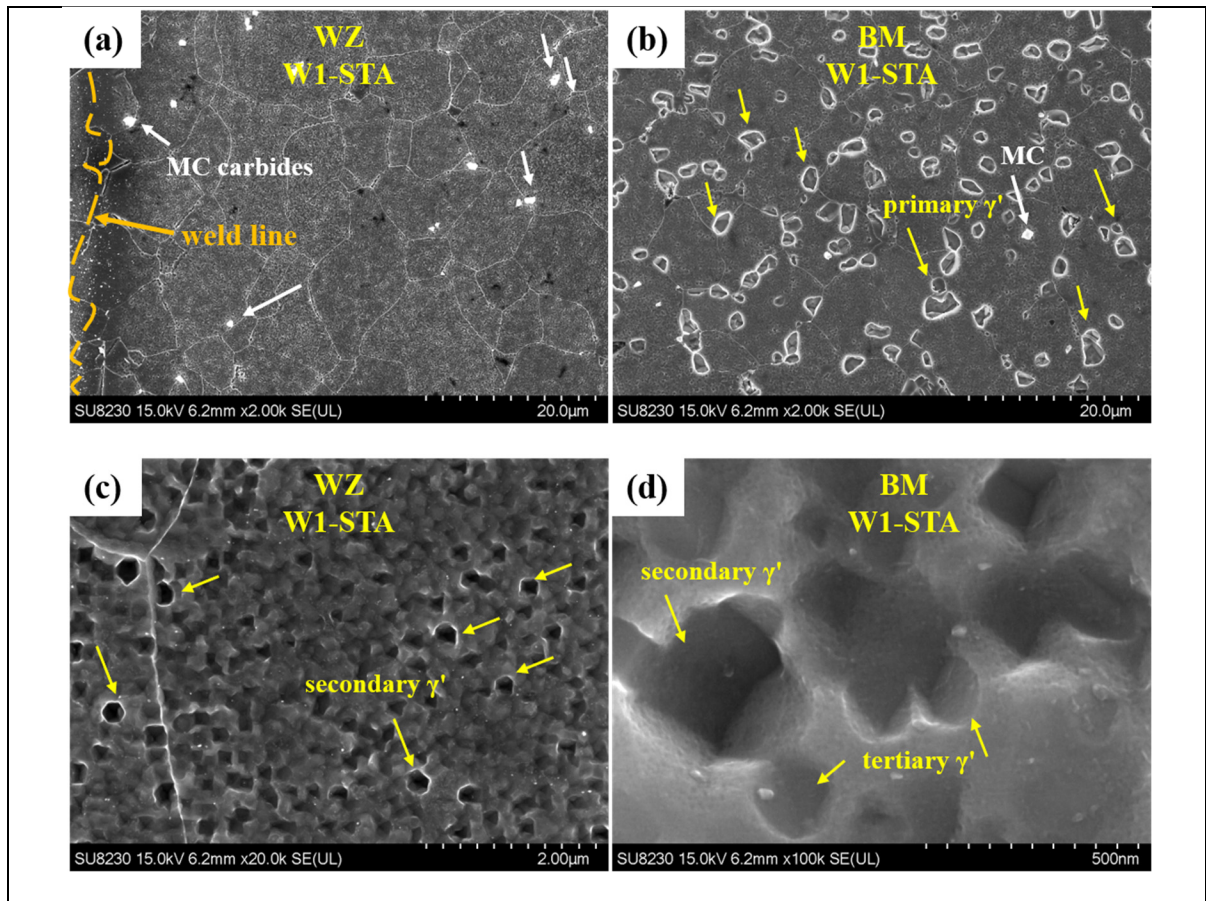


Figure 7.6 SEM images of  $\gamma'$  precipitates in sample W1-STA: (a, c) in the WZ, (b, d) in the BM of AD730<sup>TM</sup> side

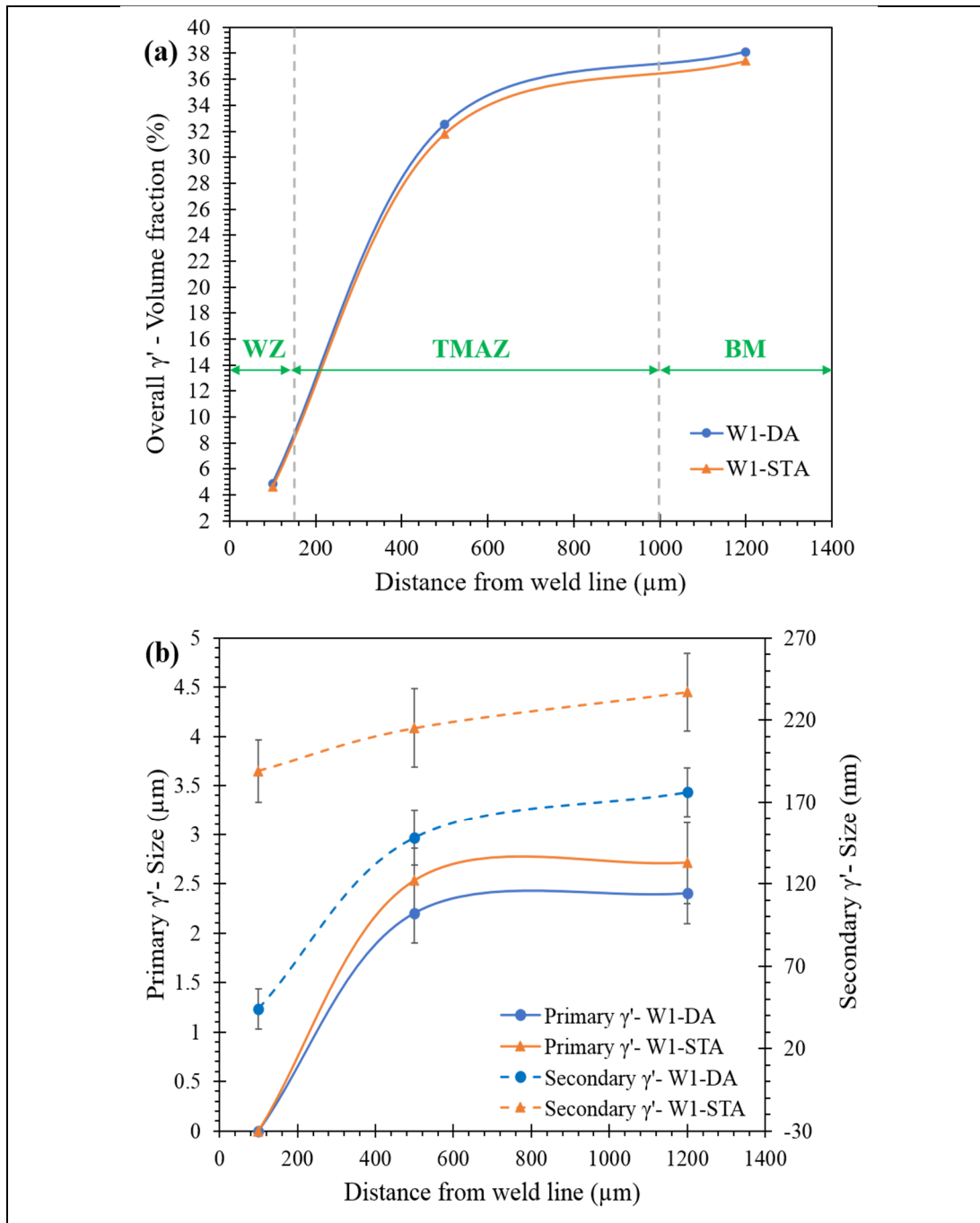


Figure 7.7 Variation of (a) the volume fraction and (b) the size of primary and secondary (and tertiary)  $\gamma'$  on AD730™ side in W1-DA and W1-STA samples from the weld line to the BM

In the IN718 alloy, in the as-LFWed conditions, secondary particles were dissolved (except for the Laves phase and MC carbides) close to the WZ due to the LFW temperature (1200-1250 °C), which was higher than the  $\gamma'$  and  $\gamma''$  dissolution temperatures ( $\gamma' = 970$  °C and  $\gamma'' = 930$  °C). On the SLM and H-SLM IN718 sides, small particles of the Laves phase dissolved and its constitutional elements (Nb and Mo) diffused to the  $\gamma$  matrix due to high temperatures (1200-1250 °C). For their part, the large Laves particles were partially dissolved and transformed to granular and finer particles since the cooling rate was high and so the time for the evolution was short (Liu, Lyu, Liu, Lin, & Huang, 2020; Tabaie, Rézaï-Aria, Flipo, et al., 2020; Tabaie, Rézaï-Aria, & Jahazi, 2020). After the PWHT (both DA and STA samples), very fine  $\gamma'$  and  $\gamma''$  were precipitated and were observed in IN718 (in both SLM and H-SLM conditions) in all zones. Generally, the same fraction of  $\gamma'/\gamma''$  is expected close to the WZ of W1-DA and W2-DA. However, as we go from the WZ toward the BM, the volume fraction of the  $\gamma''$  phase in W2-DA could be significantly higher than in W1-STA, but slightly lower than in W1-DA due to some possible  $\gamma''$  phase remnants after the SLM process in the microstructure of W1 (in the BM and almost in the TMAZ). It should be noted that both the Laves phase (Ni, Cr, Fe)<sub>2</sub>(Nb, Mo, Ti) (Nb-rich) and the  $\delta$  phase (in W1-STA) Ni<sub>3</sub>Nb (Nb and Ti-rich), in W1-STA and W1-DA can slow down the precipitation of the  $\gamma''$  and  $\gamma'$  strengthening phases (W. Huang et al., 2019; Ni et al., 2019). As reported by (Hassan & Corney, 2017; Sui, Tan, et al., 2019; X. S. Xie, Fu, Zhao, & Dong, 2010), carefully adjusting Nb, Ti, and Al is one the most effective ways of controlling the thermal stability and precipitation of  $\gamma''$  and  $\gamma'$ . The  $\delta$  particles were recognized by their morphology and their Nb and Ti contents, which was respectively lower and lower than those of the Laves particles (Table 7.2). From the EDS results, it can be seen show that the blocky particles close to the weld line are Laves phase due to their lower amounts of Nb and Ti than MC carbides (Mitchell, 2005; Mitchell et al., 1994; Vernier, Pugliara, Viguier, Andrieu, & Laffont, 2020). The Nb concentration in the  $\delta$  and in the Laves phases in the TMAZ was higher than in the WZ and lower than in the BM due to the thermomechanical gradient from the WZ to the BM during LFW, which changed the rate and diffusion distance of the elements according to (Tabaie, Rézaï-Aria, Flipo, et al., 2020; Tabaie, Rézaï-Aria, & Jahazi, 2020).

Table 7.2 EDS chemical composition analysis of Laves and  $\delta$  phases in the PWHTed samples in the TMAZ

Phase	Sample	Main constituent elements (at %)					
		Ni	Nb	Mo	Ti	Fe	Cr
Laves	W1-DA		34.87	1.74	7.76	9.74	18.09
	W1-STA	Bal.	20.17	1.45	2.63	5.06	8.90
	W2-DA		17.46	1.34	3.84	13.07	16.01
$\delta$	W1-DA		9.09	2.42	8.62	15.59	9.63
	W1-STA	Bal.	11.10	1.14	3.97	6.52	7.19
	W2-DA		8.15	2.17	6.13	14.58	12.45

According to Fig. 8 (a-i), the fraction of the Laves phase increased from the weld line to the BM zone in all three samples, as also reported by (M. Smith et al., 2017; Tabaie, Rézai-Aria, Flipo, et al., 2020). For example, Fig. 7.8 (a) shows that the Laves phase fraction in the BM of the W1-AD sample (on the IN718 side) was more than in the others. In W1-STA (Fig. 7.8 d-f), the remaining Laves particles of as-LFWed W1 were transformed into  $\delta$  and  $\gamma''$  due to the ST and aging treatment, respectively. The W2-DA sample (Fig. 7.8 g-i) contained the lowest amount of Laves particles due to the homogenization treatment that took place before LFW. The evolution of the Laves phase in the W1 and W2 samples at different locations from the weld line to the BM region has been reported by (Tabaie, Rézai-Aria, Flipo, et al., 2020). Spherical (or semi-spherical) Laves particles within the grains in the WZ were transformed to long-striped shapes in the interdendritic regions in the HAZ and BM. Therefore, variations of secondary phases such as  $\gamma'$ ,  $\gamma'/\gamma''$ ,  $\delta$ , carbides, and Laves in IN718 (SLM and H-SLM) and AD730<sup>TM</sup> alloys could provide different mechanical properties for the dissimilar joint.

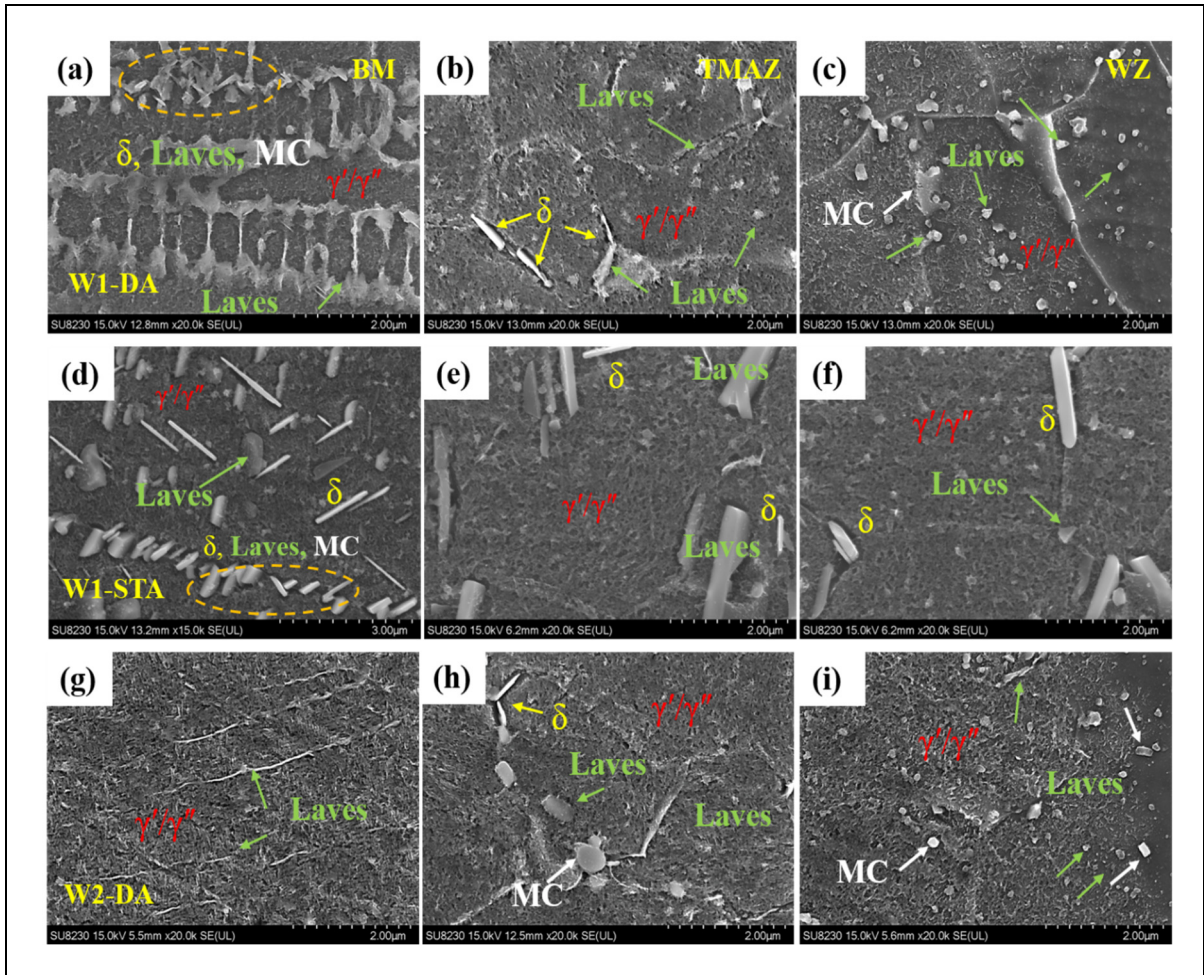


Figure 7.8 Precipitation of secondary phases in the microstructure of the PWHTed (a-c) W1-DA, (d-f) W1-STA, (g-i) W2-DA on the IN718 (SLM and H-SLM) sides (a, d, g) at the BM, (b, e, h) at the TMAZ, and (c, f, i) at the WZ

### 7.3.2 Microhardness

Figure 7.9 shows the evolution of the hardness in the PWHTed samples (W1 → W1-DA, W1-STA, and W2 → W2-DA) and its variation in different regions. Applying the proposed PWHT helped the back diffusion of segregated elements in the Laves particles into the matrix solid-solution and precipitation of  $\gamma'$ ,  $\gamma''$ , and  $\delta$  phases with the desired morphology in IN718 alloy. It also induced re-precipitation of  $\gamma'$  in AD730™ thereby allowing for the restoration of the hardness in the weldment as discussed below in detail. It must be noted that the hardness data

for as-LFWed conditions (W1 and W2) are reported from a recent publication by the present authors (Tabaie, Rézaï-Aria, Flipo, et al., 2020).

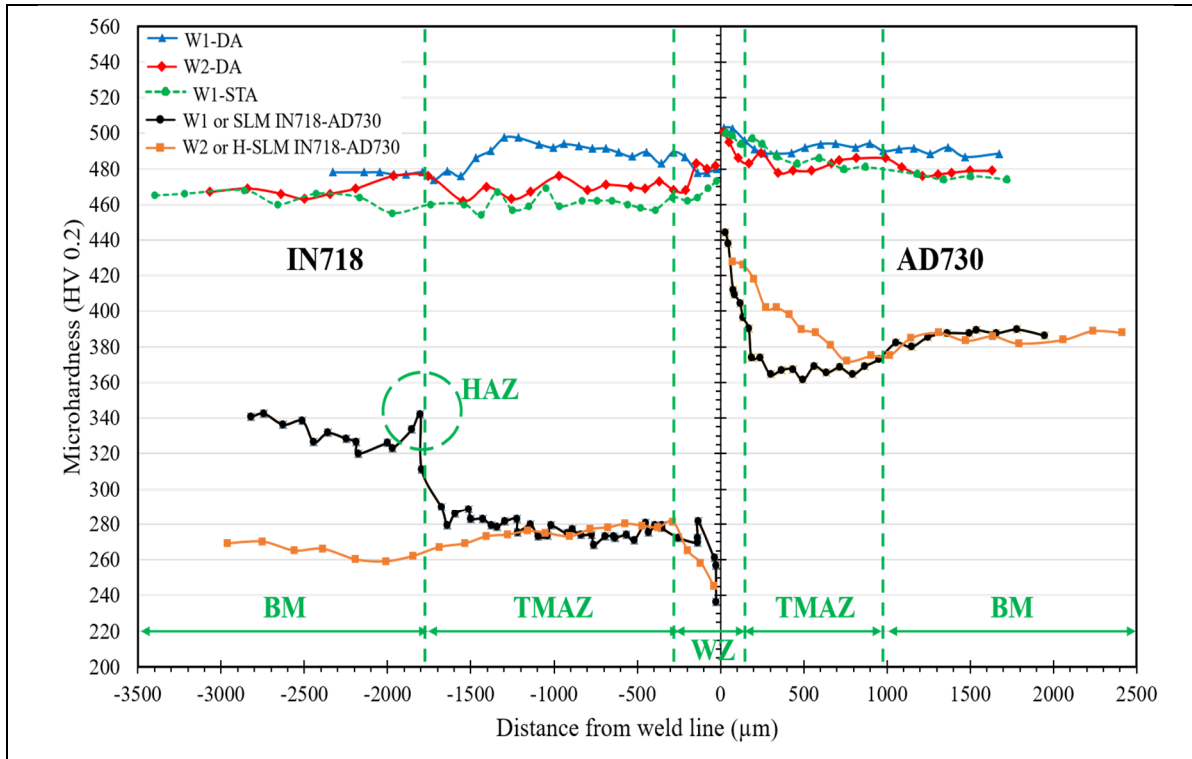


Figure 7.9 Microhardness profiles as a function of distance from the weld line of two LFWed samples

After PWHT, the hardness increased as compared to that of the as-LFWed samples (W1 and W2) in all zones. Table 7.3 provides the microhardness comparison values between the PWHT and as-LFWed conditions for both alloys in all zones. In order to better illustrate the variations, the data is presented in terms of percentage difference (i.e.,  $(PWHT/AW) \times 100$ ) in each zone of both alloys. Furthermore, in the last two columns of the Table III, the hardness differences of PWHTed samples in different locations or between the two alloys are reported.

An overall analysis of the data reported in Table 7.3 shows that the highest hardness variation occurred in the WZ of IN718 (90 % for W2-DA) and in the TMAZ of AD730<sup>TM</sup> (33.5 % for W1-DA). The minimum change was seen in the WZ of AD730<sup>TM</sup>, the BM of IN718 in W1-DA and W1-STA samples, and in the TMAZ of IN718 in W2-DA sample. However, the

relative increase in the hardness in the BM zone of IN718 in the W2-DA sample was higher than in all three samples. After PWHT, for each alloy, the maximum difference in the hardness was measured between the WZ and the BM, as reported in column 7 of the Table 7.3. These changes ranging between 17 to 25 HV are not necessarily related to variations in grain size as will be discussed below. In the last column of Table 7.3, the maximum hardness difference in the WZ of IN718 and AD730<sup>TM</sup> after PWHT is reported. These data will be used to discuss the influence of microstructural changes during PWHT on hardness evolution in each alloy in the following sections.

Table 7.3 Comparison of the microhardness values between PWHTed and as-welded samples in different zones

PWHT/AW	Alloy	WZ (%)	TMAZ (%)	HAZ (%)	BM (%)	Max. difference at PWHTed zones (HV)	Different hardness between PWHTed alloys (HV)
<b>W1-DA/W1</b>	IN718	88.2	78	42	46.5	17 (WZ-BM)	19 (WZ)
	AD730 <sup>TM</sup>	13.5	33.5	-	26.1	15 (WZ-BM)	
<b>W1-STA/W1</b>	IN718	83	65	-	41.6	10 (WZ-BM)	27 (WZ)
	AD730 <sup>TM</sup>	12.6	31.4	-	22.7	24 (WZ-BM)	
<b>W2-DA/W2</b>	IN718	90	70	-	73	20 (WZ-BM)	18 (WZ)
	AD730 <sup>TM</sup>	17	23	-	25.3	25 (WZ-BM)	

On the IN718 side, the increase in the hardness is mainly attributable to the precipitation of strengthening phases ( $\gamma' + \gamma''$ ), as well as to the coarsening of precursor  $\gamma'$  and  $\gamma''$  particles remaining from the SLM process in W1-DA in the TMAZ and in the BM. In the WZ, the re-precipitation of these phases with a higher volume fraction is generally expected to increase the hardness more than in other zones. Due to the dissolved Nb-rich Laves phase in the WZ, the Nb (a forming element of  $\gamma''$ ) level increases in the matrix. This thus enhances the precipitation of  $\gamma''$  during PWHT. Therefore, an increase in volume fraction of  $\gamma' + \gamma''$  is occurred in IN718, and thus, an 83-90% change in hardness is observed in this zone (Fig. 7.9 and Table 7.3). However, in W1-STA, due to the precipitation of  $\delta$  phase during the ST, the Nb content necessary for precipitation of  $\gamma''$  decreases in the matrix; hence, a lower fraction of  $\gamma''$  is expected in W1-STA than in the other two samples, and the change in hardness is less than them.

Furthermore, as reported by (Ling et al., 2019; Ye et al., 2020; R. Y. Zhang et al., 2020) the coherent strain strengthening induced by the precipitation of  $\gamma''$  phase and the  $\gamma'$  phase (as an ordered strain strengthening phase) are the main strengthening mechanisms in IN718 alloy. Furthermore, the  $\gamma''$  precipitation is determined the dominant hardening mechanism (Ling et al., 2019). The mismatch induced by the  $\gamma''$  phase in the matrix results in a stress field. Dislocation movement also induces the stress in the matrix. The interactions between these fields can block the dislocation movements and increase the strength of the material (J. Cormier et al., 2020; Ling et al., 2019; Ye et al., 2020). Therefore, the precipitation of mainly  $\gamma''$ ,  $\gamma'$  after PWHT and grain refinement (Tabaie, Rézaï-Aria, Flipo, et al., 2020) and solid-solution strengthening (Fayed et al., 2021; Harte et al., 2020; Ma et al., 2018; Tabaie, Rézaï-Aria, Flipo, et al., 2020; Tabaie, Rézaï-Aria, & Jahazi, 2020) could enhance the hardness of IN718 alloy. Although grain refinement is a mechanism used to increase the hardness in as-LFWed conditions (W1 and W2), the grain sizes did not change after PWHT. Therefore, the influence of secondary phases on the mechanical properties of the SLM IN718 should be considered in the present situation.

It is noteworthy that the direct-aged sample (W1-DA) has the highest hardness (the blue line in Fig. 7.9), although the Laves phase still exists due to the absence of a solution treatment. In W2-DA, due to the homogenization before LFW, the Laves particles could partially be eliminated in the microstructure. However, in W1-STA, the formation of  $\delta$  phase (needle-like structure) next to the Laves phase after heat treatment at 980 °C was observed, indicating that it had precipitated out from the dissolving Laves phase, as also reported by (Sohrabi & Mirzadeh, 2020). The direct-aged W1-DA sample is expected to have higher ultimate tensile stress but lower elongation than both W1-STA and W2-DA samples. Sui et al. (Sui, Tan, et al., 2019) reported that the presence of Laves phases (as in W1-DA) could have a strengthening effect, even if not coherent with the matrix.

Sui et al. (Sui, Tan, et al., 2019) reported that the formation and presence of the Laves phase are often accompanied by notable niobium micro-segregation, leading to coarsening and an inhomogeneous distribution of  $\gamma''$  phase. After homogenization on SLM IN718 (i.e., H-SLM in W2) as well as a significant reduction in the volume fraction of the Laves phase (Tabaie, Rézaï-Aria, Flipo, et al., 2020; Tabaie, Rézaï-Aria, & Jahazi, 2020), long-striped Laves phases are almost eliminated and transformed into spherical particles, and the distribution of the  $\gamma''$  phase becomes uniform, and the accumulated residual stress could decrease (Fayed et al., 2021; Sui, Tan, et al., 2019). Huang et al. (W. Huang et al., 2019) and Marchese et al. (Marchese, Atzeni, Salmi, & Biamino, 2020) reported that the residual stresses are gradually accumulated during SLM processes because of several repeated rapid heating-up and cooling-down of the alloys resulting in a high dislocation density which can act as strain hardening source. Therefore, the dislocation density can remain at a relatively high level after the DA due to low temperatures treatment.

It should be noted that on the IN718 side in W1 (Fig. 7.9- black line), the Laves phase volume fraction was  $\sim 18.5\%$  and  $12\text{-}15\%$  in the BM and the TMAZ, respectively. Prior to the PWHT, the average hardness of this sample in the BM was  $\sim 60$  HV higher than in the TMAZ. However, after PWHT (Fig. 7.9- blue line), the difference in hardness between the WZ and the TMAZ decreased. This, the hardness in the TMAZ was even higher ( $\sim 15$  HV) than the WZ

due to the precipitation of  $\gamma' + \gamma''$ . The crystal structure of the Laves phase becomes unstable with the reduction of Nb (Liu et al., 2020), and a high concentration of Nb will be back again into the solid-solution  $\gamma$  phase matrix, and will contribute to the precipitation of  $\gamma''$  and  $\delta$  phases ( $\text{Ni}_3\text{Nb}$ ).

On the AD730<sup>TM</sup> side (Fig. 7.9 and Table 7.3), as mentioned before, the PWHT restored the hardness in the weld regions. The hardness increased in the WZ of all samples due to the coarsening of the remaining ultrafine  $\gamma'$  during PWHT. However, this increase in the hardness was substantial in the TMAZ (~ 23-33.5% in Table 3), although the grain size was smaller than in the WZ (~5  $\mu\text{m}$  in the WZ versus ~ 25 $\mu\text{m}$  in the TMAZ). In the TMAZ, a simultaneous coarsening of the remaining  $\gamma'$  particles (primary + secondary + tertiary) and  $\gamma'$  re-precipitation could increase the hardness more than in other zones. Chamanfar et al. (Ahmad Chamanfar, 2012) reported that primary  $\gamma'$  particles reside at the grain boundaries of the Ni-based superalloy, Waspaloy, and inhibit  $\gamma$  grain growth during thermomechanical processing. In contrast, Huang et al. (Z. W. Huang et al., 2007) reported that the high strength of the 720Li alloy is mainly due to the presence of the intragranular secondary and tertiary  $\gamma'$  particles. With increasing particle size, the hardness increases to a maximum, after which it declines. This ( $\gamma'$ ) critical particle diameter, referred to as the “strongest size”, depends on the volume fraction of the particles (Ahmad Chamanfar, 2012; Jackson & Reed, 1999). The above behavior was also observed in the BM as compared to the WZ, as also reported by (Masoumi et al., 2019) in the case of an LFW of AD730<sup>TM</sup>.

Wrought superalloys such as Waspaloy and AD730<sup>TM</sup> are prone to reheat cracking during PWHT. The higher the  $\gamma'$  content or the concentration of  $\gamma'$  forming elements, the higher will be the susceptibility to reheat cracking (A. Chamanfar, M. Jahazi, A. Bonakdar, et al., 2015; Ahmad Chamanfar et al., 2015). However, the HAZ was not observed in the as-LFWed samples. Besides, no depletion of the matrix from  $\gamma'$  forming elements due to  $\gamma'$  precipitation during PWHT was observed due to the application of subsolvus heat treatment.

As reported in Table 7.3, the difference in hardness between the two alloys after PWHT was around 19 HV for W1-DA and W2-DA in the WZ. This difference was higher (27 HV) in W1-STA due to the stress relief in the WZ and the dissolution of Laves phase by Laves +  $\gamma$  (in W1)  $\rightarrow$  Laves +  $\delta$  +  $\gamma$  during the ST. The above results could be compared with those reported on dissimilar friction welding of IFWed IN718-U720Li (Z. W. Huang et al., 2007), LFWed IN718-IN713LC (Ye et al., 2020), and IFWed IN718-Incoloy 909 (Roder et al., 2005), the hardness difference between the two alloys was 65 HV (WZ and BM), 12 HV (WZ and BM), and 28 HV (for WZ) 60 HV (for BM), respectively. It must be noted that the above results were obtained after applying a one-step aging for PWHT. However, interestingly hardness measurements in all zones across the weldments, after the proposed two-step aging, show that the maximum homogeneity occurred on both alloys of the W1- DA sample (Table 7.3) (average of 17 HV for AD730<sup>TM</sup> and 15 HV for SLM IN718 between the WZ and the BM). The hardness differences between the WZ and BM were compared with those published in the literature and are summarized in the following (Fig. 7.10):

- IN718-U720Li (Z. W. Huang et al., 2007) :  $\sim$  48 HV for IN718 and  $\sim$  45 HV for U720Li.
- IN718-IN713LC (Ye et al., 2020):  $\sim$  70 HV for IN718 and  $\sim$  120 HV for IN713LC.
- IN718-Incoloy 909 (Roder et al., 2005):  $\sim$  68 HV for IN718 and  $\sim$  100 HV for Incoloy 909.
- Although the maximum hardness ( $\sim$  in the WZ) in PWHTed SLM-IN718 in the W1-DA sample was smaller (30-40 HV) than in other weldments, the hardness was more homogenous on the side of IN718 in W1-DA.

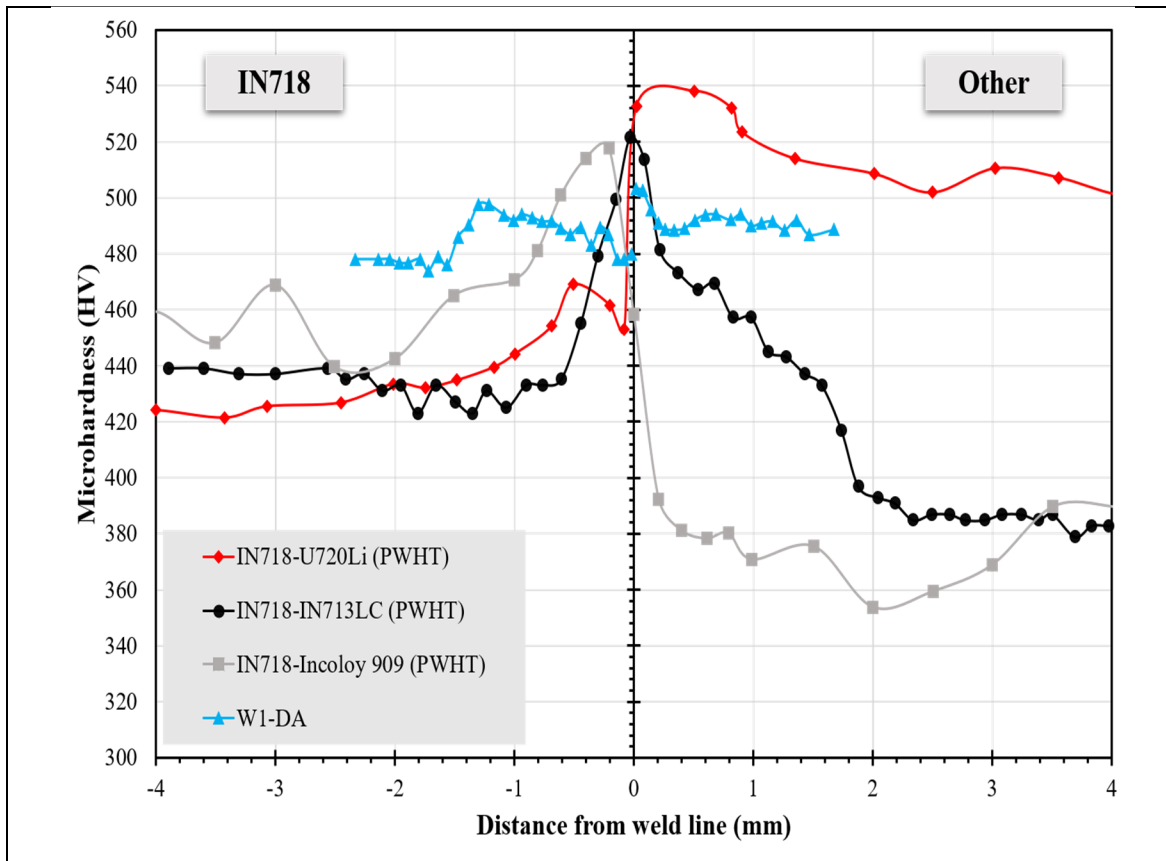


Figure 7.10 Hardness distribution across the weld interface in three other dissimilar joints after PWHT

Therefore, applying two-step aging on the LFWs of dissimilar superalloys could provide more homogeneity to the hardness of each alloy and to the weldment. A more homogenous microstructure after the PWHT could potentially provide more isotropic mechanical properties in the joint. In addition to homogeneity, the presence of  $\delta$  phase within grain boundaries of IN718 alloy in W1-STA and a larger grain size in W2 and W1-STA (in both alloys) can improve creep resistance. Masoumi et al. (Masoumi et al., 2018) reported that a specific PWHT (solutionizing at 900 °C for 2 h and aging at 730 °C for 8 h) on an LFWed fine grain AD730™ alloy resulted in a creep strength that was superior to that of as-LFWed joints.

## 7.4 Conclusions

In this study, post-weld heat treatment cycles were carried-out on linear friction welded dissimilar Ni-based superalloys fabricated by two different methods. The phase transformation and evolution of secondary phases across the weld line were studied following the PWHT. The impact of the evolution of the microstructure on the microhardness was also evaluated. The main findings can be summarized as follows:

1. The presence of ultrafine  $\gamma'$  particles in the WZ of AD730<sup>TM</sup> alloy in as-LFWed samples was revealed, and the particles coarsened during the PWHT.
2. The precipitation of the  $\gamma''$  phase in PWHTed SLM and H-SLM IN718 (W1-DA and W2-DA) is the main mechanism used to increase the hardness on the side of IN718 alloy.
3. A comparison of hardness measurements in W1-DA with W1-STA and their microstructure evolution from the WZ to the BM, shows that stress relief can be induced by PWHT cycle and likely reducing the amount of the Laves phase in the microstructure of SLM IN718. However, the hardness in W2-DA (on IN718 side) was greater (~14 HV) than in the W1-STA in the TMAZ, which can be attributed to the participation of Nb in the  $\delta$  phase formation after solution treatment (i.e., constitutional elements of Laves phase diffused into the  $\gamma$  matrix during homogenization in W2). Hence, less Nb was available for  $\gamma''$  precipitation during aging.
4. A double aging cycle based on the precipitation temperatures of the secondary phases in both alloys caused a more homogenous hardness in the joint as compared to the one-step aging previously reported in the literature.



## CONCLUSIONS

In the present research, microstructure evolution and the mechanical properties (hardness) of LFW of dissimilar superalloys fabricated by two different methods (i.e., SLM IN718 and forged AD730<sup>TM</sup>) were studied. Microstructural analyses using SEM, EDS and EBSD were performed for manufacturing processes such as LFW where hot deformation with high strain rate, rapid heating and cooling cycles takes place. Moreover, several fundamental aspects related to dissolution and precipitation of strengthening phases, and liquation phenomenon at the weld interface were identified and discussed. LFW parameters friction and forge pressures were estimated and analyzed, in order to obtain a defect free LFWed specimen. From analyses and discussions, provided in each chapter, enlisted are the drawn conclusions from this research:

1. According to the NST and NDT points of IN718 and AD730<sup>TM</sup>, the failure mechanism at nil strength temperature seems to be mostly controlled by void nucleation and growth, which occur during hot deformation and the extent of material damage is a function of temperature, applied stress, and time.
2. Liquation within the grain boundaries and the reduction in surface tension at the grain boundary-matrix interface affected by the presence of Nb and Mo rich MC. It can be reduced by diffusing these elements to the matrix via applying compression by back-diffusion mechanism.
3. High heating and cooling rates during LFW can induce a subsurface region in the HAZ of as-SLM IN718. This transitional zone called *blocky zones* was generated due to a microstructural change and a thermal gradient in the sample.
4. The hardness evolution from the bottom to the top of as-SLM IN718 shows different evolution of  $\gamma''$  and  $\delta$  phases in the SLM samples as compared to wrought materials when submitted to high heating rates. This variation should be taken into consideration of

diffusion rate and/or the solubility of Nb in the  $\gamma$  phase increased as a function of heating and cooling rates. The morphology of the Laves phase changed from fine and granular for lower rates (100 °C/s) to long-striped for higher rates (400 °C/s) demonstrating that less time was available for Nb dissolution of in the matrix and/or precipitation.

5. Microscopic analysis showed larger TMAZ on both as-SLM and H-SLM IN718 sides, as compared to AD730<sup>TM</sup>, which is due to the lower mechanical strength of IN718 at high temperatures.
6. EBSD analysis provided the variation of LAGBs and HGABs fractions in the weldment. These changes revealed that DDRX was a dominant grain refinement mechanism and recrystallization in the WZ on both sides. While CDRX was the dominant recrystallization mechanism in the TMAZ in the as-SLM or H-SLM IN718 superalloy. In contrast, for the AD730<sup>TM</sup> superalloy, DDRX was the only grain refinement mechanism for both the WZ and the TMAZ.
7. Despite the dissolution of the secondary phases in the WZ of AD730<sup>TM</sup> alloy, grain refinement was determined as a main mechanism in increasing the hardness. However, the possibility of the presence of ultrafine (nm)  $\gamma'$  could be another reason. On both as-SLM and H-SLM IN718, in the WZ, hardness decreased. It is attributed to the lower misorientation and the dissolution of secondary phases that neutralize the effect of grain refinement.
8. The microhardness evaluation of LFWed samples showed a drop in the hardness of the TMAZ in AD730<sup>TM</sup> due to the dissolution of 90 % of secondary  $\gamma'$  and all tertiary  $\gamma'$  volume fractions. On the other hand, with a decrease in distance from the weld line, the microhardness gradually increased due to grain refining in the microstructure.

9. The strength of the SLM IN718 is more dependent on the secondary phases and their morphology as precipitation hardening mechanism than the grain size, whereas on the AD730<sup>TM</sup> side, the effect of grain size (and/or even possible presence of ultrafine  $\gamma'$ ) on the strength of the alloy is more significant than that of secondary phases. This could be attributed to the absence of solid solution elements (e.g., Nb, Mo, W, Co, and Cr) in the chemical composition of secondary phases. However, both the size and the volume fraction of all phases affect the hardness and mechanical properties of the joint.
10. Comparing LFW parameters that were used in this project with other cases of similar and dissimilar LFW showed that a critical stress/strain is required to initiate plastic deformation at an appropriate process time range (10-15 s). Regarding this range, LFW can generate enough temperature for polycrystalline Ni-based superalloys (~1200 °C or higher than solvus temperature of secondary phases) at the interface to overcome the strength of the material during the process.
11. The PWHT in two-step aging caused a more homogenous hardness in the joint as compared to the one-step aging previously reported in the literature. This heat treatment cycle can stress relief and likely reduce the amount of the Laves phase in the microstructure of SLM IN718.
12. The precipitation of the  $\gamma''$  phase in PWHTed SLM and H-SLM IN718 (W1-DA and W2-DA) is the main mechanism used to increase the hardness on the side of IN718 alloy. Moreover, coarsening of  $\gamma'$  re-precipitated particles, in the WZ of AD730<sup>TM</sup> alloy in as-welded samples, after the PWHT increases the hardness in AD730<sup>TM</sup> alloy.



## RECOMMENDATIONS

In this study, the LFW of additive manufactured IN718 to forged AD730<sup>TM</sup> was studied for the first time. The main purpose of present study was to carry out a comprehensive microstructural analysis and strengthening mechanisms in the weldment after LFW. Following recommendations are suggested for future investigations in continuing the present PhD thesis:

- 1) Tensile tests at room temperature and at 650°C on as-weld and PWHTed samples in addition, investigation on effect of strengthening mechanisms on the strength of the joint.
- 2) Creep properties and fatigue resistance is one of the other properties desired for disk and blade materials. Therefore, it is suggested to investigate creep and fatigue properties and damage mechanisms on LFWed joint.
- 3) The precipitation of  $\gamma'/\gamma''$  phases in SLM IN718 was discussed based on their effect on the chemical composition and hardness of materials before and after of LFW. However, it is recommended that microscopic analysis on these phases (e.g., volume fraction).
- 4) Joining of a polycrystal (PC) superalloy to a single crystal (SC) superalloy or AMed alloys to SC present an important technological interest for the gas turbine industry as it will allow increasing the efficiency of gas turbines. To this end, LFW of SC or PC superalloys with higher fraction of  $\gamma'$  (>40%) is proposed is as a great interest from an industrial point of view in order to apply the LFW in manufacturing and/or repairing processes of hot combustion section in aero engines.
- 5) In this thesis and former projects, the effect of stress/strain on increasing diffusion were quantified and discussed in detail. It is recommended that the possibility of strain rate enhanced solute diffusivity on preventing the re-solidification products to be analyzed.



## LIST OF BIBLIOGRAPHICAL REFERENCES

- A. Devaux, B. P., M.F. Gervais, E. Georges, T. Poulain, P. Héritier. (2012). AD730TM - A New Nickel-based Superalloy for High Temperature Engine Rotative Parts. *TMS*, 911-919.
- Addison, A. C. (2010). *Linear Friction Welding Information for Production Engineering*. Retrieved from Cambridge, U.K.: TWI.
- Adegoke, O., Andersson, J., Brodin, H., & Pederson, R. (2020). Review of Laser Powder Bed Fusion of Gamma-Prime-Strengthened Nickel-Based Superalloys. *Metals*, 10(8). doi:10.3390/met10080996
- Agnoli, A., Bernacki, M., Logé, R., Franchet, J.-M., Laigo, J., & Bozzolo, N. (2015). Selective Growth of Low Stored Energy Grains During  $\delta$  Sub-solvus Annealing in the Inconel 718 Nickel-Based Superalloy. *Metallurgical and Materials Transactions A*, 46(9), 4405-4421. doi:10.1007/s11661-015-3035-9
- Akram, J., Kalvala, P. R., Jindal, V., & Misra, M. (2018). Evaluating location specific strain rates, temperatures, and accumulated strains in friction welds through microstructure modeling. *Defence Technology*, 14(2), 83-92. doi:10.1016/j.dt.2017.11.002
- A. Devaux. (2014). *Effect of aging heat-treatment on mechanical properties of AD730TM superalloy*. Paper presented at the TMS, 8th International Symposium on Superalloy 718 and Derivatives.
- Amato, K. N., Gaytan, S. M., Murr, L. E., Martinez, E., Shindo, P. W., Hernandez, J., . . . Medina, F. (2012). Microstructures and mechanical behavior of Inconel 718 fabricated by selective laser melting. *Acta Materialia*, 60(5), 2229-2239. doi:10.1016/j.actamat.2011.12.032
- Andersson, J., Sjöberg, G., & Chaturvedi, M. C. (2010). *Hot Ductility Study of Haynes 282 Superalloy*. Paper presented at the Proceeding of the 7th International Symposium on Superalloy 718 and Derivatives, TMS (The Minerals, Metals and Materials Society).
- Andersson, J., Sjöberg, G. P., Viskari, L., & Chaturvedi, M. (2013). Effect of different solution heattreatments on hot ductility of superalloys Part 2 – Allvac 718Plus. *Materials Science and Technology*, 28(6), 733-741. doi:10.1179/1743284712y.0000000002
- Aning, K., & Tien, J. K. (1980). Creep and stress rupture behavior of a wrought nickel-base superalloy in air and vacuum. *Materials Science and Engineering*, 43(1), 23-33. doi:10.1016/0025-5416(80)90203-7

- Antonsson, T., & Fredriksson, H. (2005). The effect of cooling rate on the solidification of INCONEL 718. *Metallurgical and Materials Transactions B*, 36(1), 85-96. doi:10.1007/s11663-005-0009-0
- Arakere, N. K., & Swanson, G. (2001). Fretting Stresses in Single Crystal Superalloy Turbine Blade Attachments. *Journal of Tribology*, 123(2), 413-423. doi:10.1115/1.1308032
- ASM. (1997). *ASM metals handbook - Welding, brazing and soldering*: ASM International.
- Astarita, A., Scherillo, F., Curioni, M., Aprea, P., Impero, F., Squillace, A., & Zhou, X. (2016). Study of the Linear Friction Welding Process of Dissimilar Ti-6Al-4V–Stainless Steel Joints. *Materials and Manufacturing Processes*, 31(16), 2115-2122. doi:10.1080/10426914.2016.1151048
- ASTM-International. (2015). ASTM E1382 - 97-Standard Test Methods for Determining Average Grain Size Using Semiautomatic and Automatic Image Analysis. In.
- Attallah, M. M., Jennings, R., Wang, X., & Carter, L. N. (2016). Additive manufacturing of Ni-based superalloys: The outstanding issues. *MRS Bulletin*, 41(10), 758-764. doi:10.1557/mrs.2016.211
- Azadian, S., Wei, L.-Y., & Warren, R. (2004). Delta phase precipitation in Inconel 718. *Materials Characterization*, 53(1), 7-16. doi:10.1016/j.matchar.2004.07.004
- Azarbarmas, M., Aghaie-Khafri, M., Cabrera, J. M., & Calvo, J. (2016). Dynamic recrystallization mechanisms and twinning evolution during hot deformation of Inconel 718. *Materials Science and Engineering: A*, 678, 137-152. doi:10.1016/j.msea.2016.09.100
- Balbaa, M., Mekhiel, S., Elbestawi, M., & McIsaac, J. (2020). On selective laser melting of Inconel 718: Densification, surface roughness, and residual stresses. *Materials & Design*, 193. doi:10.1016/j.matdes.2020.108818
- Barker, S. W., & Purdy, G. R. (1998). On liquid film migration in aluminium–copper alloys. *Acta Materialia*, 46(2), 511-524. doi:10.1016/s1359-6454(97)00267-x
- Bayerlein, F., Bodensteiner, F., Zeller, C., Hofmann, M., & Zaeh, M. F. (2018). Transient development of residual stresses in laser beam melting – A neutron diffraction study. *Additive Manufacturing*, 24, 587-594. doi:10.1016/j.addma.2018.10.024
- Beaubois, V., Huez, J., Coste, S., Brucelle, O., & Lacaze, J. (2004). Short term precipitation kinetics of delta phase in strain free Inconel\* 718 alloy. *Materials Science and Technology*, 20(8), 1019-1026. doi:10.1179/026708304225019830

- Bergman, T. L., Lavine, A. S., Incropera, F. P., & Dewitt, D. P. (2011). *Fundamentals of Heat and Mass Transfer* (7 ed.): John Wiley & Sons.
- Bhamji, I., Preuss, M., Threadgill, P. L., & Addison, A. C. (2011). Solid state joining of metals by linear friction welding: a literature review. *Materials Science and Technology*, 27(1), 2-12. doi:10.1179/026708310x520510
- Bhamji, I., Preuss, M., Threadgill, P. L., & Addison, A. C. (2013). Solid state joining of metals by linear friction welding: a literature review. *Materials Science and Technology*, 27(1), 2-12. doi:10.1179/026708310x520510
- Blackwell, P. L. (2005). The mechanical and microstructural characteristics of laser-deposited IN718. *Journal of Materials Processing Technology*, 170(1-2), 240-246. doi:10.1016/j.jmatprotec.2005.05.005
- Bouse, G. K. (1989). *Application of a Modified Phase Diagram to the Production of Cast Alloy 718 Components*. Paper presented at the Superalloy 718–Metallurgy Application, PA, USA.
- Brand, A. J., Karhausen, K., & Kopp, R. (1996). Microstructural simulation of nickel base alloy Incone\* 718 in production of turbine discs. *Materials Science and Technology*, 12(11), 963-969. doi:10.1179/mst.1996.12.11.963
- Brenne, F., Taube, A., Pröbstle, M., Neumeier, S., Schwarze, D., Schaper, M., & Niendorf, T. (2016). Microstructural design of Ni-base alloys for high-temperature applications: impact of heat treatment on microstructure and mechanical properties after selective laser melting. *Progress in Additive Manufacturing*, 1(3-4), 141-151. doi:10.1007/s40964-016-0013-8
- Cao, G. H., Sun, T. Y., Wang, C. H., Li, X., Liu, M., Zhang, Z. X., . . . Chen, G. F. (2018). Investigations of  $\gamma'$ ,  $\gamma''$  and  $\delta$  precipitates in heat-treated Inconel 718 alloy fabricated by selective laser melting. *Materials Characterization*, 136, 398-406. doi:10.1016/j.matchar.2018.01.006
- Cao, W. (2008). Thermal Stability Characterization of Ni-Base ATI 718Plus Superalloy. *Superalloys*, 789-797.
- Cao, X., Rivaux, B., Jahazi, M., Cuddy, J., & Birur, A. (2009). Effect of pre- and post-weld heat treatment on metallurgical and tensile properties of Inconel 718 alloy butt joints welded using 4 kW Nd:YAG laser. *Journal of Materials Science*, 44(17), 4557-4571. doi:10.1007/s10853-009-3691-5
- Cao, Y., Bai, P., Liu, F., & Hou, X. (2019). Investigation on the Precipitates of IN718 Alloy Fabricated by Selective Laser Melting. *Metals*, 9(10). doi:10.3390/met9101128

- Caron, J. L., & Sowards, J. W. (2014). Weldability of Nickel-Base Alloys. In S. Hashmi (Ed.), *Comprehensive Materials Processing* (pp. 151-179): Elsevier.
- Chadha, K., Bhattacharjee, P. P., & Jahazi, M. (2016). The Effect of Strain Reversal during High Pressure Torsion on the Microstructure Evolution and Texture of Aluminum Alloys. In *Characterization of Minerals, Metals, and Materials 2015* (pp. 107-114): Springer International Publishing.
- Chamanfar, A. (2012). *Evolution of Microstructure and Mechanical Properties in Linear Friction Welded Waspaloy*. (Doctor of Philosophy). McGill University,
- Chamanfar, A., Jahazi, M., Bonakdar, A., Morin, E., & Firoozrai, A. (2015). Cracking in fusion zone and heat affected zone of electron beam welded Inconel-713LC gas turbine blades. *Materials Science and Engineering: A*, 642, 230-240. doi:<https://doi.org/10.1016/j.msea.2015.06.087>
- Chamanfar, A., Jahazi, M., & Cormier, J. (2015). A Review on Inertia and Linear Friction Welding of Ni-Based Superalloys. *Metallurgical and Materials Transactions A*, 46(4), 1639-1669. doi:10.1007/s11661-015-2752-4
- Chamanfar, A., Jahazi, M., Gholipour, J., Wanjara, P., & Yue, S. (2010). Mechanical Property and Microstructure of Linear Friction Welded Waspaloy. *Metallurgical and Materials Transactions A*, 42(3), 729-744. doi:10.1007/s11661-010-0457-2
- Chamanfar, A., Jahazi, M., Gholipour, J., Wanjara, P., & Yue, S. (2011). Mechanical Property and Microstructure of Linear Friction Welded Waspaloy. *Metallurgical and Materials Transactions A*, 42(3), 729-744. doi:10.1007/s11661-010-0457-2
- Chamanfar, A., Jahazi, M., Gholipour, J., Wanjara, P., & Yue, S. (2012a). Maximizing the integrity of linear friction welded Waspaloy. *Materials Science and Engineering: A*, 555, 117-130. doi:10.1016/j.msea.2012.06.041
- Chamanfar, A., Jahazi, M., Gholipour, J., Wanjara, P., & Yue, S. (2012b). Suppressed liquation and microcracking in linear friction welded Waspaloy. *Materials & Design (1980-2015)*, 36, 113-122. doi:10.1016/j.matdes.2011.11.007
- Chamanfar, A., Jahazi, M., Gholipour, J., Wanjara, P., & Yue, S. (2013). Modeling Grain Size and Strain Rate in Linear Friction Welded Waspaloy. *Metallurgical and Materials Transactions A*, 44(9), 4230-4238. doi:10.1007/s11661-013-1767-y
- Chamanfar, A., Jahazi, M., Gholipour, J., Wanjara, P., & Yue, S. (2014). Evolution of flow stress and microstructure during isothermal compression of Waspaloy. *Materials Science and Engineering: A*, 615, 497-510. doi:10.1016/j.msea.2014.07.093

- Chamanfar, A., Jahazi, M., Gholipour, J., Wanjara, P., & Yue, S. (2015). Analysis of integrity and microstructure of linear friction welded Waspaloy. *Materials Characterization*, *104*, 149-161. doi:<https://doi.org/10.1016/j.matchar.2015.04.011>
- Chamanfar, A., Jahazi, M., Yue, S., Gholipour, J., & Wanjara, P. (2009). Linear friction welding behavior of Waspaloy.
- Chaturvedi, M. C. (2007). Liquation Cracking in Heat Affected Zone in Ni Superalloy Welds. *Materials Science Forum*, *546-549*, 1163-1170. doi:10.4028/[www.scientific.net/MSF.546-549.1163](http://www.scientific.net/MSF.546-549.1163)
- Chaturvedi, M. C., & Han, Y.-f. (1983). Strengthening mechanisms in Inconel 718 superalloy. *Metal Science*, *17*(3), 145-149. doi:10.1179/030634583790421032
- Cheepu, M., & Che, W. S. (2020). Characterization of Interfacial Microstructure in Friction Welds Between Inconel 718 and SM45C Steel. *Transactions of the Indian Institute of Metals*. doi:10.1007/s12666-020-01921-z
- Cheepu, M., Muthupandi, V., & Che, W. S. (2018). Improving Mechanical Properties of Dissimilar Material Friction Welds. *Applied Mechanics and Materials*, *877*, 157-162. doi:10.4028/[www.scientific.net/AMM.877.157](http://www.scientific.net/AMM.877.157)
- Chen, B., & Mazumder, J. (2017). Role of process parameters during additive manufacturing by direct metal deposition of Inconel 718. *Rapid Prototyping Journal*, *23*(5), 919-929. doi:10.1108/rpj-05-2016-0071
- Chen, X.-M., Lin, Y. C., Wen, D.-X., Zhang, J.-L., & He, M. (2014). Dynamic recrystallization behavior of a typical nickel-based superalloy during hot deformation. *Materials & Design*, *57*, 568-577. doi:10.1016/j.matdes.2013.12.072
- Chen, Y.-T., Yeh, A.-C., Li, M.-Y., & Kuo, S.-M. (2017). Effects of processing routes on room temperature tensile strength and elongation for Inconel 718. *Materials & Design*, *119*, 235-243. doi:10.1016/j.matdes.2017.01.069
- Chen, Y., Guo, Y., Xu, M., Ma, C., Zhang, Q., Wang, L., . . . Li, Z. (2019). Study on the element segregation and Laves phase formation in the laser metal deposited IN718 superalloy by flat top laser and gaussian distribution laser. *Materials Science and Engineering: A*, *754*, 339-347. doi:10.1016/j.msea.2019.03.096
- Chen, Y., Lu, F., Zhang, K., Nie, P., Elmi Hosseini, S. R., Feng, K., & Li, Z. (2016). Dendritic microstructure and hot cracking of laser additive manufactured Inconel 718 under improved base cooling. *Journal of Alloys and Compounds*, *670*, 312-321. doi:10.1016/j.jallcom.2016.01.250

- Chen, Y., Zhang, K., Huang, J., Hosseini, S. R. E., & Li, Z. (2016). Characterization of heat affected zone liquation cracking in laser additive manufacturing of Inconel 718. *Materials & Design*, *90*, 586-594. doi:10.1016/j.matdes.2015.10.155
- Chlebus, E., Gruber, K., Kuźnicka, B., Kurzac, J., & Kurzynowski, T. (2015). Effect of heat treatment on the microstructure and mechanical properties of Inconel 718 processed by selective laser melting. *Materials Science and Engineering: A*, *639*, 647-655. doi:10.1016/j.msea.2015.05.035
- Chou, C. P., & Chao, C. H. (1988). *Repair Weldability Studies of Alloy 718 Using Versatile vareststraint Test*. Paper presented at the Superalloys 1988.
- Chrostek, T. (2016). The Influence of The Heating and Cooling Rates on The Temperature of The Phase Transformation.
- Cieslak, M. J., Stephens, J. J., & Carr, M. J. (1988). A study of the weldability and weld related microstructure of cabot alloy 214. *Metallurgical Transactions A*, *19*(3), 657-667. doi:10.1007/BF02649280
- Cormier, J., & Cailletaud, G. (2010). Constitutive modeling of the creep behavior of single crystal superalloys under non-isothermal conditions inducing phase transformations. *Materials Science and Engineering: A*, *527*(23), 6300-6312. doi:10.1016/j.msea.2010.06.023
- Cormier, J., Gadaud, P., Czaplicki, M., Zhang, R. Y., Dong, H. B., Smith, T. M., . . . Semiatin, S. L. (2020). In-Situ Determination of Precipitation Kinetics During Heat Treatment of Superalloy 718. *Metallurgical and Materials Transactions A*. doi:10.1007/s11661-020-06078-4
- Cormier, J., Milhet, X., Champion, J. L., & Mendez, J. (2008). Simulation of Very High Temperature Overheating During Isothermal Creep of Single Crystal Ni-Base Superalloy. *Advanced Engineering Materials*. doi:10.1002/adem.200700248
- Cormier, J., Milhet, X., & Mendez, J. (2007). Non-isothermal creep at very high temperature of the nickel-based single crystal superalloy MC2. *Acta Materialia*, *55*(18), 6250-6259. doi:10.1016/j.actamat.2007.07.048
- Cortés, R., Rodríguez, N. K., Ambriz, R. R., López, V. H., Ruiz, A., & Jaramillo, D. (2019). Fatigue and crack growth behavior of Inconel 718-AL6XN dissimilar welds. *Materials Science and Engineering: A*, *745*, 20-30. doi:10.1016/j.msea.2018.12.087
- Cowern, N. E., Zalm, P. C., van der Sluis, P., Gravesteijn, D. J., & de Boer, W. B. (1994). Diffusion in strained Si(Ge). *Phys Rev Lett*, *72*(16), 2585-2588. doi:10.1103/PhysRevLett.72.2585

- Dalgaard, E. C. (2011). *Evolution of Microstructure, Microtexture and Mechanical Properties in Linear Friction Welded Titanium Alloys*. (Doctor of Philosophy Doctor of Philosophy). McGill University,
- Damodaram, R., Ganesh Sundara Raman, S., & Prasad Rao, K. (2014). Effect of post-weld heat treatments on microstructure and mechanical properties of friction welded alloy 718 joints. *Materials & Design*, 53, 954-961. doi:10.1016/j.matdes.2013.07.091
- Damodaram, R., Ganesh Sundara Raman, S., Satyanarayana, D. V. V., Madhusudhan Reddy, G., & Prasad Rao, K. (2014). Hot tensile and stress rupture behavior of friction welded alloy 718 in different pre-and post-weld heat treatment conditions. *Materials Science and Engineering: A*, 612, 414-422. doi:10.1016/j.msea.2014.06.076
- Damodaram, R., Raman, S. G. S., & Rao, K. P. (2013). Microstructure and mechanical properties of friction welded alloy 718. *Materials Science and Engineering: A*, 560, 781-786. doi:10.1016/j.msea.2012.10.035
- Davies, S., Jeffs, S., Lancaster, R., & Baxter, G. (2017). High Temperature Deformation Mechanisms in a DLD Nickel Superalloy. *Materials (Basel)*, 10(5). doi:10.3390/ma10050457
- Davis, J. R. (2004). *Tensile Testing*: ASM International.
- Daymond, M. R., & Bonner, N. W. (2003). Measurement of strain in a titanium linear friction weld by neutron diffraction. *Physica B: Condensed Matter*, 325, 130-137. doi:10.1016/s0921-4526(02)01514-4
- deBarbadillo, J. J., & Mannan, S. K. (2012). Alloy 718 for Oilfield Applications. *Jom*, 64(2), 265-270. doi:10.1007/s11837-012-0238-z
- Deng, D., Peng, R. L., Brodin, H., & Moverare, J. (2018). Microstructure and mechanical properties of Inconel 718 produced by selective laser melting: Sample orientation dependence and effects of post heat treatments. *Materials Science and Engineering: A*, 713, 294-306. doi:10.1016/j.msea.2017.12.043
- Devaux, A., Helstroffer, A., Cormier, J., Villechaise, P., Douin, J., Hantcherli, M., & Pettinari-Sturmel, F. (2014). *Effect of aging heat-treatment on mechanical properties of AD730TM superalloy*. Paper presented at the TMS, 8th International Symposium on Superalloy 718 and Derivatives.
- Devaux, A., Nazé, L., Molins, R., Pineau, A., Organista, A., Guédou, J. Y., . . . Héritier, P. (2008). Gamma double prime precipitation kinetic in Alloy 718. *Materials Science and Engineering: A*, 486(1-2), 117-122. doi:10.1016/j.msea.2007.08.046
- Dieter, G. E. (1988). *Mechanical metallurgy* (S. metric Ed.): McGraw-Hill book company.

- Donachie, M. J., & Donachie, S. J. (2002). *Superalloys: A Technical Guide*: ASM International.
- Egbewande, A. T., Zhang, H. R., Sidhu, R. K., & Ojo, O. A. (2009). Improvement in Laser Weldability of Incomel 738 Superalloy through Microstructural Modification. *Metallurgical and Materials Transactions A*, 40(11), 2694-2704. doi:10.1007/s11661-009-9962-6
- Fayed, E. M., Saadati, M., Shahriari, D., Brailovski, V., Jahazi, M., & Medraj, M. (2021). Optimization of the Post-Process Heat Treatment of Inconel 718 Superalloy Fabricated by Laser Powder Bed Fusion Process. *Metals*, 11(1). doi:10.3390/met11010144
- Franke, O., Durst, K., & Göken, M. (2011). Nanoindentation investigations to study solid solution hardening in Ni-based diffusion couples. *Journal of Materials Research*, 24(3), 1127-1134. doi:10.1557/jmr.2009.0135
- Fratini, L., Buffa, G., Campanella, D., & La Spisa, D. (2012). Investigations on the linear friction welding process through numerical simulations and experiments. *Materials & Design*, 40, 285-291. doi:10.1016/j.matdes.2012.03.058
- G., S., & N., I. (1991). *Grain boundary delta-phase morphology, carbides and notch rupture sensitivities of cast alloy 718*. Paper presented at the Superalloy 718—metallurgy and applications.
- Gan, B., Murakami, H., Maass, R., Meza, L., Greer, J. R., Ohmura, T., & Tin, S. (2012). NANOINDENTATION AND NANO-COMPRESSION TESTING OF Ni<sub>3</sub>Al PRECIPITATES. *Superalloys 2012*, 83-91. doi:10.1002/9781118516430.ch9
- Gan, H.-y., Cheng, M., Guo, Z.-x., Tai, Q.-a., Kozhevnikova, G., Song, H.-w., & Zhang, S.-h. (2020). Spheroidization Mechanism of Lamellar  $\delta$  Phase in Inconel 718 during Delta Processing. *Journal of Materials Engineering and Performance*, 29(6), 3852-3857. doi:10.1007/s11665-020-04909-4
- Gargani, M. (2019). *Homogenization of Inconel 718 Made by Additive Manufacturing and Suction Casting*. University of Pittsburgh,
- Geng, P., Qin, G., Li, T., Zhou, J., Zou, Z., & Yang, F. (2019). Microstructural characterization and mechanical property of GH4169 superalloy joints obtained by linear friction welding. *Journal of Manufacturing Processes*, 45, 100-114. doi:10.1016/j.jmapro.2019.06.032
- Geng, P., Qin, G., Zhou, J., & Zou, Z. (2019). Finite element models of friction behaviour in linear friction welding of a Ni-based superalloy. *International Journal of Mechanical Sciences*, 152, 420-431. doi:10.1016/j.ijmecsci.2019.01.014

- Ghorbanpour, S., Alam, M. E., Ferreri, N. C., Kumar, A., McWilliams, B. A., Vogel, S. C., . . . Knezevic, M. (2020). Experimental characterization and crystal plasticity modeling of anisotropy, tension-compression asymmetry, and texture evolution of additively manufactured Inconel 718 at room and elevated temperatures. *International Journal of Plasticity*, 125, 63-79. doi:10.1016/j.ijplas.2019.09.002
- Gifkins, R. C. (1994). Grain-boundary participation in high-temperature deformation: An historical review. *Materials Characterization*, 32(2), 59-77. doi:10.1016/1044-5803(94)90093-0
- Giraud, R., Hervier, Z., Cormier, J., Saint-Martin, G., Hamon, F., Milhet, X., & Mendez, J. (2012). Strain Effect on the  $\gamma'$  Dissolution at High Temperatures of a Nickel-Based Single Crystal Superalloy. *Metallurgical and Materials Transactions A*, 44(1), 131-146. doi:10.1007/s11661-012-1397-9
- Goel, S., Neikter, M., Capek, J., Polatidis, E., Colliander, M. H., Joshi, S., & Pederson, R. (2020). Residual stress determination by neutron diffraction in powder bed fusion-built Alloy 718: Influence of process parameters and post-treatment. *Materials & Design*, 195. doi:10.1016/j.matdes.2020.109045
- Greenwood, J. N. (1952). Intercrystalline cracking of metals. *Bull. Inst. Metals*, 12, 104-105.
- Grong, O. (1997). *Metallurgical Modelling of Welding* (Second Edition ed.): Institute of Materials.
- Grosdidier, T., Hazotte, A., & Simon, A. (1998). Precipitation and dissolution processes in  $\gamma / \gamma'$  single crystal nickel-based superalloys. *Materials Science and Engineering: A*, 256(1-2), 183-196. doi:10.1016/s0921-5093(98)00795-3
- Guimaraes, A. A., & Jonas, J. J. (1981). Recrystallization and aging effects associated with the high temperature deformation of waspaloy and inconel 718. *Metallurgical Transactions A*, 12(9), 1655-1666. doi:10.1007/bf02643571
- Handwerker, C. A., Cahn, J. W., Yoon, D. N., & Blendell, J. E. (1985). *Diffusion in Solids: Recent Developments* (M. A. Dayananda & G. E. Murch Eds.): TMS.
- Hansen, N. (2004). Hall–Petch relation and boundary strengthening. *Scripta Materialia*, 51(8), 801-806. doi:10.1016/j.scriptamat.2004.06.002
- Hariharan, A., Lu, L., Risse, J., Kostka, A., Gault, B., Jäggle, E. A., & Raabe, D. (2019). Misorientation-dependent solute enrichment at interfaces and its contribution to defect formation mechanisms during laser additive manufacturing of superalloys. *Physical Review Materials*, 3(12). doi:10.1103/PhysRevMaterials.3.123602

- Harries, D. R., & Marwick, A. D. (1980). Non-Equilibrium Segregation in Metals and Alloys. *Philosophical Transactions of the Royal Society A: Mathematical, Physical and Engineering Sciences*, 295(1413), 197-207. doi:10.1098/rsta.1980.0100
- Harrison, N. J., Todd, I., & Mumtaz, K. (2015). Reduction of micro-cracking in nickel superalloys processed by Selective Laser Melting: A fundamental alloy design approach. *Acta Materialia*, 94, 59-68. doi:10.1016/j.actamat.2015.04.035
- Harte, A., Atkinson, M., Smith, A., Drouven, C., Zaefferer, S., Quinta da Fonseca, J., & Preuss, M. (2020). The effect of solid solution and gamma prime on the deformation modes in Ni-based superalloys. *Acta Materialia*, 194, 257-275. doi:10.1016/j.actamat.2020.04.004
- Hassan, B., & Corney, J. (2017). Grain boundary precipitation in Inconel 718 and ATI 718Plus. *Materials Science and Technology*, 33(16), 1879-1889. doi:10.1080/02670836.2017.1333222
- Hatherly, F. H. a. M. (2004). *Recrystallization and related annealing phenomena* (2 ed.): Elsevier.
- Heep, L., Schwalbe, C., Heinze, C., Dlouhy, A., Rae, C. M. F., & Eggeler, G. (2021). Dislocation networks in gamma/gamma'-microstructures formed during selective laser melting of a Ni-base superalloy. *Scripta Materialia*, 190, 121-125. doi:10.1016/j.scriptamat.2020.08.019
- Henderson, M. B., Arrell, D., Larsson, R., Heobel, M., & Marchant, G. (2013). Nickel based superalloy welding practices for industrial gas turbine applications. *Science and Technology of Welding and Joining*, 9(1), 13-21. doi:10.1179/136217104225017099
- Herderick, E. (2011). Additive Manufacturing of Metals: A Review. *Materials Science and Technology*, 1413-1425.
- Hertzberg, R. W. (1996). *Deformation And Fracture Mechanics of Engineering Materials*: John Wiley & Sons.
- Hillert, M. (1983). On the driving force for diffusion induced grain boundary migration. *Scripta Metallurgica*, 17(2), 237-240. doi:10.1016/0036-9748(83)90105-9
- Holland, S., Wang, X., Fang, X. Y., Guo, Y. B., Yan, F., & Li, L. (2018). Grain boundary network evolution in Inconel 718 from selective laser melting to heat treatment. *Materials Science and Engineering: A*, 725, 406-418. doi:10.1016/j.msea.2018.04.045
- Homma, T., Takano, H., & Ozaki, T. (2019). Nanostructural analysis of welded Ti-6Al-4V by linear friction welding applied for blisk assemblies. *Materialia*, 5. doi:10.1016/j.mtla.2018.11.023

- Hosford, W. F. (2014). *Metal Forming: Mechanics And Metallurgy* (4 ed.): Cambridge University Press.
- Hosseini, E., & Popovich, V. A. (2019). A review of mechanical properties of additively manufactured Inconel 718. *Additive Manufacturing*, 30. doi:10.1016/j.addma.2019.100877
- Hu, L., O'Neil, M., Erturun, V., Benitez, R., Proust, G., Karaman, I., & Radovic, M. (2016). High-Performance Metal/Carbide Composites with Far-From-Equilibrium Compositions and Controlled Microstructures. *Sci Rep*, 6, 35523. doi:10.1038/srep35523
- Huang, K., & Logé, R. E. (2016). A review of dynamic recrystallization phenomena in metallic materials. *Materials & Design*, 111, 548-574. doi:10.1016/j.matdes.2016.09.012
- Huang, W., Yang, J., Yang, H., Jing, G., Wang, Z., & Zeng, X. (2019). Heat treatment of Inconel 718 produced by selective laser melting: Microstructure and mechanical properties. *Materials Science and Engineering: A*, 750, 98-107. doi:10.1016/j.msea.2019.02.046
- Huang, X., Chaturvedi, M. C., Richards, N. L., & Jackman, J. (1997). The effect of grain boundary segregation of boron in cast alloy 718 on HAZ microfissuring—A SIMS analysis. *Acta Materialia*, 45(8), 3095-3107. doi:10.1016/s1359-6454(97)00017-7
- Huang, Y., & Langdon, T. G. (2005). Cavitation and failure in a fine-grained Inconel 718 alloy having potential superplastic properties. *Materials Science and Engineering: A*, 410-411, 130-133. doi:10.1016/j.msea.2005.08.095
- Huang, Z., Shun, W. M., & Yao, M. (1990). A method to estimate the nil-ductility transition temperature. *Scripta Metallurgica et Materialia*, 24(4), 691-695. doi:10.1016/0956-716x(90)90225-6
- Huang, Z. W., Li, H. Y., Preuss, M., Karadge, M., Bowen, P., Bray, S., & Baxter, G. (2007). Inertia Friction Welding Dissimilar Nickel-Based Superalloys Alloy 720Li to IN718. *Metallurgical and Materials Transactions A*, 38(7), 1608-1620. doi:10.1007/s11661-007-9194-6
- Idell, Y., Levine, L. E., Allen, A. J., Zhang, F., Campbell, C. E., Olson, G. B., . . . Deutchman, H. Z. (2016). Unexpected  $\delta$ -Phase Formation in Additive-Manufactured Ni-Based Superalloy. *Jom*, 68(3), 950-959. doi:10.1007/s11837-015-1772-2
- Izquierdo, B., Plaza, S., Sánchez, J. A., Pombo, I., & Ortega, N. (2012). Numerical prediction of heat affected layer in the EDM of aeronautical alloys. *Applied Surface Science*, 259, 780-790. doi:10.1016/j.apsusc.2012.07.124

- J.L.Caron, & J.W.Sowards. (2014). Weldability of Nickel-Base Alloys. In *Comprehensive Materials Processing* (Vol. 6, pp. 151-179): Elsevier.
- Jackson, M. P., & Reed, R. C. (1999). Heat treatment of UDIMET 720Li: the effect of microstructure on properties. *Materials Science and Engineering: A*, 259(1), 85-97. doi:10.1016/s0921-5093(98)00867-3
- Jia, Q., & Gu, D. (2014). Selective laser melting additive manufacturing of Inconel 718 superalloy parts: Densification, microstructure and properties. *Journal of Alloys and Compounds*, 585, 713-721. doi:10.1016/j.jallcom.2013.09.171
- Johansson, J., & Persson, C. (2014). *Influence of Microstructure on Deformation Behaviour of Alloy 718*. Paper presented at the 8th International Symposium on Superalloy 718 and Derivatives (2014).
- Jokisch, T., Marko, A., Gook, S., Ustundag, O., Gumenyuk, A., & Rethmeier, M. (2019). Laser Welding of SLM-Manufactured Tubes Made of IN625 and IN718. *Materials (Basel)*, 12(18). doi:10.3390/ma12182967
- Jonas, J. J., Ghosh, C., Queleynec, X., & Basabe, V. V. (2013). The Critical Strain for Dynamic Transformation in Hot Deformed Austenite. *ISIJ International*, 53(1), 145-151. doi:10.2355/isijinternational.53.145
- Jouiad, M., Marin, E., Devarapalli, R. S., Cormier, J., Ravaux, F., Le Gall, C., & Franchet, J. M. (2016). Microstructure and mechanical properties evolutions of alloy 718 during isothermal and thermal cycling over-aging. *Materials & Design*, 102, 284-296. doi:10.1016/j.matdes.2016.04.048
- Kamikawa, N., Sato, K., Miyamoto, G., Murayama, M., Sekido, N., Tsuzaki, K., & Furuhashi, T. (2015). Stress-strain behavior of ferrite and bainite with nano-precipitation in low carbon steels. *Acta Materialia*, 83, 383-396. doi:10.1016/j.actamat.2014.10.010
- Karadge, M., Frankel, P., Steuwer, A., Lovell, C., Bray, S., Withers, P. J., & Preuss, M. (2006). Microstructure, Texture, Local Tensile Properties and Residual Stress Relief in Ti-6Al-4V Linear Friction Welds. *Materials Science and Technology-Association for Iron and Steel Technology*.
- Karadge, M., Preuss, M., Lovell, C., Withers, P. J., & Bray, S. (2007). Texture development in Ti-6Al-4V linear friction welds. *Materials Science and Engineering: A*, 459(1-2), 182-191. doi:10.1016/j.msea.2006.12.095
- Karadge, M., Preuss, M., Withers, P. J., & Bray, S. (2008). Importance of crystal orientation in linear friction joining of single crystal to polycrystalline nickel-based superalloys. *Materials Science and Engineering: A*, 491(1-2), 446-453. doi:10.1016/j.msea.2008.04.064

- Katnagallu, S., Vernier, S., Charpagne, M.-A., Gault, B., Bozzolo, N., & Kontis, P. (2021). Nucleation mechanism of hetero-epitaxial recrystallization in wrought nickel-based superalloys. *Scripta Materialia*, 191, 7-11. doi:10.1016/j.scriptamat.2020.09.012
- Keller, B. P., Nelson, S. E., Walton, K. L., Ghosh, T. K., Tompson, R. V., & Loyalka, S. K. (2015). Total hemispherical emissivity of Inconel 718. *Nuclear Engineering and Design*, 287, 11-18. doi:10.1016/j.nucengdes.2015.02.018
- Kim, Y. C., & Fuji, A. (2002). Factors dominating joint characteristics in Ti – Al friction welds. *Science and Technology of Welding and Joining*, 7(3), 149-154. doi:10.1179/136217102225004185
- Knapp, G. L., Raghavan, N., Plotkowski, A., & DebRoy, T. (2019). Experiments and simulations on solidification microstructure for Inconel 718 in powder bed fusion electron beam additive manufacturing. *Additive Manufacturing*, 25, 511-521. doi:10.1016/j.addma.2018.12.001
- Knock, N. O. (2010). *Characterization of Inconel 718: Using The Gleeble and Varestraint Testing Methods to Determine The Weldability of Inconel 718*. (MS in Engineering - Materials Engineering). California Polytechnic State University - San Luis Obispo,
- Knorovsky, G. A., Cieslak, M. J., Headley, T. J., Romig, A. D., & Hammett, W. F. (1989). INCONEL 718: A solidification diagram. *Metallurgical Transactions A*, 20(10), 2149-2158. doi:10.1007/bf02650300
- Kong, Y.-S., Cheepu, M., & Kim, D.-G. (2020). Microstructure and Mechanical Properties of Friction-Welded and Post-Heat-Treated Inconel 718. *Transactions of the Indian Institute of Metals*, 73(6), 1449-1453. doi:10.1007/s12666-020-01911-1
- Kozar, R. W., Suzuki, A., Milligan, W. W., Schirra, J. J., Savage, M. F., & Pollock, T. M. (2009). Strengthening Mechanisms in Polycrystalline Multimodal Nickel-Base Superalloys. *Metallurgical and Materials Transactions A*, 40(7), 1588-1603. doi:10.1007/s11661-009-9858-5
- Kringhøj, P., Larsen, A. N., & Shirayev, S. Y. (1996). Diffusion of Sb in Strained and Relaxed Si and SiGe. *Phys Rev Lett*, 76(18), 3372-3375. doi:10.1103/PhysRevLett.76.3372
- Kruth, J. P., Leu, M. C., & Nakagawa, T. (1998). Progress in Additive Manufacturing and Rapid Prototyping. *CIRP Annals*, 47(2), 525-540. doi:10.1016/s0007-8506(07)63240-5
- Kumar, S. S. S., Raghu, T., Bhattacharjee, P. P., Rao, G. A., & Borah, U. (2016). Strain rate dependent microstructural evolution during hot deformation of a hot isostatically processed nickel base superalloy. *Journal of Alloys and Compounds*, 681, 28-42. doi:10.1016/j.jallcom.2016.04.185

- Kumara, C., Deng, D., Hanning, F., Raanes, M., Moverare, J., & Nylén, P. (2019). Predicting the Microstructural Evolution of Electron Beam Melting of Alloy 718 with Phase-Field Modeling. *Metallurgical and Materials Transactions A*, 50(5), 2527-2537. doi:10.1007/s11661-019-05163-7
- Kuo, Y.-L., Horikawa, S., & Kakehi, K. (2017). The effect of interdendritic  $\delta$  phase on the mechanical properties of Alloy 718 built up by additive manufacturing. *Materials & Design*, 116, 411-418. doi:10.1016/j.matdes.2016.12.026
- Lachowicz, M., Dudziński, W., & Podrez-Radziszewska, M. (2008). TEM observation of the heat-affected zone in electron beam welded superalloy Inconel 713C. *Materials Characterization*, 59(5), 560-566. doi:10.1016/j.matchar.2007.04.010
- Lalam, S. V., Reddy, G. M., Mohandas, T., Kamaraj, M., & Murty, B. S. (2013). Continuous drive friction welding of Inconel 718 and EN24 dissimilar metal combination. *Materials Science and Technology*, 25(7), 851-861. doi:10.1179/174328408x369384
- Lalvani, H. M., & Brooks, J. W. (2016). Hot Forging of IN718 with Solution-Treated and Delta-Containing Initial Microstructures. *Metallography, Microstructure, and Analysis*, 5(5), 392-401. doi:10.1007/s13632-016-0299-4
- le Graverend, J. B., Cormier, J., Jouiad, M., Gallerneau, F., Paulmier, P., & Hamon, F. (2010). Effect of fine  $\gamma'$  precipitation on non-isothermal creep and creep-fatigue behaviour of nickel base superalloy MC2. *Materials Science and Engineering: A*, 527(20), 5295-5302. doi:10.1016/j.msea.2010.04.097
- Lee, C.-R., Um, S.-H., Kim, S.-W., Choi, C., & Lee, C.-H. (2004). A Study on Hot Ductility Behavior of Ni-based Superalloys. *Journal of Welding and Joining*, 22(2), 59-68.
- Legros, M., Dehm, G., Arzt, E., & Balk, T. J. (2008). Observation of giant diffusivity along dislocation cores. *Science*, 319(5870), 1646-1649. doi:10.1126/science.1151771
- Levy, G. N., Schindel, R., & Kruth, J. P. (2003). Rapid Manufacturing and Rapid Tooling with Layer Manufacturing (Lm) Technologies, State of the Art and Future Perspectives. *CIRP Annals*, 52(2), 589-609. doi:10.1016/s0007-8506(07)60206-6
- Li, C.-W., Yeh, A.-C., Chen, C.-S., & Wang, W.-R. (2015). Hot Ductility Loss in a Fe-Ni-Based Superalloy. *Metals*, 5(4), 2428-2434. doi:10.3390/met5042428
- Li, C., White, R., Fang, X. Y., Weaver, M., & Guo, Y. B. (2017). Microstructure evolution characteristics of Inconel 625 alloy from selective laser melting to heat treatment. *Materials Science and Engineering: A*, 705, 20-31. doi:10.1016/j.msea.2017.08.058

- Li, H. Y., Huang, Z. W., Bray, S., Baxter, G., & Bowen, P. (2007). High temperature fatigue of friction welded joints in dissimilar nickel based superalloys. *Materials Science and Technology*, 23(12), 1408-1418. doi:10.1179/174328407x243933
- Li, J., Zhao, Z., Bai, P., Qu, H., Liu, B., Li, L., . . . Guo, Z. (2019). Microstructural evolution and mechanical properties of IN718 alloy fabricated by selective laser melting following different heat treatments. *Journal of Alloys and Compounds*, 772, 861-870. doi:10.1016/j.jallcom.2018.09.200
- Li, Q., Lin, X., Wang, X., Yang, H., Song, M., & Huang, W. (2016). Research on the Grain Boundary Liquation Mechanism in Heat Affected Zones of Laser Forming Repaired K465 Nickel-Based Superalloy. *Metals*, 6(3). doi:10.3390/met6030064
- Li, W.-Y., Ma, T., & Li, J. (2010). Numerical simulation of linear friction welding of titanium alloy: Effects of processing parameters. *Materials & Design*, 31(3), 1497-1507. doi:10.1016/j.matdes.2009.08.023
- Li, W., Vairis, A., Preuss, M., & Ma, T. (2016). Linear and rotary friction welding review. *International Materials Reviews*, 61(2), 71-100. doi:10.1080/09506608.2015.1109214
- Li, W. Y., Ma, T. J., Yang, S. Q., Xu, Q. Z., Zhang, Y., Li, J. L., & Liao, H. L. (2008). Effect of friction time on flash shape and axial shortening of linear friction welded 45 steel. *Materials Letters*, 62(2), 293-296. doi:10.1016/j.matlet.2007.05.037
- Li, X., Shi, J. J., Cao, G. H., Russell, A. M., Zhou, Z. J., Li, C. P., & Chen, G. F. (2019). Improved plasticity of Inconel 718 superalloy fabricated by selective laser melting through a novel heat treatment process. *Materials & Design*, 180, 107915. doi:10.1016/j.matdes.2019.107915
- Lifshitz, I. M., & Slyozov, V. V. (1961). The kinetics of precipitation from supersaturated solid solutions. *Journal of Physics and Chemistry of Solids*, 19(1-2), 35-50. doi:10.1016/0022-3697(61)90054-3
- Lin, W., Lippold, J. C., & Baeslack III, W. A. (1993). An evaluation of heat-affected zone liquation cracking susceptibility, Part I: Development of a method for quantification. *Welding Journal*, 72, 135-153.
- Lin, Y. C., Deng, J., Jiang, Y.-Q., Wen, D.-X., & Liu, G. (2014a). Effects of initial  $\delta$  phase on hot tensile deformation behaviors and fracture characteristics of a typical Ni-based superalloy. *Materials Science and Engineering: A*, 598, 251-262. doi:10.1016/j.msea.2014.01.029
- Lin, Y. C., Deng, J., Jiang, Y.-Q., Wen, D.-X., & Liu, G. (2014b). Hot tensile deformation behaviors and fracture characteristics of a typical Ni-based superalloy. *Materials & Design*, 55, 949-957. doi:10.1016/j.matdes.2013.10.071

- Lin, Y. C., He, D.-G., Chen, M.-S., Chen, X.-M., Zhao, C.-Y., Ma, X., & Long, Z.-L. (2016). EBSD analysis of evolution of dynamic recrystallization grains and  $\delta$  phase in a nickel-based superalloy during hot compressive deformation. *Materials & Design*, *97*, 13-24. doi:10.1016/j.matdes.2016.02.052
- Lin, Y. C., Wen, D.-X., Deng, J., Liu, G., & Chen, J. (2014). Constitutive models for high-temperature flow behaviors of a Ni-based superalloy. *Materials & Design*, *59*, 115-123. doi:10.1016/j.matdes.2014.02.041
- Lin, Y. C., Wu, X.-Y., Chen, X.-M., Chen, J., Wen, D.-X., Zhang, J.-L., & Li, L.-T. (2015). EBSD study of a hot deformed nickel-based superalloy. *Journal of Alloys and Compounds*, *640*, 101-113. doi:10.1016/j.jallcom.2015.04.008
- Ling, L. S., Yin, Z., Hu, Z., Liang, J. H., Wang, Z. Y., Wang, J., & Sun, B. D. (2019). Effects of the gamma"-Ni<sub>3</sub>Nb Phase on Mechanical Properties of Inconel 718 Superalloys with Different Heat Treatments. *Materials (Basel)*, *13*(1). doi:10.3390/ma13010151
- Liu, F., Lyu, F., Liu, F., Lin, X., & Huang, C. (2020). Laves phase control of inconel 718 superalloy fabricated by laser direct energy deposition via  $\delta$  aging and solution treatment. *Journal of Materials Research and Technology*, *9*(5), 9753-9765. doi:10.1016/j.jmrt.2020.06.061
- Luo, Z., & Zhao, Y. (2019). Efficient thermal finite element modeling of selective laser melting of Inconel 718. *Computational Mechanics*, *65*(3), 763-787. doi:10.1007/s00466-019-01794-0
- Ma, T. J., Chen, X., Li, W. Y., Yang, X. W., Zhang, Y., & Yang, S. Q. (2016). Microstructure and mechanical property of linear friction welded nickel-based superalloy joint. *Materials & Design*, *89*, 85-93. doi:10.1016/j.matdes.2015.09.143
- Ma, T. J., Li, Y. G., Li, W. Y., Zhang, Y., Shi, D. G., & Vairis, A. (2017). Studies of the interfacial structure of a linear friction welded Fe/Ni joint: First principles calculation and TEM validation. *Materials Characterization*, *129*, 60-66. doi:10.1016/j.matchar.2017.04.008
- Ma, T. J., Tang, L. F., Li, W. Y., Zhang, Y., Xiao, Y., & Vairis, A. (2018). Linear friction welding of a solid-solution strengthened Ni-based superalloy: Microstructure evolution and mechanical properties studies. *Journal of Manufacturing Processes*, *34*, 442-450. doi:10.1016/j.jmapro.2018.06.011
- Maalekian, M. (2007). Friction welding – critical assessment of literature. *Science and Technology of Welding and Joining*, *12*(8), 738-759. doi:10.1179/174329307x249333

- Mahaffey, D. W., Senkov, O. N., Shivpuri, R., & Semiatin, S. L. (2016). Effect of Process Variables on the Inertia Friction Welding of Superalloys LSHR and Mar-M247. *Metallurgical and Materials Transactions A*, 47(8), 3981-4000. doi:10.1007/s11661-016-3600-x
- Mandziej, S. T. (2005). *Testing for Susceptibility to Hot Cracking on Gleeble™ Physical Simulator*: Springer, Berlin, Heidelberg.
- Manikandan, S. G. K., Sivakumar, D., Kamaraj, M., & Rao, K. P. (2012). Laves Phase Control in Inconel 718 Weldments. *Materials Science Forum*, 710, 614-619. doi:10.4028/[www.scientific.net/MSF.710.614](http://www.scientific.net/MSF.710.614)
- Manikandan, S. G. K., Sivakumar, D., Prasad Rao, K., & Kamaraj, M. (2015). Laves phase in alloy 718 fusion zone — microscopic and calorimetric studies. *Materials Characterization*, 100, 192-206. doi:10.1016/j.matchar.2014.11.035
- Marchese, G., Atzeni, E., Salmi, A., & Biamino, S. (2020). Microstructure and Residual Stress Evolution of Laser Powder Bed Fused Inconel 718 under Heat Treatments. *Journal of Materials Engineering and Performance*. doi:10.1007/s11665-020-05338-z
- Mary, C., & Jahazi, M. (2006). Linear Friction Welding of IN-718 Process Optimization and Microstructure Evolution. *Advanced Materials Research*, 15-17, 357-362. doi:10.4028/[www.scientific.net/AMR.15-17.357](http://www.scientific.net/AMR.15-17.357)
- Mary, C., & Jahazi, M. (2008). Multi-Scale Analysis of IN-718 Microstructure Evolution During Linear Friction Welding. *Advanced Engineering Materials*, 10(6), 573-578. doi:10.1002/adem.200700361
- Masoumi, F., Jahazi, M., Cormier, J., & Shahriari, D. (2014). *Dissolution kinetics and morphological changes of  $\gamma'$  in AD730™ superalloy*. Paper presented at the MATEC Web of Conferences.
- Masoumi, F., Jahazi, M., Shahriari, D., & Cormier, J. (2016). Coarsening and dissolution of  $\gamma'$  precipitates during solution treatment of AD730™ Ni-based superalloy: Mechanisms and kinetics models. *Journal of Alloys and Compounds*, 658, 981-995. doi:10.1016/j.jallcom.2015.11.002
- Masoumi, F., Shahriari, D., Jahazi, M., Cormier, J., & Devaux, A. (2016a). Kinetics and Mechanisms of  $\gamma'$  Re-precipitation in a Ni-based Superalloy. *Sci Rep*, 6, 28650. doi:10.1038/srep28650
- Masoumi, F., Shahriari, D., Jahazi, M., Cormier, J., & Devaux, A. (2016b). Kinetics and Mechanisms of  $\gamma'$  Re-precipitation in a Ni-based Superalloy. *Sci Rep*, 6, 28650.

- Masoumi, F., Shahriari, D., Jahazi, M., Cormier, J., & Flipo, B. C. D. (2017). On the Occurrence of Liquation During Linear Friction Welding of Ni-Based Superalloys. *Metallurgical and Materials Transactions A*, 48(6), 2886-2899. doi:10.1007/s11661-017-4067-0
- Masoumi, F., Shahriari, D., Monajati, H., Cormier, J., Flipo, B. C. D., Devaux, A., & Jahazi, M. (2019). Linear friction welding of AD730™ Ni-base superalloy: Process-microstructure-property interactions. *Materials & Design*, 183, 108-117. doi:<https://doi.org/10.1016/j.matdes.2019.108117>
- Masoumi, F., Thébaud, L., Shahriari, D., Jahazi, M., Cormier, J., Devaux, A., & Flipo, B. C. D. (2018). High temperature creep properties of a linear friction welded newly developed wrought Ni-based superalloy. *Materials Science and Engineering: A*, 710, 214-226. doi:10.1016/j.msea.2017.10.091
- McAndrew, A. R., Colegrove, P. A., Bühr, C., Flipo, B. C. D., & Vairis, A. (2018). A literature review of Ti-6Al-4V linear friction welding. *Progress in Materials Science*, 92, 225-257. doi:10.1016/j.pmatsci.2017.10.003
- Mcnallan, M. J., & Debroy, T. (1991). Effect of Temperature and Composition on Surface-Tension in Fe-Ni-Cr Alloys Containing Sulfur. *Metallurgical Transactions B-Process Metallurgy*, 22(4), 557-560. doi:Doi 10.1007/Bf02654294
- Medeiros, S. C., Prasad, Y. V. R. K., Frazier, W. G., & Srinivasan, R. (2000). Microstructural modeling of metadynamic recrystallization in hot working of IN 718 superalloy. *Materials Science and Engineering: A*, 293(1-2), 198-207. doi:10.1016/s0921-5093(00)01053-4
- Mejía, I., Bedolla-Jacuinde, A., Maldonado, C., & Cabrera, J. M. (2011). Hot ductility behavior of a low carbon advanced high strength steel (AHSS) microalloyed with boron. *Materials Science and Engineering: A*, 528(13-14), 4468-4474. doi:10.1016/j.msea.2011.02.040
- Miller, W. A., & Chadwick, G. A. (1967). On the magnitude of the solid/liquid interfacial energy of pure metals and its relation to grain boundary melting. *Acta Metallurgica*, 15(4), 607-614. doi:10.1016/0001-6160(67)90104-6
- Mitchell, A. (2005). *The Precipitation of Primary Carbides in IN718 and its Relation to Solidification Conditions*. Paper presented at the Superalloys 718, 625, 706 and Various Derivatives (2005).
- Mitchell, A., Schmalz, A. J., Schvezov, C., & Cockroft, S. (1994). *The precipitation of primary carbides in alloy 718*. Paper presented at the In Superalloys 718, 625 and Various Derivatives; Loria, E.A., Ed.; TMS-AIME: Warrendale, USA.

- Montazeri, M., & Ghaini, F. M. (2012). The liquation cracking behavior of IN738LC superalloy during low power Nd:YAG pulsed laser welding. *Materials Characterization*, 67, 65-73. doi:10.1016/j.matchar.2012.02.019
- Mostafa, A., Picazo Rubio, I., Brailovski, V., Jahazi, M., & Medraj, M. (2017a). Erratum: Structure, Texture and Phases in 3D Printed IN718 Alloy Subjected to Homogenization and HIP Treatments. *Metals* 2017, 7, 196. *Metals*, 7(8), 315.
- Mostafa, A., Picazo Rubio, I., Brailovski, V., Jahazi, M., & Medraj, M. (2017b). Structure, Texture and Phases in 3D Printed IN718 Alloy Subjected to Homogenization and HIP Treatments. *Metals*, 7(6). doi:10.3390/met7060196
- Mostafa, A., Shahriari, D., Rubio, I. P., Brailovski, V., Jahazi, M., & Medraj, M. (2018). Hot compression behavior and microstructure of selectively laser-melted IN718 alloy. *The International Journal of Advanced Manufacturing Technology*. doi:10.1007/s00170-017-1522-4
- Moussaoui, K., Rubio, W., Mousseigne, M., Sultan, T., & Rezai, F. (2018). Effects of Selective Laser Melting additive manufacturing parameters of Inconel 718 on porosity, microstructure and mechanical properties. *Materials Science and Engineering: A*, 735, 182-190. doi:10.1016/j.msea.2018.08.037
- Muralidharan, B. G., Shankar, V., & Gill, T. P. S. (1996). *Weldability of inconel 718 - a review* (29018458). Retrieved from Kalpakkam:
- Ni, M., Liu, S., Chen, C., Li, R., Zhang, X., & Zhou, K. (2019). Effect of heat treatment on the microstructural evolution of a precipitation-hardened superalloy produced by selective laser melting. *Materials Science and Engineering: A*, 748, 275-285. doi:10.1016/j.msea.2019.01.109
- Niang, A., Viguiet, B., & Lacaze, J. (2010). Some features of anisothermal solid-state transformations in alloy 718. *Materials Characterization*, 61(5), 525-534. doi:10.1016/j.matchar.2010.02.011
- Nicolay, A., Franchet, J. M., Cormier, J., Mansour, H., M, D. E. G., Seret, A., & Bozzolo, N. (2019). Discrimination of dynamically and post-dynamically recrystallized grains based on EBSD data: application to Inconel 718. *J Microsc*, 273(2), 135-147. doi:10.1111/jmi.12769
- Noecker, F. F., & DuPont, J. N. (2009). Metallurgical Investigation into Ductility Dip Cracking in Ni-Based Alloys: Part II. *Welding Journal*, 88(3), 62s-77s. Retrieved from <Go to ISI>://WOS:000269804000010

- Nunn, M. E. (2005). *Aero engine improvements through linear friction welding*. Paper presented at the 1st International Conference on Innovation and Integration in Aerospace Sciences, CEIA, Queen's University Belfast, Northern Ireland, UK.
- Ojo, O. A., & Chaturvedi, M. C. (2005). On the role of liquated  $\gamma'$  precipitates in weld heat affected zone microfissuring of a nickel-based superalloy. *Materials Science and Engineering: A*, 403(1-2), 77-86. doi:10.1016/j.msea.2005.04.034
- Ojo, O. A., Richards, N. L., & Chaturvedi, M. C. (2004a). Contribution of constitutional liquation of gamma prime precipitate to weld HAZ cracking of cast Inconel 738 superalloy. *Scripta Materialia*, 50(5), 641-646. doi:10.1016/j.scriptamat.2003.11.025
- Ojo, O. A., Richards, N. L., & Chaturvedi, M. C. (2004b). Microstructural study of weld fusion zone of TIG welded IN 738LC nickel-based superalloy. *Scr Mater*, 51(7), 683-688. doi:10.1016/j.scriptamat.2004.06.013
- Ola, O. T., Ojo, O. A., & Chaturvedi, M. C. (2013). Effect of deformation mode on hot ductility of a  $\gamma'$  precipitation strengthened nickel-base superalloy. *Materials Science and Engineering: A*, 585, 319-325. doi:10.1016/j.msea.2013.06.088
- Ola, O. T., Ojo, O. A., Wanjara, P., & Chaturvedi, M. C. (2011a). Analysis of Microstructural Changes Induced by Linear Friction Welding in a Nickel-Base Superalloy. *Metallurgical and Materials Transactions A*, 42(12), 3761-3777. doi:10.1007/s11661-011-0774-0
- Ola, O. T., Ojo, O. A., Wanjara, P., & Chaturvedi, M. C. (2011b). A Study of Linear Friction Weld Microstructure in Single Crystal CMSX-486 Superalloy. *Metallurgical and Materials Transactions A*, 43(3), 921-933. doi:10.1007/s11661-011-0928-0
- Oliveira, J. P., Santos, T. G., & Miranda, R. M. (2020). Revisiting fundamental welding concepts to improve additive manufacturing: From theory to practice. *Progress in Materials Science*, 107. doi:10.1016/j.pmatsci.2019.100590
- Oluwasegun, K. M., Olawale, J. O., Oyatogun, G. M., Shittu, M. D., Ige, O. O., & Malomo, B. O. (2014). In Situ Micro-mechanical Testing of a PM Nickel-Base Superalloy Weld. *Metallurgical and Materials Transactions A*, 45(11), 5127-5137. doi:10.1007/s11661-014-2462-3
- Owczarski, W. A., Duvall, D. S., & Sullivan, C. P. (1966). Model for Heat-Affected Zone Cracking in Nickel-Base Superalloys. *Weld Journal*, 45, 145-155.
- Panella, M., Signor, L., Cormier, J., Bernacki, M., & Villechaise, P. (2020). Experimental and Simulation Study of the Effect of Precipitation Distribution and Grain Size on the AD730TM Ni-Based Polycrystalline Superalloy Tensile Behavior. In *Superalloys* (pp. 570-578).

- Parimi, L. L., A. R. G., Clark, D., & Attallah, M. M. (2014). Microstructural and texture development in direct laser fabricated IN718. *Materials Characterization*, *89*, 102-111. doi:10.1016/j.matchar.2013.12.012
- Pérez, M., Dumont, C., Nodin, O., & Nouveau, S. (2018). Impact of forging direction on the recrystallization behaviour of nickel base superalloy AD730 billet material at subsolvus temperatures. *Materials Characterization*, *146*, 169-181. doi:10.1016/j.matchar.2018.10.003
- Petersen-Overleir, E. (2015). *Effect of 3D printing on the Microstructure and Mechanical Properties of an Inconel 718 Nickel-alloy*. (Master Master Thesis). University of Stavanger,
- Ping, D. H., Gu, Y. F., Cui, C. Y., & Harada, H. (2007). Grain boundary segregation in a Ni-Fe-based (Alloy 718) superalloy. *Materials Science and Engineering: A*, *456*(1-2), 99-102. doi:10.1016/j.msea.2007.01.090
- Popovich, V. A., Borisov, E. V., Popovich, A. A., Sufiiarov, V. S., Masaylo, D. V., & Alzina, L. (2017a). Functionally graded Inconel 718 processed by additive manufacturing: Crystallographic texture, anisotropy of microstructure and mechanical properties. *Materials & Design*, *114*, 441-449. doi:10.1016/j.matdes.2016.10.075
- Popovich, V. A., Borisov, E. V., Popovich, A. A., Sufiiarov, V. S., Masaylo, D. V., & Alzina, L. (2017b). Impact of heat treatment on mechanical behaviour of Inconel 718 processed with tailored microstructure by selective laser melting. *Materials & Design*, *131*, 12-22. doi:10.1016/j.matdes.2017.05.065
- Popovich, V. A., Borisov, E. V., Sufiiarov, V. S., & Popovich, A. A. (2019). Tailoring the Properties in Functionally Graded Alloy Inconel 718 Using Additive Technologies. *Metal Science and Heat Treatment*, 701-709. doi:10.1007/s11041-019-00343-z
- Pouranvari, M. (2015). Solid solution strengthening of transient liquid phase bonded nickel based superalloy. *Materials Science and Technology*, *31*(14), 1773-1780. doi:10.1179/1743284715y.0000000005
- Qian, M. (2001). *An investigation of the repair weldability of Waspaloy and Alloy 718*. (Doctor of Philosophy). The Ohio State University,
- Qian, M., & Lippold, J. C. (2002). The effect of multiple postweld heat treatment cycles on the weldability of Waspaloy (R). *Welding Journal*, *81*(11), 233s-238s. Retrieved from <Go to ISI>://WOS:000186767500012
- Qian, M., & Lippold, J. C. (2003a). The effect of annealing twin-generated special grain boundaries on HAZ liquation cracking of nickel-base superalloys. *Acta Materialia*, *51*(12), 3351-3361. doi:10.1016/s1359-6454(03)00090-9

- Qian, M., & Lippold, J. C. (2003b). Liquation phenomena in the simulated heat-affected zone of alloy 718 after multiple postweld heat treatment cycles. *WELDING JOURNAL-NEW YORK*, 82(6), 145-150.
- Qu, J.-l., Bi, Z.-n., Du, J.-h., Wang, M.-q., Wang, Q.-z., & Zhang, J. (2011). Hot Deformation Behavior of Nickel-Based Superalloy GH4720Li. *Journal of Iron and Steel Research, International*, 18(10), 59-65. doi:10.1016/s1006-706x(12)60023-5
- R. Messler, J. (2004). *Principles of welding: Processes, physics, chemistry and metallurgy*: Wiley-VCH.
- Radhakrishna, C. H., & Prasad Rao, K. (1997). The formation and control of Laves phase in superalloy 718 welds. *Journal of Materials Science*, 32(8), 1977-1984. doi:10.1023/a:1018541915113
- Radhakrishnan, B., & Thompson, R. G. (1991). A phase diagram approach to study liquation cracking in alloy 718. *Metallurgical Transactions A*, 22(4), 887-902. doi:10.1007/bf02658999
- Radhakrishnan, B., & Thompson, R. G. (1992). A model for the formation and solidification of grain boundary liquid in the heat-affected zone (HAZ) of welds. *Metallurgical Transactions A*, 23(6), 1783-1799. doi:10.1007/bf02804371
- Radhakrishnan, B., & Thompson, R. G. (1993). The effect of weld Heat-Affected zone (HAZ) liquation kinetics on the hot cracking susceptibility of alloy 718. *Metallurgical and Materials Transactions A*, 24(6), 1409-1422. doi:10.1007/bf02668209
- Rafiei, M., Mirzadeh, H., & Malekan, M. (2021). Delta processing effects on the creep behavior of a typical Nb-bearing nickel-based superalloy. *Vacuum*, 184. doi:10.1016/j.vacuum.2020.109913
- Rafiei, M., Mirzadeh, H., Malekan, M., & Sohrabi, M. J. (2019). Homogenization kinetics of a typical nickel-based superalloy. *Journal of Alloys and Compounds*, 793, 277-282. doi:10.1016/j.jallcom.2019.04.147
- Raj, R., & Ashby, M. F. (1975). Intergranular fracture at elevated temperature. *Acta Metallurgica*, 23(6), 653-666. doi:10.1016/0001-6160(75)90047-4
- Ramirez, J. E. (2012). Susceptibility of IN740 to HAZ Liquation Cracking and Ductility-Dip Cracking. *Welding Journal*, 91(4), 122s-131s. Retrieved from <Go to ISI>://WOS:000302279200015
- Raza, Hurtig, Asala, Andersson, Svensson, & Ojo. (2019). Influence of Heat Treatments on Heat Affected Zone Cracking of Gas Tungsten Arc Welded Additive Manufactured Alloy 718. *Metals*, 9(8). doi:10.3390/met9080881

- Raza, T., Andersson, J., & Svensson, L.-E. (2018). Vareststraint weldability testing of additive manufactured alloy 718. *Science and Technology of Welding and Joining*, 23(7), 606-611. doi:10.1080/13621718.2018.1437338
- Raza, T., Hurtig, K., Asala, G., Andersson, J., Svensson, L. E., & Ojo, O. A. (2019). Influence of Heat Treatments on Heat Affected Zone Cracking of Gas Tungsten Arc Welded Additive Manufactured Alloy 718. *Metals*, 9(8). doi:10.3390/met9080881
- Ricks, R. A., Porter, A. J., & Ecob, R. C. (1983). The growth of  $\gamma'$  precipitates in nickel-base superalloys. *Acta Metallurgica*, 31(1), 43-53. doi:10.1016/0001-6160(83)90062-7
- Riedel, H. (1987). *Fracture at high temperatures*. Berlin ; New York: Springer-Verlag.
- Roder, O., Helm, D., Neft, S., Albrecht, J., & Luetjering, G. (2005). *Mixed Inconel Alloy 718 Inertia Welds for Rotating Applications: Microstructures and Mechanical Properties*. Paper presented at the Superalloys 718, 625, 706 and Various Derivatives (2005).
- Ruan, J. J., Ueshima, N., & Oikawa, K. (2018). Phase transformations and grain growth behaviors in superalloy 718. *Journal of Alloys and Compounds*, 737, 83-91. doi:10.1016/j.jallcom.2017.11.327
- Sabol, G. P., & Stickler, R. (1969). Microstructure of Nickel-Based Superalloys. *Basic solid state physics*. doi:10.1002/pssb.19690350102
- Salishchev, G., Mironov, S., Zherebtsov, S., & Belyakov, A. (2010). Changes in misorientations of grain boundaries in titanium during deformation. *Materials Characterization*, 61(7), 732-739. doi:10.1016/j.matchar.2010.04.005
- SAMES, W. J. (2015). *Additive manufacturing of Inconel 718 using electron beam melting: Processing, post-processing, & mechanical properties*. (DOCTOR OF PHILOSOPHY). Texas A&M University, (3731051)
- Sarrat, L., Chamanfar, A., & Jahazi, M. (2012). Microstructure evolution of Ni base superalloys during thermomechanical processing.
- Sasajima, Y., Akabane, T., Nagai, T., Chonan, Y., & Onuki, J. (2009). Void generation during the annealing process of very narrow copper wires. *Journal of Applied Physics*, 105(7). doi:10.1063/1.3091291
- Sathiya, P., Aravindan, S., & Noorul Haq, A. (2004). Mechanical and metallurgical properties of friction welded AISI 304 austenitic stainless steel. *The International Journal of Advanced Manufacturing Technology*, 26(5-6), 505-511. doi:10.1007/s00170-004-2018-6

- Seede, R., Mostafa, A., Brailovski, V., Jahazi, M., & Medraj, M. (2018). Microstructural and Microhardness Evolution from Homogenization and Hot Isostatic Pressing on Selective Laser Melted Inconel 718: Structure, Texture, and Phases. *Journal of Manufacturing and Materials Processing*, 2(2). doi:10.3390/jmmp2020030
- Seegerstark, A. (2017). *Laser Metal Deposition using Alloy 718 Powder: Influence of Process Parameters on Material Characteristics*. (Ph.D.). University West, Trollhättan, Sweden.
- Semiatin, S. L., Mahaffey, D. W., Levkulich, N. C., & Senkov, O. N. (2017). The Radial Temperature Gradient in the Gleeble® Hot-Torsion Test and Its Effect on the Interpretation of Plastic-Flow Behavior. *Metallurgical and Materials Transactions A*, 48(11), 5357-5367. doi:10.1007/s11661-017-4296-2
- Senkov, O. N., Mahaffey, D. W., & Semiatin, S. L. (2018). A Comparison of the Inertia Friction Welding Behavior of Similar and Dissimilar Ni-Based Superalloys. *Metallurgical and Materials Transactions A*, 49(11), 5428-5444. doi:10.1007/s11661-018-4853-3
- Senkov, O. N., Mahaffey, D. W., Semiatin, S. L., & Woodward, C. (2014). Inertia Friction Welding of Dissimilar Superalloys Mar-M247 and LSHR. *Metallurgical and Materials Transactions A*, 45(12), 5545-5561. doi:10.1007/s11661-014-2512-x
- Seret, A. (2019). *Influence de la mise en forme sur les cinétiques de précipitation durcissante dans les superalliages base nickel Inconel® 625 et AD730™*. (Ph.D.). MINES ParisTech,
- Shi, D., Dong, C., Yang, X., Zhang, L., Hou, J., & Liu, Y. (2012). Experimental investigations on creep rupture strength and failure mechanism of vacuum brazed joints of a DS superalloy at elevated temperature. *Materials Science and Engineering: A*, 545, 162-167. doi:10.1016/j.msea.2012.02.099
- Shi, Z.-x., Yan, X.-f., Duan, C.-h., & Zhao, M.-h. (2017). Effect of strain rate on hot deformation characteristics of GH690 superalloy. *Transactions of Nonferrous Metals Society of China*, 27(3), 538-550. doi:10.1016/s1003-6326(17)60082-7
- Shtrikman, M. M. (2010). Linear friction welding. *Welding International*, 24(7), 563-569. doi:10.1080/09507110903569149
- Sluetz, E. J., Oberle, T. L., & Brosheer, B. C. (1968).
- Smith, M., Bichler, L., Gholipour, J., & Wanjara, P. (2017). Mechanical properties and microstructural evolution of in-service Inconel 718 superalloy repaired by linear friction welding. *The International Journal of Advanced Manufacturing Technology*, 90(5-8), 1931-1946. doi:10.1007/s00170-016-9515-2

- Smith, M., Bichler, L., & Sediako, D. (2016). Measurement of Residual Stresses in Linear Friction Welded In-Service Inconel 718 Superalloy. *Materials Science Forum*, 879, 1800-1806. doi:10.4028/[www.scientific.net/MSF.879.1800](http://www.scientific.net/MSF.879.1800)
- Smith, M. M. (2017a). *Characterization of linear friction welded in-service Inconel 718 superalloy*. (DOCTOR OF PHILOSOPHY). The University of British Columbia (Okanagan),
- Smith, M. M. (2017b). *Characterization of Linear Friction Welded In-Service Inconel 718 Superalloy*. (Doctor of Philosophy). The University of British Columbia (Okanagan),
- Smith, R. W., & Srolovitz, D. J. (1996). Void formation during film growth: A molecular dynamics simulation study. *Journal of Applied Physics*, 79(3), 1448-1457. doi:10.1063/1.360983
- Sohrabi, M. J., & Mirzadeh, H. (2019a). Estimation of homogenisation time for superalloys based on a new diffusional model. *Materials Science and Technology*, 36(3), 380-384. doi:10.1080/02670836.2019.1706906
- Sohrabi, M. J., & Mirzadeh, H. (2019b). Numerical and analytical solutions for determination of interdiffusion coefficients in superalloys during homogenization. *Materials Today Communications*, 21. doi:10.1016/j.mtcomm.2019.100631
- Sohrabi, M. J., & Mirzadeh, H. (2019c). Revisiting the Diffusion of Niobium in an As-Cast Nickel-Based Superalloy During Annealing at Elevated Temperatures. *Metals and Materials International*. doi:10.1007/s12540-019-00342-y
- Sohrabi, M. J., & Mirzadeh, H. (2020). Unexpected formation of delta ( $\delta$ ) phase in as-cast niobium-bearing superalloy at solution annealing temperatures. *Materials Letters*, 261. doi:10.1016/j.matlet.2019.127008
- Soucail, M., & Bienvenu, Y. (1996). Dissolution of the  $\gamma'$  phase in a nickel base superalloy at equilibrium and under rapid heating. *Materials Science and Engineering: A*, 220(1-2), 215-222. doi:10.1016/s0921-5093(97)80011-1
- Soucail, M., Moal, A., Naze, L., Massoni, E., Levailant, C., & Bienvenu, Y. (1992). Microstructural Study and Numerical-Simulation of Inertia Friction Welding of Astroloy. *Superalloys 1992*, 847-856. Retrieved from <Go to ISI>://WOS:A1992BW92R00084
- Steuer, S., Piegert, S., Frommherz, M., Singer, R. F., & Scholz, A. (2011). Transient Liquid Phase Bonding of Pairings of Parent Superalloy Material with Different Composition and Grain Structure. *Advanced Materials Research*, 278, 454-459. doi:10.4028/[www.scientific.net/AMR.278.454](http://www.scientific.net/AMR.278.454)

- Steuer, S., & Singer, R. F. (2014). Suppression of Boride Formation in Transient Liquid Phase Bonding of Pairings of Parent Superalloy Materials with Different Compositions and Grain Structures and Resulting Mechanical Properties. *Metallurgical and Materials Transactions A*, 45(8), 3545-3553. doi:10.1007/s11661-014-2304-3
- Sufiiarov, V. S., Borisov, E. V., & Polozov, I. A. (2014). Selective Laser Melting of the Inconel 718 Nickel Superalloy. *Applied Mechanics and Materials*, 698, 333-338. doi:10.4028/[www.scientific.net/AMM.698.333](http://www.scientific.net/AMM.698.333)
- Sui, S., Chen, J., Li, Z., Li, H., Zhao, X., & Tan, H. (2020). Investigation of dissolution behavior of laves phase in inconel 718 fabricated by laser directed energy deposition. *Additive Manufacturing*, 32. doi:10.1016/j.addma.2020.101055
- Sui, S., Chen, J., Ma, L., Fan, W., Tan, H., Liu, F., & Lin, X. (2019). Microstructures and stress rupture properties of pulse laser repaired Inconel 718 superalloy after different heat treatments. *Journal of Alloys and Compounds*, 770, 125-135. doi:10.1016/j.jallcom.2018.08.063
- Sui, S., Tan, H., Chen, J., Zhong, C., Li, Z., Fan, W., . . . Huang, W. (2019). The influence of Laves phases on the room temperature tensile properties of Inconel 718 fabricated by powder feeding laser additive manufacturing. *Acta Materialia*, 164, 413-427. doi:10.1016/j.actamat.2018.10.032
- Suzuki, K., Ito, H., Inoue, T., & Miura, H. (2009). Creep Damage Process of Ni-Base Superalloy Caused by Stress-Induced Anisotropic Atomic Diffusion. *Journal of Solid Mechanics and Materials Engineering*, 3(3), 487-497. doi:10.1299/jmmp.3.487
- Swaminathan, S., Oh-Ishi, K., Zhilyaev, A. P., Fuller, C. B., London, B., Mahoney, M. W., & McNelley, T. R. (2009). Peak Stir Zone Temperatures during Friction Stir Processing. *Metallurgical and Materials Transactions A*, 41(3), 631-640. doi:10.1007/s11661-009-0140-7
- Tabaie, S., Rézaï-Aria, F., Flipo, B. C. D., & Jahazi, M. (2020). Grain size and misorientation evolution in linear friction welding of additively manufactured IN718 to forged superalloy AD730™. *Materials Characterization*. doi:10.1016/j.matchar.2020.110766
- Tabaie, S., Rézaï-Aria, F., & Jahazi, M. (2020). Microstructure Evolution of Selective Laser Melted Inconel 718: Influence of High Heating Rates. *Metals*, 10(5), 587. doi:10.3390/met10050587
- Tabaie, S., Shahriari, D., Plouze, C., Devaux, A., Cormier, J., & Jahazi, M. (2019). Hot ductility behavior of AD730™ nickel-base superalloy. *Materials Science and Engineering: A*, 766, 138391. doi:<https://doi.org/10.1016/j.msea.2019.138391>

- Tharappel, J. T., & Babu, J. (2018). Welding processes for Inconel 718- A brief review. *IOP Conference Series: Materials Science and Engineering*, 330. doi:10.1088/1757-899x/330/1/012082
- Thébaud, L. (2017). *Etude des relations entre microstructure et propriétés mécaniques du nouveau superalliage base nickel AD730™*. (Ph.D.). ISAE-ENSMA Ecole Nationale Supérieure de Mécanique et d'Aérotechnique, Poitiers.
- Thomas, A., El-Wahabi, M., Cabrera, J. M., & Prado, J. M. (2006). High temperature deformation of Inconel 718. *Journal of Materials Processing Technology*, 177(1-3), 469-472. doi:10.1016/j.jmatprotec.2006.04.072
- Thompson, R. G., Mayo, D. E., & Radhakrishnan, B. (1991). The relationship between carbon content, microstructure, and intergranular liquation cracking in cast nickel alloy 718. *Metallurgical Transactions A*, 22(2), 557-567. doi:10.1007/bf02656823
- Thompson, R. G., Radhakrishnan, B., & Mayo, D. E. (1988). Grain Boundary Chemistry Contributions to Intergranular Hot Cracking. *Le Journal de Physique Colloques*, 49(C5), C5-471-C475-479. doi:10.1051/jphyscol:1988559
- Trosch, T., Strößner, J., Völkl, R., & Glatzel, U. (2016). Microstructure and mechanical properties of selective laser melted Inconel 718 compared to forging and casting. *Materials Letters*, 164, 428-431. doi:10.1016/j.matlet.2015.10.136
- Tucho, W. M., Cuvillier, P., Sjolyst-Kverneland, A., & Hansen, V. (2017). Microstructure and hardness studies of Inconel 718 manufactured by selective laser melting before and after solution heat treatment. *Materials Science and Engineering: A*, 689, 220-232. doi:10.1016/j.msea.2017.02.062
- Turner, R., Gebelin, J. C., Ward, R. M., & Reed, R. C. (2011). Linear friction welding of Ti-6Al-4V: Modelling and validation. *Acta Materialia*, 59(10), 3792-3803. doi:10.1016/j.actamat.2011.02.028
- TWI. (2001). *Linear Friction Welding of Blisks for Power Generation*.
- V. A. Popovich, Borisov, E. V., Heurtebise, V., Riemsdag, T., Popovich, A. A., & Sufiiarov, V. S. (2018). *Creep and Thermomechanical Fatigue of Functionally Graded Inconel 718 Produced by Additive Manufacturing*. Paper presented at the In: & Materials Society T. (eds) TMS 2018 147th Annual Meeting & Exhibition Supplemental Proceedings.
- Vairis, A., & Frost, M. (1998). High frequency linear friction welding of a titanium alloy. *Wear*, 217(1), 117-131. doi:10.1016/s0043-1648(98)00145-8

- Vairis, A., & Frost, M. (2000). Modelling the linear friction welding of titanium blocks. *Materials Science and Engineering: A*, 292(1), 8-17. doi:10.1016/s0921-5093(00)01036-4
- Vairis, A., & Frost, M. (2007). Design and Commissioning of a Friction Welding Machine. *Materials and Manufacturing Processes*, 21(8), 766-773. doi:10.1080/03602550600728356
- Vernier, S., Pugliara, A., Viguiet, B., Andrieu, E., & Laffont, L. (2020). Solid-State Phase Transformations Involving (Nb,Mo)<sub>2</sub>CrB<sub>2</sub> Borides and (Nb,Ti)<sub>2</sub>CS Carbosulfides at the Grain Boundaries of Superalloy Inconel 718. *Metallurgical and Materials Transactions A*, 51(12), 6607-6629. doi:10.1007/s11661-020-06045-z
- VishwakArma, K. R., Ojo, O. A., Wanjara, P., & Chaturvedi, M. C. (2014). Microstructural Analysis of Linear Friction-Welded 718 Plus Superalloy. *The Journal of The Minerals, Metals & Materials Society (TMS)*, 66(12), 2525–2534. doi:10.1007/s11837-014-0938-7
- Wang, X.-Y., Wen, Z.-X., Cheng, H., Gu, S.-N., & Lu, G.-X. (2019). Influences of the Heating and Cooling Rates on the Dissolution and Precipitation Behavior of a Nickel-Based Single-Crystal Superalloy. *Metals*, 9(3). doi:10.3390/met9030360
- Wang, X., & Chou, K. (2016). Electron Backscatter Diffraction Analysis of Inconel 718 Parts Fabricated by Selective Laser Melting Additive Manufacturing. *Jom*, 69(2), 402-408. doi:10.1007/s11837-016-2198-1
- Wang, X., & Chou, K. (2018). Microstructure simulations of Inconel 718 during selective laser melting using a phase field model. *The International Journal of Advanced Manufacturing Technology*, 100(9-12), 2147-2162. doi:10.1007/s00170-018-2814-z
- Wang, X., Gong, X., & Chou, K. (2015). *Review on powder-bed laser additive manufacturing of Inconel 718 parts*. Paper presented at the ASME 2015 International Manufacturing Science and Engineering Conference, Charlotte, North Carolina, USA.
- Wang, X., Gong, X., & Chou, K. (2016). Review on powder-bed laser additive manufacturing of Inconel 718 parts. *Proceedings of the Institution of Mechanical Engineers, Part B: Journal of Engineering Manufacture*, 231(11), 1890-1903. doi:10.1177/0954405415619883
- Wang, Y., Shao, W. Z., Zhen, L., Yang, C., & Zhang, X. M. (2009). Tensile deformation behavior of superalloy 718 at elevated temperatures. *Journal of Alloys and Compounds*, 471(1-2), 331-335. doi:10.1016/j.jallcom.2008.03.082

- Wang, Y., Shao, W. Z., Zhen, L., & Zhang, X. M. (2008). Microstructure evolution during dynamic recrystallization of hot deformed superalloy 718. *Materials Science and Engineering: A*, 486(1-2), 321-332. doi:10.1016/j.msea.2007.09.008
- Wang, Z., Guan, K., Gao, M., Li, X., Chen, X., & Zeng, X. (2012). The microstructure and mechanical properties of deposited-IN718 by selective laser melting. *Journal of Alloys and Compounds*, 513, 518-523. doi:10.1016/j.jallcom.2011.10.107
- Wanjara, P., Dalgaard, E., Gholipour, J., & Larose, J. (2012). Linear Friction Welding of a Single Crystal Superalloy. *Materials Science Forum*, 706-709, 3022-3027. doi:10.4028/[www.scientific.net/MSF.706-709.3022](http://www.scientific.net/MSF.706-709.3022)
- Wanjara, P., Gholipour, J., Watanabe, K., Nezaki, K., Tian, Y., & Brochu, M. (2016). Linear Friction Welding of IN718 to Ti6Al4V. *Materials Science Forum*, 879, 2072-2077. doi:10.4028/[www.scientific.net/MSF.879.2072](http://www.scientific.net/MSF.879.2072)
- Wanjara, P., & Jahazi, M. (2005). Linear friction welding of aerospace materials.
- Weaver, D. S., & Semiatin, S. L. (2007). Recrystallization and grain-growth behavior of a nickel-base superalloy during multi-hit deformation. *Scripta Materialia*, 57(11), 1044-1047. doi:10.1016/j.scriptamat.2007.07.033
- Wei, H. L., Mazumder, J., & DebRoy, T. (2015). Evolution of solidification texture during additive manufacturing. *Sci Rep*, 5, 16446. doi:10.1038/srep16446
- Whlittenberger, J. D. (1992). A Review of: "SUPERALLOYS II" edited by CT. Sims, N.S. Stoloff, and W.C. Hagel A Wiley-Interscience Publication John Wiley & Sons, New York, NY 615 pages, hardcover, 1987. *Materials and Manufacturing Processes*, 7(3), 463-468. doi:10.1080/10426919208947432
- Wilhelm, H., Furlan, R., & Moloney, K. C. (1995). *Linear Friction Bonding of Titanium Alloys for Aero-Engine Applications*. Paper presented at the World Conference on Titanium ; 8; 1995, Birmingham, London.
- Wong, K. V., & Hernandez, A. (2012). A Review of Additive Manufacturing. *ISRN Mechanical Engineering*, 2012, 1-10. doi:10.5402/2012/208760
- X, W., & K, C. (2015, 10–12 August 2015). *Residual stress in metal parts produced by powder-bed additive manufacturing processes*. Paper presented at the proceedings of the 26th International solid freeform fabrication symposium, Austin, TX.
- X, W., & K., C. (2015, 13–19 November 2015). *method to estimate residual stress in metal parts made by Selective Laser Melting*. Paper presented at the Proceedings of the ASME 2015 international mechanical engineering congress and exposition, Houston, TX.

- Xiao, F., Liu, L.-x., Yang, R.-h., Zhao, H.-k., Fang, L., & Zhang, C. (2008). Surface tension of molten Ni-(Cr, Co, W) alloys and segregation of elements. *Transactions of Nonferrous Metals Society of China*, 18(5), 1184-1188. doi:10.1016/s1003-6326(08)60202-2
- Xiao Feng, Fang Liang, & K., N. (2005). Surface tension and molten Ni and Ni-Co alloys. *Journal of Materials Science and Technology*, 201-206.
- Xie, X., Dong, J., Wang, G., You, W., Du, J., Zhao, C., . . . Carneiro, T. (2005). *The Effect of Nb, Ti, Al on Precipitation and Strengthening Behavior of 718 Type Superalloys*. Paper presented at the Superalloys 718, 625, 706 and Various Derivatives (2005).
- Xie, X. S., Fu, S. H., Zhao, S. Q., & Dong, J. X. (2010). The Precipitation Strengthening Effect of Nb, Ti and Al in Cast/Wrought Ni-Base Superalloys. *Materials Science Forum*, 638-642, 2363-2368. doi:10.4028/[www.scientific.net/MSF.638-642.2363](http://www.scientific.net/MSF.638-642.2363)
- Xu, Y., Li, W., Yang, X., & Gu, Y. (2020). Evolution of grain structure,  $\gamma'$  precipitate and hardness in friction welding and post weld heat treatment of a new Ni-Fe based superalloy. *Materials Science and Engineering: A*, 788. doi:10.1016/j.msea.2020.139596
- Yang, H., Zhu, L., Zhang, R., Zhou, J., & Sun, Z. (2020). Influence of high stacking-fault energy on the dissociation mechanisms of misfit dislocations at semi-coherent interfaces. *International Journal of Plasticity*, 126. doi:10.1016/j.ijplas.2019.09.016
- Yang, X., Li, W., Li, J., Xiao, B., Ma, T., Huang, Z., & Guo, J. (2015). Finite element modeling of the linear friction welding of GH4169 superalloy. *Materials & Design*, 87, 215-230. doi:10.1016/j.matdes.2015.08.036
- Ye, R. R., Li, H. Y., Ding, R. G., Doel, T. J. A., Bray, S., Walpole, A., & Bowen, P. (2020). Microstructure and microhardness of dissimilar weldment of Ni-based superalloys IN718-IN713LC. *Materials Science and Engineering: A*, 774. doi:10.1016/j.msea.2019.138894
- Yilbas, B. S., & Sahin, A. Z. (2014). *Friction Welding*: Springer Heidelberg New York Dordrecht London.
- Yoo, Y. S. J., Book, T. A., Sangid, M. D., & Kacher, J. (2018). Identifying strain localization and dislocation processes in fatigued Inconel 718 manufactured from selective laser melting. *Materials Science and Engineering: A*, 724, 444-451. doi:10.1016/j.msea.2018.03.127
- Zhang, C., Jahazi, M., & Tremblay, R. (2020). Simulation and experimental validation of the effect of superheat on macrosegregation in large-size steel ingots. *The International Journal of Advanced Manufacturing Technology*. doi:10.1007/s00170-020-05044-z

- Zhang, D., Niu, W., Cao, X., & Liu, Z. (2015). Effect of standard heat treatment on the microstructure and mechanical properties of selective laser melting manufactured Inconel 718 superalloy. *Materials Science and Engineering: A*, 644, 32-40. doi:10.1016/j.msea.2015.06.021
- Zhang, F., Levine, L. E., Allen, A. J., Campbell, C. E., Lass, E. A., Cheruvathur, S., . . . Idell, Y. (2017). Homogenization Kinetics of a Nickel-based Superalloy Produced by Powder Bed Fusion Laser Sintering. *Scr Mater*, 131, 98-102. doi:10.1016/j.scriptamat.2016.12.037
- Zhang, H., Qin, S., Li, H., Liu, J., Lv, Y., Wang, Y., . . . Wu, T. (2018). EBSD study of strain dependent microstructure evolution during hot deformation of a typical nickel-based superalloy. *Journal of Materials Research*, 34(2), 321-334. doi:10.1557/jmr.2018.393
- Zhang, H., Zhang, K., Jiang, S., Zhou, H., Zhao, C., & Yang, X. (2015). Dynamic recrystallization behavior of a  $\gamma'$ -hardened nickel-based superalloy during hot deformation. *Journal of Alloys and Compounds*, 623, 374-385. doi:10.1016/j.jallcom.2014.11.056
- Zhang, H. K., Xiao, H., Fang, X. W., Zhang, Q., Logé, R. E., & Huang, K. (2020). A critical assessment of experimental investigation of dynamic recrystallization of metallic materials. *Materials & Design*, 193. doi:10.1016/j.matdes.2020.108873
- Zhang, H. R., & Ojo, O. A. (2009). Non-equilibrium liquid phase dissolution of  $\delta$  phase precipitates in a nickel-based superalloy. *Philosophical Magazine Letters*, 89(12), 787-794. doi:10.1080/09500830903292346
- Zhang, H. Y., Zhang, S. H., Cheng, M., & Li, Z. X. (2010). Deformation characteristics of  $\delta$  phase in the delta-processed Inconel 718 alloy. *Materials Characterization*, 61(1), 49-53. doi:10.1016/j.matchar.2009.10.003
- Zhang, J. M., Gao, Z. Y., Zhuang, J. Y., & Zhong, Z. Y. (1999). Mathematical modeling of the hot-deformation behavior of superalloy IN718. *Metallurgical and Materials Transactions A*, 30(10), 2701-2712. doi:10.1007/s11661-999-0310-7
- Zhang, R. Y., Qin, H. L., Bi, Z. N., Li, J., Paul, S., Lee, T. L., . . . Dong, H. B. (2020). Temperature-Dependent Misfit Stress in Gamma Double Prime Strengthened Ni-Base Superalloys. *Metallurgical and Materials Transactions A*, 51(4), 1860-1873. doi:10.1007/s11661-020-05627-1
- Zhang, S., Lin, X., Wang, L., Yu, X., Yang, H., Lei, L., & Huang, W. (2021). Influence of grain inhomogeneity and precipitates on the stress rupture properties of Inconel 718 superalloy fabricated by selective laser melting. *Materials Science and Engineering: A*, 803. doi:10.1016/j.msea.2020.140702

- Zhang, Y., Li, Z., Nie, P., & Wu, Y. (2012). Effect of Heat Treatment on Niobium Segregation of Laser-Cladded IN718 Alloy Coating. *Metallurgical and Materials Transactions A*, 44(2), 708-716. doi:10.1007/s11661-012-1459-z
- Zhang, Y., Wu, L., Guo, X., Kane, S., Deng, Y., Jung, Y.-G., . . . Zhang, J. (2017). Additive Manufacturing of Metallic Materials: A Review. *Journal of Materials Engineering and Performance*, 27(1), 1-13. doi:10.1007/s11665-017-2747-y
- Zhao, D. (1993). Temperature correction in compression tests. *Journal of Materials Processing Technology*, 36(4), 467-471. doi:10.1016/0924-0136(93)90058-e
- Zhao, X., Chen, J., Lin, X., & Huang, W. (2008). Study on microstructure and mechanical properties of laser rapid forming Inconel 718. *Materials Science and Engineering: A*, 478(1-2), 119-124. doi:10.1016/j.msea.2007.05.079
- Zhao, Z. L., Ning, Y. Q., Guo, H. Z., Yao, Z. K., & Fu, M. W. (2015). Discontinuous yielding in Ni-base superalloys during high-speed deformation. *Materials Science and Engineering: A*, 620, 383-389. doi:10.1016/j.msea.2014.10.041
- Zouari, M., Bozzolo, N., & Loge, R. E. (2016). Mean field modelling of dynamic and post-dynamic recrystallization during hot deformation of Inconel 718 in the absence of  $\delta$  phase particles. *Materials Science and Engineering: A*, 655, 408-424. doi:10.1016/j.msea.2015.12.102
- Zouari, M., Logé, R., & Bozzolo, N. (2017). In Situ Characterization of Inconel 718 Post-Dynamic Recrystallization within a Scanning Electron Microscope. *Metals*, 7(11). doi:10.3390/met7110476